The Dissertation Committee for Chanseok Jeong
certifies that this is the approved version of the following dissertation:

On an inverse-source problem for elastic wave-based enhanced oil recovery

Committee:

Loukas F. Kallivokas, Supervisor

Chun Huh, Co-Supervisor

Omar Ghattas

Larry W. Lake

Lance Manuel

Kenneth H. Stokoe II

On an inverse-source problem for elastic wave-based enhanced oil recovery

by

Chanseok Jeong, B.S., M.S.E.

DISSERTATION

Presented to the Faculty of the Graduate School of
The University of Texas at Austin
in Partial Fulfillment
of the Requirements
for the Degree of

DOCTOR OF PHILOSOPHY

THE UNIVERSITY OF TEXAS AT AUSTIN
August 2011

Dedicated to my family.

Acknowledgments

I would like to express my sincere gratitude to my esteemed advisor Prof. Loukas F. Kallivokas whose guidance and support made this research possible. I really appreciate his valuable advices, care, and patience during my life-changing graduate studies. I also owe my deepest gratitude to my co-advisor Prof. Chun Huh for kindly mentoring me, as well as sharing his unparalleled research experience. This is also a great opportunity to express my respect to Prof. Larry W. Lake for his encouragement and thorough review of my research progress. I would also like to convey many thanks to Professors Omar Ghattas, Lance Manuel, and Kenneth H. Stokoe II for serving on my dissertation committee and for their helpful suggestions.

This work has been partially supported by an Academic Excellence Alliance grant with King Abdullah University of Science and Technology, in Saudi Arabia, by the Department of Petroleum and Geosystems Engineering at UT Austin, by Schlumberger, by the William S. Livingston Fellowship at UT Austin, and by the Society of Petroleum Engineers STAR Fellowship. This support is gratefully acknowledged.

I cannot be more grateful to Dr. Sezgin Kucukcoban for generously allowing me to use his two-dimensional elastic wave forward code for my inverse-source problem. Special acknowledgments also to Dr. Wen Deng for his evaluation of the threshold-acceleration level corresponding to the rock properties that I provided with him, as well as Dr. Jinho Lee for his great advice in regard to the verification of the forward numerical solution of Biot's wave equations. In addition, I have truly enjoyed sharing knowledge and scientific interests with my graduate school friends, especially, Arash Fathi, Pranav Karve, Babak Poursartip, and Jinkyu Park.

I am also pleased to thank Jeremy Schiff and other friends in Austin, Suhyun Kim in Dallas, and Gunwhi Kim in Seoul for their warm friendship and encouragement in regard to my Ph.D. studies. Lastly, I dedicate this dissertation to my family and greatly appreciate their endless love and support toward me.

On an inverse-source problem for elastic wave-based enhanced oil recovery

Publication No. ______________

Chanseok Jeong, Ph.D.
The University of Texas at Austin, 2011

Supervisor: Loukas F. Kallivokas
Co-Supervisor: Chun Huh

Despite bold steps taken worldwide for the replacement or the reduction of the world's dependence on fossil fuels, economic and societal realities suggest that a transition to alternative energy forms will be, at best, gradual. It also appears that exploration for new reserves is becoming increasingly more difficult both from a technical and an economic point of view, despite the advent of new technologies. These trends place renewed emphasis on maximizing oil recovery from known fields. In this sense, low-cost and reliable enhanced oil recovery (EOR) methods have a strong role to play.

The goal of this dissertation is to explore, using computational simulations, the feasibility of the, so-called, seismic or elastic-wave EOR method, and to provide the mathematical/computational framework under which the method can be systematically assessed, and its feasibility evaluated, on a

reservoir-specific basis. A central question is whether elastic waves can generate sufficient motion to increase oil mobility in previously bypassed reservoir zones, and thus lead to increased production rates, and to the recovery of otherwise unexploited oil.

To address the many questions surrounding the feasibility of the elastic-wave EOR method, we formulate an inverse source problem, whereby we seek to determine the excitations (wave sources) one needs to prescribe in order to induce an *a priori* selected maximization mobility outcome to a previously well-characterized reservoir. In the industry's parlance, we attempt to address questions of the form: *how does one shake a reservoir?*, or *what is the "resonance" frequency of a reservoir?*.

We discuss first the case of wellbore wave sources, but conclude that surface sources have a better chance of focusing energy to a given reservoir. We, then, discuss a partial-differential-equation-constrained optimization approach for resolving the inverse source problem associated with surface sources, and present a numerical algorithm that robustly provides the necessary excitations that maximize a mobility metric in the reservoir. To this end, we form a Lagrangian encompassing the maximization goal and the underlying physics of the problem, expressed through the side imposition of the governing partial differential equations. We seek to satisfy the first-order optimality conditions, whose vanishing gives rise to a systematic process that, in turn, leads to the prescription of the wave source signals.

We explore different (indirect) mobility metrics (kinetic energy or accel-

eration field maximization), and report numerical experiments under three different settings: (a) targeted formations within one-dimensional multi-layered elastic solids system of semi-infinite extent; (b) targeted formations embedded in a two-dimensional semi-infinite heterogeneous elastic solid medium; and (c) targeted poroelastic formations embedded within elastic heterogeneous surroundings in one dimension.

The numerical experiments, employing hypothetical subsurface formation models subjected to, initially unknown, ground surface wave sources, demonstrate that the numerical optimizer leads robustly to optimal loading signals and the illumination of the target formations. Thus, we demonstrate that the theoretical framework for the elastic wave EOR method developed in this dissertation can systematically address the application of the method on a reservoir-specific basis. From an application point of view and based on the numerical experiments reported herein, for shallow reservoirs there is strong promise for increased production. The case of deeper reservoirs can only be addressed with further research that builds on the findings of this work, as we report in the last chapter.

Table of Contents

List of Tables

List of Figures

Chapter 1

Introduction

1.1 Background

While the total global demand for hydrocarbon energy resources is projected to either remain the same or grow in the upcoming decades, the exploration for new hydrocarbon reserves, most of which are located offshore, would likely become even more onerous than it currently is [35, 51]. This persistent demand for hydrocarbon energy sources, coupled with the difficulties associated with the exploration and exploitation of new fields, has renewed emphasis on improving the efficiency of oil recovery from existing reservoirs by using enhanced oil recovery (EOR) methods [51].

Due to the strong capillarity that exists in oil and rock systems, and the highly variable permeability of an oil reservoir, only 30–50% of the original-oil-in-place (OOIP) can be produced either by a reservoir's primary oil recovery mode (natural pressure), or by a combination of water-flooding and natural pressure. Thus, in order to recover any oil still remaining in an existing reservoir, EOR methods, such as gas- and polymer-flooding, are usually employed [52, 53]. By and large, and beyond site-specific technical reasons that are also of importance, the choice of a specific EOR method is chiefly driven by economic considerations. Hence, any low-cost EOR method that is also reliable becomes a strong contender for the exploitation of the remaining reservoir capacity.

The wave-based EOR method has been proposed as one such cost-effective EOR method. The key idea behind the wave-based EOR method is that traveling waves, however they may be generated, could "shake" a reservoir sufficiently to mobilize the remaining oil, which could then be recovered by conventional means. Wave sources typically used in wave-based EOR include Vibroseis equipment atop the ground surface, and/or wellbore hydraulic pumps [15], or wellbore seismic vibrators [63, 82]. All sources are capable of generating, directly or indirectly, elastic waves. In general, it has been observed and reported that the rate of oil production increased after such applications of vibratory excitations. It also appears that such wave-based EOR methods are at least as competitive as conventional EOR methods. Firstly, because the wave-based EOR is less costly than other EOR methods [33, 79], and, secondly, because an elastic wave can indiscriminately illuminate the entire volume of an oil reservoir, whereas, due to the heterogeneity of a typical reservoir, gas- or chemical-flooding can hardly sweep it in its entirety.

The feasibility of the wave-based EOR is supported by a set of field observations showing that elastic waves induce increased production of the remaining oil. For example, it has been observed that the rate of oil production and/or the oil-water-cut ratio improve for several days following a seismic event in the broader region of an existing oil reservoir [60, 75, 77, 81]. Increased oil production has also been reported during field experiments employing wave sources at low frequencies, up to 200Hz, located atop the ground surface or within a wellbore, in active or in seemingly-depleted oil fields [5, 27, 42, 43, 44, 49, 50, 76, 83, 85].

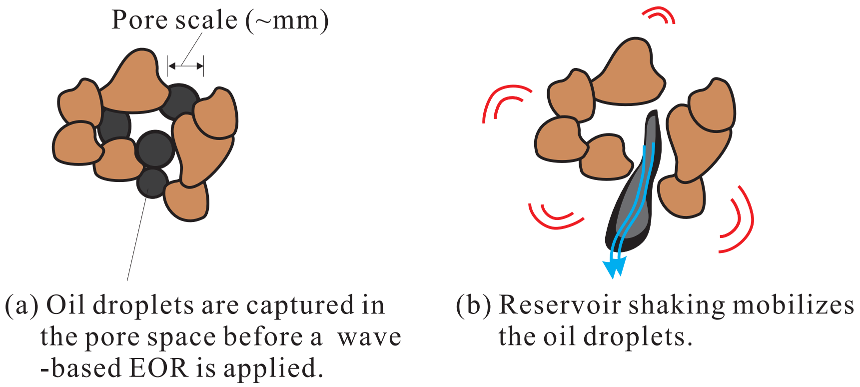

(a) Oil droplets are captured in the pore space before a wave-based EOR is applied.

(b) Reservoir shaking mobilizes the oil droplets.

Figure 1.1: The mobilization of trapped oil droplets in pore space by the vibration of the pore wall surface.

In addition to the field evidence, there have also been investigations on the underlying mechanisms of the wave-based EOR method. The suggested predominant mechanism postulates that the movement of the pore walls can mobilize oil droplets trapped in pore spaces [3, 8, 11, 31]. That is, the vibration of pore walls can dislodge the trapped droplets and coalesce them into larger ones, allowing them to be mobilized and flow (see the illustration in Fig. 1.1).

A set of experimental studies, employing ultrasound waves, have supported the dislodging mechanism of oil droplets by means of shaking of the rock matrix. Laboratory experiments using ultrasonic waves at frequencies larger than 20kHz [2, 28, 29, 30] targeting the mobilization of oil droplets in oil-saturated sandstone core samples showed that such ultrasound waves increased the recovery rate up to 25% of OOIP. However, using ultrasound waves will not lead to the mobilization of oil droplets at the reservoir scale, because waves at such high frequencies attenuate rapidly with distance [66, 68].

On the other hand, there are laboratory tests that have demonstrated dislodging of oil droplets by using elastic, or acoustic, or fluid-pressure wave sources at a low frequency range. Roberts et al.[8, 66, 67, 68] showed that dynamic stress exerted upon a solid rock matrix of a sandstone core at a low frequency (10 to 100Hz) can release trapped oil droplets. Vogler and Constantinos [80] also showed that acoustic waves of frequencies up to 300Hz can remove the nonaqueous phase liquid (NAPL) from porous permeable core samples. Spanos et al.[76] conducted experiments that showed that fluid-pressure pulsing at a frequency ranging from 30 to 60Hz can increase the oil recovery rate from confined sand packs.

In addition, Beresnev and Iassonov [34] developed a threshold capillary-trapping model: an inertial force, induced by the elastic wave on a trapped oil droplet, should exceed a threshold level in order for the trapped oil droplet to overcome the capillary force. From subsequent experiments [55] and numerical simulations [9, 10], they concluded that the acceleration of the rock matrix should be in the order of 0.1 to 10m/s^2 or more to induce oil mobilization. They further showed that such a threshold acceleration level varies depending on the average size of the pore space, the background pressure-gradient, the wave frequency, the viscosity of the remaining oil, and the capillary pressure.

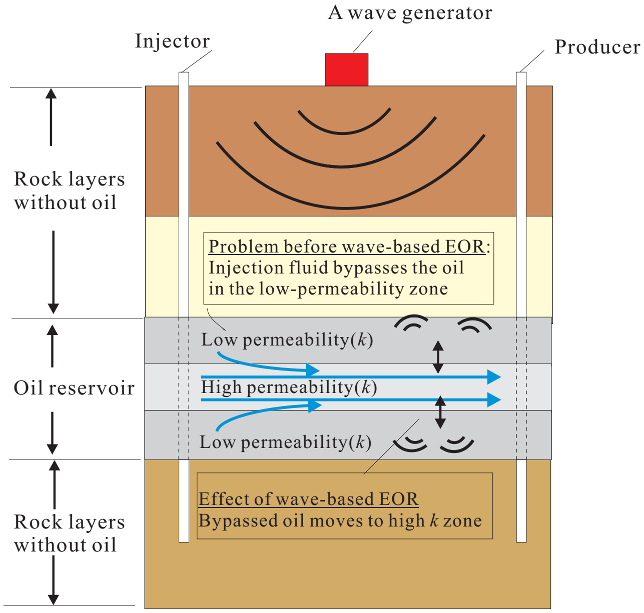

Figure 1.2: Elastic wave induces cross-flow oscillation at the interfaces between different permeability areas.

It has also been argued that reservoir shaking can lead to cross-flow at the interfaces between low- and high-permeability areas in a highly heterogeneous reservoir or in a fractured reservoir [4, 26, 33, 61, 78, 79]. In a heterogeneous reservoir, the elastic waves induce pore-pressure oscillation between layers of different permeability [4, 33]. Such pressure oscillation between areas of different permeability can effectively coax out the bypassed oil from the low- to the high-permeability area (see the illustration in Fig. 1.2). In a fractured reservoir, the direct application of hydraulic wave sources to a fracture can induce a periodic pressure gradient between a fracture and its surrounding rock matrix such that the transport of bypassed oil from the rock matrix to the fracture space can be enhanced [26, 36, 61, 78, 79] (see Fig. 1.3).

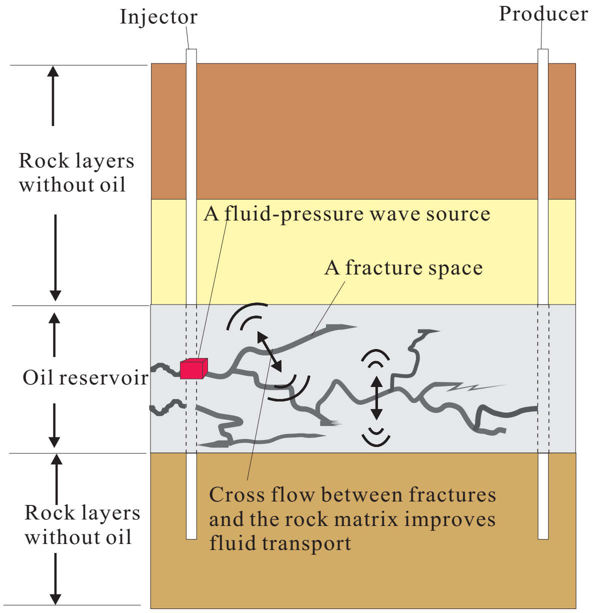

Figure 1.3: Wellbore hydraulic pumps induce cross-flow at the interface between a fracture space and surrounding rock matrix.

1.2 Research issues

The review of field observations and laboratory experiments discussed in the preceding section suggests that exposure of a reservoir to wave-induced motion may lead to increased oil mobility, and therefore facilitate increased recovery rates. To date, there have been no theoretical studies that examine the feasibility of a wave-based EOR method. This dissertation seeks to address questions that arise when a wave-based EOR method is considered. These questions include:

- Could wellbore-originating excitations generate sufficient energy to mobilize oil?

- Could surface sources generate sufficient energy to, again, increase oil mobility?
- At which frequency(ies) should the sources be operating?
- Are there conditions that could induce near-resonance conditions to an existing reservoir?
- Should the excitation signals be monochromatic, or could they be transient? (Narrowband? or Broadband?)
- Does the placement of the sources influence the induced motion?
- Can, in general, wave energy be directed and focused to a target formation by the judicious deployment and timing of sources?

Formally, to answer most of the above questions, there is a need to formulate the associated mathematical problem as an inverse-source problem. That is, for a known geostructure, containing a target formation (reservoir), and with an a priori selected maximization outcome in mind (e.g., maximum kinetic energy at the reservoir), one seeks to determine the input excitations that will realize the desired outcome.

The geostructure is first considered elastic, and in later developments poroelastic, yet arbitrarily heterogeneous in both cases. Sources are deployed on the ground surface. Due to the semi-infinite extent of the physical domain, Perfectly-Matched-Layers are used to truncate the physical domain in order to render it finite and, thus, computationally feasible.

In mathematical terms, the problem of finding the excitation signals in the time-domain, is cast as an inverse-source problem. We define a Lagrangian comprising a functional describing the metric we seek to maximize, augmented by the side-imposition of the problem's PDEs. We use the apparatus of partial-differential-constrained-optimization to resolve the ensuing minimization problem (we seek to maximize a desired metric by casting the problem as the minimization of the metric's reciprocal). Satisfaction of the first-order optimality conditions leads to a triad of state, adjoint, and control problems. We use finite elements to resolve the state and adjoint problems, and use the control problem to update the excitation signals until convergence.

We report numerical experiments for each of the physical problems considered in this research.

1.3 Dissertation outline

This dissertation is organized in a manner that attempts to incrementally address the research questions posed in section 1.2. Specifically:

In chapter 2, we discuss the feasibility of mobilizing remaining oil by means of time-harmonic fluid action at the wellbore. To this end, we examine both the closed-form solutions of rock stress waves in a homogeneous reservoir, as well as fluid-pressure waves within a fractured reservoir, induced by a wellbore hydraulic pump wave source [36]. Firstly, we investigate whether waves, induced by fluid-pressure oscillations at frequencies 0.1–200Hz at the well site, and propagating radially and away from the source in a homogeneous reservoir, can lead to the mobilization of trapped oil droplets in pore space. The numerical results show that neither a rock-stress wave nor a pore-pressure wave is likely to result in any significant remaining oil mobilization at the reservoir scale, unless the amplitude of the wave response is significantly large, as also noted in [65]. Secondly, we consider a simple one-dimensional fracture with a time-harmonic fluid injection at low frequencies (0.1-10Hz) into the fracture space. A sufficient rate of cross-flow has been observed between a fracture and the surrounding rock matrix to allow an enhanced imbibition of the injecting fluid into the rock matrix, as well as the coaxing-out of the bypassed oil from the rock matrix.

Although the modeling studies reported in chapter 2 demonstrate a desired outcome, they are based on the assumption that there will be wave sources of sufficient strength and other conditions favorable to impart oil mobilization at the reservoir scale. For instance, certain wave sources, operating within a particular frequency spectrum, could generate a resonance-like behavior of an oil reservoir. The resonance-like behavior would give rise to large rock motion within the reservoir such that the dislodging of the trapped oil droplets or the generating cross-flow could be feasible. Employing fleets of surface wave sources, for example, could impart wave-induced oil mobilization at the reservoir scale. In chapter 3, we discuss the inverse-source approach that can inversely compute the optimal loading time signal of such ground surface wave sources, leading to the maximization of desired metrics, such as, the kinetic energy or acceleration of the solid rock matrix in a selected reservoir formation [37]; for simplicity, we consider first one-dimensional compressional wave physics for semi-infinite layered media.

The numerical results of the one-dimensional modeling show that there is a set of amplification frequencies that lead to amplification of the wave motion in the targeted formation; loading signals operating, at a different set of amplification frequencies can also selectively maximize the wave energy within the target layer, while the adjacent formations stay relatively dormant. We should point out that our numerical optimizer successfully identifies optimal loading time signals with strong dominant frequency components that coincide with the exact or analytically computed amplification frequencies. The inverted excitations are well within the capability range of present-day equipment, and induce significant acceleration fields, which, in turn, appear to be capable of mobilizing oil in existing reservoirs in this one-dimensional setting.

We note that the one-dimensional setting is overly simplistic in at least two ways: first, one-dimensional excitation conditions are impossible to replicate in practice; second, the undamped one-dimensional model we adopted ignores all of the three attenuation mechanisms that are typically associated with the passage of waves in the Earth, i.e., radiation attenuation due to an expanding wave-front, intrinsic attenuation due to wave energy conversion to heat, and apparent attenuation due to scattering effects. As a result, the energy demand that is needed to attain, in practice, what one-dimensional analysis would predict is, in general, underestimated.

In chapter 4, we discuss the extension of the one-dimensional modeling to the more realistic two-dimensional setting. In this setting, we use the governing elastic wave equations endowed by Perfectly-Matched-Layers (PMLs) [46, 45, 47]. Such a two-dimensional setting is subject to the following two assumptions: first, the strip loading is stretched infinitely in a direction that is perpendicular to the cross-sectional plane (see Fig. 4.1), and second, the undamped two-dimensional model also ignores intrinsic and apparent attenuation, but captures radiation damping. We should point out that such a two-dimensional wave response can be replicated, in practice, using a fleet of Vibroseis equipments under the assumption of lateral homogeneity. Thus, based on Beresnev's threshold-acceleration criteria [9], the ensuing feasibility studies with the two-dimensional problem could reveal whether or not oil mobilization is possible by using ground surface wave sources. In general, and within the constraints of the two-dimensional setting, the numerical results show that our methodology can successfully obtain the signals necessary for inducing oil mobility in target reservoirs.

In chapter 5, we switch from elastic to poroelastic assumptions, and discuss the mathematical and numerical modeling for the identification of source time signals that can maximize the relative wave motion of the pore fluid with respect to the solid rock matrix within a porous heterogeneous permeable rock formation that is surrounded by non-permeable elastic rock formations of semi-infinite extent. We also describe the mixed finite element formulation and numerical implementation used to compute the forward wave responses of the rock matrix, as well as the pore fluid within the poroelastic formations.

The numerical results show that the optimization procedure leads to loading time signals that include the correct amplification frequencies.

Lastly, in chapter 6, we summarize the conclusions we draw from the research reported in this dissertation, and discuss future directions. We note that parts of the research reported in this dissertation have already been published [36, 37, 38].

Chapter 2

Oil mobilization via wellbore sources

It is of interest to examine whether wave sources can sufficiently stimulate a hydrocarbon formation to overcome the mobility threshold of the remaining oil. Of particular interest here is whether the waves traveling through the matrix are better energy-delivery agents than the fluid pore-pressure wave, or vice-versa. In this chapter, we study numerically the potential for oil mobility stimulation at the reservoir-scale that is due to the vibrations induced by means of a wellbore hydraulic pressure wave source (Fig. 2.1). We do so using simplified models, in an attempt to quantify the potential for increasing oil mobility. The situation where the sources are located on the ground surface is discussed in subsequent chapters.

In the first part of this chapter, we report on the wave motion solution in a homogeneous oil reservoir. Here, we study two scenarios, depending on whether the fluid or the matrix is excited (but we do not consider the coupled poroelastic case). To assess the feasibility of oil mobilization at the pore-space, we use a recently developed correlation between the oil mobilization index [33] and the wave-induced displacement field. In the second part of this chapter, we investigate whether vibrational energy can induce cross-flow in a fractured reservoir. We then examine whether a sufficient rate of cross-leakage flow could arise to displace oil from the rock formation into the reservoir fractures.

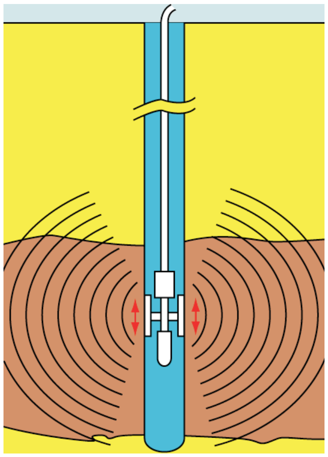

Figure 2.1: Schematic of wellbore wave source.

2.1 Wellbore-generated wave in a homogeneous reservoir

To assess the feasibility of mobilizing typically bypassed oil by vibrational means, we examine the closed-form solutions of the time-harmonic wave motion in a homogeneous reservoir induced by a wellbore-pressure wave source. For simplicity, we treat the axisymmetric problem, whereby the source is assumed to act on the walls of a well of infinite depth (Fig. 2.2).

We obtain solutions for two limiting cases: (i) the pore-pressure wave arising when the fluid alone is excited; and (ii) the stress wave of the reservoir rock arising when the matrix alone is excited. By comparing the wave behavior of these two limiting cases, we try to assess the effectiveness of delivering

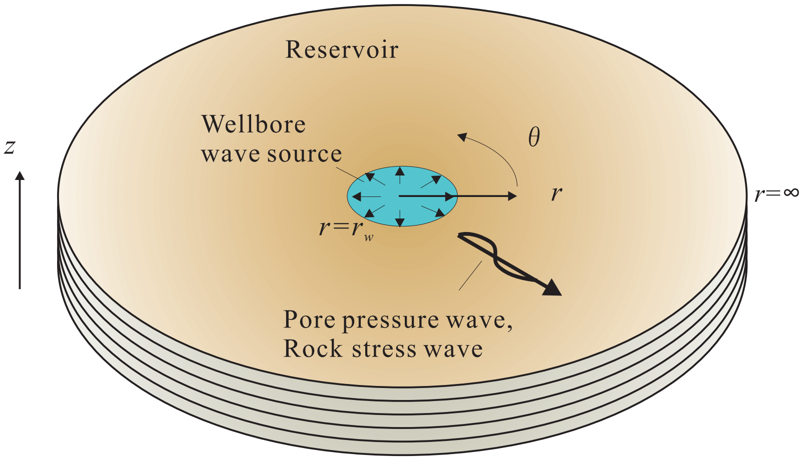

Figure 2.2: Wave propagation in a permeable elastic medium induced by a wellbore hydraulic pump wave source.

vibrational energy at a distance from the wellbore source.

2.1.1 The fluid-pressure wave in a homogeneous reservoir

To estimate how the pressure waves propagate into the reservoir, we adopt the following transient pressure diffusion equation that is commonly employed to interpret pressure test results [56, 57]:

$$\nabla^2 p(r,t) = \frac{\phi \eta c_t}{k_r} \frac{\partial p(r,t)}{\partial t}, \tag{2.1}$$

where $p(r,t)$ is the fluid pressure; r denotes radial coordinate; t is time; η is viscosity; k_r is permeability; ϕ is porosity; and $c_t = c_w + c_r$ denotes total compressibility with c_w being the fluid, and c_r the rock compressibility. Implicit in this approach is the assumption that the pressure oscillation generated at the well wall propagates only through the pore space, while the reservoir rock remains dormant. Assuming further that the pore-pressure wave propagates only in the radial direction, the pressure distribution can be calculated from:

$$\frac{1}{r}\frac{\partial}{\partial r}\left(r\frac{\partial p(r,t)}{\partial r}\right) = \frac{\phi\eta c_t}{k_r}\frac{\partial p(r,t)}{\partial t}, \tag{2.2}$$

The boundary condition at the well wall ($r = r_w$) is:

$$p(r_w, t) = \hat{p}_w e^{i\omega t}, \tag{2.3}$$

where $\hat{p}_w$ is the input pressure amplitude (this pressure is in addition to the static reservoir pressure). At the far field, there also holds:

$$\lim_{r\to\infty} p(r,t) = 0. \tag{2.4}$$

Since the generated pressure wave will also be harmonic, i.e., $p(r,t) = \hat{p}(r)e^{i\omega t}$, (2.2) reduces to:

$$\frac{\partial^2 \hat{p}}{\partial r^2} + \frac{1}{r}\frac{\partial \hat{p}}{\partial r} - \beta^2 \hat{p} = 0, \quad \text{with} \quad \beta^2 = \frac{i\omega\phi\eta c_t}{k_r}. \tag{2.5}$$

The general solution to the above equation is [1]:

$$\hat{p}(r) = a_1 I_0(\beta r) + a_2 K_0(\beta r), \tag{2.6}$$

where I_0 and K_0 are the zeroth-order modified Bessel functions of the first and second kind, respectively. To satisfy the radiation condition, (2.4), a_1 should vanish. Then, using the boundary condition, (2.3), there results:

$$\hat{p}(r) = \hat{p}_w \frac{K_0(\beta r)}{K_0(\beta r_w)}. \tag{2.7}$$

Pore-pressure wave amplitude decay in a homogeneous reservoir

Because the pressure propagation in the reservoir is of a diffusive nature, the pressure oscillation amplitude decreases with distance from the wellbore, largely depending on the pressure diffusivity parameter $\beta^2 = i\omega\phi\eta c_t/k_r$. Fig. 2.3 shows the effects of the oscillation frequency (ω) on the pressure amplitude (normalized with respect to the source amplitude $\hat{p}_w$), as a function of the radial distance r from the wellbore (the curves are shown on a semilog scale; the ordinate represents the modulus of the pressure amplitude $\hat{p}(r)$, which is, in general, complex). For the curves shown, we used $\eta = 1$cp (=0.001Pa·s), $k_r = 100$md $(= 9.87\times10^{-14}\text{m}^2)$, $\phi = 0.3$, $r_w = 0.06$m, and $c_t = 1.5\times10^{-9}\text{Pa}^{-1}$.

We observe that the pressure amplitude decreases very rapidly with distance, unless the frequency is extremely low. This is expected since, due to the tortuosity of the pore space, the pressure wave attenuates fairly fast. In general, the pressure wave propagation is governed by the pressure diffusivity: as the fluid viscosity or the compressibility increases, or the permeability decreases, the diffusivity β increases, and the pressure amplitude attenuates more sharply. We discuss next the elastic (rock) wave.

2.1.2 The elastic wave in a homogeneous reservoir

Whereas, owing to the tortuosity of the pore space, the propagation of fluid pressure oscillations through the pore space is highly attenuated, the propagation of elastic deformation in the reservoir rock could be more effective. When a pressure oscillation is applied at the well wall by injecting (or

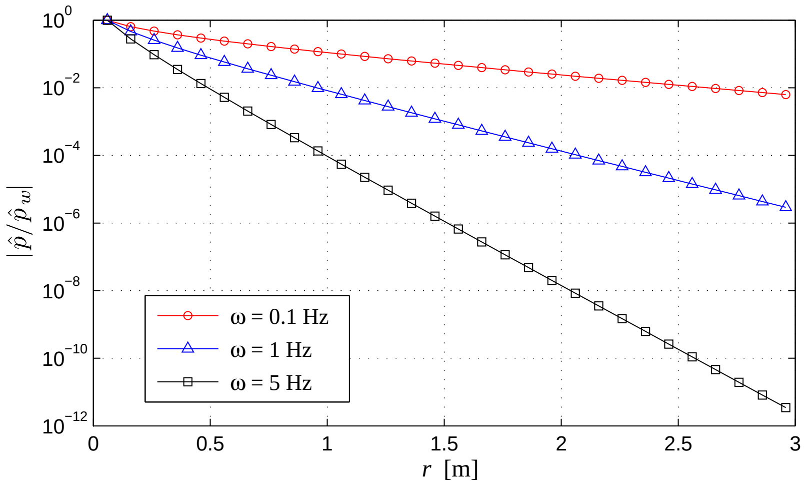

Figure 2.3: Modulus of normalized pressure wave $\hat{p}(r)/\hat{p}_w$ in a homogeneous reservoir – pore pressure solution only as a function of distance from the wellbore source; various excitation frequencies.

producing) a fluid, the rock face at the wellbore will be deformed, and the deformation will propagate through the reservoir's matrix, engaging both the matrix and the fluid. In the interest of an approximate assessment, we will assume that the reservoir is a homogeneous elastic medium, and will not consider the coupled poroelastic case. While highly simplistic, the model allows for the study of the vibrational energy propagation through the reservoir rock.

In a cylindrical coordinate system, the elastic wave motion is governed by the following equations [25]:

$$\begin{aligned}
\frac{\partial \sigma_{rr}}{\partial r} + \frac{1}{r}\frac{\partial \sigma_{r\theta}}{\partial \theta} + \frac{\partial \sigma_{rz}}{\partial z} + \frac{\sigma_{rr} - \sigma_{\theta\theta}}{r} &= \rho \frac{\partial^2 u_r}{\partial t^2}, \\
\frac{\partial \sigma_{r\theta}}{\partial r} + \frac{1}{r}\frac{\partial \sigma_{\theta\theta}}{\partial \theta} + \frac{\partial \sigma_{\theta z}}{\partial z} + \frac{2\sigma_{r\theta}}{r} &= \rho \frac{\partial^2 u_\theta}{\partial t^2}, \\
\frac{\partial \sigma_{rz}}{\partial r} + \frac{1}{r}\frac{\partial \sigma_{\theta z}}{\partial \theta} + \frac{\partial \sigma_{\theta zz}}{\partial z} + \frac{\sigma_{rz}}{r} &= \rho \frac{\partial^2 u_z}{\partial t^2},
\end{aligned} \tag{2.8}$$

where (r, θ, z) denote coordinates; t is time; ρ is the composite density of the matrix and the fluid; u denotes displacement; and σ denotes the stress tensor. Here, we consider the axisymmetric problem, for which there holds: $u_r \neq 0$, $u_\theta = u_z = 0$, $\frac{\partial \cdot}{\partial r} \neq 0$, $\frac{\partial \cdot}{\partial z} = 0$, and $\frac{\partial \cdot}{\partial \theta} = 0$. Then, (2.8) reduces to the following:

$$\frac{\partial \sigma_{rr}}{\partial r} + \frac{\sigma_{rr} - \sigma_{\theta\theta}}{r} = \rho \frac{\partial^2 u_r}{\partial t^2}. \tag{2.9}$$

We assume further the presence of material damping, which we express in terms of a Voigt model [84]. Then, the constitutive law becomes:

$$\sigma_{ij} = \lambda \varepsilon_{kk} \delta_{ij} + 2\mu \varepsilon_{ij} + \lambda' \frac{\partial \varepsilon_{kk}}{\partial t} \delta_{ij} + 2\mu' \frac{\partial \varepsilon_{ij}}{\partial t}, \qquad i, j = r, \theta, \tag{2.10}$$

where λ, μ are the Lamé constants with $\lambda = 2\mu\nu/(1 - 2\nu)$, and ν denoting Poisson's ratio; δ_{ij} is the Kronecker delta; λ' and ν' are viscous loss parameters; ε is the strain tensor, and repeated indices imply summation. Due to the assumption of axisymmetry, the only surviving strain tensor components are:

$$\varepsilon_{rr} = \frac{\partial u_r}{\partial r}, \quad \varepsilon_{\theta\theta} = \frac{u_r}{r}. \tag{2.11}$$

Substitution of (2.10) and (2.11) into the equation of motion, (2.9), results in:

$$\left\{ \frac{\partial^2 u_r}{\partial r^2} + \frac{1}{r} \frac{\partial u_r}{\partial r} - \frac{u_r}{r^2} \right\} + \alpha \frac{\partial}{\partial t} \left\{ \frac{\partial^2 u_r}{\partial r^2} + \frac{1}{r} \frac{\partial u_r}{\partial r} - \frac{u_r}{r^2} \right\} = \frac{1}{c^2} \frac{\partial^2 u_r}{\partial t^2}, \tag{2.12}$$

where c denotes the dilatational wave velocity $c = \sqrt{(\lambda + 2\mu)/\rho}$, and $\alpha = (\lambda' + 2\mu')/(\lambda + 2\mu)$ is the attenuation factor. Assuming a harmonic solution of the form $u_r(r, t) = \hat{u}_r(r) e^{i\omega t}$, (2.12) reduces to:

$$\frac{\partial^2 \hat{u}_r}{\partial r^2} + \frac{1}{r} \frac{\partial \hat{u}_r}{\partial r} - \frac{\hat{u}_r}{r^2} + k^2 \hat{u}_r = 0, \tag{2.13}$$

where $k = \frac{\omega}{c}\sqrt{\frac{1-i\omega\alpha}{1+(\omega\alpha)^2}}$. With the introduction of the auxiliary variable $z = kr$, (2.13) becomes:

$$z^2\frac{\partial^2 \hat{u}_r}{\partial z^2} + z\frac{\partial \hat{u}_r}{\partial z} + (z^2 - 1)\hat{u}_r = 0. \tag{2.14}$$

Equation (2.14) is a Bessel equation of the first-order [1]. The general solution of (2.14) is

$$\hat{u}_r(z) = c_1 H_1^{(1)}(z) + c_2 H_1^{(2)}(z), \tag{2.15}$$

where $H_1^{(1)}(z)$ and $H_1^{(2)}(z)$ are the first-order Hankel functions of the first and second kind, respectively. To obtain the constants in (2.15), we first look at the asymptotic behavior of Hankel functions, $H_1^{(1)}(z)$ and $H_1^{(2)}(z)$ [1] :

$$H_1^{(1)}(z) = H_1^{(1)}(kr) \sim \sqrt{\frac{2}{\pi kr}}e^{i\left(kr-\frac{3\pi}{4}\right)}, \tag{2.16}$$

$$H_1^{(2)}(z) = H_1^{(2)}(kr) \sim \sqrt{\frac{2}{\pi kr}}e^{-i\left(kr-\frac{3\pi}{4}\right)}. \tag{2.17}$$

When the time-dependent term ($e^{i\omega t}$) is taken into account, (2.16) and (2.17) represent incoming and outgoing propagating waves, respectively. Since the generated waves ought to be outgoing, c_1 in (2.15) vanishes, and the general solution for the amplitude of the radial displacement reduces to:

$$\hat{u}_r(r) = c_2 H_1^{(2)}(kr). \tag{2.18}$$

To resolve the last remaining constant c_2, we use the boundary condition at the well wall:

$$\sigma_{rr}(r_w, t) = -\hat{p}_w e^{i\omega t}. \tag{2.19}$$

In the frequency domain, the radial stress component can be cast as:

$$\hat{\sigma}_{rr} = (\lambda + 2\mu)(1 + \alpha i\omega)\hat{\varepsilon}_{rr}, \tag{2.20}$$

where we assumed that $\sigma_{rr} = \hat{\sigma}_{rr} e^{i\omega t}$ and $\varepsilon_{rr} = \hat{\varepsilon}_{rr} e^{i\omega t}$. Then, the following holds [1]:

$$\hat{\varepsilon}_{rr} = \frac{\partial \hat{u}_r(r)}{\partial r} = \frac{\partial}{\partial r}\left[c_2 H_1^{(2)}(kr)\right] = c_2 k \left[H_0^{(2)}(kr) - \frac{1}{kr} H_1^{(2)}(kr)\right]. \tag{2.21}$$

Inserting (2.21) into (2.20), while taking into account the boundary condition (2.19), yields the constant c_2 as:

$$c_2 = -\frac{\hat{p}_w}{(\lambda + 2\mu)(1 + \alpha i\omega)k\left[H_0^{(2)}(kr_w) - \frac{1}{kr_w} H_1^{(2)}(kr_w)\right]}. \tag{2.22}$$

Thus, the solution for the amplitude of the rock displacement in the frequency-domain becomes:

$$\hat{u}_r(r) = -\frac{\hat{p}_w H_1^{(2)}(kr)}{(\lambda + 2\mu)(1 + \alpha i\omega)k\left[H_0^{(2)}(kr_w) - \frac{1}{kr_w} H_1^{(2)}(kr_w)\right]}. \tag{2.23}$$

Rock wave amplitude decay in a homogeneous reservoir

Figures 2.4 and 2.5 show the radial deformation amplitude of the matrix rock $\hat{u}_r(r)$, when there is damping, as a function of distance. We used a wellbore pressure oscillation amplitude $p_w = 2 \times 10^6$Pa, a wave source frequency $\omega = 1$Hz, shear modulus $\mu = 6 \times 10^8$Pa, Poisson's ratio $\nu = 0.3$, mass density $\rho = 2100$kg/m^3, and wave velocity $c = 1000$m/s. Fig. 2.4 shows the real and imaginary parts of $\hat{u}_r(r)$. As the rock deformation propagates, some phase shift also occurs, and with frequency 1Hz, the wavelengths are fairly large, and the resulting motion is quite small. Fig. 2.5 depicts the modulus of $\hat{u}_r(r)$ plotted in semi-log scale as a function of distance and for several excitation frequencies; all curves clearly exhibit the expected exponential decay.

However, a comparison of the pressure wave decay performance shown earlier in Fig. 2.3 for the purely diffusive propagation of the pore fluid, and those of Figures 2.4 and 2.5 for the rock wave case, show much more rapid decay associated with the former case than the latter. In short, it appears that the elastic wave is a more effective vibrational energy delivery agent than the pore-pressure waves, as also mentioned in [65].

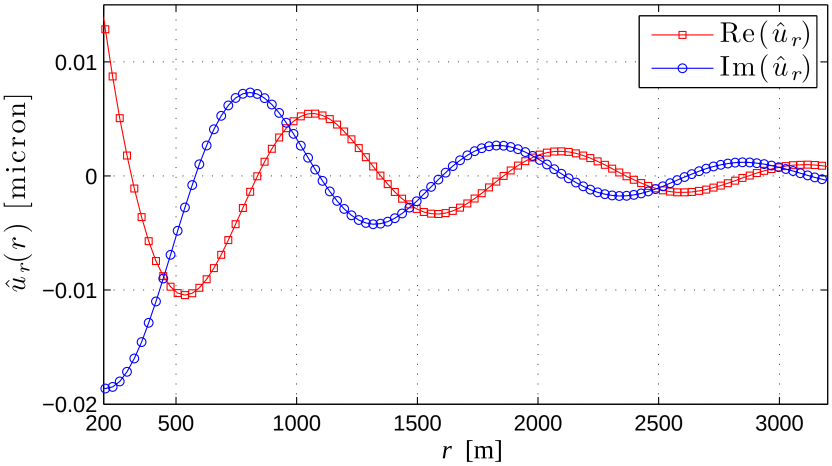

Figure 2.4: Real and imaginary parts of the wave amplitude displacement field $\hat{u}_r(r)$ as a function of distance (rock velocity $c = 1000$m/s, attenuation factor $\alpha = 0.03$s, source frequency 1Hz).

Fig. 2.6 shows the dependence of the amplitude of the stress wave on the attenuation factor. As expected, the rock deformation wave attenuates faster as the attenuation factor increases.

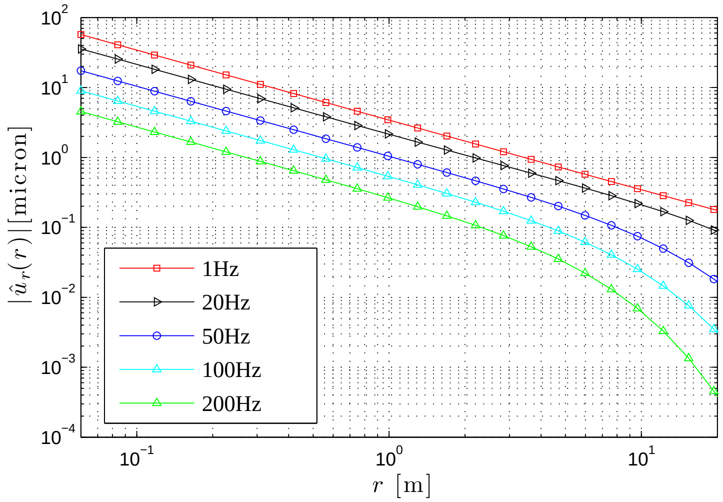

Figure 2.5: Modulus of the displacement field of the rock stress wave $\hat{u}_r(r)$ as a function of distance for several frequencies (wave velocity $c = 1000$m/s, attenuation factor $\alpha = 0.01$s).

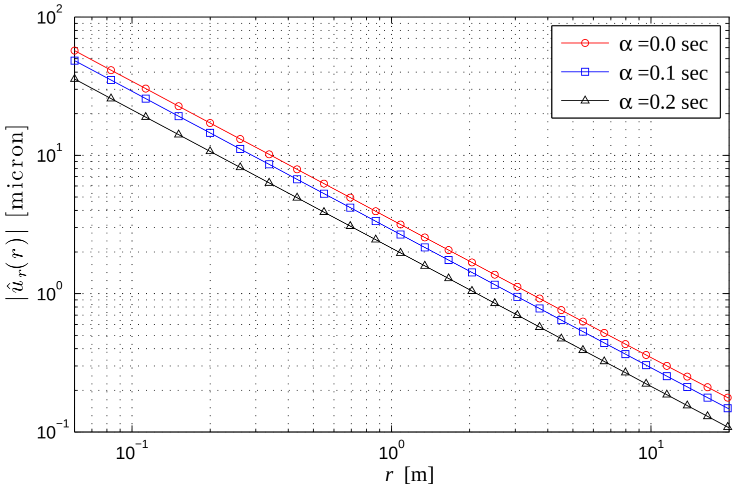

Figure 2.6: Modulus of the displacement field of the rock stress wave $\hat{u}_r(r)$ as a function of distance for several attenuation factors (wave velocity $c = 1000$m/s, frequency 1Hz).

2.1.3 Oil mobility estimation in a homogeneous reservoir

To obtain a qualitative estimate on the effectiveness of the mobilization of oil remaining in a homogeneous reservoir, we adopt the approach proposed in [33] (the Huh model). Figures 2.7 and 2.8 (originally depicted in [33]) show remaining oil displacement efficiency curves in terms of the rock displacement amplitude and the excitation frequency for two different pore radii of 100μm and 200μm, respectively. The underlying approximate model is based on the calculation of the average fluid velocity in a pore in response to rock oscillation, and then estimation of the remaining oil mobilization efficiency by using the well-known Capillary Number Correlation [64]. In Figures 2.7 and 2.8, S_o denotes the post-vibration remaining oil, whereas S_{ori} denotes the remaining oil originally contained in the rock formation. Therefore, $S_o/S_{ori} = 1$ implies that no remaining oil is mobilized, while $S_o/S_{ori} = 0$ means that all remaining oil is mobilized. Figures 2.7 and 2.8 suggest that oil mobilizes more easily: (i) when the rock displacement is larger; (ii) when the excitation frequency is higher, and; (iii) when the pore is wider.

We use the previously obtained rock displacement amplitudes due to the wellbore source as input to the Huh model (for various excitation frequencies), in order to estimate the oil mobilization index S_o/S_{ori}. To this end, Table 2.1 lists the mobilization index in the neighborhood of the wellbore source, i.e., for distances ranging between 0.07 and 5m. We assumed a pore radius of 200μm, attenuation factor $\alpha = 0.01$s, and amplitude of the wellbore pressure oscillation p_w of 2×10^6Pa. As it can be seen from Table 2.1, some oil mobilization occurs at higher frequencies, whereas there is, effectively, no oil mobilization for lower frequencies. For a pore radius of 100μm, which represents lower-permeability rock, the remaining oil mobilization efficiency decreases even further.

In addition to Huh's model for estimating the remaining oil mobilization index, we also use Beresnev's threshold-acceleration level model [9] to examine the mobilization of trapped oil droplets. As discussed in chapter 1, Beresnev suggests that, in general, rock wave motion of which the acceleration amplitude is as large as 0.1 to 10m/s^2, is needed for dislodging such oil droplets trapped in constricted pore space. To employ the Beresnev's model, we compute the modulus of acceleration field of rock wave motion as follows:

$$\begin{aligned} \left| \frac{\partial^2 \hat{u}_r(r)}{\partial t^2} \right| &= |(i\omega)^2 \hat{u}_r(r)| \\ &= \omega^2 |\hat{u}_r(r)|. \end{aligned} \tag{2.24}$$

Fig. 2.9 shows the amplitudes of the acceleration fields of the rock wave motions for wave velocity $c = 1000$m/s and attenuation factor $\alpha = 0.01$s at different frequencies. Fig. 2.9 demonstrates that the acceleration amplitudes of wave response exceeds 0.1 to 10m/s^2 – the Beresnev's suggested threshold-acceleration level – only at the area close to the wellbore ($r < 1$m) and only at frequencies higher than 100Hz.

By employing the aforementioned two oil mobilization-estimation models, we have thus far observed that the mobilization of trapped oil droplets is feasible only in the area close to a wellbore, and only at high frequencies.

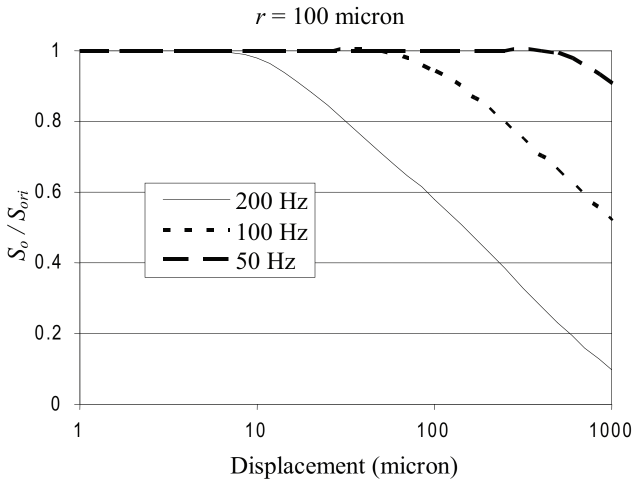

Figure 2.7: Remaining oil displacement efficiency with respect to the rock displacement and the frequency for a pore radius of 100μm [33] ($S_o/S_{ori} = 1$ implies that no remaining oil is mobilized, and $S_o/S_{ori} = 0$ means that all remaining oil is mobilized).

	200Hz		100Hz		50Hz		20Hz	
r(m)	$\|\hat{u}_r\|$(μm)	S_o/S_{ori}	$\|\hat{u}_r\|$(μm)	S_o/S_{ori}	$\|\hat{u}_r\|$(μm)	S_o/S_{ori}	$\|\hat{u}_r\|$(μm)	S_o/S_{ori}
0.07	3.88	0.82	7.70	0.95	14.9	0.99	30.5	1
0.1	2.72	0.89	5.39	0.97	10.4	1	21.4	1
1	0.263	1	0.531	1	1.04	1	2.14	1
5	0.0313	1	0.0808	1	0.186	1	0.435	1

Table 2.1: Mobilization index S_o/S_{ori} at locations proximal to the source; various frequencies ($S_o/S_{ori} = 1$ implies that no remaining oil is mobilized, and $S_o/S_{ori} = 0$ means that all remaining oil is mobilized).

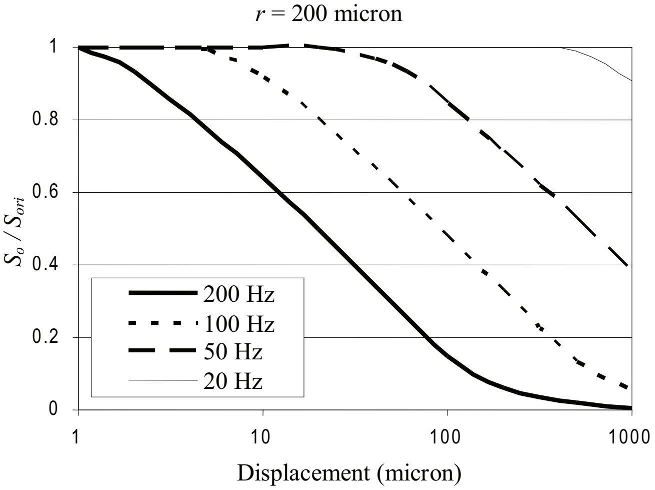

Figure 2.8: Remaining oil displacement efficiency with respect to the rock displacement and the frequency for a pore radius of 200μm [33] ($S_o/S_{ori} = 1$ implies that no remaining oil is mobilized, and $S_o/S_{ori} = 0$ means that all remaining oil is mobilized).

2.2 Time-harmonic water flooding into a fractured reservoir

As discussed in section 2.1, the fluid pore-pressure wave attenuates fairly rapidly with distance because its propagation through the tortuous pore pathways is highly impeded. On the other hand, if the reservoir has a network of fractures which have medium to high permeability, the pressure wave could propagate rapidly through that network, with amplitude that still maintains reasonable magnitude away from the wellbore. The pressure oscillation in a fracture could bring about an exchange of fluids between the fractures and the matrix, thereby potentially enhancing the imbibition of injected water (or surfactant) into the matrix, and the subsequent expulsion of oil from the

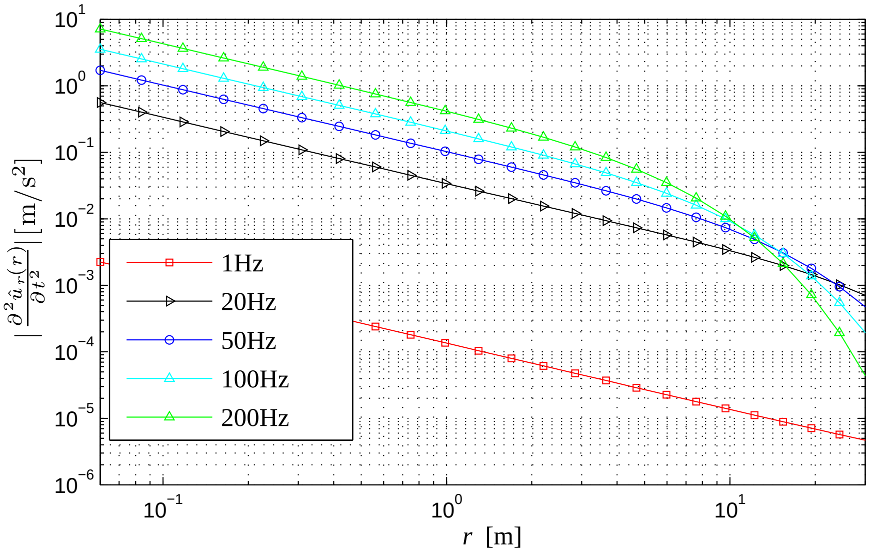

Figure 2.9: Modulus of acceleration of rock stress wave (wave velocity $c = 1000\mathrm{m/s}$ and attenuation factor $\alpha = 0.01\mathrm{s}$).

matrix.

2.2.1 The fluid-pressure wave in a fractured reservoir

In this section, we estimate the pressure distribution in the fracture when fluid oscillations are initiated at the wellbore, and study whether the propagation of pressure waves through a fracture network can effectively induce exchange of fluids between the fracture and the matrix. For simplicity, the propagation of pressure wave is considered in a one-dimensional fracture (Fig. 2.10). We assume that the vertical fracture has a uniform gap width w, length x_f, height h, and constant permeability k_f. We denote by q_f the rate of fluid leakage from the fracture into the matrix zone.

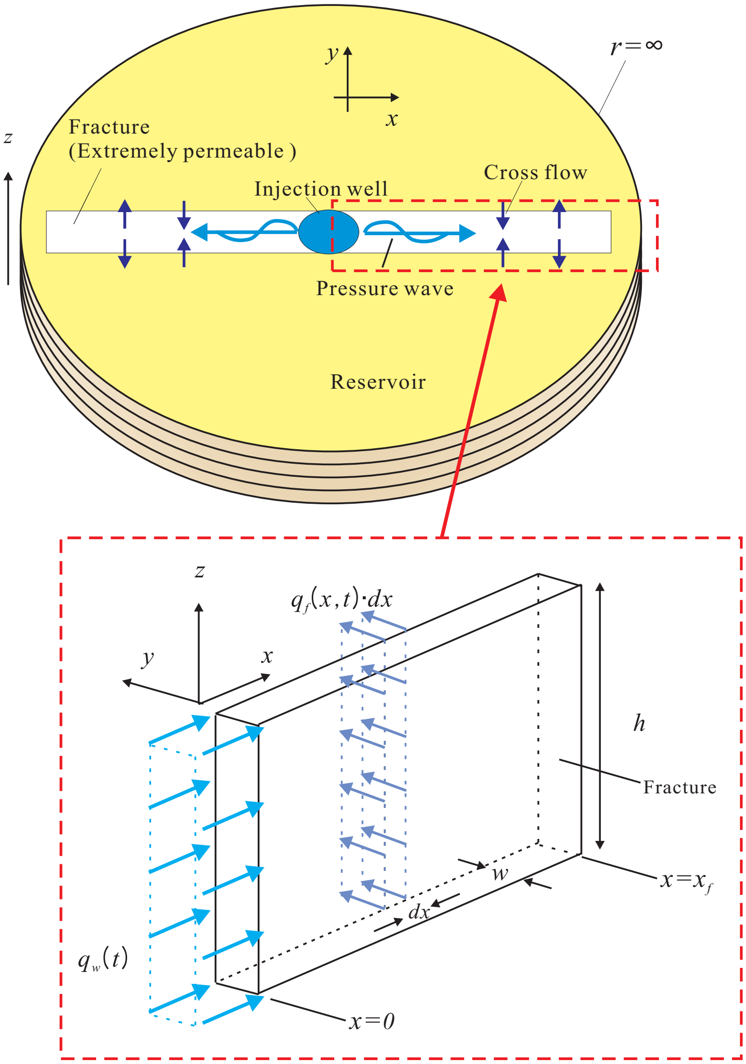

Figure 2.10: Propagation of pressure wave in a fractured reservoir. Fluid is injected into the fracture at a rate of $q_w(t)$, with fluid leaking through the fracture wall at a rate $q_f(x,t)$.

At the wellbore ($x = 0$), a periodic injection/production of fluid is applied with a frequency of ω:

$$q_w(t) = \hat{q}_w e^{i\omega t}, \tag{2.25}$$

where $\hat{q}_w$ is the rate amplitude (q_w, $\hat{q}_w$ denote fluid volume rates). The pressure distribution in such a one-dimensional fracture can be calculated from the pressure transient equation [17]:

$$\frac{\partial^2 p_f(x,t)}{\partial x^2} - \frac{\eta}{k_f}\frac{q_f(x,t)}{wh} = \frac{\phi_f \eta c_{tf}}{k_f}\frac{\partial p_f(x,t)}{\partial t}. \tag{2.26}$$

where $p_f(x,t)$ is the fluid pressure distribution; η is the viscosity; k_f is permeability; ϕ_f is porosity; $c_{tf} = c_w + c_f$, where c_w is fluid compressibility, and c_f is fracture compressibility, and c_{tf} is the total compressibility; and $q_f(x,t)$ is the fluid leakage rate (measured in volume rate per unit length) into the rock formation. The boundary conditions are:

$$\frac{\partial p_f}{\partial x} = -\frac{\eta q_w}{2whk_f}, \quad \text{at} \quad x = 0, \tag{2.27}$$

$$\frac{\partial p_f}{\partial x} = 0, \qquad \text{at} \quad x = x_f. \tag{2.28}$$

The pressure distribution in the surrounding rock matrix formation can be obtained from the pressure transient equation [56, 57]:

$$\left(\frac{\partial^2}{\partial x^2} + \frac{\partial^2}{\partial y^2}\right) p_r(x,y,t) = \frac{\phi_r \eta c_{tr}}{k_r}\frac{\partial p_r(x,y,t)}{\partial t}, \tag{2.29}$$

where $p_r(x,y,t)$ denotes the pressure in the formation, ϕ_r, k_r, and c_{tr} are porosity, permeability, and total compressibility, respectively, for the rock formation. The interface conditions are:

$$p_r = p_f, \qquad \text{at} \quad y = 0 \quad \text{and} \quad 0 \le x \le x_f, \tag{2.30}$$

$$\frac{\partial p_r}{\partial y} = -\frac{\eta q_f}{2hk_r}, \quad \text{at} \quad y = 0 \quad \text{and} \quad 0 \le x \le x_f, \tag{2.31}$$

and the radiation condition is:

$$\lim_{x,y\to\infty} p_r = 0. \tag{2.32}$$

We assume time-harmonic solution of the form:

$$\begin{aligned} p_f(x,t) &= \hat{p}_f(x)e^{i\omega t}, \\ q_f(x,t) &= \hat{q}_f(x)e^{i\omega t}, \\ p_r(x,t) &= \hat{p}_r(x)e^{i\omega t}. \end{aligned} \tag{2.33}$$

We discuss two cases: first, if the leakage effect is assumed to be negligible, (2.26) reduces to the pressure diffusion equation in the fracture:

$$\frac{\partial^2 \hat{p}_f(x)}{\partial x^2} - D_f^2 \hat{p}_f(x) = 0; \quad D_f^2 = \frac{i\omega\phi_f\eta c_{tf}}{k_f}. \tag{2.34}$$

The solution of (2.34) is:

$$\hat{p}_f(x) = a_1 e^{D_f x} + a_2 e^{-D_f x}. \tag{2.35}$$

Using the boundary conditions (2.27) and (2.28), we obtain the amplitude of the pressure in the fracture:

$$\hat{p}_f(x) = \frac{R_f}{D_f}\frac{\cosh[D_f(x_f - x)]}{\sinh[D_f x_f]}, \tag{2.36}$$

where

$$R_f = \frac{\eta \hat{q}_w}{2whk_f}. \tag{2.37}$$

On the other hand, if there is a significant leakage of fluids from the fracture to the formation, (2.26) and (2.29) must be solved simultaneously. Accordingly, we seek solutions of the pressure-wave in the surrounding rock matrix propagating away from the fracture, of the form:

$$p_r(x,y,t) = \hat{p}_{rx}(x) e^{-D_r y} e^{i\omega t}, \qquad D_r^2 = \frac{i\omega \phi_r \eta c_{tr}}{k_r}, \tag{2.38}$$

where $e^{-D_r y}$ represents the outgoing wave motion associated with the time-harmonic term $e^{i\omega t}$. We remark that (2.38) is an approximated form of the pressure-wave in the rock formation[1]. By virtue of the interface conditions (2.30) and (2.31):

$$\hat{p}_{rx}(x) = \hat{p}_f(x) = \frac{\eta \hat{q}_f}{2D_r h k_r}, \tag{2.39}$$

or

$$\hat{q}_f = \hat{p}_f \frac{2D_r h k_r}{\eta}, \tag{2.40}$$

Inserting (2.40) into (2.26) yields:

$$\frac{\partial^2 \hat{p}_f(x)}{\partial x^2} - \left(\overline{D}_f^2\right) \hat{p}_f(x) = 0, \tag{2.41}$$

where

$$\overline{D}_f^2 = \frac{2k_r D_r}{k_f w} + \frac{\phi_f \eta c_{tf} i\omega}{k_f} = \frac{2k_r D_r}{k_f w} + D_f^2. \tag{2.42}$$

---

[1] (2.38) satisfies (2.29), provided that $\frac{\partial^2 \hat{p}_{rx}(x)}{\partial x^2} = 0$.

The solution of (2.41), valid when the leakage effect is not negligible, is obtained as:

$$\hat{p}_f(x) = \frac{R_f}{\overline{D}_f}\frac{\cosh[\overline{D}_f(x_f - x)]}{\sinh[\overline{D}_f x_f]}. \tag{2.43}$$

Combining either (2.36) or (2.43) with (2.38), the resulting amplitude of the pressure distribution within the rock formation becomes:

$$\hat{p}_r(x, y) = \hat{p}_f(x)e^{-D_r y}. \tag{2.44}$$

Pressure wave decay in a fractured reservoir

Figures 2.11 and 2.12 show the effects of the oscillation frequency ω, (a) on the pressure modulus, and (b) on the leakage rate, both of which are given as a function of distance from the wellbore. In Fig. 2.11, the distribution of the pressure modulus is shown for the two cases that depend on whether the leakage effect is ignored or not. The pressure modulus is also shown for different frequencies ranging from 0.1 to 10Hz in Fig. 2.13 (where the leakage effect is taken into account). For all plots we used η = 1cp (= 0.001Pa·s), k_f = 5×10^5md (= 4.935×10^{-10}m^2), k_r = 100md (= 9.870×10^{-14}m^2), $\hat{q}_w$ = 10Barrel/Day (= 1.84×10^{-5}m^3/s), ϕ_f= 0.4, ϕ_r= 0.2, and w= 0.01m, h= 0.3m, x_f=20m, $c_{tr} = 1.5 \times 10^{-10}$Pa^{-1}, and $c_{tf} = 1.5 \times 10^{-9}$Pa^{-1}.

Comparing the pressure amplitude distributions of Figures 2.11 and 2.13 with those for the radial cases of Fig. 2.3, we see that the pressure wave can propagate in the fracture much more effectively, even though the amplitude decreases with distance. As with the radial pressure diffusion cases of Fig. 2.3, and the elastic (rock deformation) cases of Figures 2.4 to 2.6, the pressure wave propagation efficiency decreases with increase in oscillation frequency. We remark that, with leakage into the matrix zone, the modulus of pressure wave in the fracture decreases even further.

Fig. 2.12 shows that the amplitude of the flow rate in and out of the formation neighboring a fracture could be sizeable enough to force the oil out from the rock formation, suggesting that the vibration application to fractured reservoirs could indeed enhance oil recovery from tight matrix zones. We also conjecture that harmonic water injection into a fracture of a lower frequency leads to greater sweep efficiency in a fractured reservoir, as mentioned in [26].

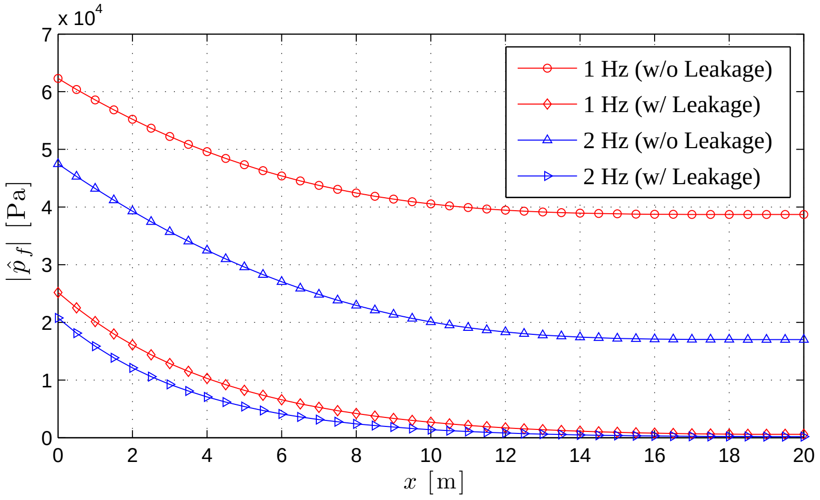

Figure 2.11: Pressure oscillation amplitude versus distance in fracture for two frequencies 1Hz and 2Hz (shown are two cases depending on whether the wall leakage effect is ignored or not)

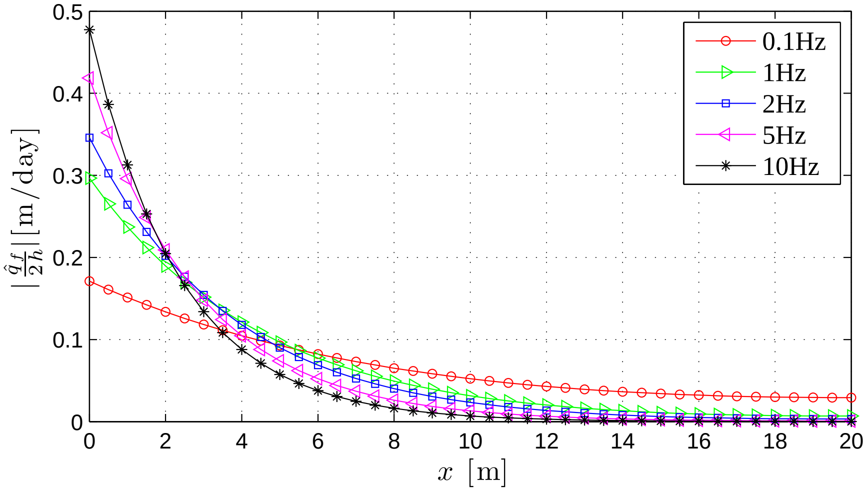

Figure 2.12: Leakage rate amplitude versus distance in fracture for wave frequencies 0.1Hz to 10Hz

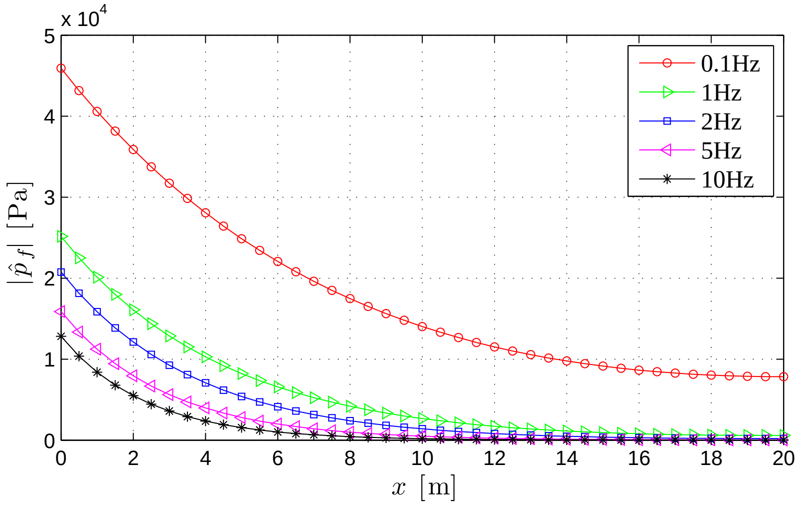

Figure 2.13: Pressure oscillation amplitude versus distance in fracture for wave frequencies 0.1Hz to 10Hz with leakage flow on the fracture wall surface

2.3 Summary

To study the feasibility of vibration-based EOR via wellbore action, in this chapter we used simple prototype problems of homogeneous and fractured reservoirs subjected to wellbore oscillating fluids. We discussed closed-form solutions of time-harmonic wave motions in homogeneous and fractured reservoirs induced by fluid-pressure oscillation imposed at the wellbore. It appears that generating pressure waves in a fractured reservoir can induce cross-flow, which can then displace oil from the rock matrix. In the case of a homogeneous reservoir, it is feasible to stimulate the mobilization of trapped oil droplets in the pore space only if the wave motion is strong enough, which is unlikely with wellbore sources only.

Thus, wellbore action alone does not appear sufficient for inducing oil mobility in non-fractured reservoirs. However, the fact that in non-fractured reservoirs waves traveling through the matrix are better energy-delivery agents suggests that if sufficient energy is imparted to the rock matrix, then, perhaps, oil mobility would be induced. We turn next to surface sources in an attempt to examine whether they could deliver and focus energy better than localized wellbore sources.

Chapter 3

Oil mobilization via ground sources – The elastic inverse-source problem in 1D

When ground sources are used to induce oil mobility, the questions are multifold: which frequencies must the sources operated at? or, which transient signals must be used to drive the sources so that the motion be maximized within the reservoir? To answer these questions, we adopt an inverse-source approach: in this chapter, we discuss an optimization problem for the identification of an optimal time signal that can maximize a desired motion metric (kinetic energy or acceleration) of a rock matrix in a targeted formation within a one-dimensional layered medium of semi-infinite extent. To this end, we cast the problem into a minimization problem by employing the reciprocal of a functional expressing the spatial and temporal integral of the desired metric within the target zone.

The objective functional is then augmented by the side imposition of the governing partial differential equation, and associated conditions, via Lagrange multipliers. The satisfaction of the first-order optimality conditions of the augmented functional gives rise to state, adjoint, and control problems; we numerically solve these problems using the finite element method. Numerical experiments show that such an optimization scheme successfully leads to the following sought-after objectives: (a) the maximization of the kinetic energy or acceleration of the target layer with all layers active; and (b) the maximization of the kinetic energy or acceleration of the target layer while the adjacent formations are forced to remain relatively dormant.

3.1 Problem definition

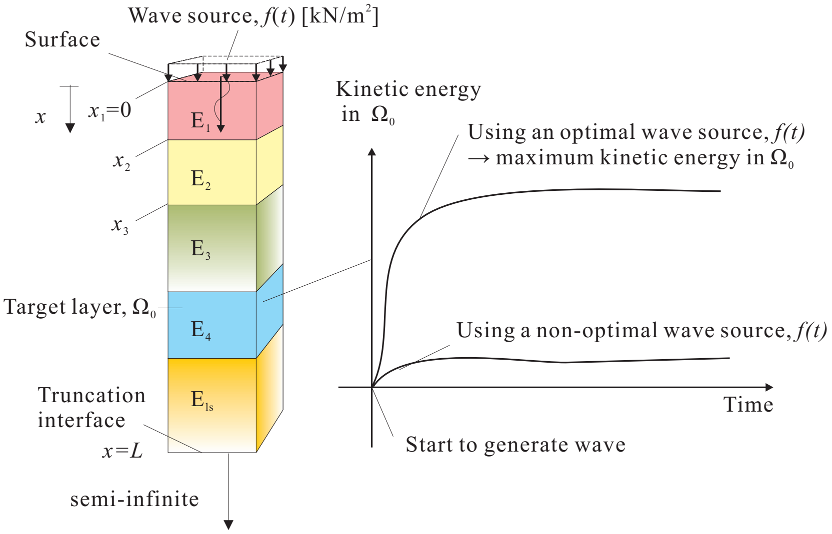

Figure 3.1: Schematic of inverse-source problem: a layered semi-infinite medium truncated at depth $x = L$, subjected to an unknown surface excitation. Ω_0 denotes the target layer. The right graph is the sought outcome: the maximization of Ω_0's kinetic energy.

3.1.1 Governing wave physics

A semi-infinite heterogeneous (layered) medium is subjected to an excitation on the surface ($x = 0$), whose temporal variability $f(t)$ is unknown. We seek to identify $f(t)$, such that the kinetic energy within a target region (layer) Ω_0 is maximized (Fig. 3.1). The semi-infinite extent of the original domain is truncated through the introduction of a truncation boundary at some depth $x = L$. The propagation of compressional elastic waves within the truncated layered medium ($\Omega = (0, L)$) can be described by the following initial and boundary value problem (IBVP): find the one-dimensional displacement field $u \equiv u(x,t)$ such that:

$$\begin{aligned}
\frac{\partial}{\partial x}\left(E(x)\frac{\partial u(x,t)}{\partial x}\right) - \rho(x)\frac{\partial^2 u(x,t)}{\partial t^2} &= 0, \qquad x \in (0, L), \quad t \in (0, T], && \text{(3.1a)}\\
E(0)\frac{\partial u}{\partial x}(0,t) + f(t) &= 0, \qquad t \in (0, T], && \text{(3.1b)}\\
\frac{\partial u}{\partial x}(L,t) + \frac{1}{c(L)}\frac{\partial u}{\partial t}(L,t) &= 0, \qquad t \in (0, T], && \text{(3.1c)}\\
u(x,0) &= 0, \qquad x \in (0, L), && \text{(3.1d)}\\
\frac{\partial u}{\partial t}(x,0) &= 0, \qquad x \in (0, L), && \text{(3.1e)}
\end{aligned}$$

where x denotes location, and t denotes time; T denotes the total observation time, E represents modulus[1], ρ represents density, and $c = \sqrt{E/\rho}$ is the wave propagation speed. Condition (3.1b) is the surface excitation condition; (3.1c) is the truncation interface condition, which is exact for homogeneous domains, but only approximate for heterogeneous domains, and; (3.1d) and (3.1e) indicate that the system is initially at rest. Equation (3.1a) accounts, in general, for arbitrary heterogeneity (i.e., $E \equiv E(x)$); though the approach we follow applies to arbitrarily heterogeneous domains, we restrict the presentation, and

---

[1] For example, for compressional waves $E = \lambda + 2\mu$, where λ and μ are the Lamé constants.

the numerical results, to layered domains, comprising N_{ls} layers. In such a case, (3.1a) holds within each layer, and E_i refers to the resident i-th layer modulus; in addition, the following interface conditions must hold:

$$E_i \left[\frac{\partial u}{\partial x}\right]_{x=x_{i+1}^-} = E_{i+1} \left[\frac{\partial u}{\partial x}\right]_{x=x_{i+1}^+}, \quad i = 1 \ldots (N_{\text{ls}} - 1), \tag{3.2}$$

$$u\Big|_{x=x_{i+1}^-} = u\Big|_{x=x_{i+1}^+}, \quad i = 1 \ldots (N_{\text{ls}} - 1), \tag{3.3}$$

where (3.2) and (3.3) are the traction and displacement interface continuity conditions, respectively.

3.1.2 Objective functional

If the excitation $f(t)$ were known, the IBVP (1) can be solved to obtain the medium's response $u(x,t)$. The excitation, however, is unknown: to estimate it, we minimize the following functional:

$$\mathcal{L} = \frac{1}{\int_{\Omega_0} \int_0^T \rho(x) [\frac{\partial u}{\partial t}(x,t)]^2 dt dx}, \tag{3.4}$$

which involves the reciprocal of the target layer's kinetic energy[2], evaluated over the entire observation time. We remark that (3.4) is only one of various candidate functionals that could be cast with the goal of maximizing oil droplet mobility in a targeted zone (e.g., maximizing the acceleration field). Numerically, we have experimented with (3.4), as well as with the following

---

[2] We omit the usual $\frac{1}{2}$ term implicated in the kinetic energy's definition from the denominator of (3.4), since it does not affect the subsequent optimization process.

functional:

$$\mathcal{L} = \frac{\int_{\Omega \setminus \Omega_0} \int_0^T \rho(x)[\frac{\partial u}{\partial t}(x,t)]^2 dt dx}{\int_{\Omega_0} \int_0^T \rho(x)[\frac{\partial u}{\partial t}(x,t)]^2 dt dx}, \tag{3.5}$$

which aims at maximizing the target's kinetic energy (Ω_0), while keeping the neighboring layers ($\Omega \setminus \Omega_0$) as dormant as possible. The minimization of either (3.4) or (3.5) is tantamount to a constrained optimization problem owing to its subjugation to the governing IBVP. From a wave propagation point of view, we note that the IBVP (1) models compressional waves only: this is a consequence of our considering the one-dimensional prototype, but is in no way a limitation of the described approach.

3.2 Mathematical modeling

3.2.1 Augmented functional

To tackle the optimization problem constrained by the governing wave physics, we side-impose via Lagrange multipliers (or adjoint variables) the governing IBVP to either of the two minimization functionals (3.4) or (3.5). The governing IBVP involves the unknown excitation, parameterized using a finite set of parameters. The process must yield the optimal excitation parameters.

There arises a Lagrangian functional, for which we seek a stationary point by enforcing the vanishing of the first-order optimality conditions. Three optimality conditions are necessary: the first results from the variation of the augmented functional with respect to the Lagrange multipliers. As it will be shown, the resulting form is simply the original IBVP or state problem. The variation with respect to the state variable u, will lead to an adjoint problem for the Lagrange multipliers, which is a final value boundary value problem (FBVP). Lastly, it is the third problem – the control problem – arising from variations with respect to the excitation parameters, that will allow the iterative update of the excitation parameters until convergence.

The side imposition of the governing partial differential equation (3.1a), and the associated boundary and initial conditions, (3.1b) to (3.1e), to the objective functional (3.4) via Lagrange multipliers λ, λ_0, λ_L, λ_u, and λ_v yields the augmented functional $\mathcal{A}$:

$$\begin{aligned}
\mathcal{A} \;=\; & \Bigg\{ \left(\frac{1}{\int_{\Omega_0} \int_0^T \rho[\frac{\partial u}{\partial t}(x,t)]^2 dt dx} \right) \\
& + \int_0^L \int_0^T \lambda(x,t) \left[\frac{\partial}{\partial x} \left(E(x) \frac{\partial u(x,t)}{\partial x} \right) - \rho \frac{\partial^2 u(x,t)}{\partial t^2} \right] dt dx \\
& + \int_0^T \lambda_0(t) \left[E(0) \frac{\partial u}{\partial x}(0,t) + f(t) \right] dt \\
& + \int_0^T \lambda_L(t) E(L) \left[\frac{\partial u}{\partial x}(L,t) + \frac{1}{c} \frac{\partial u}{\partial t}(L,t) \right] dt \\
& + \int_0^L \lambda_u(x) \left[\frac{\rho}{T} u(x,0) \right] dx + \int_0^L \lambda_v(x) \left[\rho \frac{\partial u}{\partial t}(x,0) \right] dx \Bigg\} \quad , \qquad (3.6)
\end{aligned}$$

where the notation of Lagrange multiplier differs depending on the side-constraint: $\lambda(x,t)$, $\lambda_0(t)$, $\lambda_L(t)$, $\lambda_u(x)$, and $\lambda_v(x)$ denote the Lagrange multipliers for imposing the governing PDE (3.1a), the Neumann boundary condition (3.1b), the truncation boundary condition (3.1c), and the initial conditions (3.1d) and (3.1e), respectively, in the augmented functional (3.6). Nevertheless, the dimensions of the Lagrange multipliers are identical to each other; and, as it will be shown, $\lambda(x,t)$ can absorb the other Lagrange multipliers such that the ensuing adjoint problem is constructed solely in terms of $\lambda(x,t)$.

3.2.2 The first-order optimality conditions

Next, we enforce the vanishing of the first variations of the augmented functional $\mathcal{A}$ with respect to the state variable (u), the adjoint variables (λ, λ_0, λ_L, λ_u, and λ_v), and a metric ξ expressing the parameterization of the unknown excitation $f(t)$. As it will be shown:

$$\begin{array}{ll} \left\{ \begin{array}{c} \delta_\lambda \mathcal{A} = 0 \\ \delta_{\lambda_0} \mathcal{A} = 0 \\ \delta_{\lambda_L} \mathcal{A} = 0 \\ \delta_{\lambda_u} \mathcal{A} = 0 \\ \delta_{\lambda_v} \mathcal{A} = 0 \end{array} \right\} & : \text{ yields the state IBV problem,} \\ \quad\ \delta_u \mathcal{A} = 0 & : \text{ yields the adjoint FBV problem,} \\ \quad\ \delta_\xi \mathcal{A} = 0 & : \text{ yields the control problem.} \end{array}$$

3.2.2.1 The first optimality condition

The variation of $\mathcal{A}$ with respect to λ, λ_0, λ_L, λ_u, and λ_v should vanish for arbitrary $\delta\lambda$, $\delta\lambda_0$, $\delta\lambda_L$, $\delta\lambda_u$, and $\delta\lambda_v$ (henceforth, we drop the functional dependence for brevity wherever there is no ambiguity):

$$\delta_\lambda \mathcal{A} = \int_0^L \int_0^T \delta\lambda \left[\frac{\partial}{\partial x}\left(E \frac{\partial u}{\partial x} \right) - \rho \frac{\partial^2 u}{\partial t^2} \right] dt dx = 0, \tag{3.7a}$$

$$\delta_{\lambda_0} \mathcal{A} = \int_0^T \delta\lambda_0 \left[E \frac{\partial u}{\partial x} + f(t) \right] dt \bigg|_{x=0} = 0, \tag{3.7b}$$

$$\delta_{\lambda_L} \mathcal{A} = \int_0^T \delta\lambda_L \left[E \frac{\partial u}{\partial x} + \frac{E}{c} \frac{\partial u}{\partial t} \right] dt \bigg|_{x=L} = 0, \tag{3.7c}$$

$$\delta_{\lambda_u} \mathcal{A} = \int_0^L \delta\lambda_u \left[\frac{\rho}{T} u \right] dx \bigg|_{t=0} = 0, \tag{3.7d}$$

$$\delta_{\lambda_v} \mathcal{A} = \int_0^L \delta\lambda_v \left[\rho \frac{\partial u}{\partial t} \right] dx \bigg|_{t=0} = 0. \tag{3.7e}$$

For (3.7) to vanish for arbitrary $\delta\lambda$, $\delta\lambda_0$, $\delta\lambda_L$, $\delta\lambda_u$, and $\delta\lambda_v$, the following state problem must be satisfied:

$$\frac{\partial}{\partial x}\left(E \frac{\partial u}{\partial x} \right) - \rho \frac{\partial^2 u}{\partial t^2} = 0, \quad x \in (0, L), \quad t \in (0, T], \tag{3.8a}$$

$$E(0) \frac{\partial u}{\partial x}(0, t) + f(t) = 0, \quad t \in (0, T], \tag{3.8b}$$

$$\frac{\partial u}{\partial x}(L, t) + \frac{1}{c} \frac{\partial u}{\partial t}(L, t) = 0, \quad t \in (0, T], \tag{3.8c}$$

$$u(x, 0) = 0, \quad x \in (0, L), \tag{3.8d}$$

$$\frac{\partial u}{\partial t}(x, 0) = 0, \quad x \in (0, L). \tag{3.8e}$$

As it can be seen, the resulting state problem is identical to the IBVP (1). We remark that, in the layered case, (3.8a) is written for every layer, and that the interface continuity conditions are formally recoverable; we will illustrate the layered case with the adjoint problem.

3.2.2.2 The second optimality condition

The variation of the augmented functional $\mathcal{A}$ with respect to the state variable u should vanish for arbitrary δu. There results:

$$\begin{aligned}
\delta_u \mathcal{A} =& \delta_u \Bigg[\left(\frac{1}{\int_{\Omega_0} \int_0^T \rho [\frac{\partial u}{\partial t}]^2 dt dx} \right) \\
&+ \int_0^L \int_0^T \lambda \left[\frac{\partial}{\partial x} \left(E \frac{\partial u}{\partial x} \right) - \rho \frac{\partial^2 u}{\partial t^2} \right] dt dx \\
&+ \int_0^T \lambda_0 \left[E \frac{\partial u}{\partial x} + f(t) \right] dt \bigg|_{x=0} + \int_0^T \lambda_L \left[E \frac{\partial u}{\partial x} + \frac{E}{c} \frac{\partial u}{\partial t} \right] dt \bigg|_{x=L} \\
&+ \int_0^L \lambda_u \left[\frac{\rho}{T} u \right] dx \bigg|_{t=0} + \int_0^L \lambda_v \left[\rho \frac{\partial u}{\partial t} \right] dx \bigg|_{t=0} \Bigg] = 0. \qquad (3.9)
\end{aligned}$$

Equation (3.9) can be rearranged as (the variational procedure, used for deriving (3.10) from (3.9), is described in Appendix A):

$$\begin{aligned}
\delta_u \mathcal{A} =& \int_0^L \int_0^T \delta u \left[\frac{\partial}{\partial x} \left(\frac{\partial \lambda}{\partial x} E \right) - \rho \frac{\partial^2 \lambda}{\partial t^2} + \mathcal{E}(x) \rho \frac{\partial^2 u}{\partial t^2} \right] dt dx \\
&+ \int_0^L \delta u \left[\rho \frac{\partial \lambda}{\partial t} - \mathcal{E}(x) \rho \frac{\partial u}{\partial t} \right] dx \bigg|_{t=T} \\
&- \int_0^L \left[\rho \lambda \frac{\partial \delta u}{\partial t} \right] dx \bigg|_{t=T} + \left[\lambda_L \frac{E}{c} \delta u \right]_{x=L, t=T} \\
&- \int_0^T \left[\lambda E \frac{\partial \delta u}{\partial x} \right] dt \bigg|_{x=0} + \int_0^T \left[\lambda_0 E \frac{\partial \delta u}{\partial x} \right] dt \bigg|_{x=0} \\
&+ \int_0^T \left[\lambda E \frac{\partial \delta u}{\partial x} \right] dt \bigg|_{x=L} + \int_0^T \left[\lambda_L E \frac{\partial \delta u}{\partial x} \right] dt \bigg|_{x=L} \\
&+ \int_0^T \left[E \frac{\partial \lambda}{\partial x} \delta u \right] dt \bigg|_{x=0} - \int_0^T \left[\frac{\partial \lambda_L}{\partial t} \frac{E}{c} + E \frac{\partial \lambda}{\partial x} \right] \delta u dt \bigg|_{x=L} \\
&+ \sum_{i=1}^{N_{\mathrm{ls}}-1} \Bigg\{ \left[\int_0^T \lambda E \frac{\partial \delta u}{\partial x} dt \right]_{x=x_{i+1}^-} - \left[\int_0^T \lambda E \frac{\partial \delta u}{\partial x} dt \right]_{x=x_{i+1}^+} \\
&\qquad - \left[\int_0^T E \frac{\partial \lambda}{\partial x} \delta u dt \right]_{x=x_{i+1}^-} + \left[\int_0^T E \frac{\partial \lambda}{\partial x} \delta u dt \right]_{x=x_{i+1}^+} \Bigg\} = 0,
\end{aligned} \tag{3.10}$$

where

$$\mathcal{E}(x) = \begin{cases} \frac{2}{\left(\int_{\Omega_0} \int_0^T \rho [\frac{\partial u(x,t)}{\partial t}]^2 dt dx \right)^2}, & x \in \Omega_0, \\ 0, & x \in \Omega \setminus \Omega_0 \end{cases} . \tag{3.11}$$

For (3.10) to be satisfied for arbitrary δu, we require the satisfaction of the following *adjoint problem*:

$$\frac{\partial}{\partial x}\left(E\frac{\partial \lambda}{\partial x}\right) - \rho\frac{\partial^2 \lambda}{\partial t^2} = -\mathcal{E}(x)\rho\frac{\partial^2 u}{\partial t^2}, \quad x \in (0, L), \ \ t \in [0, T), \tag{3.12a}$$

$$\frac{\partial \lambda}{\partial x}(0, t) = 0, \quad t \in [0, T), \tag{3.12b}$$

$$\frac{\partial \lambda}{\partial x}(L, t) - \frac{1}{c(L)}\frac{\partial \lambda}{\partial t}(L, t) = 0, \quad t \in [0, T), \tag{3.12c}$$

$$\lambda(x, T) = 0, \quad x \in (0, L), \tag{3.12d}$$

$$\frac{\partial \lambda}{\partial t}(x, T) = \mathcal{E}(x)\frac{\partial u}{\partial t}(x, T), \quad x \in (0, L), \tag{3.12e}$$

with the continuity conditions:

$$\lambda\big|_{x=x_{i+1}^-} \ = \ \lambda\big|_{x=x_{i+1}^+} \ , \tag{3.13}$$

$$E_i\left[\frac{\partial \lambda}{\partial x}\right]_{x=x_{i+1}^-} \ = \ E_{i+1}\left[\frac{\partial \lambda}{\partial x}\right]_{x=x_{i+1}^+} \ , \tag{3.14}$$

and

$$\lambda_L(t) = -\lambda(L, t), \tag{3.15}$$

$$\lambda_0(t) = \lambda(0, t). \tag{3.16}$$

The adjoint problem has structure identical to the state problem, except for the following differences: whereas the state problem is driven by the excitation term in the surface condition (3.1b), the adjoint problem is driven by body forces localized to the target layer, and expressed in terms of the accelerations of the state problem (per (3.12a)). Secondly, as it can be seen from (3.12d) and (3.12e), the adjoint problem is a final value BVP; and thirdly, the sign of the time derivative in the truncation condition (3.12c) has been changed when compared with the truncation condition of the state problem (3.1c), owing to the reversal of the time line in the adjoint problem.

The preceding development was based upon using (3.4) as the objective functional. If, to force the neighboring layers to be silent, we choose (3.5), the resulting state and adjoint problems remain the same as derived above, provided the definition of $\mathcal{E}(x)$ is replaced by:

$$\mathcal{E}(x) = \begin{cases} \frac{2\int_{\Omega\setminus\Omega_0}\int_0^T \rho[\frac{\partial u(x,t)}{\partial t}]^2 dt dx}{\left(\int_{\Omega_0}\int_0^T \rho[\frac{\partial u(x,t)}{\partial t}]^2 dt dx\right)^2}, & x \in \Omega_0, \\ \\ \frac{-2}{\left(\int_{\Omega_0}\int_0^T \rho[\frac{\partial u(x,t)}{\partial t}]^2 dt dx\right)}, & x \in \Omega \setminus \Omega_0 \end{cases} \quad . \tag{3.17}$$

3.2.2.3 The third optimality condition

We consider the variation of the augmented functional $\mathcal{A}$ with respect to a scalar variable ξ, tantamount to parameter f_i – a nodal force of the discretized force function $f(t)$ (see (3.33)). To this end, we require the following:

$$\begin{aligned} \delta_\xi \mathcal{A} = \frac{\partial}{\partial \xi}\Bigg\{ & \left(\frac{1}{\int_{\Omega_0}\int_0^T \rho[\frac{\partial u}{\partial t}]^2 dt dx}\right) + \int_0^L \int_0^T \lambda \left[\frac{\partial}{\partial x}\left(E\frac{\partial u}{\partial x}\right) - \rho\frac{\partial^2 u}{\partial t^2}\right] dt dx \\ & + \int_0^T \lambda \left[E\frac{\partial u}{\partial x} + f(t)\right] dt\Bigg|_{x=0} - \int_0^T \lambda \left[E\frac{\partial u}{\partial x} + \frac{E}{c}\frac{\partial u}{\partial t}\right] dt\Bigg|_{x=L} \\ & + \int_0^L \lambda_u \left[\frac{\rho}{T} u\right] dx\Bigg|_{t=0} + \int_0^L \lambda_v \left[\rho\frac{\partial u}{\partial t}\right] dx\Bigg|_{t=0} \Bigg\} = 0 \quad . \end{aligned} \tag{3.18}$$

After some manipulation (the explicit derivation of the control problem is shown in Appendix A), (3.18) reduces to the *control problem*:

$$\delta_\xi \mathcal{A}(= \nabla_\xi \mathcal{A}) = \int_0^T \lambda \frac{\partial f(t)}{\partial \xi} dt \bigg|_{x=0} = 0, \tag{3.19}$$

where λ, again, denotes the solution of the adjoint problem. We remark that $\delta_\xi \mathcal{A}$ is equivalent to the gradient of the objective functional $\nabla_\xi \mathcal{L}$, since the side-imposed constraints to the augmented functional $\mathcal{A}$ vanish at the stationary point owing to the satisfaction of the state problem. To obtain the excitation parameters, we use a gradient-based minimization process and $\int_0^T \lambda \frac{\partial f(t)}{\partial \xi} dt \big|_{x=0}$, in the control equation (3.19), as the reduced gradient. The details are given in the next section; if (3.5) were to be used instead of (3.4), the control problem remains unaltered.

3.3 Numerical implementation

Satisfaction of the first-order optimality conditions, upon discretization, gives rise to a Karush-Kuhn-Tucker (KKT) system [41, 48]. Stationarity can be achieved by solving the state, adjoint, and control problems either as a fully coupled problem (a full-space solution approach), or via a reduced-space approach. Since the computational cost associated with a full-space approach is rather significant, we solve the KKT system by projecting the state and adjoint variables into the space of the control variables. Such a reduced-space solution approach entails the following steps: (a) first the state problem is solved for a trial form of the excitation; (b) the adjoint problem is then solved using, as driver, the acceleration field of the state problem (per (3.12a)); (c) finally, updates to the parameters defining the trial form of the excitation are obtained via a gradient-based scheme that uses the control equation (3.19) as the reduced gradient: at each iteration of the gradient-based scheme the control equation provides the search-direction for the parameter updates.

3.3.1 State and adjoint problems semi-discrete forms

The first two steps entail the solution of both an IBVP (the state problem), and a FBVP (the adjoint problem). We use a classic Galerkin finite element approach to resolve the discrete state and adjoint problems. To this end, we multiply (3.1a) and (3.12a) by test functions, $w(x)$ and $v(x)$, respectively, and integrate by parts, to arrive at the following weak forms:

$$\int_0^L \left[E\frac{\partial w}{\partial x}\frac{\partial u}{\partial x} + \rho w \frac{\partial^2 u}{\partial t^2} \right] dx + \frac{E(L)}{c(L)} w(L) \frac{\partial u(L)}{\partial t} = w(0) f(t), \tag{3.20}$$

$$\int_0^L \left[E\frac{\partial v}{\partial x}\frac{\partial \lambda}{\partial x} + \rho v \frac{\partial^2 \lambda}{\partial t^2} \right] dx - \frac{E(L)}{c(L)} v(L) \frac{\partial \lambda(L)}{\partial t} = \int_0^L \left[v \mathcal{E} \rho \frac{\partial^2 u}{\partial t^2} \right] dx. \tag{3.21}$$

We introduce the following approximations:

$$w(x) = \mathbf{w}^T \boldsymbol{\phi}(x), \quad u(x) = \boldsymbol{\phi}(x)^T \mathbf{u}(t), \tag{3.22}$$

$$v(x) = \mathbf{v}^T \boldsymbol{\phi}(x), \quad \lambda(x) = \boldsymbol{\phi}(x)^T \boldsymbol{\lambda}(t), \tag{3.23}$$

where $\mathbf{u}(t)$ and $\boldsymbol{\lambda}(t)$ denote the vectors of the nodal solutions of $u(x,t)$ and $\lambda(x,t)$, respectively; $\mathbf{w}$ and $\mathbf{v}$ denote the vectors of the nodal quantities of the test functions, $w(x)$ and $v(x)$, respectively; and $\boldsymbol{\phi}(x)$ represents a vector of shape functions. Then, (3.20) and (3.21) are reduced into the following semi-discrete forms:

$$\mathbf{M}\frac{\partial^2\mathbf{u}(t)}{\partial t^2}+\mathbf{C}\frac{\partial\mathbf{u}(t)}{\partial t}+\mathbf{K}\mathbf{u}(t)=\mathbf{F}(t), \tag{3.24}$$

$$\mathbf{M}\frac{\partial^2\boldsymbol{\lambda}(t)}{\partial t^2}-\mathbf{C}\frac{\partial\boldsymbol{\lambda}(t)}{\partial t}+\mathbf{K}\boldsymbol{\lambda}(t)=\mathbf{P}(t), \tag{3.25}$$

where

$$\mathbf{M} = \int_0^L \left[\rho(x)\boldsymbol{\phi}(x)\boldsymbol{\phi}^T(x)\right]dx, \tag{3.26}$$

$$\mathbf{C} = \frac{E(L)}{c(L)}\boldsymbol{\phi}(L)\boldsymbol{\phi}^T(L), \tag{3.27}$$

$$\mathbf{K} = \int_0^L \left[E(x)\frac{\partial\boldsymbol{\phi}(x)}{\partial x}\frac{\partial\boldsymbol{\phi}^T(x)}{\partial x}\right]dx, \tag{3.28}$$

$$\mathbf{F}(t) = \boldsymbol{\phi}(0)f(t), \tag{3.29}$$

$$\mathbf{P}(t) = \int_0^L \left[\mathcal{E}\rho\boldsymbol{\phi}\boldsymbol{\phi}^T\right]dx\frac{\partial^2\mathbf{u}(t)}{\partial t^2}. \tag{3.30}$$

We solve (3.24) and (3.25) by using a Newmark time-integration scheme such that the state and adjoint solutions at each time step are obtained from the following linear system of equations:

$$\begin{aligned}&\left[\mathbf{K}+\mathbf{C}\frac{2}{\Delta t}+\mathbf{M}\frac{4}{(\Delta t)^2}\right]\mathbf{u}_{(n+1)} = \\ &\mathbf{C}\left[\frac{2}{\Delta t}\mathbf{u}_{(n)}+\frac{\partial\mathbf{u}_{(n)}}{\partial t}\right]+\mathbf{M}\left[\frac{4\mathbf{u}_{(n)}}{(\Delta t)^2}+\frac{4}{\Delta t}\frac{\partial\mathbf{u}_{(n)}}{\partial t}+\frac{\partial^2\mathbf{u}_{(n)}}{\partial t^2}\right]+\mathbf{F}_{(n+1)},\end{aligned} \tag{3.31}$$

$$\begin{aligned}&\left[\mathbf{K}+\mathbf{C}\frac{2}{\Delta t}+\mathbf{M}\frac{4}{(\Delta t)^2}\right]\boldsymbol{\lambda}_{(n)} = \\ &\mathbf{C}\left[\frac{2}{\Delta t}\boldsymbol{\lambda}_{(n+1)}-\frac{\partial\boldsymbol{\lambda}_{(n+1)}}{\partial t}\right]+\mathbf{M}\left[\frac{4\boldsymbol{\lambda}_{(n+1)}}{(\Delta t)^2}-\frac{4}{\Delta t}\frac{\partial\boldsymbol{\lambda}_{(n+1)}}{\partial t}+\frac{\partial^2\boldsymbol{\lambda}_{(n+1)}}{\partial t^2}\right]+\mathbf{P}_{(n)},\end{aligned} \tag{3.32}$$

where Δt denotes time step, and subscripts (n) and $(n+1)$ denote evaluation of the nodal vectors at the n-th and $(n+1)$-th time step. Note that the traversal of the time line in (3.32) is reversed with respect to (3.31). Moreover, reflecting the presence of similar operators in both the state and adjoint continuous problems, notice that matrices $\boldsymbol{K}$, $\boldsymbol{C}$, and $\boldsymbol{M}$ are shared by both discrete forms, requiring their formation only once per inversion iteration. We remark that there is only one system matrix inversion needed per (excitation) inversion iteration, owing to the fact that the left-hand-sides of (3.31) and (3.32) are identical.

3.3.2 Wave source parameterization

We consider an, as yet, unknown loading time signal $f(t)$, for which arbitrary temporal variability is allowed. To compute such an unknown arbitrary time signal $f(t)$, we first parameterize it as:

$$f(t) = \sum_{i=1}^{n_f} f_i \varphi_i(t) = \mathbf{f} \boldsymbol{\varphi}^T(t) \quad , \tag{3.33}$$

where $\varphi_i(t)$ and f_i denote the i-th shape function and discretized excitation parameter, respectively; $\mathbf{f}$ is the vector of force parameters f_i, and $\boldsymbol{\varphi}$ is the vector of shape functions $\varphi_i(t)$; and n_f is the total number of parameters; we use quadratic shape functions for $\varphi_i(t)$ (Fig. 3.2).

Following the temporal approximation of $f(t)$, the control equation (3.19) becomes:

$$\delta_\xi \mathcal{A} = \int_0^T \lambda \frac{\partial f(t)}{\partial f_i} dt \bigg|_{x=0} = \int_0^T \lambda \varphi_i(t) dt \bigg|_{x=0} = 0. \tag{3.34}$$

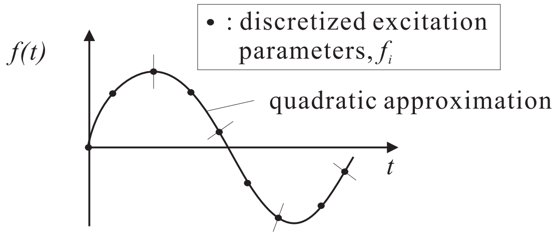

Figure 3.2: Schematic of parameterization of the unknown excitation $f(t)$ using quadratic shape functions

We remark that the reduced gradient of the original functional $\mathcal{L}$ can be cast as:

$$\nabla_{f_i}\mathcal{L} = \left. \int_0^T \lambda \varphi_i(t)dt \right|_{x=0}, \tag{3.35}$$

which forms the basis for the parameter updates. The procedure is outlined next.

3.3.3 The gradient-based minimization process

We perform a minimization process to arrive at a solution satisfying the first-order optimality conditions starting from $\mathbf{f}_{(0)}$ – the set of the initially guessed excitation parameters. At each iteration, we first solve the state problem using the excitation parameters obtained from the previous iteration; then, we solve the adjoint problem using the state solution; finally, using the adjoint solutions, we compute the value of the gradient (3.35). Then, we update the excitation parameters as:

$$\mathbf{f}_{(k+1)} = \mathbf{f}_{(k)} + \mathbf{g}\theta_{(k)}, \tag{3.36}$$

where $\mathbf{f}_{(k)}$ denotes the parameter vector at the k-th iteration; $\theta_{(k)}$ denotes the step-length for the k-th iteration; $\mathbf{g}$ denotes the search-direction, which is obtained using the reduced gradient (3.35) and a conjugate-gradient (CG) scheme [19, 59]. We use the optimal value of $\theta_{(k)}$ such that sufficient decrease of the minimization functional is ensured at each iteration. That is, (a) if the sufficient decrease is not met, we use a backtracking method [59] – reducing the step-length by a factor of α until the sufficient decrease condition is satisfied; (b) after the excitation parameters are updated, we increase the step-length at the next iteration by multiplying it by β to improve the rate of convergence. In the applications we used $\alpha = 0.9$ and $\beta = 1.1$. The entire algorithm is summarized in Algorithm 1.

Algorithm 1 Optimization Algorithm

```
Set TOL=$10^{-8}$, $\alpha = 0.9$ and $\beta = 1.1$
Set $k = 0$ and Initial Force Parameters $\mathbf{f}_{(0)}$
Compute $\mathcal{L}_{(k)}$
while ($e >$ TOL) do
    Solve State Problem, (3.24), and Save State Variables
    Solve Adjoint Problem, (3.25), and Save Adjoint Variables
    Compute the Search-Direction $\mathbf{g}$ Using CG
    while ($\mathcal{L}(\mathbf{f}_{(k)} + \theta_{(k)}\mathbf{g}) > \mathcal{L}(\mathbf{f}_{(k)} - \frac{1}{2}\theta_{(k)}\nabla\mathcal{L}(\mathbf{f}_{(k)}))$) do
        $\theta_{(k)} \leftarrow \alpha\theta_{(k)}$
    end while
    Update Excitation Parameters, $\mathbf{f}_{(k+1)}$ Using (3.36), and Compute $\mathcal{L}_{(k+1)}$
    Compute the Iterative Norm, $e = \frac{|\mathcal{L}_{(k+1)} - \mathcal{L}_{(k)}|}{|\mathcal{L}_{(k)}|}$:
    $\theta_{(k+1)} \leftarrow \beta\theta_{(k)}$, and $k \leftarrow k + 1$
end while
```

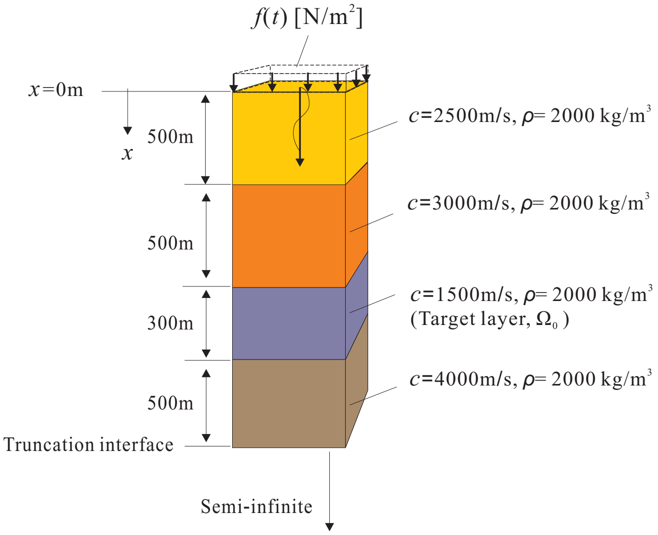

Figure 3.3: A four-layer heterogeneous domain.

3.4 Numerical results

We report on numerical experiments to highlight the application of the outlined procedure. We consider a layered-medium with 4 layers as depicted in Fig. 3.3. The loading is located on the surface (x=0m), and the truncation interface boundary is imposed at x=1800m. The layers are increasingly stiffer with depth, but are intercepted by a soft layer at 1000m, which becomes the target layer. We use linear isoparametric elements for the finite element solution of the state and adjoint problems. We use an unknown force function $f(t)$ within the T observation duration; such a time signal $f(t)$ is discretized using quadratic (or, cubic) shape functions and a number of discretized excitation parameters. We require that the discretized excitation parameters not exceed 50kN/m^2. Even though excitation parameters do not exceed 50kN/m^2, the interpolated loading time signal can reach up to 60kN/m^2 (see Figures 3.5 and 3.6)[3].

The reduced gradient components are then evaluated as in (3.35): we validated the derivation and implementation of the state, adjoint, and control equations by comparing the values of the components of the gradient obtained using (3.35) to those of a numerically-computed gradient obtained via a finite difference scheme, as described in (3.37); both gradients were in excellent agreement.

$$\nabla_{f_i}\mathcal{L} = \frac{\mathcal{L}\big|_{f_i+\Delta f_i} - \mathcal{L}\big|_{f_i-\Delta f_i}}{2\Delta f_i}. \tag{3.37}$$

3.4.1 Wave source optimal time signal – maximum kinetic energy – unconstrained neighbors

By minimizing the objective functional (3.4), we attempt to identify an unknown optimal time signal that can maximize the kinetic energy within the targeted layer of the 4-layered system depicted in Fig. 3.3. To this end, we use the perturbation loading, shown in Fig. 3.4(a), as the initial guess. Such a time signal is temporally discretized by using the quadratic shape functions and 100 discretized force parameters (50 quadratic elements). We remark that the block symbols in Fig. 3.4(a) represent the discretized force parameters utilized for the temporal approximation of a loading time signal (we use these symbols

---

[3] A modern Vibroseis can deliver dynamic pressure up to 60kN/m^2 to the ground surface: the dimension of the loading plate of a modern Vibroseis is 2.5m by 1.2m, and the peak force amplitude is 180kN [40].

in all similar plots). The total observation time is $T = 10$s, and the time step is 0.004s. We use linear isoparametric elements for the finite element solution of the state and adjoint problems with an element size of 4m.

The optimization process converges after 126 iterations to the near-periodic rectangular excitation shown in Fig. 3.6(a); the dominant frequency of the converged loading is 1.3Hz (see the frequency spectrum of the converged loading shown in Fig. 3.6(b)). As seen in Fig. 3.7, the value of the objective functional (3.4) decreases as the iteration number increases: (3.4) decreases rapidly between the first and the 50-th iterations, and then its rate slows down. Fig. 3.5 shows that the optimizer already identify a near-sinusoidal-like time signal with the dominant frequency of 1.3Hz before the 50-th iteration. The optimizer then further changes the amplitude information while the dominant frequency component 1.3Hz remains unaltered during the ensuing iterations.

We note that the optimization process results in the rendering of a complete time signal, including frequency content and amplitudes that differ significantly from those of the initial guess. For example, Fig. 3.4(b) depicts the frequency spectrum of the initial guess, and displays a drastically different frequency content than that of Fig. 3.6(b).

Fig. 3.8 shows that the total kinetic energy in the target layer Ω_0, for the converged optimized excitation, is much larger than the kinetic energy for a non-optimized loading $f(t) = 50 \sin(6.28t)\text{kN/m}^2$ that uses a frequency f of 1Hz. The amplitude of this non-optimized monochromatic loading is set approximately close to the dominant amplitude of the optimized loading.

The total kinetic energy in Ω_0 is defined as $\int_{\Omega_0} K(x,t)d\Omega$, whereas the kinetic energy is defined as:

$$K(x,t) = \frac{1}{2}\rho\left[\frac{\partial u(x,t)}{\partial t}\right]^2, \quad \text{in} \quad \text{J/m}^3 \tag{3.38}$$

Next, we are concerned with kinetic energy measures both in the target layer Ω_0 and within its neighbors. It is important to notice here that, as shown in Fig. 3.9(c), the kinetic energy distribution using the non-optimized source results in fairly low activity, when compared to the energy distribution shown in Fig. 3.9(a) that corresponds to the optimized source or that shown in Fig. 3.9(b) that corresponds to the sinusoidal loading $f(t) = 50\sin(8.17t)$ kN/m^2 [1.3Hz]. Note further that, in this case, it is not only the target layer's energy that was affected but also that of the layers lying above the target.

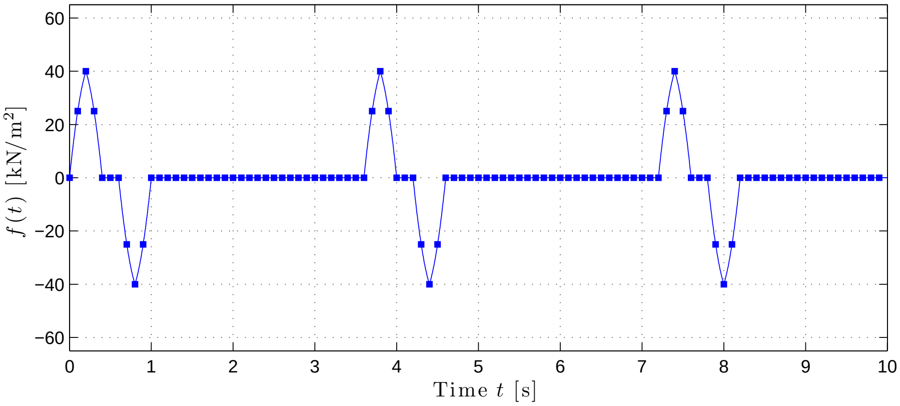

(a) The initially guessed loading time signal (the blocks symbolize the discretized excitation parameters)

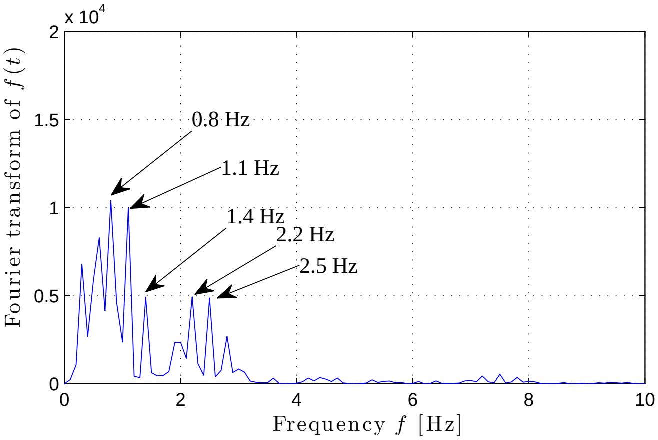

(b) The frequency spectrum of the initially guessed loading time signal

Figure 3.4: The initially guessed loading time signal for the maximization of the kinetic energy in a targeted formation.

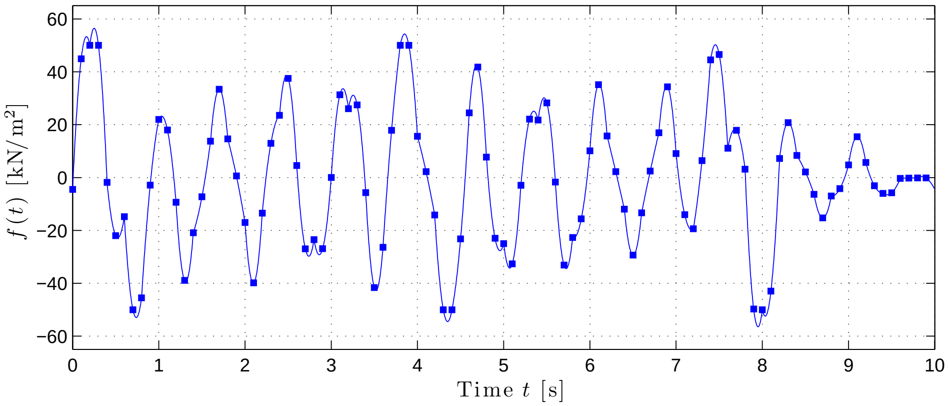

(a) The guessed loading time signal at the 50-th iteration

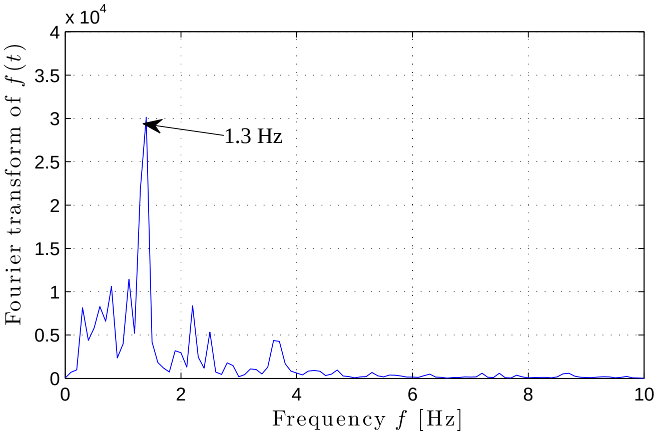

(b) The frequency spectrum of the guessed loading time signal at the 50-th iteration

Figure 3.5: The loading time signal at the 50-th iteration in the course of the maximization of the kinetic energy in a targeted formation.

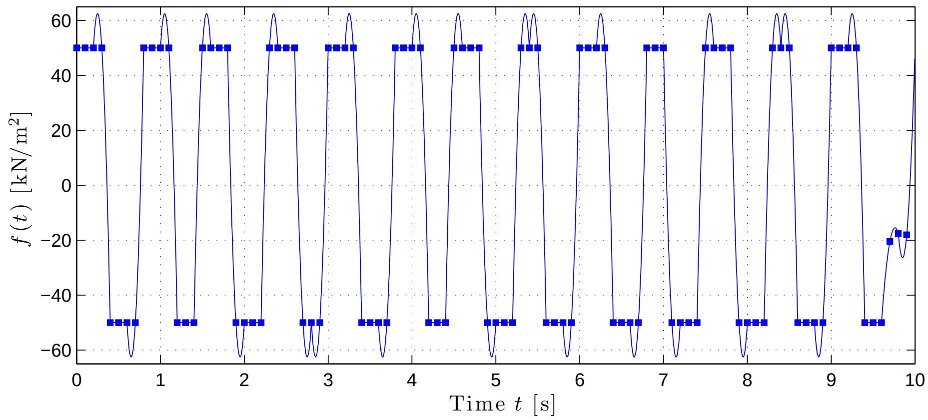

(a) The optimized loading time signal

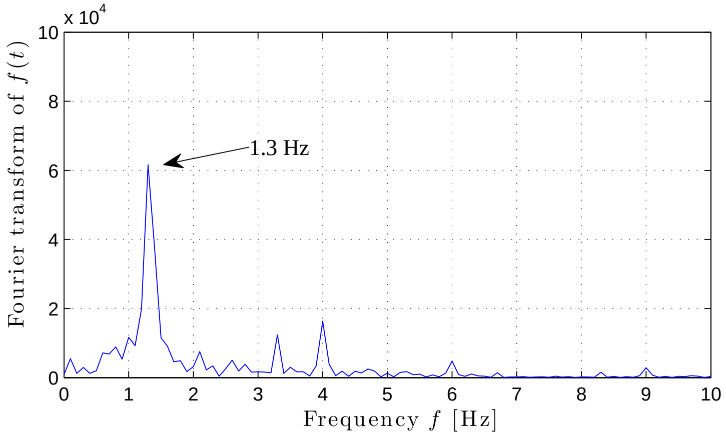

(b) The frequency spectrum of the optimized loading time signal

Figure 3.6: The optimized loading time signal, obtained after 126 iterations, for the maximization of the kinetic energy in a targeted layer.

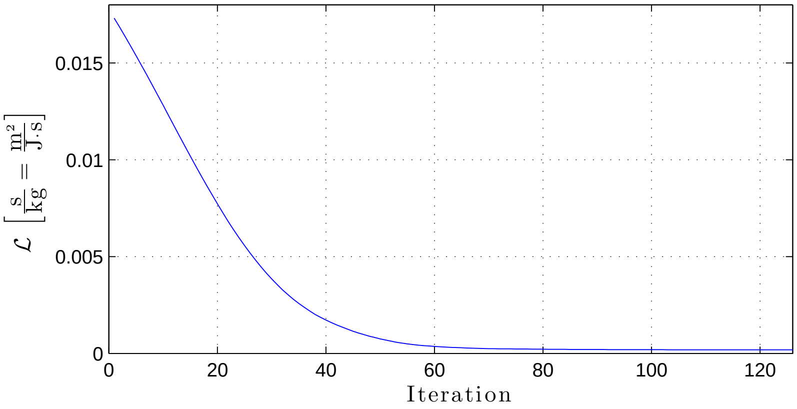

Figure 3.7: Convergence of the objective functional (3.4) with respect to the iteration number.

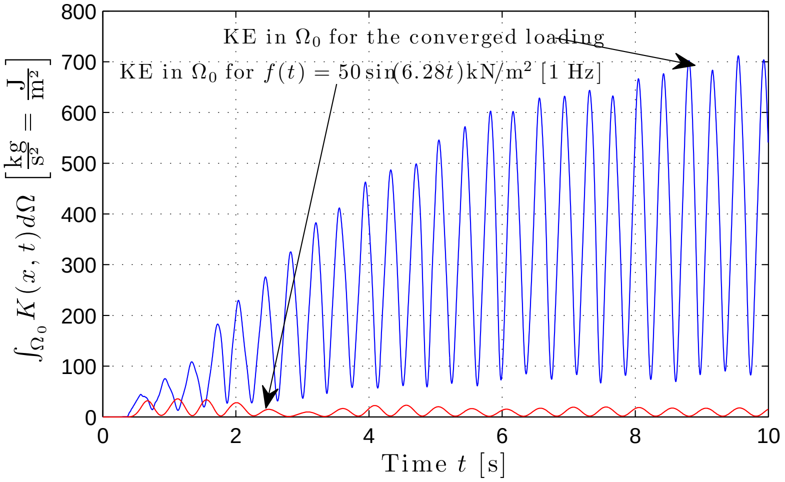

Figure 3.8: The kinetic energy in the target layer Ω_0, for the converged loading shown in Fig. 3.6, is much larger than that corresponding to a non-optimized loading.

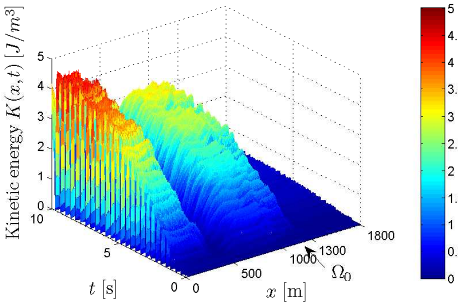

(a) Kinetic energy for the converged excitation shown in Fig. 3.6

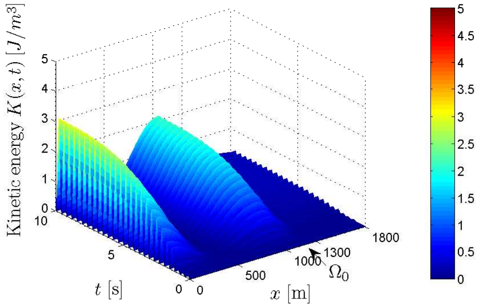

(b) Kinetic energy corresponding to $f(t)$=50 $\sin(8.17t)$ kN/m^2 operating at the dominant frequency of the converged excitation (1.3Hz) shown in Fig. 3.6

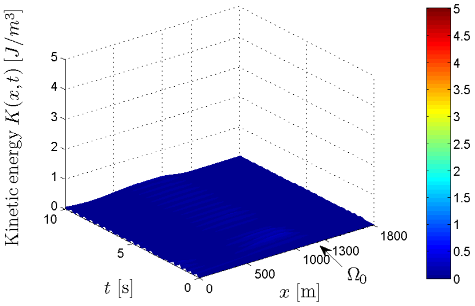

(c) Kinetic energy for a non-optimized source $f(t) = 50\sin(6.28t)$kN/m^2 operating at 1Hz

Figure 3.9: Temporal and spatial distribution of kinetic energy for different loading time signals.

3.4.2 Wave source optimal time signal – maximum kinetic energy – silent neighbors

We next seek to identify the loading time signal $f(t)$ that maximizes the kinetic energy in the target layer Ω_0 by minimizing the objective functional (3.5). This attempts to keep the rest of the domain relatively inert. The initial guess is shown in Fig. 3.10.

Figure 3.13 illustrates that the objective functional (3.5) drops quickly during the first 50 iterations while the optimizer identifies a sinusoidal-like time signal with a dominant frequency of 2.2Hz (see Fig. 3.11). After discovering such dominant frequency information, the optimizer adjusts the amplitude to further minimize the objective functional and yields the optimal loading time signal (Fig. 3.12). As it can be seen in Fig. 3.12, the finally converged loading, obtained after 314 iterations, appears to be a near-sinusoidal loading of non-uniform amplitudes with a dominant frequency of 2.2Hz.

Figure 3.14 shows that the lastly-converged excitation selectively maximizes the distribution of kinetic energy in the target layer Ω_0. By contrast, the kinetic energy distribution for a non-optimized loading time signal, e.g. for $f(t) = 50\sin(6.28t)\text{kN/m}^2$, which uses 6.28rad/s or 1Hz, does not show the selective wave energy focusing behavior[4]. However, a monochromatic loading, $f(t) = 50\sin(14.11t)\text{kN/m}^2$, which uses 14.11rad/s or 2.2Hz – the dominant frequency of the lastly-converged loading – also leads to the selective wave-

---

[4] We use peak amplitude of the optimized loading (approximately 50kN/m^2) as the amplitude for the non-optimized monochromatic loading.

energy focusing in the target layer, while exhibiting stronger energy levels than the original lastly converged excitation.

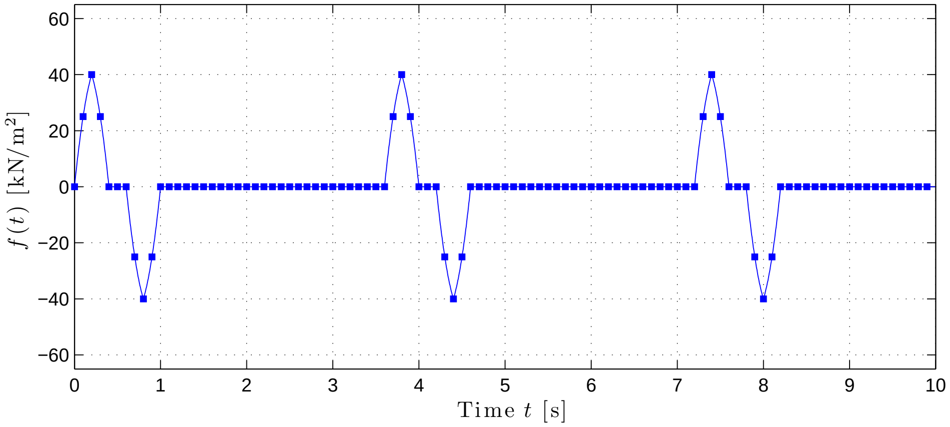

(a) The initially guessed loading time signal

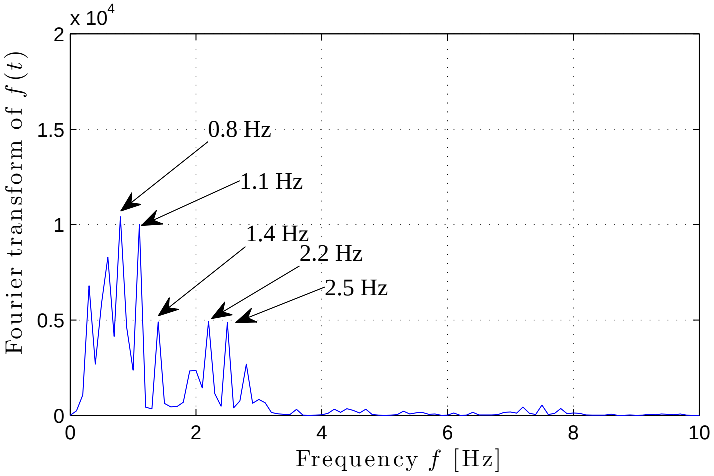

(b) The frequency spectrum of the initially guessed loading time signal

Figure 3.10: The initially guessed loading time signal for the selective maximization of the kinetic energy in a targeted formation (silent neighbors).

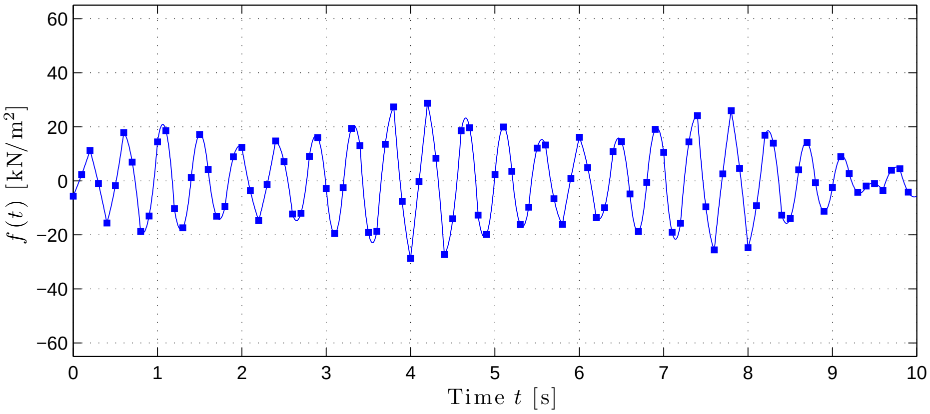

(a) The guessed loading time signal at the 50-th iteration

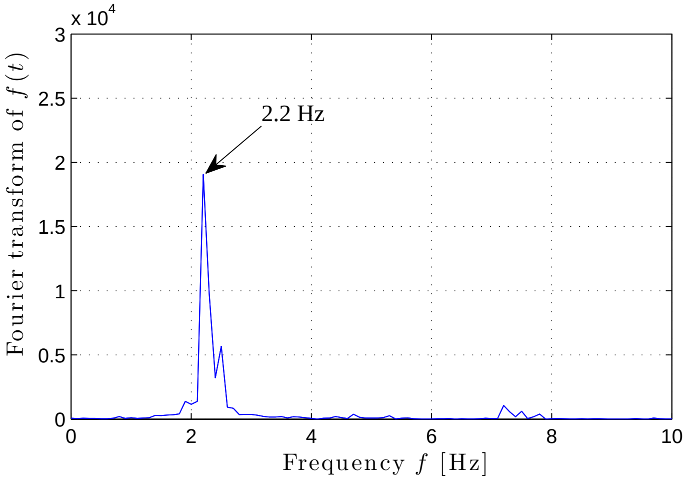

(b) The frequency spectrum of the guessed loading time signal at the 50-th iteration

Figure 3.11: The guessed loading time signal, at the 50-th iteration, in the course of the selective maximization of the kinetic energy in a targeted formation (silent neighbors).

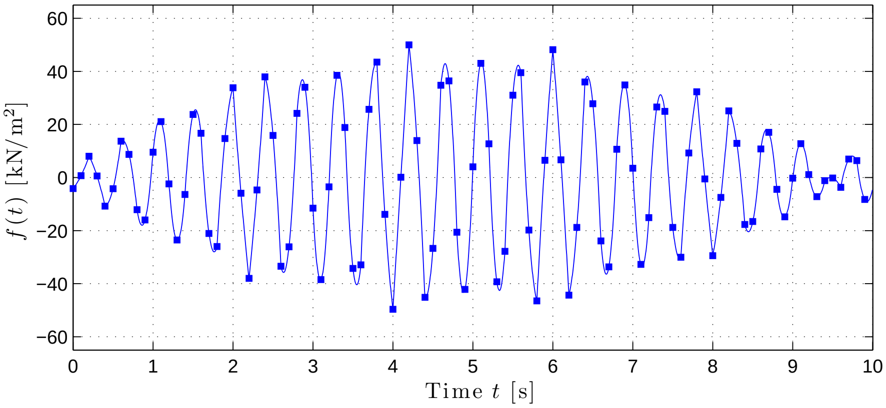

(a) The optimized loading time signal

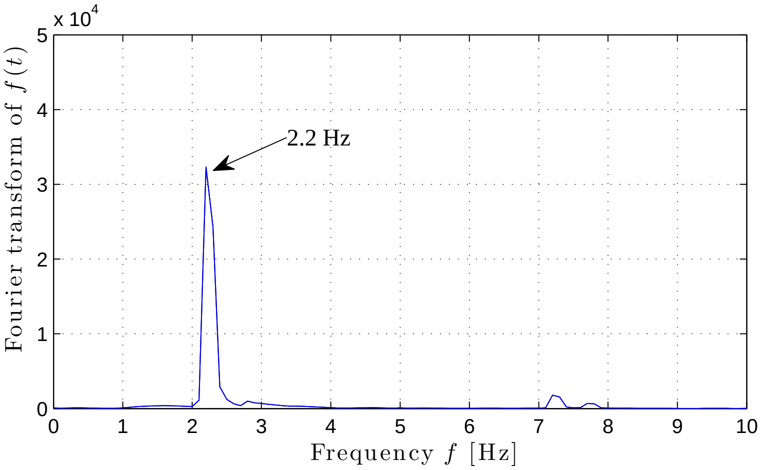

(b) The frequency spectrum of the optimized loading time signal

Figure 3.12: The optimized loading time signal, obtained after 314 iterations, for the selective maximization of the kinetic energy in a targeted formation (silent neighbors).

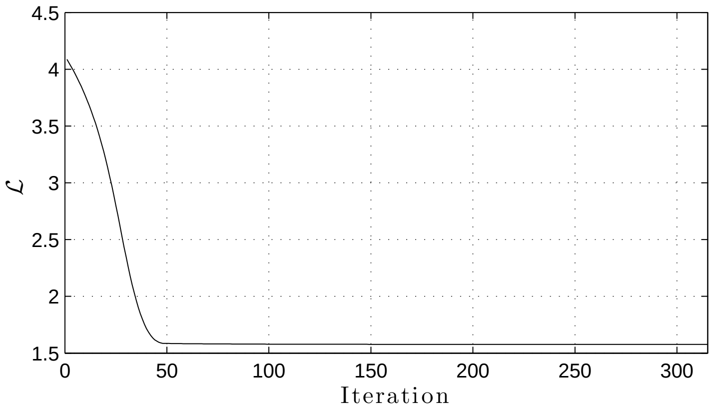

Figure 3.13: Convergence of the objective functional (3.5) with respect to the iteration number.

3.4.3 Verification of the optimization results

Thus far, we have shown that the outlined optimization process can lead to arbitrary excitation signals, which contain strong single-frequency components. It is of interest to study the relation of the optimized signal's frequencies to the exact frequencies necessary for maximizing the kinetic energy in the target layer, in order to assess the optimizer's performance. The one-dimensional nature of the prototype problem lends itself easily to the exact solution. We remark that, since the problem involves a domain of semi-infinite extent, there are no resonant frequencies in the classic sense. However, there is a set of frequencies for which the response is amplified compared to others: for the remainder, we term these frequencies, amplification frequencies. To obtain them, we study the frequency dependence of the wave response in the prototype 4-layered system shown in Fig. 3.3 by considering the time-harmonic

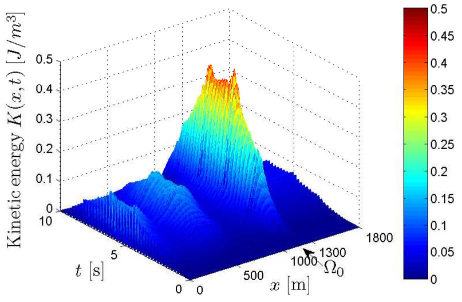

(a) Kinetic energy for the converged excitation shown in Fig. 3.12

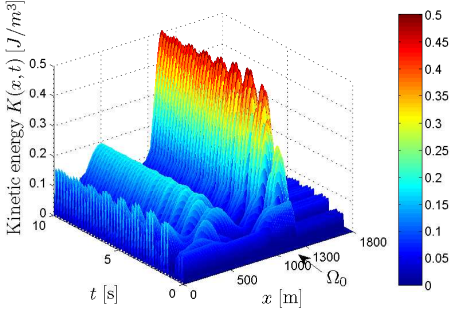

(b) Kinetic energy corresponding to $f(t)$=50 $\sin(14.11t)$ kN/m^2 operating at the dominant frequency of the converged excitation (2.19Hz) shown in Fig. 3.12

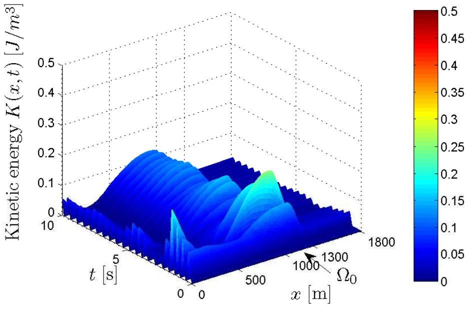

(c) Kinetic energy for a non-optimized source $f(t)$=50 $\sin(6.28t)$kN/m^2 operating at 1Hz

Figure 3.14: Temporal and spatial distribution of kinetic energy for different loading time signals.

response within each layer:

$$
\begin{aligned}
&u_1(x,t) = [A_{11}\exp(-ik_1x) + A_{12}\exp(ik_1x)]\exp(i\omega t), \quad 0 = x_1 \le x < x_2,\\
&u_2(x,t) = [A_{21}\exp(-ik_2x) + A_{22}\exp(ik_2x)]\exp(i\omega t), \quad x_2 \le x < x_3,\\
&u_3(x,t) = [A_{31}\exp(-ik_3x) + A_{32}\exp(ik_3x)]\exp(i\omega t), \quad x_3 \le x < x_4,\\
&u_4(x,t) = [A_{41}\exp(-ik_4x)]\exp(i\omega t), \quad x_4 \le x,
\end{aligned}
\tag{3.39}
$$

where ω denotes the radial frequency of the wave motions; $k_n = \omega/c_n$ denotes the wavenumber in the n-th layer, and c_n denotes the wave speed in the n-th layer. With the time harmonic factor $\exp(i\omega t)$, $A_{n1}\exp(-ik_nx)$ and $A_{n2}\exp(ik_nx)$ represent the outgoing and reflected waves in the n-th layer with amplitudes A_{n1} and A_{n2} respectively. In addition, on the surface ($x = 0$), there holds:

$$
E_1\frac{\partial u_1(x,t)}{\partial x} = P\exp(i\omega t). \tag{3.40}
$$

The following continuity conditions also hold:

$$
\begin{aligned}
u_1(x_2,t) = u_2(x_2,t), &\quad E_1\frac{\partial u_1(x_2,t)}{\partial x} = E_2\frac{\partial u_2(x_2,t)}{\partial x},\\
u_2(x_3,t) = u_3(x_3,t), &\quad E_2\frac{\partial u_2(x_3,t)}{\partial x} = E_3\frac{\partial u_3(x_3,t)}{\partial x},\\
u_3(x_4,t) = u_4(x_4,t), &\quad E_3\frac{\partial u_3(x_4,t)}{\partial x} = E_4\frac{\partial u_4(x_4,t)}{\partial x}.
\end{aligned}
\tag{3.41}
$$

Therefore, (3.39)–(3.41) give rise to the following system of equations:

$$\begin{bmatrix} -E_1ik_1, E_1ik_1,\ 0,\ 0,\ 0,\ 0,\ 0 \\ e^{-ik_1x_2},\ e^{ik_1x_2},\ -e^{-ik_2x_2},\ -e^{ik_2x_2},\ 0,\ 0,\ 0 \\ -E_1ik_1e^{-ik_1x_2},\ E_1ik_1e^{ik_1x_2},\ E_2ik_2e^{-ik_2x_2},\ -E_2ik_2e^{ik_2x_2},\ 0,\ 0,\ 0 \\ 0,\ 0,\ e^{-ik_2x_3},\ e^{ik_2x_3},\ -e^{-ik_3x_3},\ -e^{ik_3x_3},\ 0 \\ 0,\ 0,\ -E_2ik_2e^{-ik_2x_3},\ E_2ik_2e^{ik_2x_3},\ E_3ik_3e^{-ik_3x_3},\ -E_3ik_3e^{ik_3x_3},\ 0 \\ 0,\ 0,\ 0,\ 0,\ e^{-ik_3x_4},\ e^{ik_3x_4},\ -e^{-ik_4x_4} \\ 0,\ 0,\ 0,\ 0,\ -E_3ik_3e^{-ik_3x_4},\ E_3ik_3e^{ik_3x_4},\ E_4ik_4e^{-ik_4x_4} \end{bmatrix} \begin{bmatrix} A_{11} \\ A_{12} \\ A_{21} \\ A_{22} \\ A_{31} \\ A_{32} \\ A_{41} \end{bmatrix} = \begin{bmatrix} P \\ 0 \\ 0 \\ 0 \\ 0 \\ 0 \\ 0 \end{bmatrix}. \tag{3.42}$$

Solving for the coefficients $A_{11}, ..., A_{41}$ in (3.42) leads to the solution for the total wave-fields in (3.39) (there are no real roots to the determinant). For example: for the given stratification shown in Fig. 3.3 and for a force amplitude of $P = 50\text{kN/m}^2$, the time-harmonic response solution $u_3(x,t)$ in the target layer becomes:

$$u_3(x,t) = \frac{\left(\frac{22}{5}ie^{-\frac{i\omega(-1300+x)}{1500}} - 2ie^{\frac{i\omega(-1300+x)}{1500}}\right)e^{i\omega t}}{\omega\left(165e^{-\frac{17}{30}i\omega} - 5e^{-\frac{7}{30}i\omega} - 11e^{\frac{7}{30}i\omega} - 22e^{\frac{i\omega}{6}} + 363e^{\frac{17}{30}i\omega} - 106e^{-\frac{i\omega}{6}}\right)}. \tag{3.43}$$

Clearly, (3.43) has no resonant frequencies for $\omega \neq 0$. The same applies to the motion within the other layers. However, there are frequencies for which the motion is amplified. Figure 3.15 depicts the distribution of the amplitude of the particle velocity $|\frac{\partial u}{\partial t}|$ of the time-harmonic motion with respect to space, and for a frequency sweep between 0 and 20Hz. Notice that, at discrete frequencies close to 1.34Hz, 4.01Hz, 6.67Hz, etc, there is strong motion amplification in *all* layers, not just the target. By contrast, at frequencies close to 2.26, 4.89, 7.50, ..., 19.9Hz, etc, motion amplification is only observed in the target layer. The first of these frequencies (2.26Hz) is precisely the frequency our optimizer converged to in the last numerical experiment.

3.4.4 Optimal time signal with higher dominant frequency content

As shown earlier, the optimization process that we described successfully recovers the loading time signals exhibiting strong components at the amplification frequencies shown in Fig. 3.15. For example, Fig. 3.6(b) shows motion amplification at 1.3Hz (compare with 1.34Hz of Fig. 3.15), whereas Fig. 3.12(b) shows 2.2Hz (compare with 2.26Hz of Fig. 3.15; silent neighbors). As seen in Fig. 3.16, such recovered frequencies 1.3 and 2.2Hz account for the global minima of the objective functionals, respectively, (3.4) and (3.5), with respect to the excitation frequency.

In addition to such amplification frequencies as 1.3 and 2.2Hz, we suggest that the optimizer can reconstruct loading time signals exhibiting strong components at other amplification frequencies, such as 4.0Hz and 6.7Hz of Fig. 3.16(a), or 4.9Hz and 7.4Hz of Fig. 3.16(b). To this end, we employ a periodic unknown force function that has np periods within an observation duration T; each period here is temporally discretized using quadratic shape functions and nf discretized force parameters. The unknown force time signal

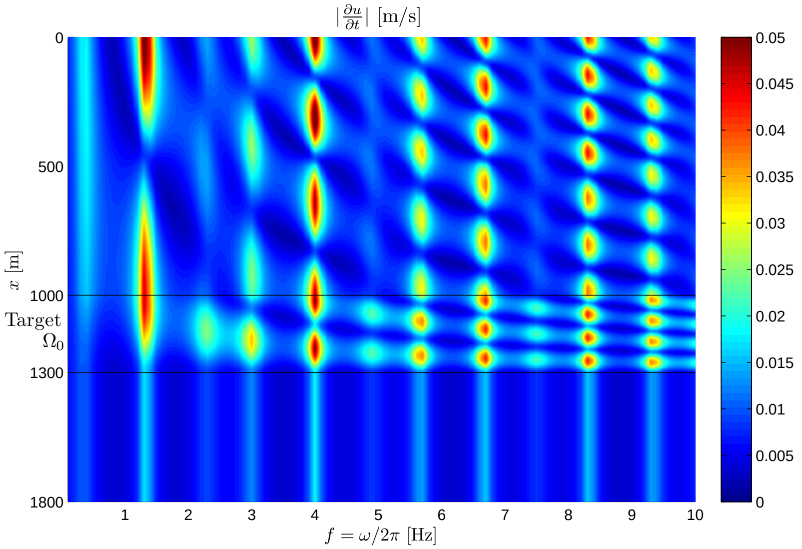

(a) Frequencies $f = 0.1 - 10.0$Hz

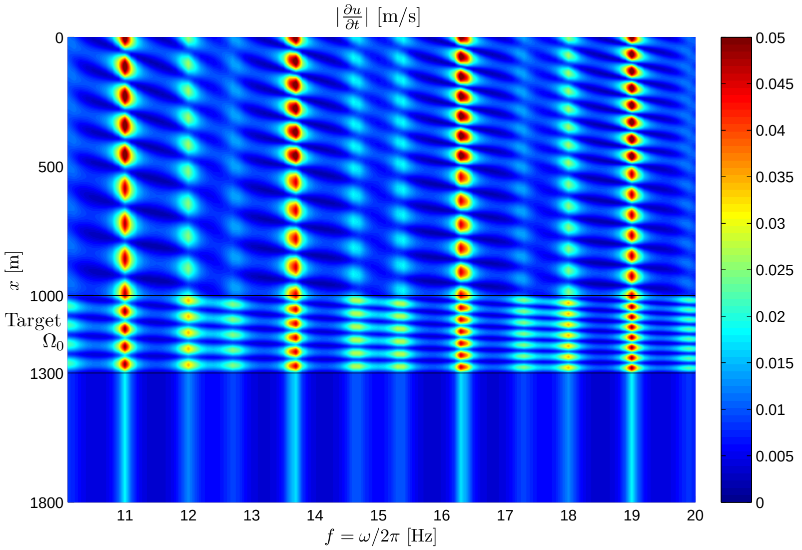

(b) Frequencies $f = 10.1 - 20.0$Hz

Figure 3.15: Frequency sweep of the amplitude of particle velocity $\left|\frac{\partial u}{\partial t}\right|$, for frequency $f = \frac{\omega}{2\pi}$, within the truncated semi-infinite layered system, shown in Fig. 3.3.

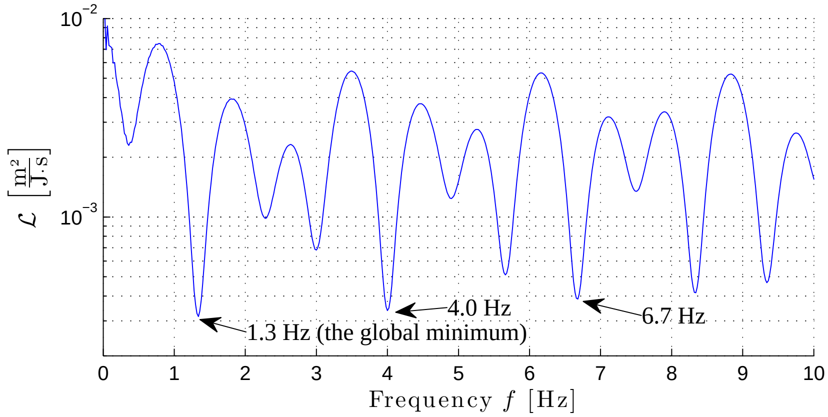

(a) $\mathcal{L}$ in (3.4)

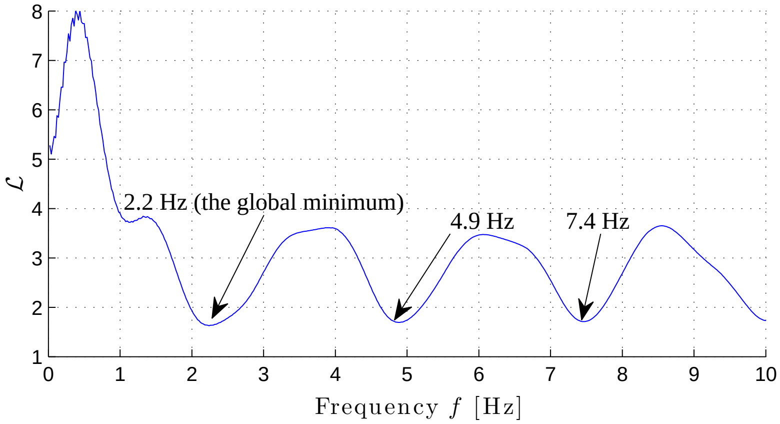

(b) $\mathcal{L}$ in (3.5)

Figure 3.16: The values of the objective functionals (3.4) and (3.5) for a sinusoidal loading time signal $f(t) = 50 \sin(2\pi f t)\mathrm{kN/m^2}$ for frequencies f =0.1–10Hz.

$f(t)$ can be described as follows:

$$f(t) = \sum_{j=1}^{np} \sum_{i=1}^{nf} f_i \varphi_{(i+nf(j-1))}(t). \tag{3.44}$$

Thus, the reduced gradient components are then evaluated as:

$$\nabla_{f_i} \mathcal{L} = \int_0^T \lambda \sum_{j=1}^{np} \varphi_{(i+nf(j-1))}(t) dt \bigg|_{x=0}. \tag{3.45}$$

By using the gradient (3.45), we identify such periodic optimal loading time signals. The numerical results are reported in Figures 3.17 and 3.18. For these experiments, we used the observation duration of $T = 10$s and a time step 0.002s. Each period is temporally discretized by using 40 discretized force parameters (20 quadratic elements). As seen in Fig. 3.17, the minimization of (3.4), employing periodic loading time signals with the period 1s and 0.3s, leads to the near-rectangular signals with dominant frequencies, 4 and 6.7Hz, respectively. Figure 3.18 shows that the minimization of (3.5) with periodic loading time signals with the period 2s and 1.5s leads to the sinusoidal-like signals with dominant frequencies, 5 and 7.35Hz, respectively.

Although there is no clear correlation between the period of an initially guessed loading time signal and the dominant frequency of its ensuing converged signal, it is evident that employing an initially guessed loading time signal of a shorter period yields an optimal loading time signal of a higher dominant frequency.

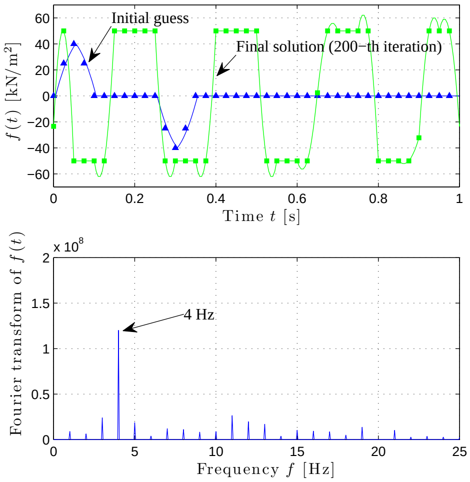

(a) The optimized excitation signal of a loading period of 1s

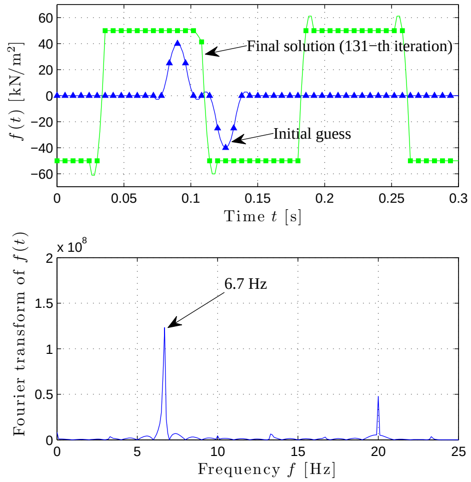

(b) The optimized excitation signal of a loading period of 0.3s

Figure 3.17: Inverted-for periodic loading time signals, obtained via the minimization of (3.4) (all layers active), show strong components at theoretical amplification frequencies 4.0 and 6.7Hz.

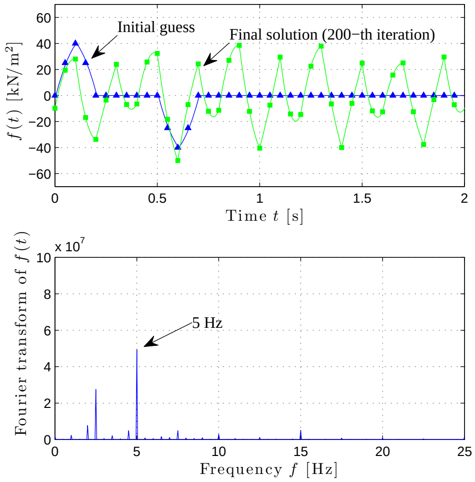

(a) The optimized excitation signal of a loading period of 2s

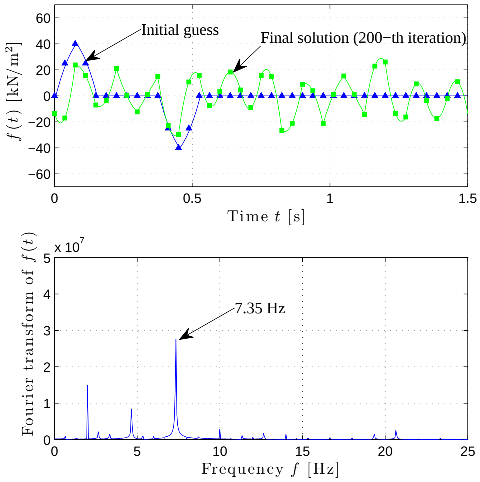

(b) The optimized excitation signal of a loading period of 1.5s

Figure 3.18: Inverted-for periodic loading time signals, obtained via the minimization of (3.5) (silent neighbors), show strong components at theoretical amplification frequencies 5.0 and 7.35Hz.

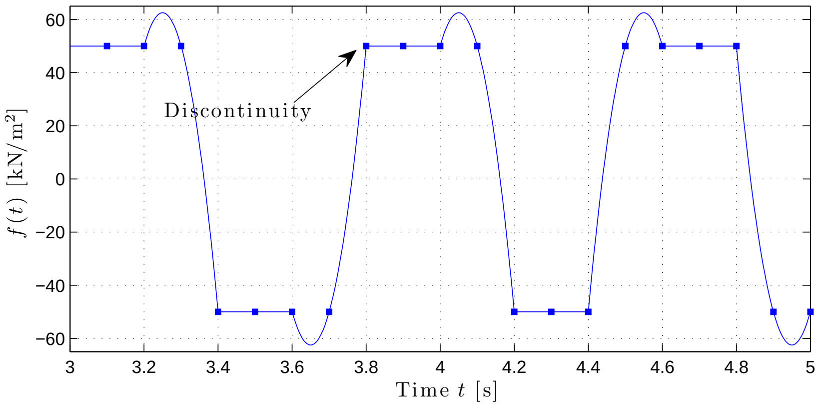

(a) The optimized loading time signal shown in Fig. 3.6(a) (obtained via the minimization of (3.4) – all layers active)

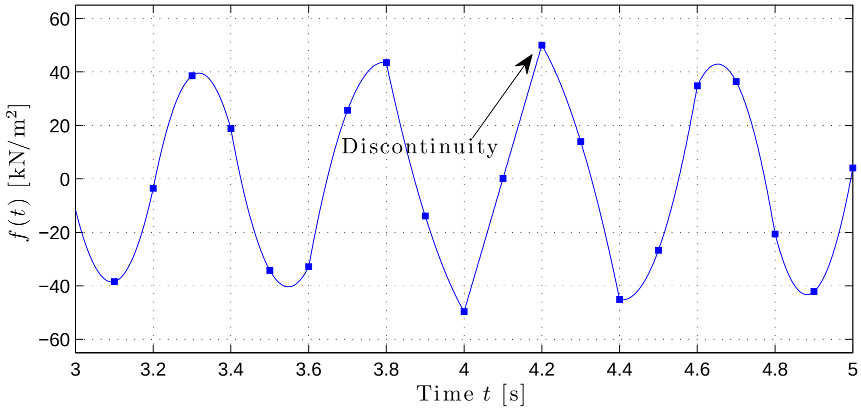

(b) The optimized loading time signal shown in Fig. 3.12(a) (obtained via the minimization of (3.5) – silent neighbors)

Figure 3.19: Close-up views of the optimized loading time signals, temporally approximated by quadratic shape functions (derivatives are not smooth).

3.4.5 Time signal smoothing

As seen in Fig. 3.19, the optimized time signals, which are temporally approximated via quadratic shape functions, are likely to be non-smooth (they are only C^0 continuous, and could then introduce very high frequency components). To alleviate such non-smoothness of the optimized force time signals, we employ Hermite cubic basis functions, which automatically ensure the C^1 continuity for the temporal approximation of $f(t)$. Hence, we approximate $f(t)$ as the following:

$$f(t) = \sum_{i=1}^{nf} f_i \varphi_i(t) + \sum_{i=1}^{nf} f'_i \varphi'_i(t), \tag{3.46}$$

whereby n_f denotes the number of the discretized force parameters; f_i denotes the discretized force parameters; f'_i denotes the slope parameters. The global basis function $\varphi_i(t)$ denotes the i-th basis function that accounts for the approximation of the amplitude of $f(t)$ with vanishing slopes, i.e., $\frac{\partial f(t)}{\partial t} = 0$, at all discretized force points; the basis function $\varphi'_i(t)$ is the i-th basis function that accounts for the determination of the slope at the discretized force points while the continuity of such slopes is ensured. The basis functions $\varphi_i(t)$ and $\varphi'_i(t)$ have the following properties:

$$\varphi_i(t_j) = \begin{cases} 1 & \text{if } i = j \\ 0 & \text{if } i \neq j \end{cases}, \qquad \frac{\partial \varphi_i(t_j)}{\partial t} = 0, \tag{3.47}$$

$$\varphi'_i(t_j) = 0, \qquad \frac{\partial \varphi'_i(t_j)}{\partial t} = \begin{cases} 1 & \text{if } i = j \\ 0 & \text{if } i \neq j \end{cases}, \tag{3.48}$$

where t_i denotes the time for the i-th discretized force points for the temporal approximation. Here, we use Hermite polynomial shape functions [7] to construct such global basis functions $\varphi_i(t)$ and $\varphi_i'(t)$. Then, the reduced gradients become:

$$\nabla_{f_i}\mathcal{L} = \int_0^T \lambda\varphi_i(t)dt\bigg|_{x=0}, \tag{3.49}$$

$$\nabla_{f_i'}\mathcal{L} = \int_0^T \lambda\varphi_i'(t)dt\bigg|_{x=0}. \tag{3.50}$$

We perform numerical experiments to seek smooth optimal time signals by employing the reduced gradients (3.49) and (3.50). We solve state and adjoint problems by using a time interval of 0.004s for the total observation duration T of 10s. A guessed non-periodic excitation signal is discretized by using 100 discretized force parameters f_i and 100 slope parameters f_i'.

First, we identify the smooth optimal time signal that can maximize the kinetic energy in Ω_0 with all layers active by minimizing (3.4). To this end, the optimization process starts with the initial guess seen in Fig. 3.20(a), while all the slope parameters are initially set to be zero as shown in Fig. 3.20(b). After 151 iterations, the optimizer arrives at the smooth near-rectangular-shaped time signal shown in Fig. 3.21(a). The close-up view in Fig. 3.21(b) demonstrates that this optimized time signal is quite smooth as opposed to the non-smooth signal of the quadratic temporal approximation shown in Fig. 3.6(a). We remark that the dominant frequency of the smooth optimal loading time signal, 1.3Hz, remains unaltered from that of the quadratically approximated non-smooth optimized time signal.

In addition, we also identify a smooth optimal time signal that can selectively maximize the kinetic energy in Ω_0 with silent neighbors by minimizing (3.5) with the same initial guess, as shown in Fig. 3.20. We obtain the smooth optimized time signal shown in Fig. 3.22. The dominant frequency 2.2Hz of this smooth optimal time signal is, again, unaltered from that of the non-smooth optimized time signal shown in Fig. 3.12(a).

These experiments show that our numerical optimizer, employing the Hermite cubic approximation of a guessed loading time signal, successfully leads to smooth optimized time signals that still maintain the theoretical amplification frequencies.

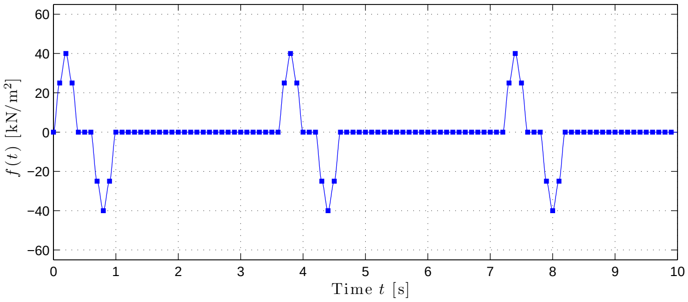

(a) The initially guessed loading time signal

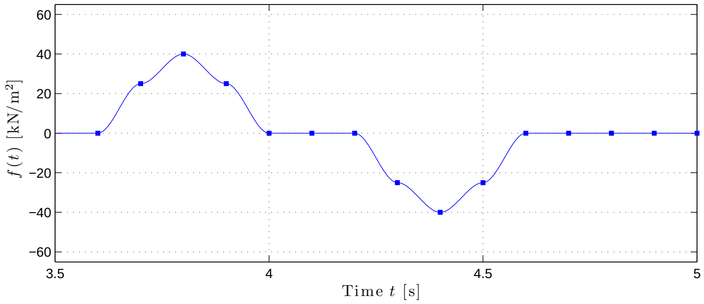

(b) Close-up view of the initially guessed loading time signal

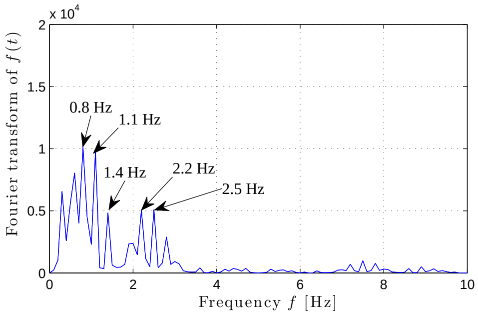

(c) The frequency spectrum of the initially guessed loading time signal

Figure 3.20: The initially guessed loading time signal, temporally approximated by using Hermite shape functions, for the maximization of the kinetic energy in Ω_0.

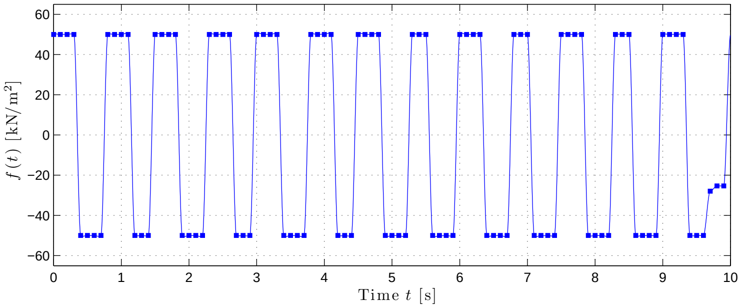

(a) The optimized loading time signal

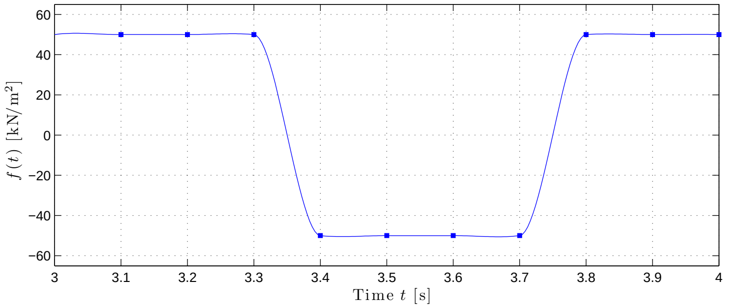

(b) Close-up view of the optimized loading time signal

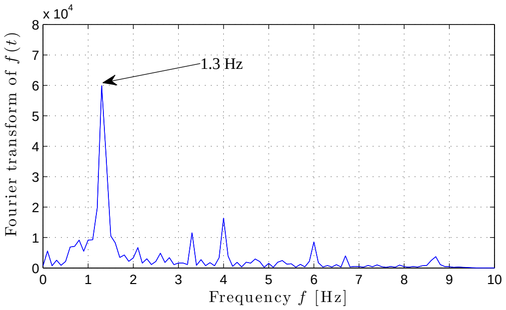

(c) The frequency spectrum of the optimized loading time signal

Figure 3.21: The smooth optimal loading time signal is recovered after 151 iterations (unconstrained neighbors, Hermite approximation of a guessed loading time signal).

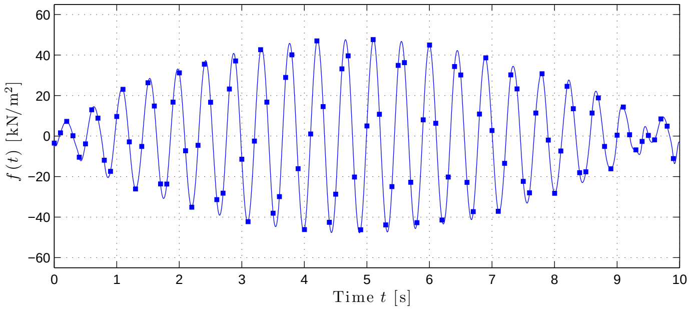

(a) The optimized loading time signal

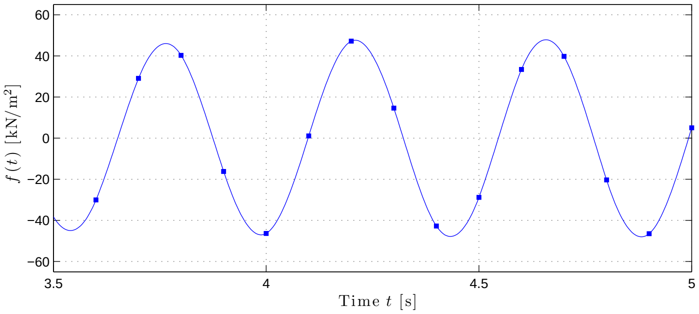

(b) Close-up view of the optimized loading time signal

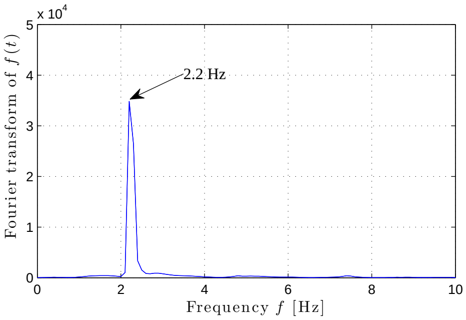

(c) The frequency spectrum of the optimized loading time signal

Figure 3.22: The smooth optimal loading time signal is recovered after 761 iterations (silent neighbors, Hermite approximation of a guessed loading time signal).

3.4.6 Wave source optimal time signals – maximum acceleration – unconstrained or silent neighbors

As discussed earlier in chapters 1 and 2, Beresnev [9] argued that, if the acceleration field of a rock matrix within an oil reservoir exceeds a threshold value (0.1–10m/s^2), the inertial forces on the trapped oil droplets could overcome the capillary forces between the droplets and the pore-wall.

Thus, we investigate the possibility of inducing higher acceleration fields while keeping the force amplitudes within the range of force that can be delivered by present-day equipment. To this end, one could modify the objective functional in order to seek to maximize the acceleration field within the target layer instead of the kinetic energy. In this scenario, the functional is then cast as:

$$\mathcal{L} = \frac{1}{\int_{\Omega_0} \int_0^T [\frac{\partial^2 u}{\partial t^2}(x,t)]^2 dt dx}, \tag{3.51}$$

replacing (3.4) or, in the silent neighbors case, as:

$$\mathcal{L} = \frac{\int_{\Omega \setminus \Omega_0} \int_0^T [\frac{\partial^2 u}{\partial t^2}(x,t)]^2 dt dx}{\int_{\Omega_0} \int_0^T [\frac{\partial^2 u}{\partial t^2}(x,t)]^2 dt dx}, \tag{3.52}$$

replacing (3.5). There result the following changes to the adjoint problem:

- Equation (3.11) is replaced by:

$$\mathcal{E}(x) = \begin{cases} \frac{2}{\left(\int_{\Omega_0} \int_0^T [\frac{\partial^2 u(x,t)}{\partial t^2}]^2 dt dx\right)^2}, & x \in \Omega_0, \\ 0, \quad x \in \Omega \setminus \Omega_0, & \end{cases}, \tag{3.53}$$

- equation (3.17) is replaced by:

$$\mathcal{E}(x) = \begin{cases} \dfrac{2\int_{\Omega\setminus\Omega_0}\int_0^T [\frac{\partial^2 u(x,t)}{\partial t^2}]^2 dt dx}{\left(\int_{\Omega_0}\int_0^T [\frac{\partial^2 u(x,t)}{\partial t^2}]^2 dt dx\right)^2}, & x \in \Omega_0, \\ \\ \dfrac{-2}{\int_{\Omega_0}\int_0^T [\frac{\partial^2 u(x,t)}{\partial t^2}]^2 dt dx}, & x \in \Omega \setminus \Omega_0, \end{cases}, \tag{3.54}$$

- the adjoint problem (3.12) is replaced by:

$$\frac{\partial}{\partial x}\left(E\frac{\partial \lambda}{\partial x}\right) - \rho\frac{\partial^2 \lambda}{\partial t^2} = \mathcal{E}(x)\frac{\partial^4 u}{\partial t^4}, \quad x \in (0, L), \;\; t \in [0, T), \tag{3.55}$$

$$\frac{\partial \lambda}{\partial x}(0, t) = 0, \quad t \in [0, T), \tag{3.56}$$

$$\frac{\partial \lambda}{\partial x}(L, t) - \frac{1}{c(L)}\frac{\partial \lambda}{\partial t}(L, t) = 0, \quad t \in [0, T), \tag{3.57}$$

$$\lambda(x, T) = -\frac{\mathcal{E}(x)}{\rho}\frac{\partial^2 u}{\partial t^2}(x, T), \quad x \in (0, L), \tag{3.58}$$

$$\frac{\partial \lambda}{\partial t}(x, T) = -\frac{\mathcal{E}(x)}{\rho}\frac{\partial^3 u}{\partial t^3}(x, T) + \frac{\lambda(x, T)}{\rho}\frac{E}{c}\delta(x - l), \quad x \in (0, L), \tag{3.59}$$

  whereby $\delta(x - l)$ denotes Dirac delta[5], and

- equation (3.30) is replaced by:

$$\mathbf{P}(t) = -\int_0^L \left[\mathcal{E}\rho\boldsymbol{\phi}\boldsymbol{\phi}^T\right] dx \frac{\partial^4 \mathbf{u}(t)}{\partial t^4}. \tag{3.60}$$

Here, we remark that the above adjoint problem is driven by (a) the body force term in (3.55), which uses the fourth derivative of the displacement $u(x, t)$ with respect to time t; (b) the final value terms in (3.58) and (3.59), which employ the second and third derivative of $u(x, t)$ with respect to time t. We compute

---

[5] We implemented the final value condition (3.59) without the singular term $\frac{\lambda}{\rho}\frac{E}{c}\delta(x - l)$. Nevertheless, the optimizer computes the search direction correctly.

the third and fourth derivatives of the discrete solution of $u(x,t)$ with respect to time t via the finite-difference scheme [16] as the following:

$$\frac{\partial^4 u(x,t)}{\partial t^4} = \frac{\frac{\partial^2 u(x,t+\Delta t)}{\partial t^2} - 2\frac{\partial^2 u(x,t)}{\partial t^2} + \frac{\partial^2 u(x,t-\Delta t)}{\partial t^2}}{(\Delta t)^2}, \quad t \neq 0 \text{ and } t \neq T, \tag{3.61}$$

$$\frac{\partial^4 u(x,T)}{\partial t^4} = \frac{\frac{\partial^2 u(x,T)}{\partial t^2} - 2\frac{\partial^2 u(x,T-\Delta t)}{\partial t^2} + \frac{\partial^2 u(x,T-2\Delta t)}{\partial t^2}}{(\Delta t)^2}, \tag{3.62}$$

$$\frac{\partial^4 u(x,0)}{\partial t^4} = \frac{\frac{\partial^2 u(x,2\Delta t)}{\partial t^2} - 2\frac{\partial^2 u(x,\Delta t)}{\partial t^2} + \frac{\partial^2 u(x,0)}{\partial t^2}}{(\Delta t)^2}, \tag{3.63}$$

$$\frac{\partial^3 u(x,T)}{\partial t^3} = \frac{\frac{\partial^2 u(x,T)}{\partial t^2} - \frac{\partial^2 u(x,T-\Delta t)}{\partial t^2}}{(\Delta t)}, \tag{3.64}$$

where Δt denotes the time step used for computing the discrete solution of the state and adjoint problems.

We then identify non-periodic unknown optimal loading time signals that minimize the acceleration-based objective functional (3.51). To this end, we use initially guessed loading signals that are temporally discretized by employing the quadratic shape functions with 200, 400, and 500 discretized force parameters, respectively. The total observation time is 10s, and the time step is 0.001s. Fig. 3.23 shows that the optimization procedures, using 200, 400, and 500 discretized force points, lead to optimal loading time signals, of which the dominant frequencies are, 8.3, 11.0, and 13.7Hz, respectively. We should point out that, when (3.51) is minimized, the temporal discretization of a guessed loading time signal controls the dominant frequency of a converged loading time signal. That is, increasing the number of force parameters recovers an optimal loading signal of a higher dominant frequency. We explain this behavior as follows.

Recalling (3.43), the amplitude of the acceleration field of the time-harmonic response at a particular point within a targeted inclusion is *nearly proportional* to the frequency ω, as in the following:

$$\frac{\partial^2 u_3(x,t)}{\partial t^2} = \\ -\omega \times \frac{\left(\frac{22}{5} i e^{-\frac{i\omega(-1300+x)}{1500}} - 2ie^{\frac{i\omega(-1300+x)}{1500}}\right) e^{i\omega t}}{\left(165e^{-\frac{17}{30}i\omega} - 5e^{-\frac{7}{30}i\omega} - 11e^{\frac{7}{30}i\omega} - 22e^{\frac{i\omega}{6}} + 363e^{\frac{17}{30}i\omega} - 106e^{-\frac{i\omega}{6}}\right)}, \tag{3.65}$$

whereas the amplitude of the velocity field of the time-harmonic response at a particular point within a targeted inclusion is not proportional to the frequency ω:

$$\frac{\partial u_3(x,t)}{\partial t} = \\ \frac{i\left(\frac{22}{5} i e^{-\frac{i\omega(-1300+x)}{1500}} - 2ie^{\frac{i\omega(-1300+x)}{1500}}\right) e^{i\omega t}}{\left(165e^{-\frac{17}{30}i\omega} - 5e^{-\frac{7}{30}i\omega} - 11e^{\frac{7}{30}i\omega} - 22e^{\frac{i\omega}{6}} + 363e^{\frac{17}{30}i\omega} - 106e^{-\frac{i\omega}{6}}\right)}. \tag{3.66}$$

Accordingly, as seen in Fig. 3.26, the value of the acceleration-based objective functional (3.51) for a sinusoidal loading $f(t) = 50\sin(2\pi f t)\text{kN/m}^2$ with respect to frequencies f tends to decrease as the frequency increases. Thus, the minimizer of (3.51) recovers the highest frequency that the temporal discretization of a guessed loading time signal can allow.

Fig. 3.24 shows that the amplitude of the acceleration field within the targeted inclusion for the optimized loading time signal, shown in Fig. 3.23(c), is up to 6m/s^2. Such amplitudes are much larger than those, shown in Fig. 3.25, for the optimal loading time signal obtained for the maximization of the kinetic energy.

On the other hand, as seen in Fig. 3.23(d), the minimization of the other acceleration-based objective functional (3.52) (silent acceleration in the neighbors) gives rise to the time signal of the dominant frequency of 2.2Hz. This frequency is identical to that of the optimal loading time signal, shown in Fig. 3.12, that is obtained by minimizing (3.5) (the maximization of the kinetic energy in the target with silent adjacent layers). Fig. 3.26(b) also shows that the frequency sweep of the objective functional (3.52) has the global minimum at 2.2Hz. That is, as opposed to (3.51), (3.52) does not tend to decrease with respect to the increasing frequency because the near-proportional frequency dependency of the denominator of (3.52) is eliminated by that of the numerator of (3.52).

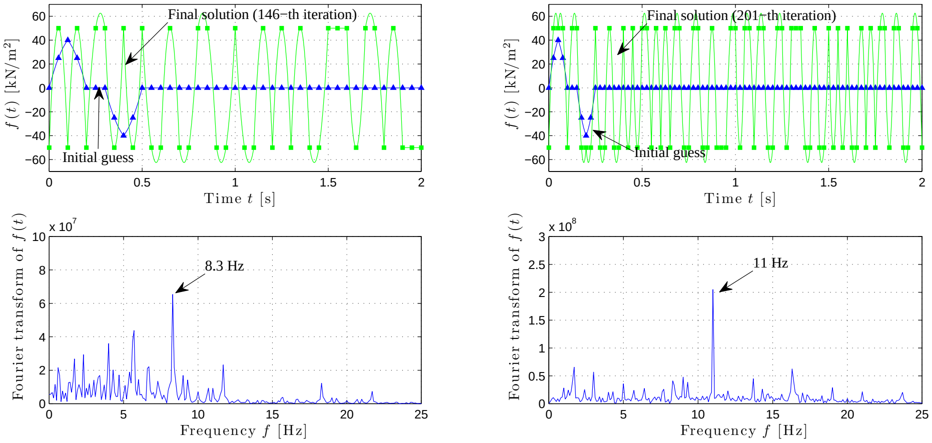

(a) The optimal $f(t)$ obtained via the minimization of (3.51) (all layers active) with 200 discretized force parameters

(b) The optimal $f(t)$ obtained via the minimization of (3.51) (all layers active) with 400 discretized force parameters

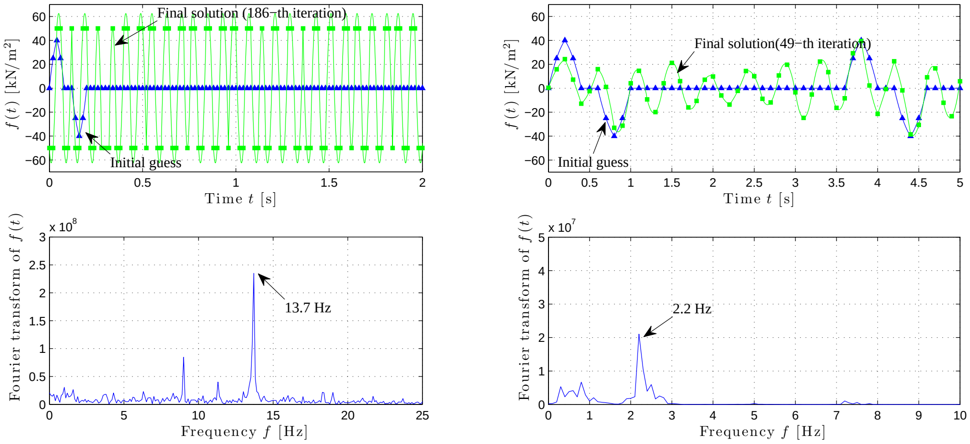

(c) The optimal $f(t)$ obtained via the minimization of (3.51) (all layers active) with 500 discretized force parameters

(d) The optimal $f(t)$ obtained via the minimization of (3.52) (silent acceleration in neighbors) with 100 discretized force parameters

Figure 3.23: The optimized loading time signals for the maximization of the acceleration in Ω_0.

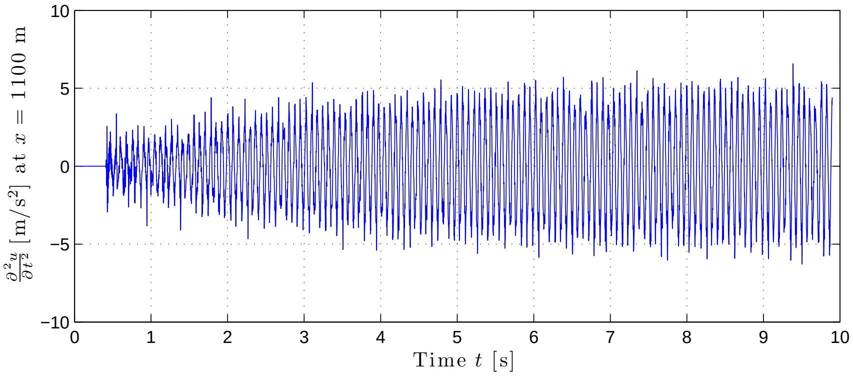

(a) The acceleration at $x = 1100$m

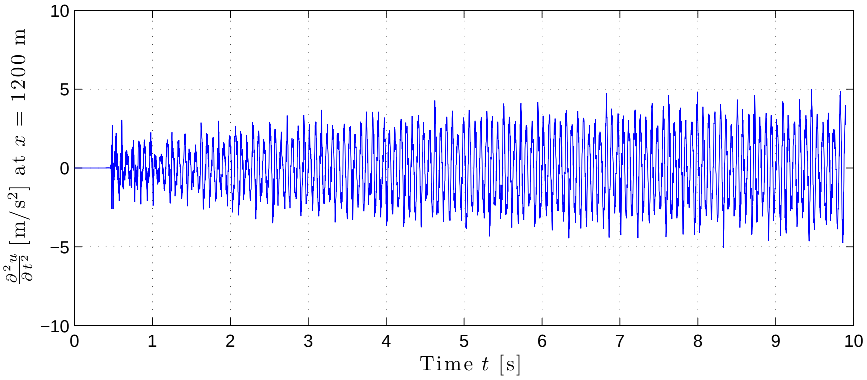

(b) The acceleration at $x = 1200$m

Figure 3.24: The acceleration in the target formation Ω_0, for the converged loading in Fig. 3.23(c).

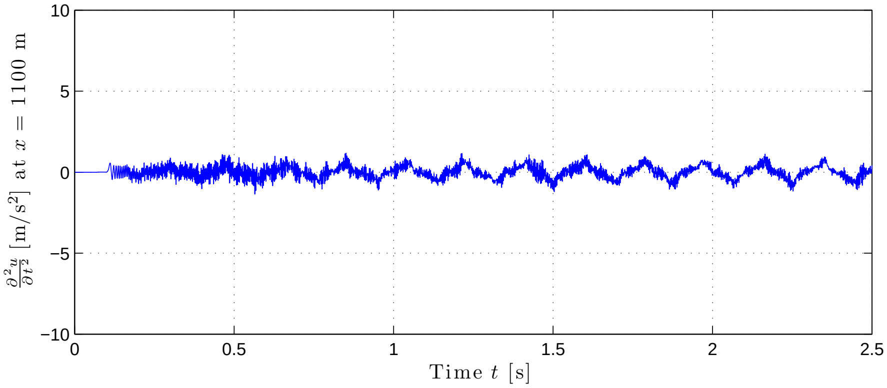

(a) The acceleration at $x = 1100$m

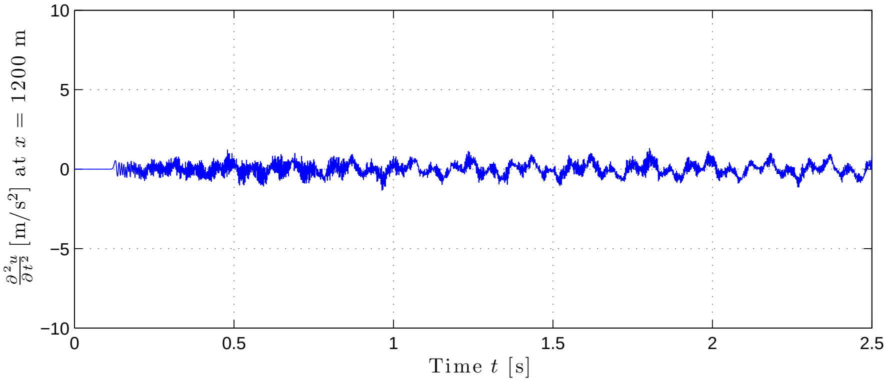

(b) The acceleration at $x = 1200$m

Figure 3.25: The acceleration in the targeted formation Ω_0 for the optimized loading signal in Fig. 3.6 (maximization of kinetic energy in Ω_0 with all layers active).

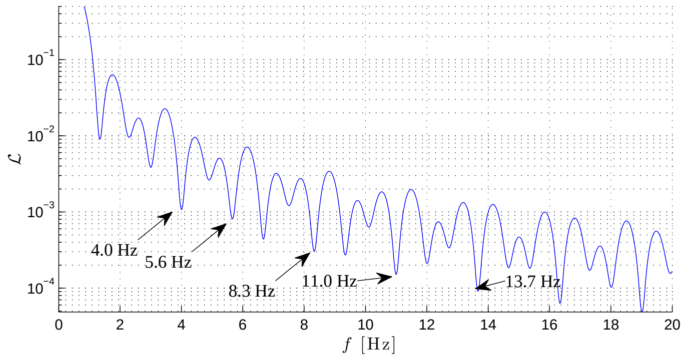

(a) The objective functional (3.51): all layers active

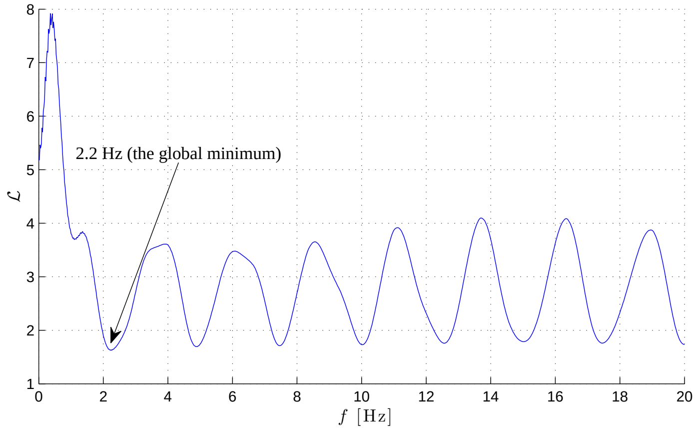

(b) The objective functional (3.52): silent neighbors

Figure 3.26: Distribution of acceleration-based objective functionals (3.51) and (3.52) for sinusoidal loading $f(t) = 50 \sin(2\pi f t) \mathrm{kN/m^2}$ with respect to frequencies f.

3.5 Summary

- We described a systematic process that allows for the determination of an unknown excitation that can maximize mobility in a targeted formation embedded within a heterogeneous domain. We cast the problem as an inverse-source problem, and used the PDE-constrained optimization scheme to arrive at the trio of state, adjoint, and control problems. Solving the problem triplet yields an unknown optimal excitation, which over many others, resulted in large kinetic energy or acceleration distribution within the target formation.

- Numerical results showed that our numerical optimizer nicely recovers nearly-monochromatic optimal wave source loading signals with dominant frequency that coincides with one of the theoretical amplification frequencies. The kinetic energy in the target layer for the optimized wave source signals, employing one of a set of the amplification frequencies, is several times larger than that for a non-optimized wave source signal. The optimizer also identified a wave source loading signal, containing one of the other set of amplification frequencies, that can selectively maximize the kinetic energy in the target layer, while the kinetic energy in the neighboring layers is minimized.

- We also demonstrated that a smooth optimal loading time signal can be obtained by employing Hermite cubic shape functions for the temporal approximation of such a loading time signal. Thus, using Hermite cubic shape functions could reduce high frequency components, associated with the non-smoothness of a loading signal approximated by using quadratic shape functions.

- The optimization process, employing the acceleration-based objective functional, produced excitations that can induce significant acceleration fields (up to 6m/s^2), which appear capable of mobilizing oil in existing reservoirs in this one-dimensional setting.

- The procedure, nearly unaltered, could be extended to the all-important three dimensional elastic wave case with fluid-saturated solid inclusion. In the next chapter, we will discuss the extension of this approach to a more realistic two-dimensional setting, and examine if the maximization of wave energy or acceleration within a targeted inclusion is possible. The feasibility of oil-mobilization will be discussed more in detail in the 2D setting.

Chapter 4

Oil mobilization via ground sources – The elastic inverse-source problem in 2D

In this chapter, we extend the one-dimensional development of chapter 3 to the more realistic two-dimensional case. The goal is to identify optimal loading signals of ground surface wave sources that can maximize desired metrics (the wave energy or the amplitude of an acceleration field) within a targeted elastic solid inclusion embedded in a two-dimensional semi-infinite heterogeneous elastic solid medium. We consider the two-dimensional elastic wave physics equations, endowed by Perfectly-Matched-Layers (PMLs) as the wave-absorbing conditions at the truncation boundary. We again use the PDE-constrained optimization approach to arrive at optimized source signals. In order to satisfy the first-order optimality conditions, we numerically solve the state and adjoint problems by using now a mixed finite element method. We report numerical results of inverting the optimal time signals that maximize the kinetic energy or the acceleration field within a hypothetical hydrocarbon reservoir inclusion.

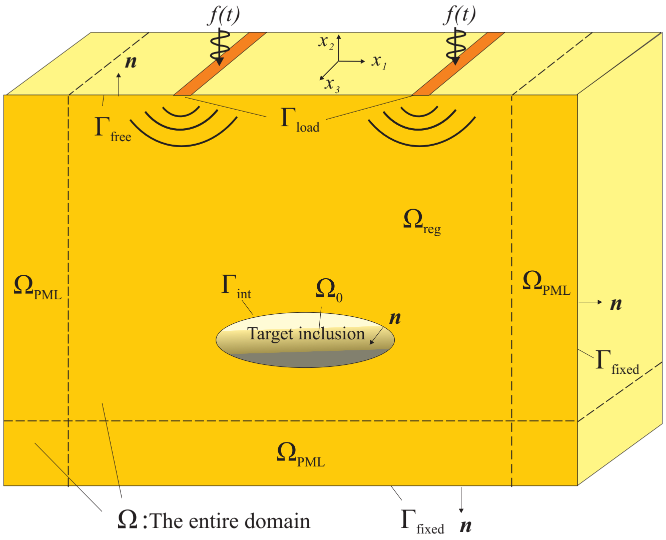

Figure 4.1: The problem definition: the target inclusion Ω_0 embedded within a semi-infinite heterogeneous host.

4.1 Problem definition

4.1.1 Governing wave physics

We consider a targeted inclusion Ω_0 that is embedded in a semi-infinite elastic solid medium subjected to multiple dynamic strip loadings located on the free surface (Fig. 4.1). For simplicity, we adopt plane-strain assumptions: spatially, the wave motion depends on x_1 and x_2.

Referring to Fig. 4.1, the targeted elastic inclusion Ω_0, as well as the exterior domain $\Omega \setminus \Omega_0$ are occupied by a linear elastic solid. Hereby, Perfectly-Matched-Layers (PMLs), denoted by Ω_{PML}, are adopted to implement wave-absorbing conditions at the truncation interfaces [45, 46, 47]. In Fig. 4.1, Ω_{reg} denotes the regular domain, i.e., the entire domain except for Ω_{PML}. The elastic wave response is governed by the following wave equations (for brevity, the space and time dependency of the variables and coefficients are dropped):

$$\mathbf{div}\left(\frac{\partial \mathbf{S}_{\mathrm{a}}^{T}}{\partial t}\right) - \rho \frac{\partial^2 \mathbf{u}_{\mathrm{a}}}{\partial t^2} = \mathbf{0}, \quad \boldsymbol{x} \in \Omega_0, \quad t \in (0, T], \tag{4.1a}$$

$$\mathcal{D}\left[\frac{\partial^2 \mathbf{S}_{\mathrm{a}}}{\partial t^2}\right] - \frac{1}{2}\left[\nabla \frac{\partial \mathbf{u}_{\mathrm{a}}}{\partial t} + \left(\nabla \frac{\partial \mathbf{u}_{\mathrm{a}}}{\partial t}\right)^T\right] = \mathbf{0}, \quad \boldsymbol{x} \in \Omega_0, \quad t \in (0, T], \tag{4.1b}$$

and

$$\mathbf{div}\left(\frac{\partial \mathbf{S}_{\mathrm{b}}^{T}}{\partial t}\tilde{\Lambda}_e + \mathbf{S}_{\mathrm{b}}^{T}\tilde{\Lambda}_p\right) - \rho\left(a\frac{\partial^2 \mathbf{u}_{\mathrm{b}}}{\partial t^2} + b\frac{\partial \mathbf{u}_{\mathrm{b}}}{\partial t} + c\mathbf{u}_{\mathrm{b}}\right) = \mathbf{0}, \\ \boldsymbol{x} \in \Omega \setminus \Omega_0, \quad t \in (0, T], \tag{4.2a}$$

$$\begin{aligned} &\Lambda_e^T\left(\mathcal{D}\left[\frac{\partial^2 \mathbf{S}_{\mathrm{b}}}{\partial t^2}\right]\right)\Lambda_e + \Lambda_e^T\left(\mathcal{D}\left[\frac{\partial \mathbf{S}_{\mathrm{b}}}{\partial t}\right]\right)\Lambda_p \\ &+ \Lambda_p^T\left(\mathcal{D}\left[\frac{\partial \mathbf{S}_{\mathrm{b}}}{\partial t}\right]\right)\Lambda_e + \Lambda_p^T(\mathcal{D}\left[\mathbf{S}_{\mathrm{b}}\right])\Lambda_p \\ &- \frac{1}{2}\left[\Lambda_p^T \nabla \mathbf{u}_{\mathrm{b}} + (\nabla \mathbf{u}_{\mathrm{b}})^T \Lambda_p\right] - \frac{1}{2}\left[\Lambda_e^T \nabla \frac{\partial \mathbf{u}_{\mathrm{b}}}{\partial t} + \left(\nabla \frac{\partial \mathbf{u}_{\mathrm{b}}}{\partial t}\right)^T \Lambda_e\right] = \mathbf{0}, \\ &\qquad \boldsymbol{x} \in \Omega \setminus \Omega_0, \quad t \in (0, T], \end{aligned} \tag{4.2b}$$

where $\boldsymbol{x} = (x_1, x_2)$ denotes location, t denotes time; T denotes the total observation time. (4.1a) and (4.1b) denote, respectively, the equation of motion and the combined constitutive and kinematic equation in the targeted elastic solid medium Ω_0; (4.2a) and (4.2b) denote, respectively, the equation of motion and the combined constitutive and kinematic equation in the surrounding elastic solid medium $\Omega \setminus \Omega_0$, which includes Ω_{PML}. $\mathbf{u}(\boldsymbol{x}, t)$ denotes the displacement field,

$$\mathbf{u}(\boldsymbol{x},t) = \begin{bmatrix} u_1(\boldsymbol{x},t) \\ u_2(\boldsymbol{x},t) \end{bmatrix}, \tag{4.3}$$

and $\mathbf{S}(\boldsymbol{x},t)$ denotes the stress history tensor, which is defined as the following:

$$\begin{aligned} \mathbf{S}(\boldsymbol{x},t) &= \begin{bmatrix} S_{11}(\boldsymbol{x},t) & S_{12}(\boldsymbol{x},t) \\ S_{21}(\boldsymbol{x},t) & S_{22}(\boldsymbol{x},t) \end{bmatrix} \\ &= \int_0^t \boldsymbol{\sigma}(\boldsymbol{x},\tau)d\tau. \end{aligned} \tag{4.4}$$

In (4.4), $\boldsymbol{\sigma}(\boldsymbol{x},t)$ denotes the second-order stress tensor. Thus, $\frac{\partial \mathbf{S}}{\partial t}(\boldsymbol{x},t)$ is equal to the stress tensor $\boldsymbol{\sigma}(\boldsymbol{x},t)$. We remark that (4.1) and (4.2) are differential equations in terms of both the displacement and the stress-history tensor; the equations of $\mathbf{u}(\boldsymbol{x},t)$ and $\mathbf{S}(\boldsymbol{x},t)$ with the subscript 'a' and 'b' are satisfied in, Ω_0 and $\Omega \setminus \Omega_0$, respectively. $\mathcal{D}(\boldsymbol{x})$ denotes the fourth-order compliance tensor and square brackets following $\mathcal{D}$ denote tensor operation. The strain tensor can be obtained as:

$$\boldsymbol{\varepsilon}(\boldsymbol{x},t) = \mathcal{D}(\boldsymbol{x}) \left[\frac{\partial \mathbf{S}}{\partial t}(\boldsymbol{x},t) \right], \tag{4.5}$$

or

$$\begin{bmatrix} \frac{\partial u_1}{\partial x_1} & \frac{\partial u_1}{\partial x_2} \\ \frac{\partial u_2}{\partial x_1} & \frac{\partial u_2}{\partial x_2} \end{bmatrix} = \begin{bmatrix} \frac{(1-\nu^2)}{E}\frac{\partial S_{11}}{\partial t} - \frac{\nu(1+\nu)}{E}\frac{\partial S_{22}}{\partial t} & \frac{(1+\nu)}{E}\frac{\partial S_{12}}{\partial t} \\ \frac{(1+\nu)}{E}\frac{\partial S_{21}}{\partial t} & \frac{(1-\nu^2)}{E}\frac{\partial S_{22}}{\partial t} - \frac{\nu(1+\nu)}{E}\frac{\partial S_{11}}{\partial t} \end{bmatrix}. \tag{4.6}$$

In (4.1) and (4.2), $\rho(\boldsymbol{x})$ is the mass density of the elastic solid medium; $\tilde{\Lambda}_e(\boldsymbol{x})$, $\tilde{\Lambda}_p(\boldsymbol{x})$, $\Lambda_e(\boldsymbol{x})$, and $\Lambda_p(\boldsymbol{x})$ are coordinate stretching tensors, and $a(\boldsymbol{x})$, $b(\boldsymbol{x})$, and $c(\boldsymbol{x})$ are attenuation coefficients [45, 46, 47]. The system is also subjected to the following boundary conditions:

$$\mathbf{u}_{\mathrm{b}}(\boldsymbol{x},t) = \mathbf{0}, \quad \boldsymbol{x} \in \Gamma_{\text{fixed}}, \tag{4.7a}$$

$$\frac{\partial \mathbf{S}_{\mathrm{b}}^T(\boldsymbol{x},t)}{\partial t}\boldsymbol{n}(\boldsymbol{x}) = \mathbf{f}(\boldsymbol{x},t), \quad \boldsymbol{x} \in \Gamma_{\text{load}}, \tag{4.7b}$$

$$\left(\frac{\partial \mathbf{S}_{\mathrm{b}}^T(\boldsymbol{x},t)}{\partial t}\tilde{\Lambda}_e(\boldsymbol{x}) + \mathbf{S}_{\mathrm{b}}^T(\boldsymbol{x},t)\tilde{\Lambda}_p(\boldsymbol{x})\right)\boldsymbol{n}(\boldsymbol{x}) = \mathbf{0}, \quad \boldsymbol{x} \in \Gamma_{\text{free}} \setminus \Gamma_{\text{load}}, \tag{4.7c}$$

where $\boldsymbol{n}$ denotes the outward normal unit vector on a boundary Γ; the vector force function $\mathbf{f}(\boldsymbol{x},t)$ is decomposed into the x_1-directional force function $f_1(\boldsymbol{x},t)$ and the x_2-directional force function $f_2(\boldsymbol{x},t)$; we consider a vibrational force only in the vertical-direction, i.e., $f_1(\boldsymbol{x},t) = 0$. In addition to the boundary conditions, the governing equations (4.1) and (4.2) are coupled via the interface conditions on Γ_{int}:

$$\mathbf{u}_{\mathrm{a}}(\boldsymbol{x},t) = \mathbf{u}_{\mathrm{b}}(\boldsymbol{x},t), \qquad \boldsymbol{x} \in \Gamma_{\text{int}}, \tag{4.8a}$$

$$\frac{\partial \mathbf{S}_{\mathrm{a}}^T(\boldsymbol{x},t)}{\partial t}\boldsymbol{n}(\boldsymbol{x}) = \frac{\partial \mathbf{S}_{\mathrm{b}}^T(\boldsymbol{x},t)}{\partial t}\boldsymbol{n}(\boldsymbol{x}), \qquad \boldsymbol{x} \in \Gamma_{\text{int}}, \tag{4.8b}$$

where (4.8a) and (4.8b) denote the continuity of, respectively, displacements and tractions on Γ_{int}. The governing equations (4.1) and (4.2) are also accompanied by zero initial conditions:

$$\mathbf{u}(\boldsymbol{x},0) = \mathbf{0}, \quad \frac{\partial \mathbf{u}}{\partial t}(\boldsymbol{x},0) = \mathbf{0}, \quad \boldsymbol{x} \in \Omega, \tag{4.9a}$$

$$\mathbf{S}(\boldsymbol{x},0) = \mathbf{0}, \quad \frac{\partial \mathbf{S}}{\partial t}(\boldsymbol{x},0) = \mathbf{0}, \quad \boldsymbol{x} \in \Omega. \tag{4.9b}$$

4.1.2 Objective functional

Considering the governing physics, we seek to identify the loading time signals of the wave sources that can maximize the kinetic energy in a target inclusion Ω_0. To this end, we inversely compute the loading time signal information of the wave sources that can minimize the following objective functional:

$$\mathcal{L} = \frac{1}{\int_{\Omega_0} \int_0^T \rho \left[\left(\frac{\partial u_{\mathrm{a}_1}}{\partial t} \right)^2 + \left(\frac{\partial u_{\mathrm{a}_2}}{\partial t} \right)^2 \right] dt d\Omega}. \tag{4.10}$$

Alternatively, we also try to maximize the kinetic energy in the target inclusion Ω_0 while the kinetic energy in the neighboring formations $\Omega_{\mathrm{reg}} \backslash \Omega_0$ is minimized. To this end, we inversely compute the time signal of wave sources that can minimize the following objective functional:

$$\mathcal{L} = \frac{\int_{\Omega_{\mathrm{reg}} \backslash \Omega_0} \int_0^T \rho \left[\left(\frac{\partial u_{\mathrm{b}_1}}{\partial t} \right)^2 + \left(\frac{\partial u_{\mathrm{b}_2}}{\partial t} \right)^2 \right] dt d\Omega}{\int_{\Omega_0} \int_0^T \rho \left[\left(\frac{\partial u_{\mathrm{a}_1}}{\partial t} \right)^2 + \left(\frac{\partial u_{\mathrm{a}_2}}{\partial t} \right)^2 \right] dt d\Omega}. \tag{4.11}$$

The denominators of (4.10) and (4.11) include the temporal integral of the kinetic energy that is spatially integrated over Ω_0; the numerator of (4.11) is the temporal integral of the kinetic energy that is spatially integrated over the formations surrounding the reservoir ($\Omega_{\mathrm{reg}} \setminus \Omega_0$). We remark that the form of an objective functional could be altered depending on a metric to be minimized or maximized. For instance, an alternative objective functional could be cast in terms of the acceleration field as:

$$\mathcal{L} = \frac{1}{\int_{\Omega_0} \int_0^T \left[\left(\frac{\partial^2 u_{\mathrm{a}_1}}{\partial t^2} \right)^2 + \left(\frac{\partial^2 u_{\mathrm{a}_2}}{\partial t^2} \right)^2 \right] dt d\Omega}. \tag{4.12}$$

Equation (4.12) is the reciprocal of the temporal integral of the square of the amplitude of the acceleration field that is integrated within the targeted inclusion Ω_0, such that the minimization of (4.12) can lead to optimal loading time signals that can maximize acceleration within Ω_0.

4.2 Mathematical modeling

4.2.1 Augmented functional

To minimize the objective functional $\mathcal{L}$ (4.10) (or (4.11), (4.12)), subjected to the governing wave physics (4.1)–(4.9), we build an augmented functional $\mathcal{A}$ by the side-imposition of the PDEs (4.1) and (4.2), as well as the Neumann boundary condition (4.7b) to the objective functional by using Lagrange multipliers ($\boldsymbol{\lambda}_{u_{\mathrm{a}}}(\boldsymbol{x},t)$, $\boldsymbol{\lambda}_{u_{\mathrm{b}}}(\boldsymbol{x},t)$, $\boldsymbol{\lambda}_{S_{\mathrm{a}}}(\boldsymbol{x},t)$, $\boldsymbol{\lambda}_{S_{\mathrm{b}}}(\boldsymbol{x},t)$, and $\boldsymbol{\lambda}_{\mathrm{F}}(\boldsymbol{x},t)$) as follows:

$$\begin{aligned}
\mathcal{A} =& \frac{1}{\int_{\Omega_0}\int_0^T \rho\left[\left(\frac{\partial u_{\mathrm{a}_1}}{\partial t}\right)^2+\left(\frac{\partial u_{\mathrm{a}_2}}{\partial t}\right)^2\right]dtd\Omega} \\
&+\int_{\Omega_0}\int_0^T \boldsymbol{\lambda}_{u_{\mathrm{a}}}\cdot\left[\mathbf{div}\left(\frac{\partial \mathbf{S}_{\mathrm{a}}^T}{\partial t}\right)-\rho\frac{\partial^2\mathbf{u}_{\mathrm{a}}}{\partial t^2}\right]dtd\Omega \\
&+\int_{\Omega_0}\int_0^T \boldsymbol{\lambda}_{S_{\mathrm{a}}} : \left[\mathcal{D}\left[\frac{\partial^2\mathbf{S}_{\mathrm{a}}}{\partial t^2}\right]-\frac{1}{2}\left\{\nabla\frac{\partial\mathbf{u}_{\mathrm{a}}}{\partial t}+\left(\nabla\frac{\partial\mathbf{u}_{\mathrm{a}}}{\partial t}\right)^T\right\}\right]dtd\Omega \\
&+\int_{\Omega\setminus\Omega_0}\int_0^T \boldsymbol{\lambda}_{u_{\mathrm{b}}}\cdot\left[\mathbf{div}\left(\frac{\partial \mathbf{S}_{\mathrm{b}}^T}{\partial t}\tilde{\Lambda}_e+\mathbf{S}_{\mathrm{b}}^T\tilde{\Lambda}_p\right)\right. \\
&\qquad\qquad\left.-\rho\left(a\frac{\partial^2\mathbf{u}_{\mathrm{b}}}{\partial t^2}+b\frac{\partial\mathbf{u}_{\mathrm{a}}}{\partial t}+c\mathbf{u}_{\mathrm{b}}\right)\right]dtd\Omega \\
&+\int_{\Omega\setminus\Omega_0}\int_0^T \boldsymbol{\lambda}_{S_{\mathrm{b}}} : \left[\Lambda_e^T\left(\mathcal{D}\left[\frac{\partial^2\mathbf{S}_{\mathrm{b}}}{\partial t^2}\right]\right)\Lambda_e+\Lambda_e^T\left(\mathcal{D}\left[\frac{\partial\mathbf{S}_{\mathrm{b}}}{\partial t}\right]\right)\Lambda_p\right.
\end{aligned}$$

$$
\begin{aligned}
&+\Lambda_p^T\left(\mathcal{D}\left[\frac{\partial \mathbf{S}_\mathrm{b}}{\partial t}\right]\right)\Lambda_e+\Lambda_p^T(\mathcal{D}\left[\mathbf{S}_\mathrm{b}\right])\Lambda_p\\
&-\frac{1}{2}\left\{\Lambda_p^T\nabla\mathbf{u}_\mathrm{b}+(\nabla\mathbf{u}_\mathrm{b})^T\Lambda_p\right\}\\
&-\frac{1}{2}\left\{\Lambda_e^T\nabla\frac{\partial\mathbf{u}_\mathrm{b}}{\partial t}+\left(\nabla\frac{\partial\mathbf{u}_\mathrm{b}}{\partial t}\right)^T\Lambda_e\right\}\Bigg]\,dtd\Omega\\
&+\int_{\Gamma_\mathrm{load}}\int_0^T\boldsymbol{\lambda}_\mathrm{F}\cdot\left[\frac{\partial\mathbf{S}_\mathrm{b}^T}{\partial t}\boldsymbol{n}-\mathbf{f}(\boldsymbol{x},t)\right]dtd\Gamma, \qquad (4.13)
\end{aligned}
$$

whereas the other associated conditions in (4.7a), (4.7c), (4.8), and (4.9) are implicitly imposed to the augmented functional. In (4.13), the vector Lagrange multipliers $\boldsymbol{\lambda}_{u_\mathrm{a}}$, $\boldsymbol{\lambda}_{u_\mathrm{b}}$, and $\boldsymbol{\lambda}_\mathrm{F}$ are used for the side-imposition of the vector equations, (4.1a), (4.2a), and (4.7b), respectively, via the dot product $(\cdot)$; the second-order tensor Lagrange multipliers $\boldsymbol{\lambda}_{S_\mathrm{a}}$ and $\boldsymbol{\lambda}_{S_\mathrm{b}}$ are used for the imposition of the tensor equations, (4.1b) and (4.2b), respectively, via the tensor inner product $(:)$. We remark that the dimensions of $\boldsymbol{\lambda}_{u_\mathrm{a}}$, $\boldsymbol{\lambda}_{u_\mathrm{b}}$, and $\boldsymbol{\lambda}_\mathrm{F}$ differ from those of $\boldsymbol{\lambda}_{S_\mathrm{a}}$ and $\boldsymbol{\lambda}_{S_\mathrm{b}}$.

4.2.2 The first-order optimality conditions

We solve for the stationarity of the augmented functional $\mathcal{A}$ in (4.13) by seeking to satisfy the first-order optimality conditions of $\mathcal{A}$. That is, the variations of $\mathcal{A}$ with respect to the arbitrary variations of the state variables ($\mathbf{u}_\mathrm{a}$, $\mathbf{u}_\mathrm{b}$, $\mathbf{S}_\mathrm{a}$, and $\mathbf{S}_\mathrm{b}$), the adjoint (Lagrange) variables ($\boldsymbol{\lambda}_{u_\mathrm{a}}$, $\boldsymbol{\lambda}_{u_\mathrm{b}}$, $\boldsymbol{\lambda}_{S_\mathrm{a}}$, $\boldsymbol{\lambda}_{S_\mathrm{b}}$, and $\boldsymbol{\lambda}_\mathrm{F}$), as well as the control variable (ξ) should vanish as follows.

4.2.2.1 The first optimality condition

The first optimality condition requires that the variation of $\mathcal{A}$ with respect to the adjoint variables ($\boldsymbol{\lambda}_{u_\mathrm{a}}$, $\boldsymbol{\lambda}_{u_\mathrm{b}}$, $\boldsymbol{\lambda}_{S_\mathrm{a}}$, $\boldsymbol{\lambda}_{S_\mathrm{b}}$, and $\boldsymbol{\lambda}_\mathrm{F}$) should vanish, i.e., $\delta_\lambda \mathcal{A} = 0$, for arbitrary variations $\delta\boldsymbol{\lambda}_{u_\mathrm{a}}$, $\delta\boldsymbol{\lambda}_{u_\mathrm{b}}$, $\delta\boldsymbol{\lambda}_{S_\mathrm{a}}$, $\delta\boldsymbol{\lambda}_{S_\mathrm{b}}$, and $\delta\boldsymbol{\lambda}_\mathrm{F}$. Such a vanishing variational condition recovers the state problem, which is identical to the governing wave physics described in (4.1)–(4.9).

4.2.2.2 The second optimality condition

The second optimality condition requires that the variation of $\mathcal{A}$ with respect to the state variables ($\mathbf{u}_\mathrm{a}$, $\mathbf{u}_\mathrm{b}$, $\mathbf{S}_\mathrm{a}$, and $\mathbf{S}_\mathrm{b}$) should vanish, i.e., $\delta_{\mathbf{u},\mathbf{S}}\mathcal{A} = 0$, for arbitrary variations $\delta\mathbf{u}_\mathrm{a}$, $\delta\mathbf{u}_\mathrm{b}$, $\delta\mathbf{S}_\mathrm{a}$, and $\delta\mathbf{S}_\mathrm{b}$. Such a vanishing variation condition recovers the following adjoint problem (the explicit derivation of the adjoint problem is shown in Appendix B):

The adjoint problem:

$$\frac{\partial^2 \boldsymbol{\lambda}_{u_\mathrm{a}}}{\partial t^2}\rho + \mathbf{div}\left(\frac{\partial \boldsymbol{\lambda}_{S_\mathrm{a}}^{sym}}{\partial t}\right) = \rho\mathcal{E}\frac{\partial^2 \mathbf{u}_\mathrm{a}}{\partial t^2}, \qquad \boldsymbol{x} \in \Omega_0,\ t \in [0,T), \tag{4.14a}$$

$$\mathcal{D}\left[\frac{\partial^2 \boldsymbol{\lambda}_{S_\mathrm{a}}^{sym}}{\partial t^2}\right] + \frac{1}{2}\left[\nabla\frac{\partial \boldsymbol{\lambda}_{u_\mathrm{a}}}{\partial t} + \left(\nabla\frac{\partial \boldsymbol{\lambda}_{u_\mathrm{a}}}{\partial t}\right)^T\right] = \mathbf{0}, \qquad \boldsymbol{x} \in \Omega_0,\ t \in [0,T), \tag{4.14b}$$

and

$$\frac{\partial^2 \boldsymbol{\lambda}_{u_\mathrm{b}}}{\partial t^2}\rho a - \frac{\partial \boldsymbol{\lambda}_{u_\mathrm{b}}}{\partial t}\rho b + \boldsymbol{\lambda}_{u_\mathrm{b}}\rho c + \mathbf{div}\left(-\Lambda_p \boldsymbol{\lambda}_{S_\mathrm{b}}^{sym} + \Lambda_e \frac{\partial \boldsymbol{\lambda}_{S_\mathrm{b}}^{sym}}{\partial t}\right) = \rho \mathcal{E} \frac{\partial^2 \mathbf{u}_\mathrm{b}}{\partial t^2}, \qquad \boldsymbol{x} \in \Omega \setminus \Omega_0,\ t \in [0, T), \tag{4.15a}$$

$$\frac{1}{2}\left[\tilde{\Lambda}_e \left(\nabla \frac{\partial \boldsymbol{\lambda}_{u_\mathrm{b}}}{\partial t}\right)^T + \left(\nabla \frac{\partial \boldsymbol{\lambda}_{u_\mathrm{b}}}{\partial t}\right)\tilde{\Lambda}_e\right] - \frac{1}{2}\left[\tilde{\Lambda}_p (\nabla \boldsymbol{\lambda}_{u_\mathrm{b}})^T + (\nabla \boldsymbol{\lambda}_{u_\mathrm{b}})\tilde{\Lambda}_p\right] + \mathcal{D}\left[\Lambda_e^T \frac{\partial^2 \boldsymbol{\lambda}_{S_\mathrm{b}}^{sym}}{\partial t^2}\Lambda_e - \Lambda_e^T \frac{\partial \boldsymbol{\lambda}_{S_\mathrm{b}}^{sym}}{\partial t}\Lambda_p - \Lambda_p^T \frac{\partial \boldsymbol{\lambda}_{S_\mathrm{b}}^{sym}}{\partial t}\Lambda_e + \Lambda_p^T \boldsymbol{\lambda}_{S_\mathrm{b}}^{sym}\Lambda_p\right] = \mathbf{0}, \qquad \boldsymbol{x} \in \Omega \setminus \Omega_0,\ t \in [0, T), \tag{4.15b}$$

whereby $\boldsymbol{\lambda}_{S_\mathrm{a}}^{sym}$ and $\boldsymbol{\lambda}_{S_\mathrm{b}}^{sym}$ denote the symmetric part of, respectively, $\boldsymbol{\lambda}_{S_\mathrm{a}}$ and $\boldsymbol{\lambda}_{S_\mathrm{b}}$, that is, $\boldsymbol{\lambda}_{S_\mathrm{a}}^{sym} = \left(\boldsymbol{\lambda}_{S_\mathrm{a}} + \boldsymbol{\lambda}_{S_\mathrm{a}}^T\right)/2$ and $\boldsymbol{\lambda}_{S_\mathrm{b}}^{sym} = \left(\boldsymbol{\lambda}_{S_\mathrm{b}} + \boldsymbol{\lambda}_{S_\mathrm{b}}^T\right)/2$; the coefficient $\mathcal{E}(\boldsymbol{x})$ in the body force term in (4.14a) and (4.15a) is defined as:

$$\mathcal{E}(\boldsymbol{x}) = \begin{cases} \dfrac{2}{\left(\int_{\Omega_0}\int_0^T \rho\left[\frac{\partial \mathbf{u}_\mathrm{a}}{\partial t}\cdot\frac{\partial \mathbf{u}_\mathrm{a}}{\partial t}\right]dt d\Omega\right)^2}, & \boldsymbol{x} \in \Omega_0, \\ 0, & \boldsymbol{x} \in \Omega \setminus \Omega_0 \end{cases}. \tag{4.16}$$

The solutions of the adjoint PDEs, (4.14) and (4.15), are subject to the boundary conditions:

$$\left(-\Lambda_p \boldsymbol{\lambda}_{S_\mathrm{b}}^{sym} + \Lambda_e \frac{\partial \boldsymbol{\lambda}_{S_\mathrm{b}}^{sym}}{\partial t}\right)\boldsymbol{n} = \mathbf{0}, \quad \boldsymbol{x} \in \Gamma_\text{free}, \tag{4.17a}$$

$$\boldsymbol{\lambda}_{u_\mathrm{b}} = \mathbf{0}, \quad \boldsymbol{x} \in \Gamma_\text{fixed}, \tag{4.17b}$$

$$\boldsymbol{\lambda}_\mathrm{F} = -\boldsymbol{\lambda}_{u_\mathrm{b}}, \quad \boldsymbol{x} \in \Gamma_\text{load}, \tag{4.17c}$$

with the interface conditions:

$$\boldsymbol{\lambda}_{u_\mathrm{a}} = \boldsymbol{\lambda}_{u_\mathrm{b}}, \quad \boldsymbol{\lambda}_{S_\mathrm{a}}\boldsymbol{n} = \boldsymbol{\lambda}_{S_\mathrm{b}}\boldsymbol{n}, \quad \boldsymbol{x} \in \Gamma_\text{int}, \tag{4.18}$$

and the final value conditions:

$$\boldsymbol{\lambda}_{u_\mathrm{a}} = \mathbf{0}, \quad \frac{\partial \boldsymbol{\lambda}_{u_\mathrm{a}}}{\partial t} = \mathcal{E}\frac{\partial \mathbf{u}_\mathrm{a}}{\partial t}, \quad \boldsymbol{\lambda}_{S_\mathrm{a}}^{sym} = \mathbf{0}, \quad \frac{\partial \boldsymbol{\lambda}_{S_\mathrm{a}}^{sym}}{\partial t} = \mathbf{0}, \quad \boldsymbol{x} \in \Omega_0, \ t = T, \tag{4.19a}$$

$$\boldsymbol{\lambda}_{u_\mathrm{b}} = \mathbf{0}, \quad \frac{\partial \boldsymbol{\lambda}_{u_\mathrm{b}}}{\partial t} = \mathcal{E}\frac{\partial \mathbf{u}_\mathrm{b}}{\partial t}, \quad \boldsymbol{\lambda}_{S_\mathrm{b}}^{sym} = \mathbf{0}, \quad \frac{\partial \boldsymbol{\lambda}_{S_\mathrm{b}}^{sym}}{\partial t} = \mathbf{0}, \quad \boldsymbol{x} \in \Omega \setminus \Omega_0, \ t = T. \tag{4.19b}$$

We remark that the adjoint PDEs (4.14) and (4.15) include governing operators similar to those in the state PDEs (4.1) and (4.2), while the body force terms $\rho\mathcal{E}\frac{\partial^2 \mathbf{u}_\mathrm{a}}{\partial t^2}$ and $\rho\mathcal{E}\frac{\partial^2 \mathbf{u}_\mathrm{b}}{\partial t^2}$ in the adjoint problem implicate the solution of the state problem. We also remark that, as opposed to the state IBVP, the adjoint problem is a FBVP, of which the final values, in (4.19), are provided by the coefficient $\mathcal{E}(\boldsymbol{x})$ and the state solution.

If the objective functional (4.11) – the silent neighboring formations – is minimized, the adjoint problem remains unaltered except that the coefficient $\mathcal{E}(\boldsymbol{x})$ is modified to:

$$\mathcal{E}(\boldsymbol{x}) = \begin{cases} \dfrac{2\Big(\int_{\Omega_\mathrm{reg}\setminus\Omega_0}\int_0^T \rho\Big[\frac{\partial \mathbf{u}_\mathrm{b}}{\partial t}\cdot\frac{\partial \mathbf{u}_\mathrm{b}}{\partial t}\Big]dtd\Omega\Big)}{\Big(\int_{\Omega_0}\int_0^T \rho\Big[\frac{\partial \mathbf{u}_\mathrm{a}}{\partial t}\cdot\frac{\partial \mathbf{u}_\mathrm{a}}{\partial t}\Big]dtd\Omega\Big)^2}, & \boldsymbol{x} \in \Omega_0, \\[2ex] \dfrac{-2}{\Big(\int_{\Omega_0}\int_0^T \rho\Big[\frac{\partial \mathbf{u}_\mathrm{a}}{\partial t}\cdot\frac{\partial \mathbf{u}_\mathrm{a}}{\partial t}\Big]dtd\Omega\Big)}, & \boldsymbol{x} \in \Omega_\mathrm{reg}\setminus\Omega_0, \\[2ex] 0, & \boldsymbol{x} \in \Omega \setminus \Omega_\mathrm{reg} \end{cases} . \tag{4.20}$$

If the acceleration-based objective functional (4.12) is employed, the adjoint equations change. First, the adjoint PDEs (4.14a) and (4.15a), respectively, are replaced by:

$$\frac{\partial^2 \boldsymbol{\lambda}_{u_\mathrm{a}}}{\partial t^2}\rho + \mathbf{div}\left(\frac{\partial \boldsymbol{\lambda}_{S_\mathrm{a}}^{sym}}{\partial t}\right) = -\mathcal{E}\frac{\partial^4 \mathbf{u}_\mathrm{a}}{\partial t^4}, \quad \boldsymbol{x} \in \Omega_0, \quad t \in [0, T), \tag{4.21}$$

$$\frac{\partial^2 \boldsymbol{\lambda}_{u_\mathrm{b}}}{\partial t^2}\rho a - \frac{\partial \boldsymbol{\lambda}_{u_\mathrm{b}}}{\partial t}\rho b + \boldsymbol{\lambda}_{u_\mathrm{b}}\rho c + \mathbf{div}\left(-\Lambda_p \boldsymbol{\lambda}_{S_\mathrm{b}}^{sym} + \Lambda_e \frac{\partial \boldsymbol{\lambda}_{S_\mathrm{b}}^{sym}}{\partial t}\right) = -\mathcal{E}\frac{\partial^4 \mathbf{u}_\mathrm{b}}{\partial t^4},$$
$$\boldsymbol{x} \in \Omega \setminus \Omega_0, \quad t \in [0, T), \tag{4.22}$$

whereas the other adjoint PDEs (4.14b) and (4.15b) remain unaltered. We remark that, in (4.21) and (4.22), the right-hand-side body force terms include the fourth derivative of the state solutions with respect to time t, as well as a new coefficient $\mathcal{E}(\boldsymbol{x})$, which is re-defined as:

$$\mathcal{E}(\boldsymbol{x}) = \begin{cases} \dfrac{2}{\left(\int_{\Omega_0} \int_0^T \left[\frac{\partial^2 \mathbf{u}_\mathrm{a}}{\partial t^2} \cdot \frac{\partial^2 \mathbf{u}_\mathrm{a}}{\partial t^2}\right] dt d\Omega\right)^2} \quad , & \boldsymbol{x} \in \Omega_0, \\ 0 \quad , & \boldsymbol{x} \in \Omega \setminus \Omega_0 \end{cases}. \tag{4.23}$$

Second, the final value conditions (4.19) are replaced by:

$$\boldsymbol{\lambda}_{u_\mathrm{a}} = -\frac{\mathcal{E}}{\rho}\frac{\partial^2 \mathbf{u}_\mathrm{a}}{\partial t^2}, \quad \frac{\partial \boldsymbol{\lambda}_{u_\mathrm{a}}}{\partial t} = -\frac{\mathcal{E}}{\rho}\frac{\partial^3 \mathbf{u}_\mathrm{a}}{\partial t^3},$$
$$\boldsymbol{\lambda}_{S_\mathrm{a}}^{sym} = \mathbf{0}, \quad \frac{\partial \boldsymbol{\lambda}_{S_\mathrm{a}}^{sym}}{\partial t} = \mathbf{0}, \qquad \boldsymbol{x} \in \Omega_0, \quad t = T, \tag{4.24a}$$

$$\boldsymbol{\lambda}_{u_\mathrm{b}} = -\frac{\mathcal{E}}{\rho a}\frac{\partial^2 \mathbf{u}_\mathrm{a}}{\partial t^3}, \quad \frac{\partial \boldsymbol{\lambda}_{u_\mathrm{b}}}{\partial t} = -\frac{\mathcal{E}}{\rho a}\frac{\partial^3 \mathbf{u}_\mathrm{b}}{\partial t^3} - \frac{\mathcal{E} b}{\rho a^2}\frac{\partial^2 \mathbf{u}_\mathrm{a}}{\partial t^2},$$
$$\boldsymbol{\lambda}_{S_\mathrm{b}}^{sym} = \mathbf{0}, \quad \frac{\partial \boldsymbol{\lambda}_{S_\mathrm{b}}^{sym}}{\partial t} = \mathbf{0}, \qquad \boldsymbol{x} \in \Omega \setminus \Omega_0, \quad t = T. \tag{4.24b}$$

4.2.2.3 The third optimality condition

The third optimality condition requires $\delta_\xi \mathcal{A} = 0$, i.e., the vanishing variation of $\mathcal{A}$ with respect to the control parameter $\xi = f_{2_i}$ – the value of a discretized force parameters used for parameterizing $f_2(t)$ – as in:

$$f_2(t) = \sum_{i=1}^{n_f} f_{2_i} \varphi_i(t), \tag{4.25}$$

where $\varphi_i(t)$ denotes the i-th shape function that is used for approximating the time signal $f_2(t)$ with respect to time t. Then, such a vanishing variation, $\delta_{f_{2_i}} \mathcal{A} = 0$, leads to the following control problem (the explicit derivation of the control problem is detailed in Appendix B):

The control problem:

$$\delta_{f_{2_i}} \mathcal{A} (= \nabla_{f_{2_i}} \mathcal{A}) = \int_{\Gamma_{\text{load}}} \int_0^T \left[\lambda_{u_2}(\boldsymbol{x}, t) \frac{\partial f_2(t)}{\partial f_{2_i}} \right] dt d\Gamma = 0. \tag{4.26}$$

We remark that the control equation (4.26) provides $\nabla_{f_{2_i}} \mathcal{L}$ – the gradient of the objective functional $\mathcal{L}$ – since the side-imposed constraints of the augmented functional $\mathcal{A}$ vanish owing to the satisfaction of the state problem. Thus, with the aid of this gradient $\nabla_{f_{2_i}} \mathcal{L}$, we can employ a gradient-based minimization to find a stationary point of the objective functional $\mathcal{L}$. In the next section, we discuss the numerical implementation required to solve the state, adjoint, and control problems for the satisfaction of the first-order optimality conditions.

4.3 Numerical implementation

As already discussed in the previous chapter, in this non-linear minimization problem, we iteratively identify a stationary point by using a gradient-based minimization approach until satisfaction of the first-order optimality conditions – the triplet of the state, adjoint, and control equations. The iterative procedure undergoes the following steps: (a) we solve the state problem by using an initially guessed loading time signal; (b) the adjoint problem is then, in turn, solved by using the state solution; and (c) the ensuing computation of the control problem results in the gradient $\nabla_{f_{2_i}}\mathcal{L}$, and the control parameters f_{2_i} are updated by virtue of a conjugate-gradient (CG) scheme [19, 59] with an inexact line-search method [59]. The numerical optimizer repeats steps (a) to (c) until the control parameters converge (the detailed algorithm of such parameter updates is described in Algorithm 1 in chapter 3). In the following subsections, we describe the classic Galerkin finite element method utilized for solving the state and adjoint problems, appropriately adjusted to account for the mixed form of the two-dimensional problem.

4.3.1 State problem semi-discrete form

To derive the weak form of the state problem, we firstly take the inner product between a vector test function $\mathbf{w}_{\mathrm{a}}(\boldsymbol{x})$ and the PDE (4.1a) and integrate over Ω_0; similarly, we integrate the inner product between a test function $\mathbf{w}_{\mathrm{b}}(\boldsymbol{x})$ and the PDE (4.2a) over $\Omega \setminus \Omega_0$. Then, by virtue of the divergence theorem and the continuity of displacements and tractions on Γ_{int}, the summation of the two integrals leads to the following weak form of the equations of motion of the state problem:

$$\int_{\Gamma_{\text{free}}} \mathbf{w}_{\text{b}} \cdot \left\{ \left(\frac{\partial \mathbf{S}_{\text{b}}^T}{\partial t} \tilde{\Lambda}_e + \mathbf{S}_{\text{b}}^T \tilde{\Lambda}_p \right) \boldsymbol{n} \right\} d\Gamma - \int_{\Omega_0} \nabla \mathbf{w}_{\text{a}} : \frac{\partial \mathbf{S}_{\text{a}}^T}{\partial t} + \mathbf{w}_{\text{a}} \cdot \rho \frac{\partial^2 \mathbf{u}_{\text{a}}}{\partial t^2} \, d\Omega$$
$$- \int_{\Omega \setminus \Omega_0} \nabla \mathbf{w}_{\text{b}} : \left(\frac{\partial \mathbf{S}_{\text{b}}^T}{\partial t} \tilde{\Lambda}_e + \mathbf{S}_{\text{b}}^T \tilde{\Lambda}_p \right) + \mathbf{w}_{\text{b}} \cdot \rho \left(a \frac{\partial^2 \mathbf{u}_{\text{b}}}{\partial t^2} + b \frac{\partial \mathbf{u}_{\text{b}}}{\partial t} + c \mathbf{u}_{\text{b}} \right) d\Omega = 0. \tag{4.27}$$

Equation (4.27) is then simplified to:

$$\int_{\Omega} \nabla \mathbf{w} : \left(\frac{\partial \mathbf{S}^T}{\partial t} \tilde{\Lambda}_e + \mathbf{S}^T \tilde{\Lambda}_p \right) + \mathbf{w} \cdot \rho \left(a \frac{\partial^2 \mathbf{u}}{\partial t^2} + b \frac{\partial \mathbf{u}}{\partial t} + c \mathbf{u}_{\text{b}} \right) d\Omega$$
$$= \int_{\Gamma_{\text{load}}} \mathbf{w} \cdot \left\{ \frac{\partial \mathbf{S}^T}{\partial t} \boldsymbol{n} \right\} d\Gamma, \tag{4.28}$$

where the variables with the subscripts ‘a’ and ‘b’ are merged into the variables without the subscripts as the following:

$$\mathbf{w}(\boldsymbol{x}) = \mathbf{w}_{\text{a}}(\boldsymbol{x}), \quad \mathbf{u}(\boldsymbol{x}, t) = \mathbf{u}_{\text{a}}(\boldsymbol{x}, t), \quad \mathbf{S}(\boldsymbol{x}, t) = \mathbf{S}_{\text{a}}(\boldsymbol{x}, t), \quad \boldsymbol{x} \in \Omega_0,$$
$$\mathbf{w}(\boldsymbol{x}) = \mathbf{w}_{\text{b}}(\boldsymbol{x}), \quad \mathbf{u}(\boldsymbol{x}, t) = \mathbf{u}_{\text{b}}(\boldsymbol{x}, t), \quad \mathbf{S}(\boldsymbol{x}, t) = \mathbf{S}_{\text{b}}(\boldsymbol{x}, t), \quad \boldsymbol{x} \in \Omega \setminus \Omega_0. \tag{4.29}$$

Next, after taking the tensor inner product between a test function $\mathbf{T}_{\text{a}}(\boldsymbol{x})$ and the state PDE (4.1b), we integrate the tensor inner product over Ω_0. Then, we integrate another tensor inner product between a test function $\mathbf{T}_{\text{b}}(\boldsymbol{x})$ and (4.2b) over $\Omega \setminus \Omega_0$. The summation of the two integrals, via the continuity conditions in (4.8), gives rise to the weak form of the combined kinematic and constitutive equations of the state problem:

$$\begin{aligned}\int_{\Omega} \mathbf{T} : \Bigg\{ & \left(\mathcal{D}\left[\frac{\partial^2 \mathbf{S}}{\partial t^2}\right]\right)\Lambda_e + \Lambda_e^T \left(\mathcal{D}\left[\frac{\partial \mathbf{S}}{\partial t}\right]\right)\Lambda_p \\ & + \Lambda_p^T \left(\mathcal{D}\left[\frac{\partial \mathbf{S}}{\partial t}\right]\right)\Lambda_e + \Lambda_p^T \left(\mathcal{D}\left[\mathbf{S}\right]\right)\Lambda_p \\ & - \frac{1}{2}\left[\Lambda_p^T \nabla \mathbf{u} + (\nabla \mathbf{u})^T \Lambda_p\right] - \frac{1}{2}\left[\Lambda_e^T \nabla \frac{\partial \mathbf{u}}{\partial t} + \left(\nabla \frac{\partial \mathbf{u}}{\partial t}\right)^T \Lambda_e\right] \Bigg\} \, d\Omega = 0, \end{aligned} \tag{4.30}$$

with another merged variable $\mathbf{T}(\boldsymbol{x})$:

$$\begin{aligned} \mathbf{T}(\boldsymbol{x}) &= \mathbf{T}_{\mathrm{a}}(\boldsymbol{x}), \quad \boldsymbol{x} \in \Omega_0, \\ \mathbf{T}(\boldsymbol{x}) &= \mathbf{T}_{\mathrm{b}}(\boldsymbol{x}), \quad \boldsymbol{x} \in \Omega \setminus \Omega_0. \end{aligned} \tag{4.31}$$

Then, we introduce the approximation of the test functions $\mathbf{w}(\boldsymbol{x})$ and $\mathbf{T}(\boldsymbol{x})$ and the trial functions $\mathbf{u}(\boldsymbol{x}, t)$ and $\mathbf{S}(\boldsymbol{x}, t)$:

$$\begin{aligned} w_i(\boldsymbol{x}) &= \mathbf{w}_i^T \boldsymbol{\Phi}(\boldsymbol{x}), \\ T_{ij}(\boldsymbol{x}) &= \mathbf{T}_{ij}^T \boldsymbol{\Psi}(\boldsymbol{x}), \\ u_i(\boldsymbol{x}, t) &= \boldsymbol{\Phi}(\boldsymbol{x})^T \mathbf{u}_i(t), \\ S_{ij}(\boldsymbol{x}, t) &= \boldsymbol{\Psi}(\boldsymbol{x})^T \mathbf{S}_{ij}(t), \quad i, j = 1, 2, \end{aligned} \tag{4.32}$$

where $\mathbf{u}_i(t)$ and $\mathbf{S}_{ij}(t)$ denote the vectors of nodal solutions of the state solutions $u_i(\boldsymbol{x}, t)$ and $S_{ij}(\boldsymbol{x}, t)$; $\mathbf{w}_i$ and $\mathbf{T}_{ij}$ denote the vectors of nodal quantities of the test functions $w_i(\boldsymbol{x})$ and $T_{ij}(\boldsymbol{x})$; $\boldsymbol{\Phi}(\boldsymbol{x})$ and $\boldsymbol{\Psi}(\boldsymbol{x})$ denote the vectors of the shape functions (we use a quadratic shape function pair for $\boldsymbol{\Phi}(\boldsymbol{x})$ and $\boldsymbol{\Psi}(\boldsymbol{x})$ to ensure stable solutions [45, 46, 47]). Then, (4.28) and (4.30), in turn, result in the semi-discrete form:

$$\mathbf{M}_{\mathrm{st}}\frac{\partial^2\mathbf{ST}(t)}{\partial t^2}+\mathbf{C}_{\mathrm{st}}\frac{\partial\mathbf{ST}(t)}{\partial t}+\mathbf{K}_{\mathrm{st}}\mathbf{ST}(t)=\mathbf{F}_{\mathrm{st}}, \tag{4.33}$$

where the solution vector of the state problem, $\mathbf{ST}(t)$, is defined as the following:

$$\mathbf{ST}(t)=\begin{bmatrix}\mathbf{u}_1(t)\\ \mathbf{u}_2(t)\\ \mathbf{S}_{11}(t)\\ \mathbf{S}_{22}(t)\\ \mathbf{S}_{12}(t)\end{bmatrix}. \tag{4.34}$$

The specific forms of the matrices $\mathbf{M}_{\mathrm{st}}$, $\mathbf{C}_{\mathrm{st}}$, and $\mathbf{K}_{\mathrm{st}}$, as well as the force vector $\mathbf{F}_{\mathrm{st}}$ in (4.33) are (we show the components of each matrix in Appendix C):

$$\mathbf{M}_{\mathrm{st}}=\begin{bmatrix}M_{11}^{\mathrm{st}} & 0 & 0 & 0 & 0\\ 0 & M_{22}^{\mathrm{st}} & 0 & 0 & 0\\ 0 & 0 & M_{33}^{\mathrm{st}} & M_{34}^{\mathrm{st}} & 0\\ 0 & 0 & M_{43}^{\mathrm{st}} & M_{44}^{\mathrm{st}} & 0\\ 0 & 0 & 0 & 0 & M_{55}^{\mathrm{st}}\end{bmatrix}, \tag{4.35}$$

$$\mathbf{C}_{\mathrm{st}}=\begin{bmatrix}C_{11}^{\mathrm{st}} & 0 & C_{13}^{\mathrm{st}} & 0 & C_{15}^{\mathrm{st}}\\ 0 & C_{22}^{\mathrm{st}} & 0 & C_{24}^{\mathrm{st}} & C_{25}^{\mathrm{st}}\\ C_{31}^{\mathrm{st}} & 0 & C_{33}^{\mathrm{st}} & C_{34}^{\mathrm{st}} & 0\\ 0 & C_{42}^{\mathrm{st}} & C_{43}^{\mathrm{st}} & C_{44}^{\mathrm{st}} & 0\\ C_{51}^{\mathrm{st}} & C_{52}^{\mathrm{st}} & 0 & 0 & C_{55}^{\mathrm{st}}\end{bmatrix}, \tag{4.36}$$

$$\mathbf{K}_{\mathrm{st}}=\begin{bmatrix}K_{11}^{\mathrm{st}} & 0 & K_{13}^{\mathrm{st}} & 0 & K_{15}^{\mathrm{st}}\\ 0 & K_{22}^{\mathrm{st}} & 0 & K_{24}^{\mathrm{st}} & K_{25}^{\mathrm{st}}\\ K_{31}^{\mathrm{st}} & 0 & K_{33}^{\mathrm{st}} & K_{34}^{\mathrm{st}} & 0\\ 0 & K_{42}^{\mathrm{st}} & K_{43}^{\mathrm{st}} & K_{44}^{\mathrm{st}} & 0\\ K_{51}^{\mathrm{st}} & K_{52}^{\mathrm{st}} & 0 & 0 & K_{55}^{\mathrm{st}}\end{bmatrix}, \tag{4.37}$$

$$\mathbf{F}_{\mathrm{st}}=\begin{bmatrix}0\\ \int_{\Gamma_{\mathrm{load}}}\boldsymbol{\Phi}f_2(t)\\ 0\\ 0\\ 0\end{bmatrix}. \tag{4.38}$$

4.3.2 Adjoint problem semi-discrete form

Similarly to the weak forms of the state problem, we derive the weak forms of the adjoint problem. First, the summation of weak forms of the PDEs (4.14a) and (4.15a) is:

$$\begin{aligned}\int_{\Omega} \mathbf{w} \cdot \left(\frac{\partial^2 \boldsymbol{\lambda}_u}{\partial t^2} \rho a - \frac{\partial \boldsymbol{\lambda}_u}{\partial t} \rho b + \boldsymbol{\lambda}_u \rho c \right) d\Omega & \\ - \int_{\Omega} \nabla \mathbf{w} : \left(-\Lambda_p \boldsymbol{\lambda}_S^{sym} + \Lambda_e \frac{\partial \boldsymbol{\lambda}_S^{sym}}{\partial t} \right) d\Omega & \\ = \int_{\Omega} \mathbf{w} \cdot \rho \mathcal{E} \frac{\partial^2 \mathbf{u}}{\partial t^2} \, d\Omega, & \end{aligned} \tag{4.39}$$

and the summation of the weak forms of the other two PDEs (4.14b) and (4.15b) is:

$$\begin{aligned}\int_{\Omega} \mathbf{T} : \Bigg\{ \frac{1}{2} \left(\tilde{\Lambda}_e \left(\nabla \frac{\partial \boldsymbol{\lambda}_u}{\partial t} \right)^T + \left(\nabla \frac{\partial \boldsymbol{\lambda}_u}{\partial t} \right) \tilde{\Lambda}_e \right) - \frac{1}{2} \left(\tilde{\Lambda}_p (\nabla \boldsymbol{\lambda}_u)^T + (\nabla \boldsymbol{\lambda}_u) \tilde{\Lambda}_p \right) & \\ + \mathcal{D} \Bigg[\Lambda_e^T \frac{\partial^2 \boldsymbol{\lambda}_S^{sym}}{\partial t^2} \Lambda_e - \Lambda_e^T \frac{\partial \boldsymbol{\lambda}_S^{sym}}{\partial t} \Lambda_p - \Lambda_p^T \frac{\partial \boldsymbol{\lambda}_S^{sym}}{\partial t} \Lambda_e + \Lambda_p^T \boldsymbol{\lambda}_S^{sym} \Lambda_p \Bigg\} \Bigg] \, d\Omega = 0. & \end{aligned} \tag{4.40}$$

In (4.39) and (4.40), the adjoint variables are merged ($\mathbf{w}(\boldsymbol{x})$ and $\mathbf{T}(\boldsymbol{x})$ are already merged per (4.29) and (4.31)) as in:

$$\begin{aligned} \boldsymbol{\lambda}_u(\boldsymbol{x}, t) &= \boldsymbol{\lambda}_{u_{\mathrm{a}}}(\boldsymbol{x}, t), \quad \boldsymbol{\lambda}_S^{sym}(\boldsymbol{x}, t) = \boldsymbol{\lambda}_{S_{\mathrm{a}}}^{sym}(\boldsymbol{x}, t), \quad \boldsymbol{x} \in \Omega_0, \\ \boldsymbol{\lambda}_u(\boldsymbol{x}, t) &= \boldsymbol{\lambda}_{u_{\mathrm{b}}}(\boldsymbol{x}, t), \quad \boldsymbol{\lambda}_S^{sym}(\boldsymbol{x}, t) = \boldsymbol{\lambda}_{S_{\mathrm{b}}}^{sym}(\boldsymbol{x}, t), \quad \boldsymbol{x} \in \Omega \setminus \Omega_0. \end{aligned} \tag{4.41}$$

Next, along with the approximation of the test functions $\mathbf{w}(\boldsymbol{x})$ and $\mathbf{T}(\boldsymbol{x})$ as shown in (4.32), we introduce the approximation of the adjoint solutions as:

$$\begin{aligned} \lambda_{u_i}(\boldsymbol{x}, t) &= \boldsymbol{\Phi}(\boldsymbol{x})^T \boldsymbol{\lambda}_{u_i}(t), \\ \lambda_{S_{ij}}^{sym}(\boldsymbol{x}, t) &= \boldsymbol{\Psi}(\boldsymbol{x})^T \boldsymbol{\lambda}_{S_{ij}}^{sym}(t), \quad i, j = 1, 2, \end{aligned} \tag{4.42}$$

where $\boldsymbol{\lambda}_{u_i}(t)$ and $\boldsymbol{\lambda}^{sym}_{S_{ij}}(t)$ denote the vectors of nodal solutions of the adjoint problem. Then, the weak forms (4.39) and (4.40) reduce to the following semi-discrete form:

$$\mathbf{M}_{\text{adj}} \frac{\partial^2 \boldsymbol{\lambda}(t)}{\partial t^2} + \mathbf{C}_{\text{adj}} \frac{\partial \boldsymbol{\lambda}(t)}{\partial t} + \mathbf{K}_{\text{adj}} \boldsymbol{\lambda}(t) = \mathbf{F}_{\text{adj}}. \tag{4.43}$$

Hereby, the solution vector of the adjoint problem $\boldsymbol{\lambda}(t)$ is defined as the following:

$$\boldsymbol{\lambda}(t) = \begin{bmatrix} \boldsymbol{\lambda}_{u_1}(t) \\ \boldsymbol{\lambda}_{u_2}(t) \\ \boldsymbol{\lambda}^{sym}_{S_{11}}(t) \\ \boldsymbol{\lambda}^{sym}_{S_{22}}(t) \\ \boldsymbol{\lambda}^{sym}_{S_{12}}(t) \end{bmatrix}, \tag{4.44}$$

and the specific forms of the matrices $\mathbf{M}_{\text{adj}}$, $\mathbf{C}_{\text{adj}}$, $\mathbf{K}_{\text{adj}}$, and $\mathbf{F}_{\text{adj}}$ are as follows (we show the components of each matrix in Appendix C):

$$\mathbf{M}_{\text{adj}} = \begin{bmatrix} M^{\text{adj}}_{11} & 0 & 0 & 0 & 0 \\ 0 & M^{\text{adj}}_{22} & 0 & 0 & 0 \\ 0 & 0 & M^{\text{adj}}_{33} & M^{\text{adj}}_{34} & 0 \\ 0 & 0 & M^{\text{adj}}_{43} & M^{\text{adj}}_{44} & 0 \\ 0 & 0 & 0 & 0 & M^{\text{adj}}_{55} \end{bmatrix}, \tag{4.45}$$

$$\mathbf{C}_{\text{adj}} = \begin{bmatrix} C^{\text{adj}}_{11} & 0 & C^{\text{adj}}_{13} & 0 & C^{\text{adj}}_{15} \\ 0 & C^{\text{adj}}_{21} & 0 & C^{\text{adj}}_{24} & C^{\text{adj}}_{25} \\ C^{\text{adj}}_{31} & 0 & C^{\text{adj}}_{33} & C^{\text{adj}}_{34} & 0 \\ 0 & C^{\text{adj}}_{42} & C^{\text{adj}}_{43} & C^{\text{adj}}_{44} & 0 \\ C^{\text{adj}}_{51} & C^{\text{adj}}_{52} & 0 & 0 & C^{\text{adj}}_{55} \end{bmatrix}, \tag{4.46}$$

$$
\mathbf{K}_{\text{adj}} = \begin{bmatrix} K_{11}^{\text{adj}} & 0 & K_{13}^{\text{adj}} & 0 & K_{15}^{\text{adj}} \\ 0 & K_{22}^{\text{adj}} & 0 & K_{24}^{\text{adj}} & K_{25}^{\text{adj}} \\ K_{31}^{\text{adj}} & 0 & K_{33}^{\text{adj}} & K_{34}^{\text{adj}} & 0 \\ 0 & K_{42}^{\text{adj}} & K_{43}^{\text{adj}} & K_{44}^{\text{adj}} & 0 \\ K_{51}^{\text{adj}} & K_{52}^{\text{adj}} & 0 & 0 & K_{55}^{\text{adj}} \end{bmatrix}, \tag{4.47}
$$

$$
\mathbf{F}_{\text{adj}} = \begin{bmatrix} \mathcal{E} \int_{\Omega} \rho \mathbf{\Phi} \mathbf{\Phi}^T d\Omega \frac{\partial^2 \mathbf{u}_1}{\partial t^2} \\ \mathcal{E} \int_{\Omega} \rho \mathbf{\Phi} \mathbf{\Phi}^T d\Omega \frac{\partial^2 \mathbf{u}_2}{\partial t^2} \\ 0 \\ 0 \\ 0 \end{bmatrix}. \tag{4.48}
$$

If the acceleration-based objective functional (4.12) is employed, we address (4.43) by using the same $\mathbf{M}_{\text{adj}}$, $\mathbf{C}_{\text{adj}}$, and $\mathbf{K}_{\text{adj}}$ shown in (4.45)–(4.47) while the force vector $\mathbf{F}_{\text{adj}}$ in (4.48) is replaced by:

$$
\mathbf{F}_{\text{adj}} = \begin{bmatrix} -\mathcal{E} \int_{\Omega} \mathbf{\Phi} \mathbf{\Phi}^T d\Omega \frac{\partial^4 \mathbf{u}_1}{\partial t^4} \\ -\mathcal{E} \int_{\Omega} \mathbf{\Phi} \mathbf{\Phi}^T d\Omega \frac{\partial^4 \mathbf{u}_2}{\partial t^4} \\ 0 \\ 0 \\ 0 \end{bmatrix}. \tag{4.49}
$$

Time integration

We then resolve the time-dependent discrete forms (4.33) and (4.43) by using the Newmark time integration scheme: the state and adjoint solutions at each time step are obtained by solving the following systems of equations:

$$\begin{aligned}
&\left[\mathbf{M}_{\text{st}} + \mathbf{C}_{\text{st}}\frac{\Delta t}{2} + \mathbf{K}_{\text{st}}\frac{(\Delta t)^2}{4}\right]\frac{\partial^2 \mathbf{ST}_{(n+1)}}{\partial t^2} \\
&= \mathbf{F}_{\text{st}\,(n+1)} - \mathbf{C}_{\text{st}}\left[\frac{\partial \mathbf{ST}_{(n)}}{\partial t} + \frac{\partial^2 \mathbf{ST}_{(n)}}{\partial t^2}\frac{\Delta t}{2}\right] \\
&\quad - \mathbf{K}_{\text{st}}\left[\mathbf{ST}_{(n)} + \frac{\partial \mathbf{ST}_{(n)}}{\partial t}(\Delta t) + \frac{\partial^2 \mathbf{ST}_{(n)}}{\partial t^2}\frac{(\Delta t)^2}{4}\right],
\end{aligned} \tag{4.50}$$

$$\begin{aligned}
&\left[\mathbf{M}_{\text{adj}} - \mathbf{C}_{\text{adj}}\frac{\Delta t}{2} + \mathbf{K}_{\text{adj}}\frac{(\Delta t)^2}{4}\right]\frac{\partial^2 \boldsymbol{\lambda}_{(n)}}{\partial t^2} \\
&= \mathbf{F}_{\text{adj}\,(n)} - \mathbf{C}_{\text{adj}}\left[\frac{\partial \boldsymbol{\lambda}_{(n+1)}}{\partial t} - \frac{\partial^2 \boldsymbol{\lambda}_{(n+1)}}{\partial t^2}\frac{\Delta t}{2}\right] \\
&- \mathbf{K}_{\text{adj}}\left[\boldsymbol{\lambda}_{(n+1)} - \frac{\partial \boldsymbol{\lambda}_{(n+1)}}{\partial t}\Delta t + \frac{\partial^2 \boldsymbol{\lambda}_{(n+1)}}{\partial t^2}\frac{(\Delta t)^2}{4}\right],
\end{aligned} \tag{4.51}$$

where Δt is the time step; the subscripts (n) and $(n+1)$ denote the evaluation of the nodal vectors at the n-th and $(n+1)$-th time steps; the time-line of the evaluation of the solution in (4.51) is reversed with respect to that of (4.50). By using the discrete solution of the adjoint problem, the gradient of the objective functional, i.e., $\nabla_{f_{2_i}}\mathcal{L}$, is computed based on the control equation (4.26) in the following manner:

$$\begin{aligned}
\nabla_{f_{2_i}}\mathcal{L} &= \int_{\Gamma_{\text{load}}}\int_0^T \left[\lambda_{u_2}(\boldsymbol{x},t)\frac{\partial f_2(t)}{\partial f_{2_i}}\right] dt d\Gamma \\
&= \int_{\Gamma_{\text{load}}}\int_0^T \left[\boldsymbol{\Phi}^T(\boldsymbol{x})\boldsymbol{\lambda}_{u_2}(t)\frac{\partial f_2(t)}{\partial f_{2_i}}\right] dt d\Gamma \\
&= \int_{\Gamma_{\text{load}}}\left[\boldsymbol{\Phi}^T(\boldsymbol{x})\int_0^T \left\{\boldsymbol{\lambda}_{u_2}(t)\varphi_i(t)\right\} dt\right] d\Gamma.
\end{aligned} \tag{4.52}$$

We have thus far discussed the numerical implementation for solving the state and adjoint problems, as well as for evaluating the reduced gradient of the objective functional. We validated the derivation and implementation of the state, adjoint, and control problems by comparing the values of the components of the gradient computed by (4.52) with those of the numerical gradient obtained by the finite difference scheme (per (3.37)); the values of the components of both gradients are in excellent agreement. Using the numerical optimizer, implemented as per the above discussion, we conduct numerical experiments as follows.

4.4 Numerical results

We present numerical experiments conducted for a hypothetical subsurface formation model (Fig. 4.2), which comprises 4 layers and a targeted oil reservoir inclusion embedded between the third and fourth layers. The width and height of the targeted oil reservoir inclusion are 160m and 32m, respectively; the distance from the ground surface to the bottom of the inclusion is 200m. This dome-shaped inclusion exemplifies a typical shallow oil reservoir structure underneath an impermeable curved cap stratum. Figures 4.2(a,b,c) differ from each other only with respect to the location of the wave sources.

In this example, we postulate that the elastic modulus E for each layer becomes larger as the depth increases, whereas E for the inclusion is smaller than those of the surrounding layers[1]. We consider a mass density $\rho = 2200\text{kg/m}^3$, and Poisson's ratio $\nu = 0.2$. Then, utilizing known values of

---

[1] The poroelastic medium partially saturated with fluid or gas phases is generally softer than the surrounding media [23].

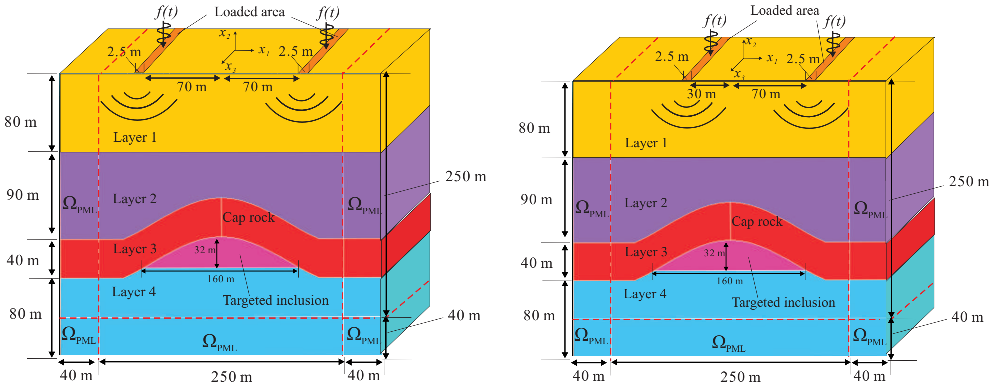

(a) Two symmetric wave sources (b) Two asymmetric wave sources

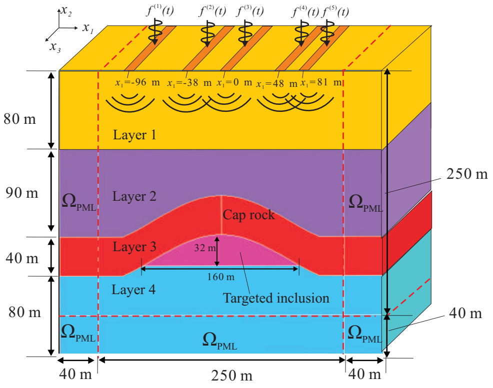

(c) Five aymmetric wave sources

Figure 4.2: Subsurface formation model: a targeted hydrocarbon reservoir inclusion Ω_0 buried in a semi-infinite heterogeneous medium subjected to various ground wave sources; wave velocity values are shown in Table 4.1.

E, ρ, and ν, a compressional wave velocity v_p and a shear wave velocity v_s of each formation can be obtained as:

$$v_p = \sqrt{\frac{\lambda + 2\mu}{\rho}} = \sqrt{\frac{E(1-\nu)}{\rho(1+\nu)(1-2\nu)}},$$
$$v_s = \sqrt{\frac{\mu}{\rho}} = \sqrt{\frac{E}{2\rho(1+\nu)}}, \tag{4.53}$$

where λ without any subscript denotes Lamé's first parameter, and μ denotes shear modulus. Such elastic moduli and wave velocities of this subsurface formation model are shown in Table 4.1. For this formation model, we seek the source time signals that can maximize the wave motion in the targeted inclusion. To tackle this optimization problem, we approximate the solutions of the state and adjoint problems by using isoparametric quadrilateral (or triangular) quadratic elements. Here, the sizes of the elements are approximately 4.0m or less in order to accommodate at least 12 nodes (6 elements) per wavelength: the minimum wavelength in this model is 27.5m corresponding to a frequency f up to 50Hz.

	E [N/m^2]	v_p [m/s]	v_s [m/s]
Target	1.0×10^{10}	2247	1376
Layer 1	2.0×10^{10}	3178	1946
Layer 2	2.4×10^{10}	3482	2132
Layer 3	3.0×10^{10}	3892	2384
Layer 4	3.6×10^{10}	4264	2611

Table 4.1: Elastic moduli and wave velocities of the layers of the subsurface formation model shown in Fig. 4.2.

4.4.1 Forward solution

We compute the forward solution of the wave response within the subsurface formation model (Fig. 4.2(a)) that is subjected to the two symmetric wave sources, each described by a modified Ricker pulse loading signal as shown in Fig. 4.3. The time signal of this Ricker pulse is:

$$f_2(t) = -50 \times \frac{(0.25\eta^2 - 0.5)e^{(-0.25\eta^2)} - 13.0e^{-13.5}}{0.5 + 13.0e^{-13.5}} \quad [\mathrm{kN/m^2}], \quad t \le \bar{t},$$
$$\eta = \omega_r t - 3\sqrt{6}, \quad \bar{t} = \frac{6\sqrt{6}}{\omega_r}, \tag{4.54}$$

where $\omega_r = 2\pi f$ denotes the central frequency of the pulse signal; we employ $f = 20$Hz as the central frequency (Fig. 4.3(b)). For the solution, we use a time step of $\Delta t =$0.001s. Fig. 4.4 shows the amplitudes of the displacement of the wave response for the Ricker pulse. No discernible reflection of the wave is generated from the fixed boundary attached to Ω_{PML}, as well as from the interface between Ω_{reg} and Ω_{PML} [45, 46, 47]. In addition, we note that the wave motion is much larger along the ground surface than in the reservoir inclusion. Below, we attempt to identify the optimal loading signals that can lead to strong focusing of the wave energy on the reservoir inclusion.

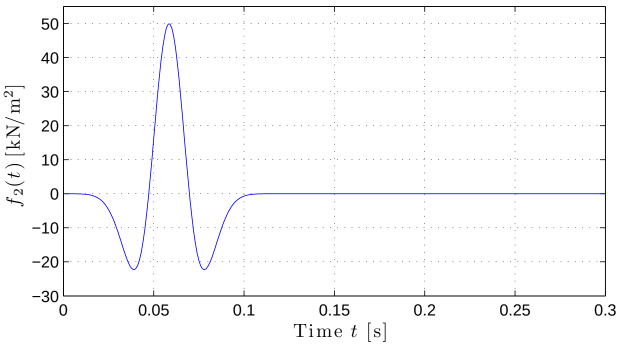

(a) The Ricker pulse time signal

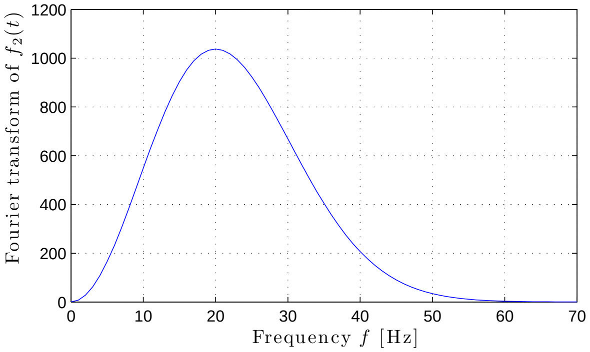

(b) The frequency spectrum of the Ricker pulse signal

Figure 4.3: The Ricker pulse signal with the central frequency $f = \frac{\omega_r}{2\pi} = 20$Hz.

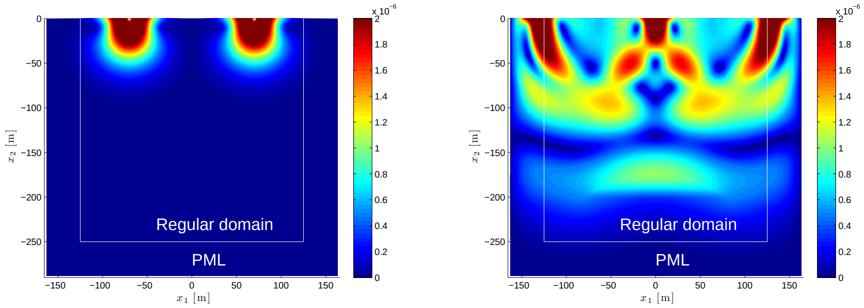

(a) Time $t = 0.05$s (b) Time $t = 0.10$s

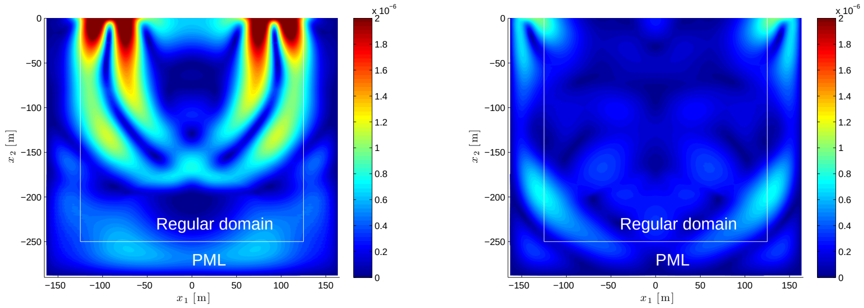

(c) Time $t = 0.15$s (d) Time $t = 0.20$s

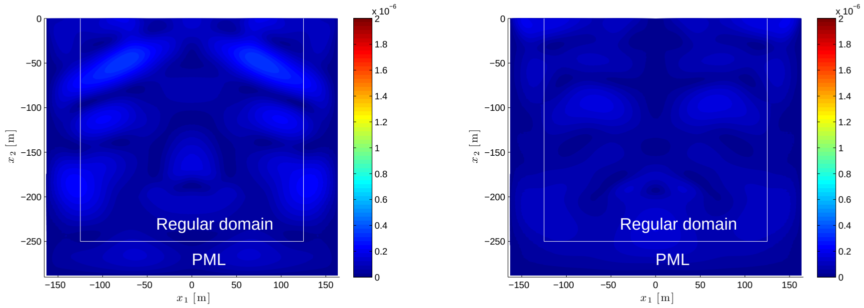

(e) Time $t = 0.25$s (f) Time $t = 0.30$s

Figure 4.4: The amplitude of displacement field, $|u| = \sqrt{u_1^2 + u_2^2}$ [m], of the wave response of the formation model (Fig. 4.2(a)) subjected to the two symmetric wave sources that use the Ricker pulse loading signal shown in Fig. 4.3.

4.4.2 Numerical experiments – case numbering

We conducted numerical optimization experiments for three different configurations of the wave sources: 1. two symmetric wave sources (Fig. 4.2(a)); 2. two independent asymmetric wave sources (Fig. 4.2(b)); and 3. five independent asymmetric wave sources (Fig. 4.2(c)). We also considered three different functionals, that is, maximization of the kinetic energy in Ω_0 with all layers active (A); maximization of the kinetic energy in Ω_0 with silent neighbors (B); and maximization of the acceleration in Ω_0 with all layers active (C). The complete summary of all results are shown in Table 4.4 (section 4.5) using the corresponding case number[2]. Below describe the details of only a subset of the numerical experiments, namely cases 1A, 1B, 1C, 2B, and 3B.

4.4.2.1 Wave sources optimal signals (case 1A)

We identify the optimal loading time signals for two symmetric wave sources that can maximize the kinetic energy within the target inclusion Ω_0 shown in Fig. 4.2(a), without forcing the neighboring formations to be silent. To this end, we seek to minimize (4.10) by using the initial time signal, temporally discretized by 200 quadratic elements (400 discretized force parameters), shown in Fig. 4.5(a). We require that the amplitude of the load does not exceed 50kN/m^2. The block symbols of the close-up view of the initially guessed signal in Fig. 4.5(b) represent the discretized force parameters utilized for the

---

[2] For instance, the case number 1A refers to the optimization conducted for the identification of loading time signals of two symmetric wave sources (1) that can lead to maximization of the kinetic energy of rock matrix in Ω_0 with all layers active (A).

temporal approximation of the loading time signal: we use such symbols in all similar plots. The frequency spectrum of the initially guessed loading is shown in Fig. 4.5(c). The initially guessed signal has a broad frequency spectrum, which, as it will be seen, differs significantly from that of the finally converged time signal: the optimization process is unbiased with respect to the initial guess. The total observation time is 2s, and the time step is 0.001s.

Fig. 4.6 shows that our numerical optimizer converges, after 66 iterations, to a time signal with a dominant frequency of 29Hz. Fig. 4.7 shows that the frequency of 29Hz corresponds to the global minimum of the distribution of the objective functional (4.10) with respect to the frequency f for a sinusoidal loading $f_2(t) = 50\sin(2\pi f)\text{kN/m}^2$ for the formation model subject to the two symmetric wave sources shown in Fig. 4.2(a). That is, the optimizer successfully recovered a monochromatic signal corresponding to one of the formation's amplification frequencies.

As in our one-dimensional work, the maximization of the kinetic energy within a target inclusion with all layers active is likely to recover a rectangularly shaped time signal (see the close-up view in Fig. 4.6(b)). Such a rectangularly shaped time signal contains a few high frequency components. Thus, the kinetic energy within Ω_0 for such a rectangularly shaped optimized loading time signal is larger than that for the monochromatic time signal $f_2(t) = 50\sin(2\pi \times 29t)\text{kN/m}^2$ that uses the dominant frequency of the rectangularly shaped signal (Fig. 4.8(a) vs Fig. 4.8(b)). Notice that the kinetic energy distribution within Ω_0 for the converged time signal is much larger than that of the non-optimal sinusoidal loading $f_2(t) = 50\sin(2\pi f t)\text{kN/m}^2$ using non-optimal frequencies, such as $f = 25\text{Hz}$ and 35Hz (Fig. 4.8(a) vs Figures 4.9(a,b)).

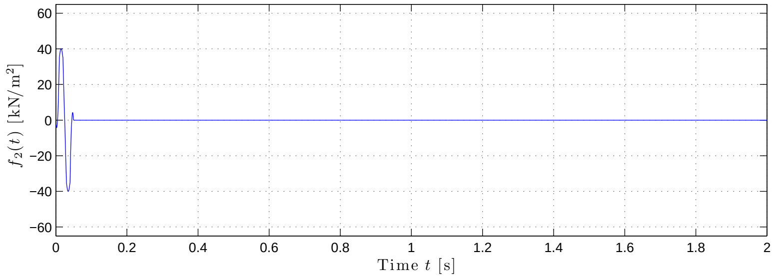

(a) The initially guessed loading time signal

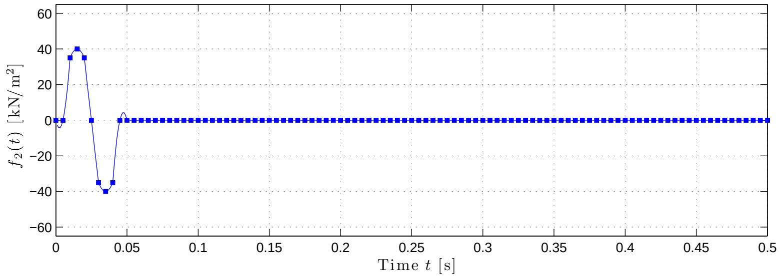

(b) Close-up view of the initially guessed loading time signal (0–0.5s); the blocks symbolize the discretized excitation parameters

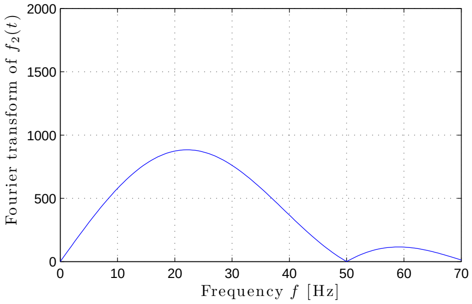

(c) The frequency spectrum of the initially guessed loading time signal

Figure 4.5: The initially guessed loading time signal for the maximization of the kinetic energy in Ω_0 of the formation model (Fig. 4.2(a)) (minimizing (4.10)).

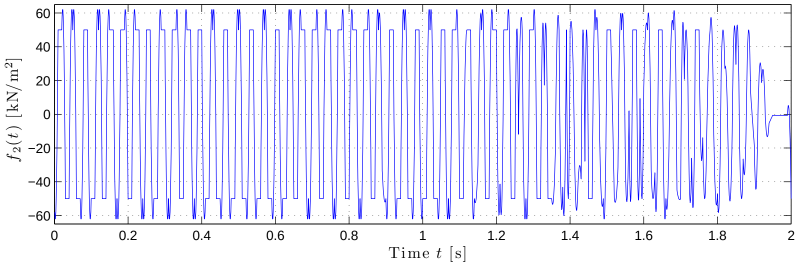

(a) The converged loading time signal

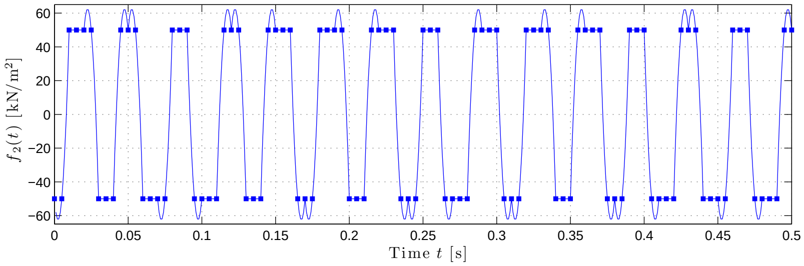

(b) Close-up view of converged loading time signal (0–0.5s)

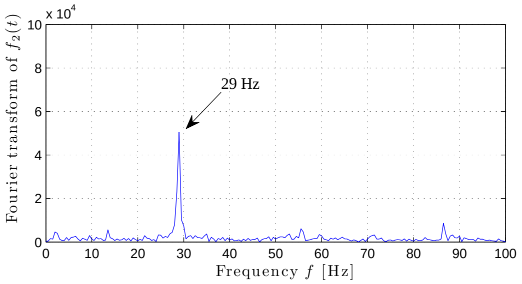

(c) The frequency spectrum of the converged loading time signal

Figure 4.6: The loading time signal that converged after 66 iterations by minimizing (4.10): the maximization of the kinetic energy in Ω_0 of the formation model (Fig. 4.2(a)).

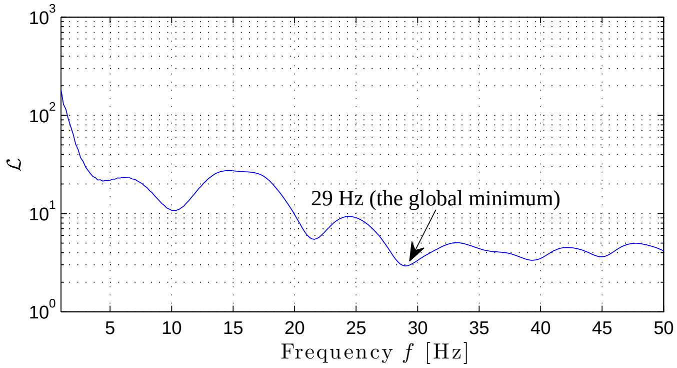

Figure 4.7: Frequency sweep of the objective functional (4.10) using a harmonic load $f_2(t) = 50\sin(2\pi f t)\mathrm{kN/m^2}$ for the formation model shown in Fig. 4.2(a).

4.4.2.2 Wave sources optimal signals (case 1B)

Next, we explore the possibility of maximizing the kinetic energy within Ω_0 while the kinetic energy within the surrounding areas $\Omega \setminus \Omega_0$ is minimized by considering again the two symmetric wave sources (Fig. 4.2(a)). In particular, we aim to reduce the strong wave energy along the free surface via our optimization scheme by minimizing the objective functional (4.11).

The optimization process begins again with the initially guessed perturbation loading time signal that is temporally discretized by 200 quadratic elements (400 discretized force parameters) as shown in Fig. 4.5; the total observation time is 2s, and the time step is 0.001s. After 71 iterations, the optimizer results in a sinusoidally shaped time signal with a dominant frequency of 29.5Hz (Fig. 4.10). This frequency corresponds to the global minimum of the objective functional (4.11), as shown in Fig. 4.12. That is, the optimizer

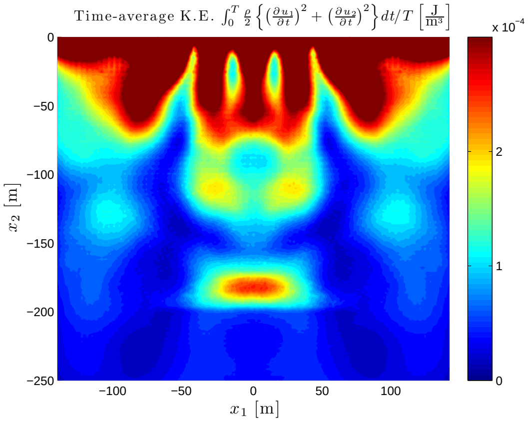

(a) Kinetic energy for the converged optimal loading time signal in Fig. 4.6

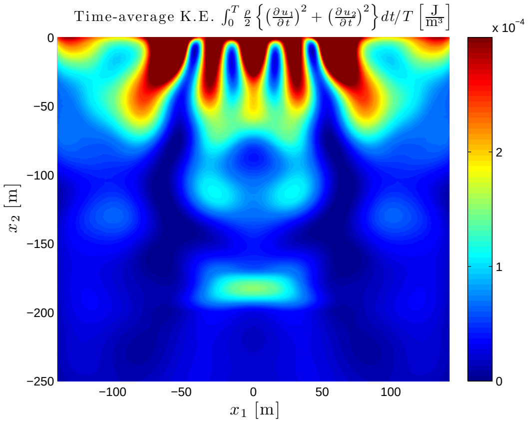

(b) Kinetic energy for a loading time signal $f_2(t) = 50\sin(2\pi f t)\mathrm{kN/m^2}$, $f = 29\mathrm{Hz}$ (the dominant frequency of the converged loading in Fig. 4.6)

Figure 4.8: The time-averaged kinetic energy (K. E.) distributions in Ω_{reg} of the formation model shown in Fig. 4.2(a) for the converged optimal loading time signal shown in Fig. 4.6, and the monocromatic loading that uses the dominant frequency of the optimal time signal.

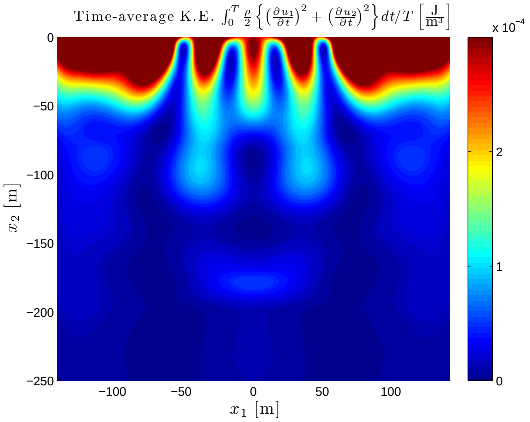

(a) Kinetic energy for a non-optimal time signal $f_2(t) = 50\sin(2\pi f t)\mathrm{kN/m^2}$, $f = 25\mathrm{Hz}$

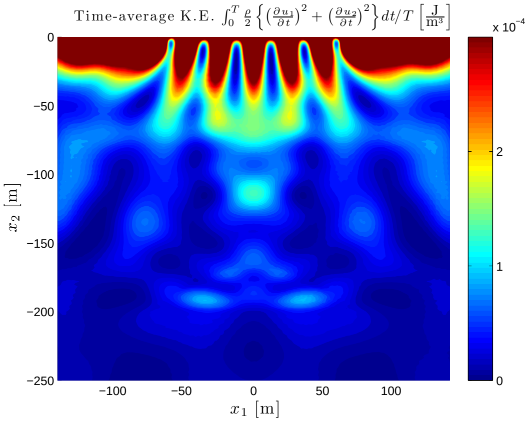

(b) Kinetic energy for a non-optimal time signal $f_2(t) = 50\sin(2\pi f t)\mathrm{kN/m^2}$, $f = 35\mathrm{Hz}$

Figure 4.9: The time-averaged kinetic energy distributions in Ω_{reg} of the formation model shown in Fig. 4.2(a) for sinusoidal loadings that use non-optimal frequencies $f = 25$ and 35Hz.

successfully identifies the minimum of the objective functional (4.11).

We point out that the recovered frequency of 29.5Hz is quite close to the amplification frequency of 29Hz, recovered in the previous experiment (all layers active). That is, the optimizer arrives at a stationary point for (4.11) largely due to maximizing the kinetic energy in the inclusion, rather than by minimizing the wave energy in the neighboring formations. Fig. 4.11 illustrates that, despite enforcing silent neighbors, a large portion of the wave energy still remains along the ground surface for the optimized time signals, and reducing such a strong ground surface wave seems challenging. In the remaining experiments (case numbers 2B and 3B), we will discuss again the possibility of inducing a relatively small ground surface motion by using independent wave sources in asymmetric locations.

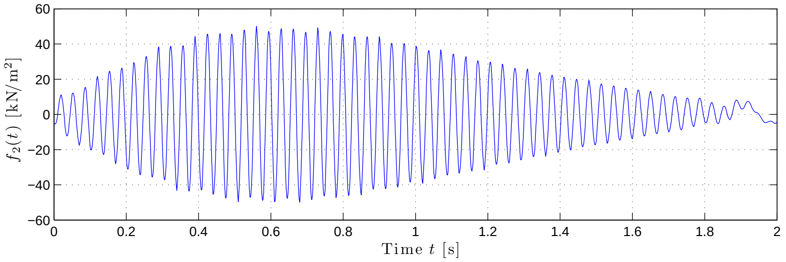

(a) The converged loading time signal

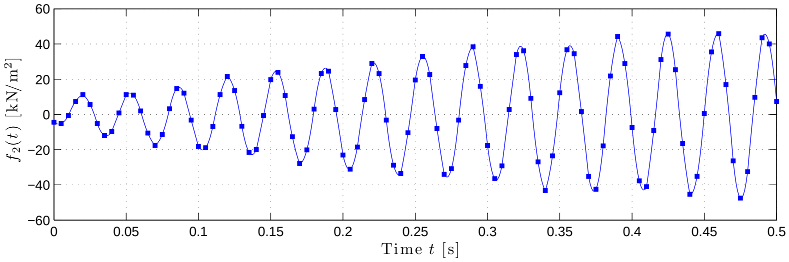

(b) Close-up view of converged loading time signal (0–0.5s)

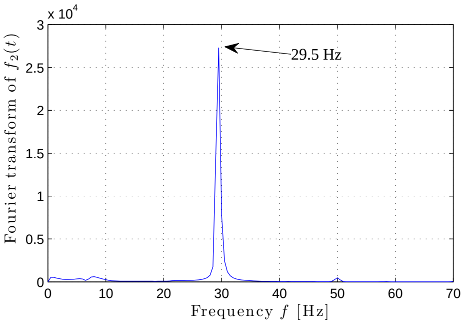

(c) The frequency spectrum of the converged loading time signal

Figure 4.10: The loading time signal that converged after 71 iterations by minimizing (4.11): the maximization of the kinetic energy in Ω_0 with silent neighbors of the formation model (Fig. 4.2(a)).

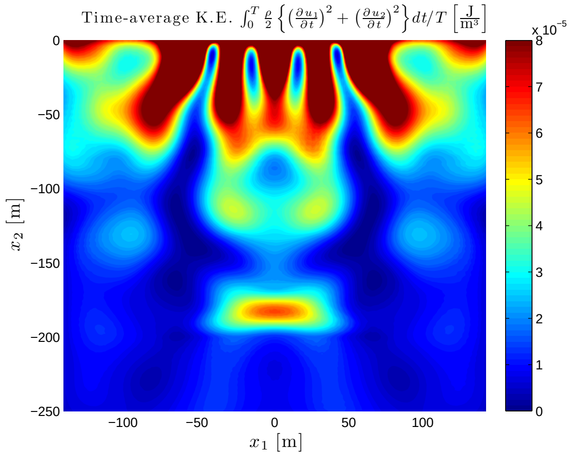

Figure 4.11: The time-averaged kinetic energy distribution in Ω_{reg} of the formation model shown in Fig. 4.2(a) for the converged loading time signal shown in Fig. 4.10.

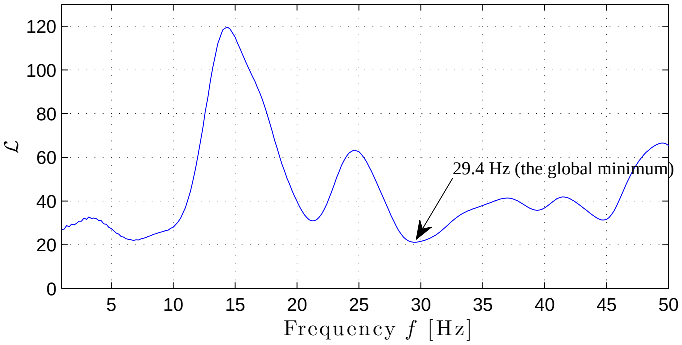

Figure 4.12: Frequency sweep of the objective functional (4.11) using a harmonic load $f_2(t) = 50\sin(2\pi f t)\mathrm{kN/m}^2$ for the formation model shown in Fig. 4.2(a).

4.4.2.3 Wave sources optimal signals (case 1C)

Next, we test the optimization approach by seeking to maximize the acceleration field within a targeted inclusion Ω_0, by using the acceleration-based objective functional (4.12) for the formation model subjected the two symmetric ground wave sources, as shown in Fig. 4.2(a). This time, we use 100 and 200 discretized force parameters for each numerical experiment. The total observation time is 2s, and the time step is 0.001s.

Figures 4.13(a) and 4.13(b) show that the optimization procedures, using 100 and 200 discretized force parameters, yield signals with frequencies 21 and 49Hz, respectively (a higher frequency is recovered when more force parameters are used). We remark that the amplitude of the acceleration field within the targeted inclusion Ω_0 tends to be greater for a higher frequency (the frequency sweep of (4.12), shown in Fig. 4.14, demonstrates that the value of (4.12) is smaller for a higher frequency). Thus, the optimizer leads to an optimal loading time signal showing a dominant frequency equal to the highest frequency the temporal discretization will support.

The amplitude of the acceleration field $\left|\frac{\partial^2 u}{\partial t^2}\right| = \sqrt{\left(\frac{\partial^2 u_1}{\partial t^2}\right)^2 + \left(\frac{\partial^2 u_2}{\partial t^2}\right)^2}$ shown in Fig. 4.15, induced either by the converged optimized excitation time signal that is shown in Fig. 4.6(a) or by the other optimized time signal shown in Fig. 4.13(b), is as large as the threshold acceleration value (0.1–10m/s^2) for the mobilization of the trapped oil droplets that Beresnev[9] suggested. Overall, in this two-dimensional setting again, if one is interested in maximizing the acceleration field, the higher the frequency, the stronger the acceleration is.

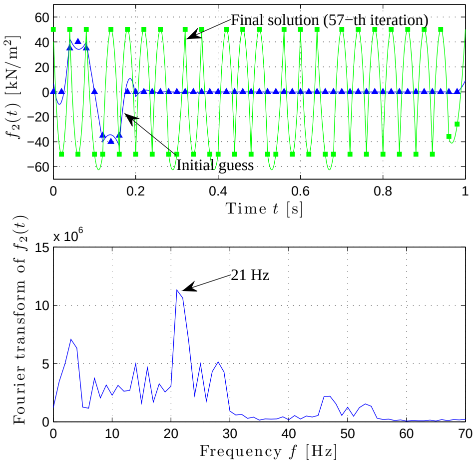

(a) The optimal loading time signal discretized by using 100 force parameters

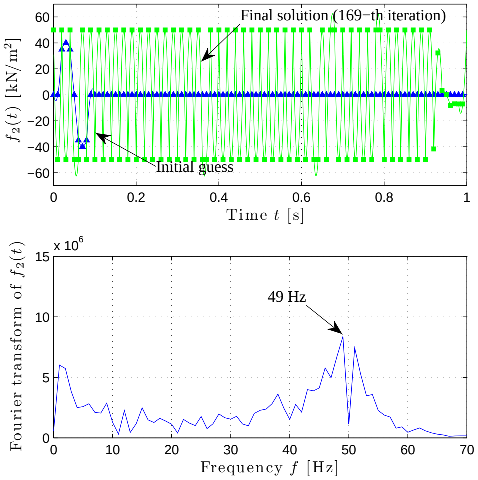

(b) The optimal loading time signal discretized by using 200 force parameters

Figure 4.13: Optimal time signals converged via the minimization of (4.12).

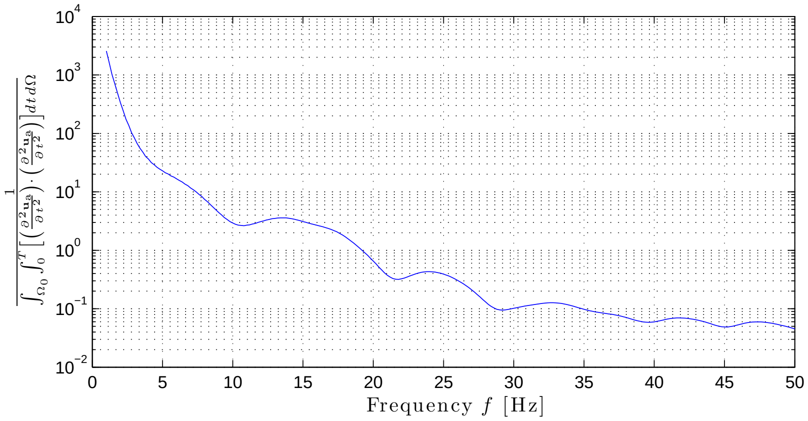

Figure 4.14: Frequency sweep of the objective functional (4.12) using a harmonic load $f_2(t) = 50\sin(2\pi f t)\text{kN/m}^2$ for the formation model shown in Fig. 4.2(a).

4.4.2.4 Wave sources optimal signals (case 2B)

We considered next two strip surface loading wave sources situated in asymmetric locations – the centroids of the strip loading areas are respectively located at (-30m, 0m) and (70m, 0m) – shown in Fig. 4.2(b). The total observation time is 2s, and the time step is 0.001s; we temporally discretize an initial perturbation-like loading time signal for each wave source $f(t)$ only for the initial duration of 0.3s ($f(t) = 0$ for $t > 0.3$s). While inverting time signals of such a short duration (0.3s vs 2s in Fig. 4.10), we investigated the possibility of recovering pulse-shaped time signals in lieu of the previously recovered sinusoidally shaped time signals.

We start with two identical initially guessed time signals (Fig. 4.16) at the two loading locations, $x_1 = -30$m and $x_1 = 70$m. The time signal for each wave source changes its amplitude independently during the iteration

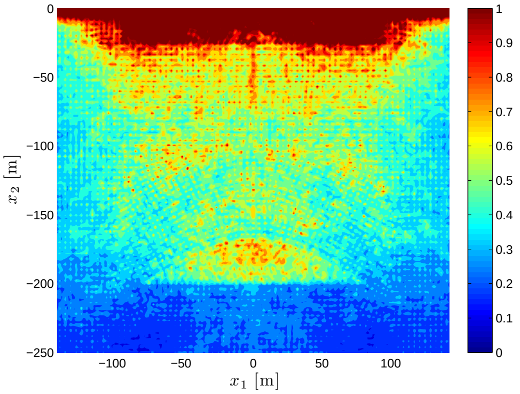

(a) Acceleration field for the converged loading signal shown in Fig. 4.6 (maximization of kinetic energy in Ω_0 with all layers active)

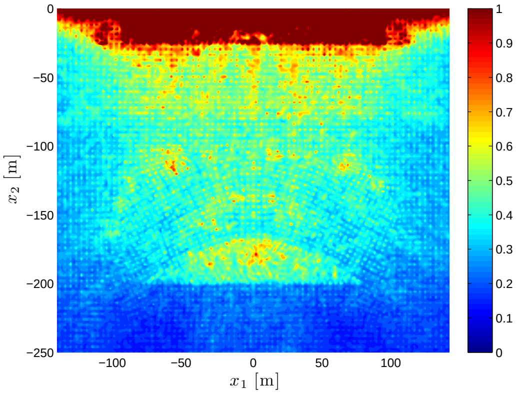

(b) Acceleration field for the converged loading signal shown in Fig. 4.13(b) (maximization of acceleration in Ω_0 with all layers active)

Figure 4.15: The maximum amplitude of the acceleration field $\left|\frac{\partial^2 u}{\partial t^2}\right|$ [m/s^2] of the wave responses in Ω_{reg} for the converged excitations shown in Fig. 4.6 and 4.13(b), respectively, for the formation model of Fig. 4.2(a).

procedure, i.e., $f_2(t)\Big|_{x_1=-30\text{m}} \neq f_2(t)\Big|_{x_1=70\text{m}}$. After the first 36 iterations, the optimizer arrives at the time signals for which the dominant frequencies are 10.3Hz and 28.3Hz (Fig. 4.17). However, after the 80-th iteration, the time signals converge into pulses for which the dominant frequencies are 8.8Hz (Fig. 4.18). That is, the optimizer first converges into a local minimum basin associated with dominant frequencies 10.3 and 28.3Hz. It then converges to another local minimum basin pertaining to a dominant frequency of 8.8Hz after about 80 iterations (see the distribution of the objective functional (4.11) in Fig. 4.20). Fig. 4.18 shows that the converged signals are nearly identical.

Fig. 4.19 shows that, even though the dominant frequency of the final converged loading time signals corresponds to the global minimum, the kinetic energy within the targeted inclusion for the final converged loading is smaller than the one that corresponds to the signals shown in Fig. 4.17 (36 iterations). However, the surface wave motion is much weaker for the final converged loading time signals than for the loading signals recovered after 36 iterations.

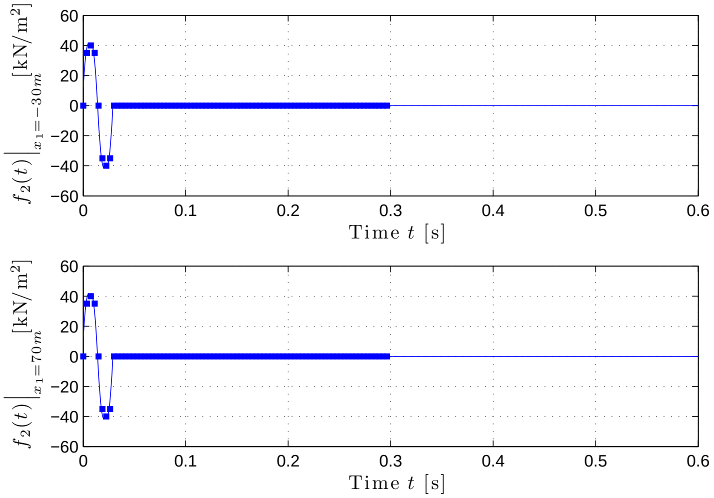

(a) The initially guessed loading time signals

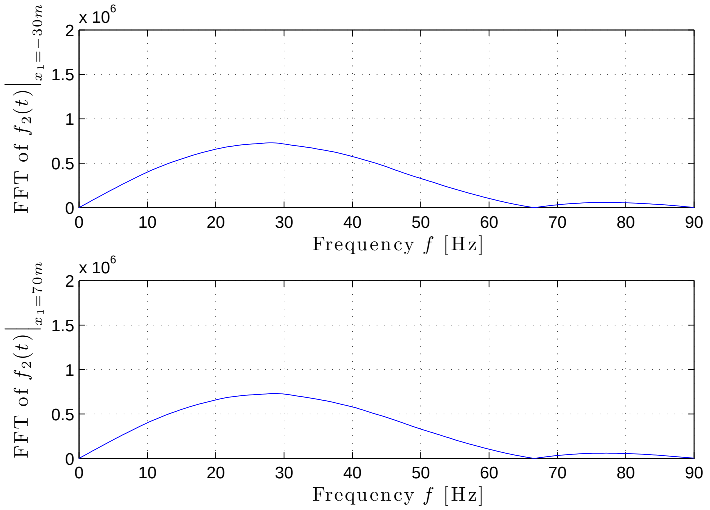

(b) The frequency spectra of the initially guessed loading time signals

Figure 4.16: The initially guessed loading time signals of the two independent wave sources at $x_1 = -30$m and $x_1 = 70$m for the maximization of the kinetic energy in Ω_0 with silent neighbors via the minimization of (4.11) for formation model shown in Fig. 4.2(b).

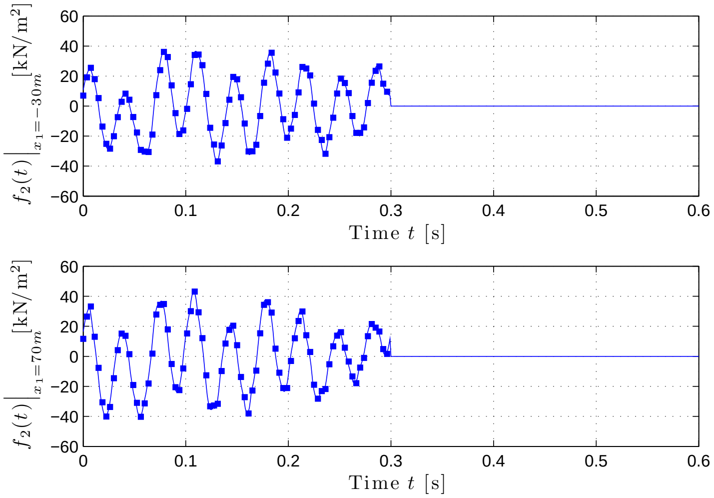

(a) The guessed loading time signals at the 36-th iteration

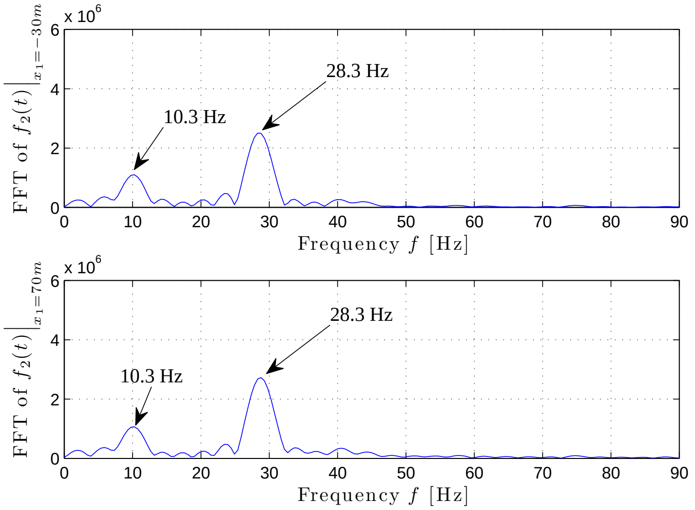

(b) The frequency spectra of the guessed loading time signals at the 36-th iteration

Figure 4.17: Optimized loading time signals at the 36-th iteration of the optimization process (minimizing (4.11)) for the two independent wave sources of asymmetric locations shown in Fig. 4.2(b).

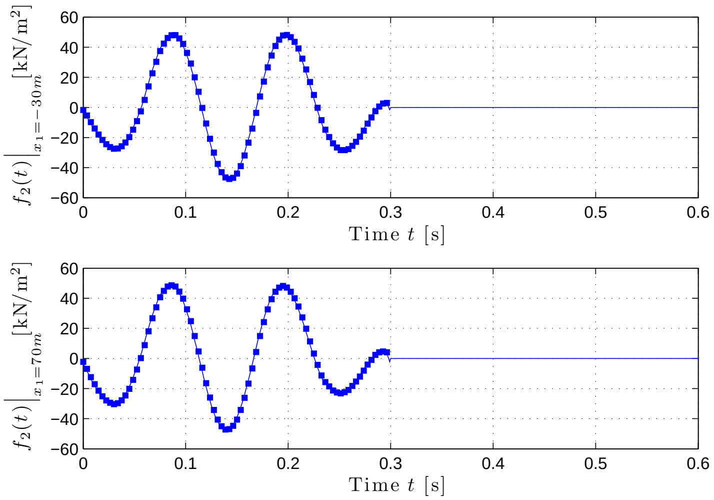

(a) The finally converged loading time signals

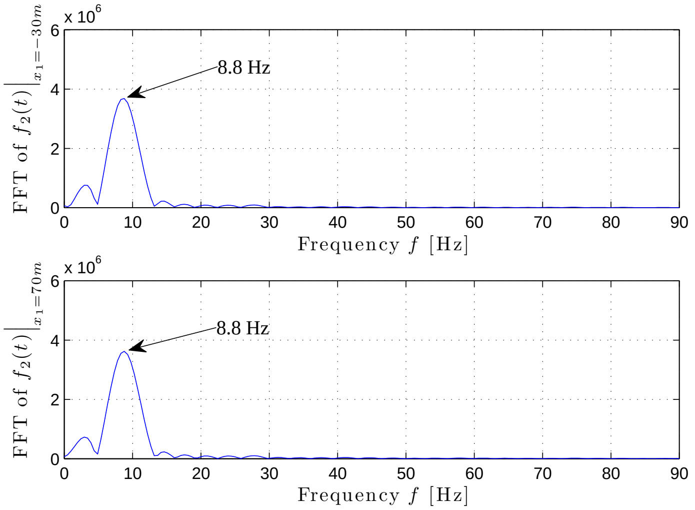

(b) The frequency spectra of the finally converged loading time signals

Figure 4.18: Optimized loading time signals (final) after 80 iterations of the optimization process (minimizing (4.11)) for the two independent wave sources of asymmetric locations shown in Fig. 4.2(b).

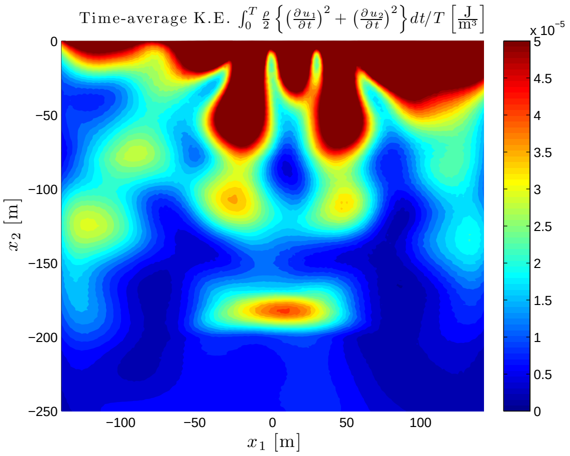

(a) Kinetic energy for the guessed loading time signals at the 36-th iteration (Fig. 4.17)

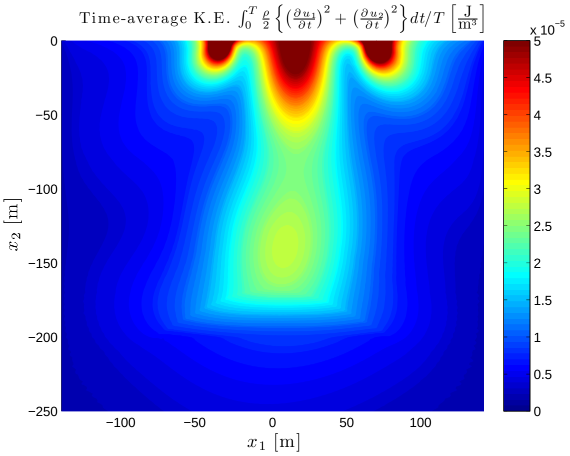

(b) Kinetic energy for the loading time signals, converged after 80 iterations (Fig. 4.18)

Figure 4.19: The time-averaged kinetic energy distributions in Ω_{reg} of the formation model shown in Fig. 4.2(b) for the loading time signals shown in Figures 4.17 and 4.18.

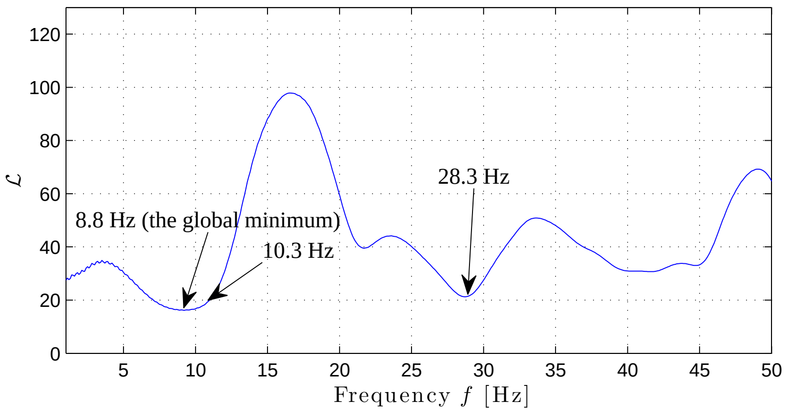

Figure 4.20: Frequency sweep of the objective functional (4.11) using a harmonic load $f_2(t) = 50\sin(2\pi f t)\mathrm{kN/m}^2$ for the formation model shown in Fig. 4.2(b): the frequency accountable for the global minimum for the two asymmetric wave sources differs from that for the two symmetric wave sources (8.8Hz vs 29.5Hz).

4.4.2.5 Wave sources optimal signals (case 3B)

We considered next five independent wave sources located at asymmetric locations, as shown in Fig. 4.2(c). Here, $f_2^{(1)}(t)$, $f_2^{(2)}(t)$, $f_2^{(3)}(t)$, $f_2^{(4)}(t)$, and $f_2^{(5)}(t)$ denote independent loading time signals of the strip loading wave sources whose centroids are located at $x_1 = -96$, -38, 0, 48, and 81m on the ground surface ($x_2 = 0$m) respectively.

The total observation time is 2s, and the time step is 0.001s; we discretize the loading time signals by using 40 quadratic elements (80 discretized force parameters) for a duration of 0.4s. The optimization process starts with five different initially guessed perturbation-like time signals, as shown in Fig. 4.21; the frequency spectra of the initial signals are shown in Fig. 4.22. After 140 iterations, the optimizer arrives at the time signals shown in Fig. 4.23 with the frequency spectra shown in Fig. 4.24. We remark that the finally converged time signals are nearly sinusoidal with a strong dominant frequency of 29Hz (the frequency accounting for the global minimum of the objective functional (4.11) for a harmonic excitation $f_2(t) = 50\sin(2\pi ft)\text{kN/m}^2$ for the formation model shown in Fig. 4.2(c), as shown in Fig. 4.26).

Fig. 4.25 shows that employing five asymmetric wave sources leads to quite a clear focusing of the wave energy in the targeted inclusion, with an even more effective minimization of the surface wave energy than in previous experiments (Fig. 4.25 vs. Fig. 4.11 and Fig. 4.19).

Similar to experiment 2B, the optimization process that employs independent loading signals for five wave sources in asymmetric locations also resulted in signals exhibiting the same dominant frequency. We thus conjecture that the kinetic energy within a targeted inclusion is likely to be maximized when the wave sources have spectra with dominant frequencies coinciding with one (or more) of the formation's amplification frequencies. The described procedure successfully recovers the amplification frequencies under a variety of loading conditions.

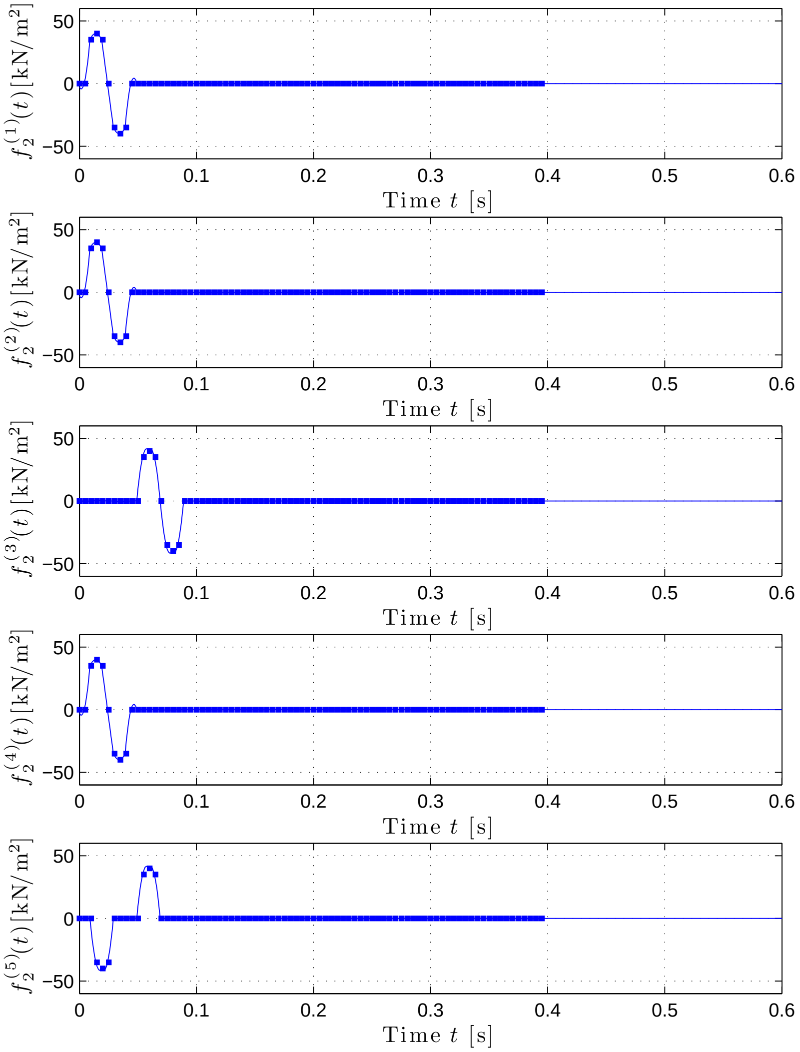

Figure 4.21: The initially guessed loading time signals of the five wave sources at asymmetric locations for the formation model shown in Fig. 4.2(c) for the maximization of the kinetic energy in Ω_0 with silent neighbors (minimizing (4.11)).

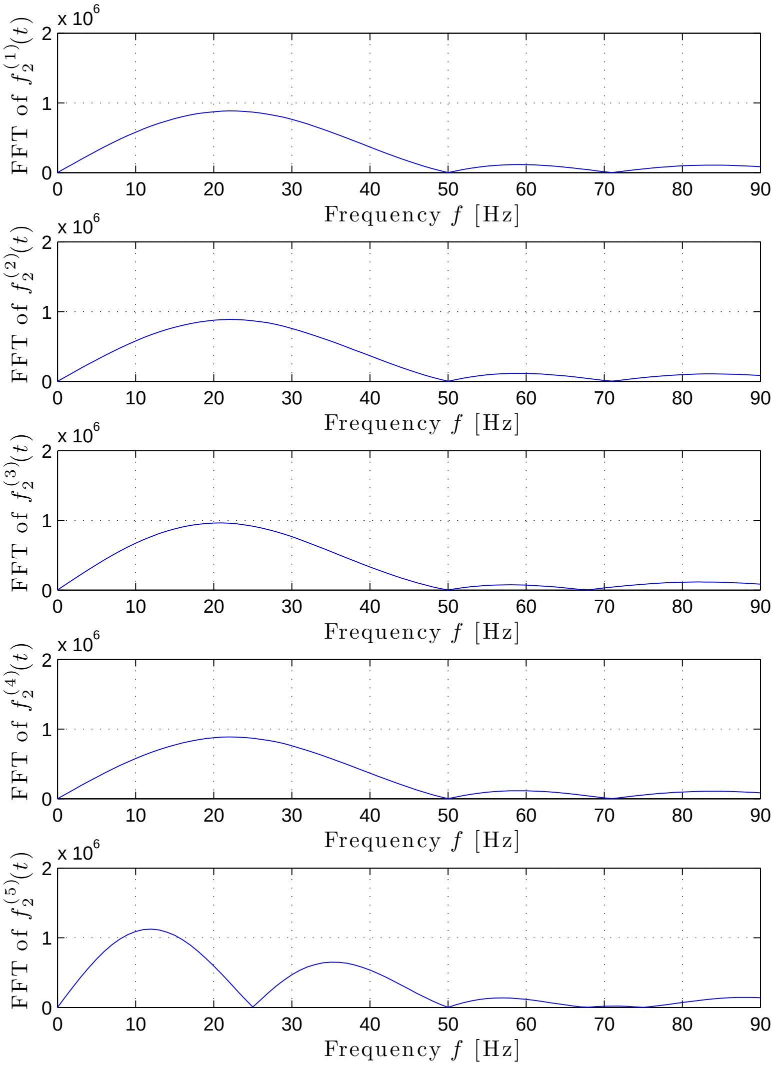

Figure 4.22: The frequency spectra of the initially guessed loading time signals shown in Fig. 4.21.

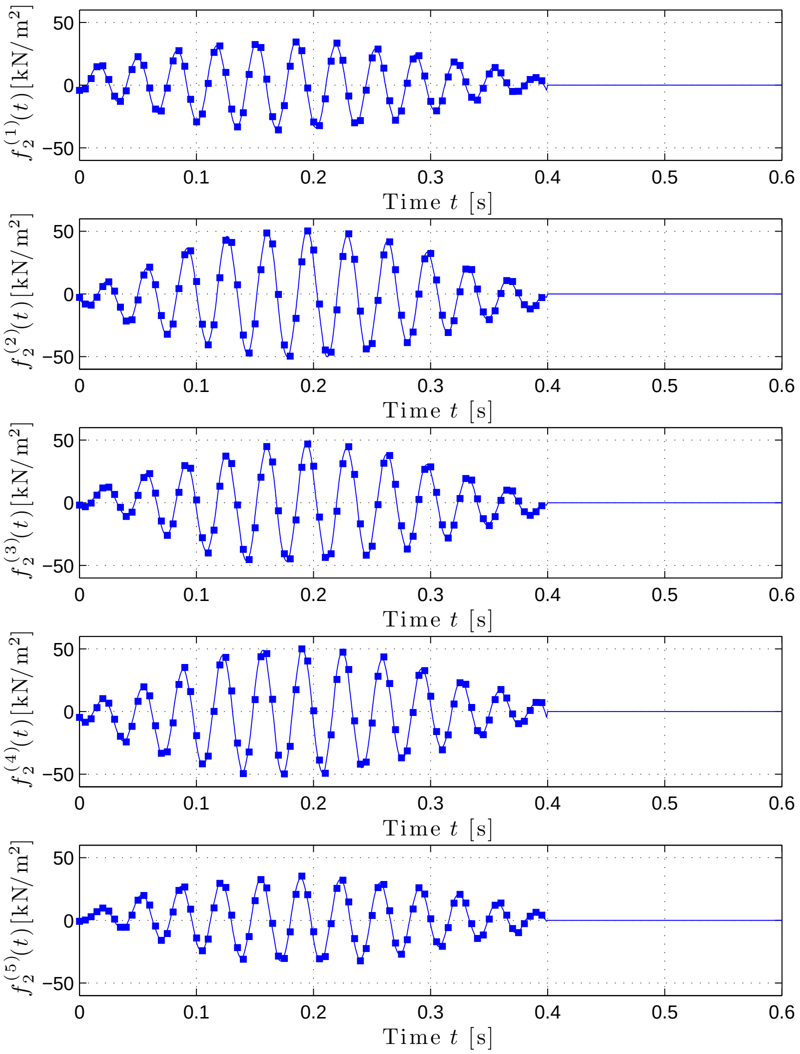

Figure 4.23: The finally converged loading time signals of the five wave sources at asymmetric locations for the formation model shown in Fig. 4.2(c) after 140 iterations of the optimization process for the maximization of the kinetic energy in Ω_0 with silent neighbors (minimizing (4.11)).

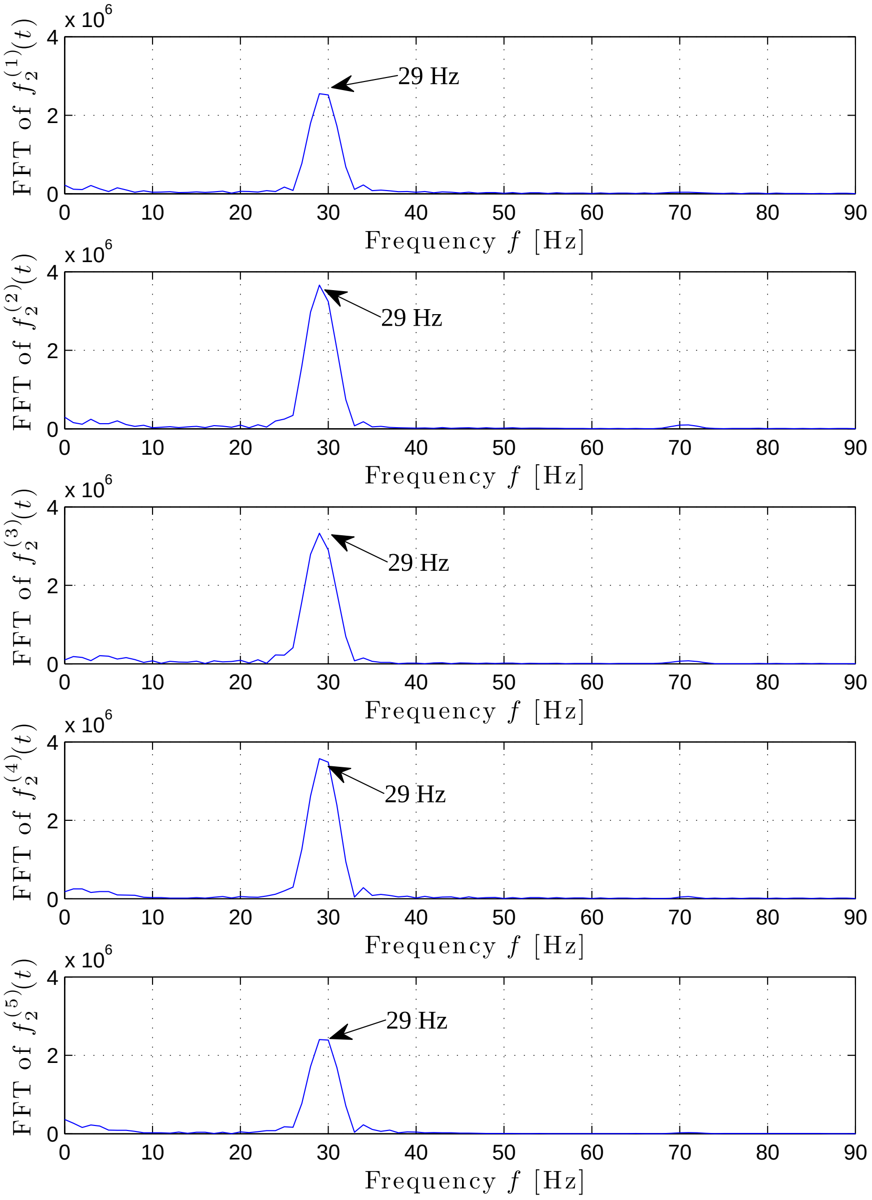

Figure 4.24: The frequency spectra of the finally converged loading time signals shown in Fig. 4.23.

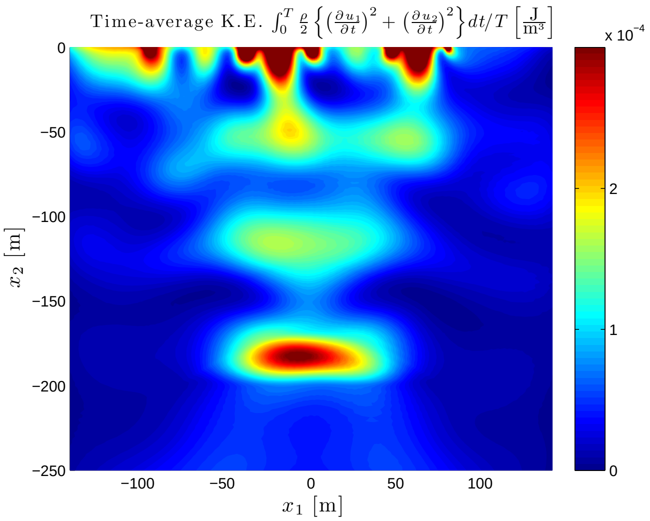

Figure 4.25: The time-averaged kinetic energy distribution in Ω_{reg} for the optimized loading time signals of the five wave sources, shown in Fig. 4.23, for the formation model shown in Fig. 4.2(c).

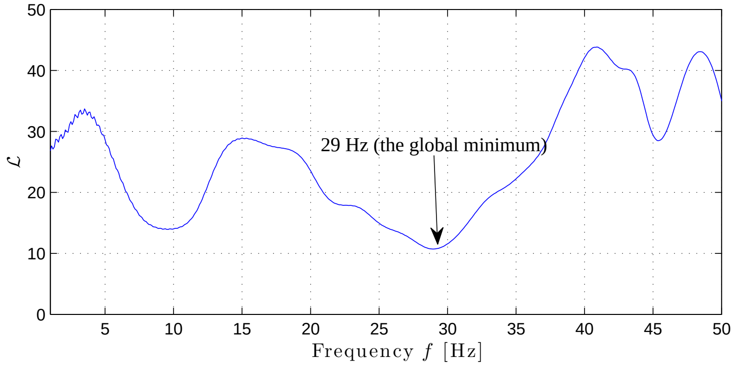

Figure 4.26: Frequency sweep of the objective functional (4.11) using a harmonic load $f_2(t) = 50\sin(2\pi ft)\mathrm{kN/m^2}$ for the formation model shown in Fig. 4.2(c).

4.5 Feasibility of dislodging trapped oil droplets in 2D

In order to investigate the feasibility of dislodging trapped oil droplets within the target inclusion in the two-dimensional setting, we utilized the values of threshold-acceleration for different frequencies, shown in Table 4.2, computed by using Beresnev's threshold model suggested in [10] (the model is taking into account the viscosity of pore fluid), as well as realistic values for the fluid-saturated porous permeable rock properties (Table 4.3).

In Table 4.3, (a) $r_{\max}$ and $r_{\min}$ denote the maximum and minimum radii, respectively, of the cross-section of pore space in an axisymmetric sinusoidally constricted pore channel; (b) the background pressure gradient 35185Pa/m corresponds to a Darcy flow-rate of 1ft/day of fluid of viscosity 1cp within a porous permeable rock of permeability 100md; and (c) the capillary pressure, i.e., $P_c = \frac{2\sigma \cos\theta}{r}$, of 800Pa corresponds to interface tension σ of 0.04N/m, a radius of curvature r of 100micron, and an oil/water contact angle θ of $0°$.

The threshold values shown in Table 4.2 are up to 1.6m/s^2, for frequencies up to 50Hz. Summary table 4.4 shows that the optimized loadings in the optimization cases 1A, 3A, and 3C produced acceleration field whose amplitude is as large as the threshold values. Thus, the optimized loads could initiate the dislodging-based mobilization of the trapped oil droplets in a fluid-saturated porous permeable rock in the target reservoir of the shallow formation model shown in Fig. 4.2. We suggest that the mobilization of trapped oil droplets could be further facilitated if sources are optimally placed, in addition to be optimally operated at the optimized signals for this subsurface formation model (or even for deeper reservoir formation models).

Frequency [Hz]	Threshold-acceleration [m/s^2]
10	0.4
20	0.7
30	1
40	1.3
50	1.6

Table 4.2: Threshold-acceleration levels evaluated by using Beresnev's latest threshold-acceleration model [10], as well as the fluid-saturated porous permeable rock properties shown in Table 4.3.

Maximum pore radius $r_{\max}$	200micron
Minimum pore radius $r_{\min}$	100micron
Background pressure gradient	35185Pa/m
Water viscosity	1cp
Oil viscosity	5cp
Capillary pressure	800Pa
Interface tension σ	40dyne/cm = 0.04N/m

Table 4.3: Fluid-saturated porous permeable rock properties used for evaluating the threshold-acceleration value for the mobilization of trapped oil droplets.

4.6 Summary

A brief summary of the results of the optimization experiments is shown in Table 4.4. We also show the spatial distributions of the time-averaged kinetic energy and the maximum acceleration amplitude for the optimized loading time signals, as well as the monochromatic loadings corresponding to the dominant frequencies of the optimized loading signals in Figures 4.27–4.35.[3]

Optimization Case Number	Locations of wave sources	Maximized metric in the reservoir Ω_0	Dominant frequency of optimized loading [Hz]	Time-average kinetic energy in Ω_0 [J/m^3]	Maximum amplitude of $\frac{\partial^2 u}{\partial t^2}$ in Ω_0 [m/s^2]
1A	Two symmetric sources located at x_1 =-70, 70m (Fig. 4.2(a))	Kinetic energy (all layers active)	29	3×10^{-4}	1.0
1B		Kinetic energy (silent neighbors)	29.5	8×10^{-5}	0.1
1C		Acceleration (all layers active)	49	1×10^{-4}	0.6
2A	Two asymmetric sources located at x_1 = -30, 70m (Fig. 4.2(b))	Kinetic energy (all layers active)	28.5	1×10^{-4}	0.5
2B		Kinetic energy (silent neighbors)	8.8 (a pulse)	2×10^{-5}	0.02
2C		Acceleration (all layers active)	50	1×10^{-4}	0.6
3A	Five asymmetric sources located at x_1 = -96, -38, 0, 48, 81m (Fig. 4.2(c))	Kinetic energy (all layers active)	29	1.4×10^{-3}	1.2
3B		Kinetic energy (silent neighbors)	29	3×10^{-4}	0.2
3C		Acceleration (all layers active)	45	3×10^{-4}	1.2

Table 4.4: Summary of our numerical experiments.

Our observations from the numerical experiments are the following.

---

[3] In Figures 4.27–4.35, we employ uniform values of the upper limits of the side color scale bars: 3×10^{-4}J/m^3 for the time-averaged K. E. distribution and 1m/s^2 for the maximum amplitude of acceleration field.

- Table 4.4 shows that there is a dominant amplification frequency at 29Hz that leads to the maximization of the kinetic energy within the reservoir Ω_0 in almost all the cases, and under a variety of loading conditions. The particular frequency, as shown by the frequency sweep, corresponds to one of the discrete amplification frequencies of the formation. It is not a resonant frequency in the classical sense (i.e., a frequency for which the motion becomes unbounded under undamped conditions), since the medium is semi-infinite in extent, but, rather, a frequency that will generate a large response. The frequency depends on the formation's characteristics (geometry, properties, etc). This amplification frequency can be obtained either by the optimization procedure described herein, or by conducting a frequency sweep (objective functional versus frequency).

- It also appears that the location of the wave sources is critical in arriving at motion maximization. As was seen in the case of two wave sources, there is a significant shift of the dominant frequency of the optimized signals from 29Hz (two symmetric sources), to 8.8Hz (two asymmetric sources). In other words, we conjecture that optimally located sources could produce a stronger motion amplification effect (the case with the two asymmetric sources), than the amplification effect due to non-optimally located sources operating at the reservoir's amplification frequency. Though not explored in this work, it is possible to enhance the presented optimization process to include a search for the optimal placement of the wave sources as well.

Moreover, as was seen in the case of the five asymmetric wave sources, it is also possible to reduce the concentration of the energy near the surface, thus leading to better focusing and illumination of the target reservoir.

- Even with multiple independent wave sources at non-optimal asymmetric locations, our optimizer generally leads to optimal excitation signals of a single dominant frequency – the dominant reservoir's amplification frequency. Thus, we conjecture that multiple monochromatic sources operating at one of the reservoir's amplification frequencies, even if not optimally placed, will still result in significant motion within the target reservoir.

- We also observed that the optimizer will not only result in monochromatic signals, which could have been obtained by a frequency sweep, but also in transient pulse-like loadings, depending on the maximization outcome and the source and reservoir characteristics.

- The temporal discretization of the initially-guessed loading time signal controls the frequency content of the optimal loading signal that can maximize the acceleration within the reservoir. In short, a greater number of force parameters leads to a higher dominant frequency. In general, when it comes to maximizing the acceleration field, there is a linear relation between the acceleration and the optimal frequency: higher frequencies will result in stronger acceleration fields.

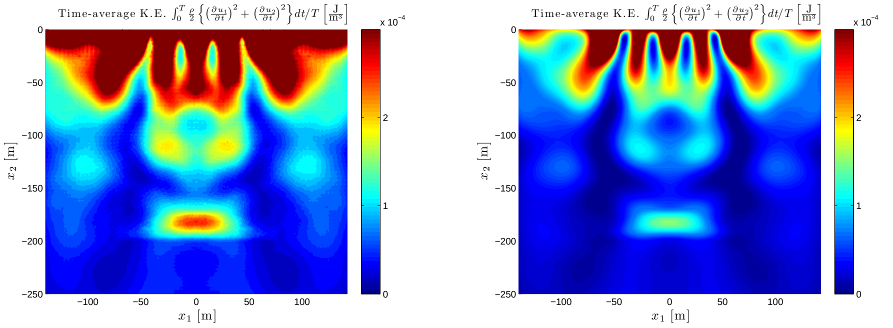

(a) K.E. for the optimized $f(t)$ (b) K.E. for the sinusoidal loading

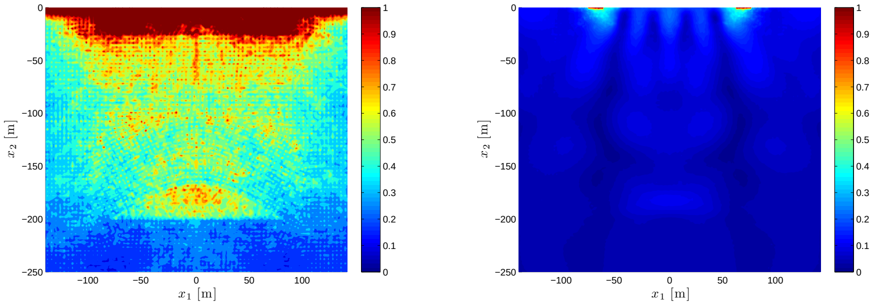

(c) Maximum amplitude of $\frac{\partial^2 u}{\partial t^2}$ for the optimized $f(t)$ (d) Maximum amplitude of $\frac{\partial^2 u}{\partial t^2}$ for the sinusoidal loading

Figure 4.27: The distributions of the time-averaged kinetic energy [J/m^3] and the maximum amplitude of $\frac{\partial^2 u}{\partial t^2}$ [m/s^2] in Ω_{reg} for the optimized loading signals or the sinusoidal loading signal $f_2(t) = 50\sin(2\pi \times 29t)$kN/m^2 that employs the dominant frequencies of the optimized signals (the case 1A in Table 4.4).

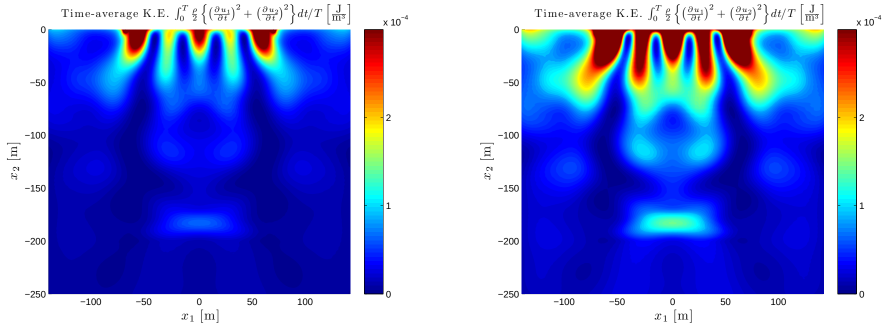

(a) K.E. for the optimized $f(t)$

(b) K.E. for the sinusoidal loading

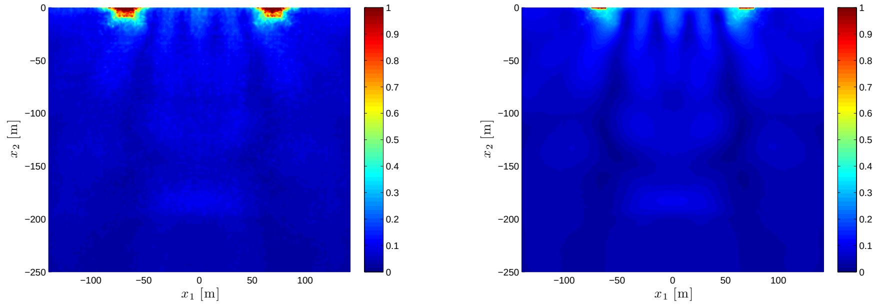

(c) Maximum amplitude of $\frac{\partial^2 u}{\partial t^2}$ for the optimized $f(t)$

(d) Maximum amplitude of $\frac{\partial^2 u}{\partial t^2}$ for the sinusoidal loading

Figure 4.28: The distributions of the time-averaged kinetic energy [J/m^3] and the maximum amplitude of $\frac{\partial^2 u}{\partial t^2}$ [m/s^2] in Ω_{reg} for the optimized loading signals or the sinusoidal loading signal $f_2(t) = 50\sin(2\pi \times 29.5t)$kN/m^2 that employs the dominant frequencies of the optimized signals (the case 1B in Table 4.4).

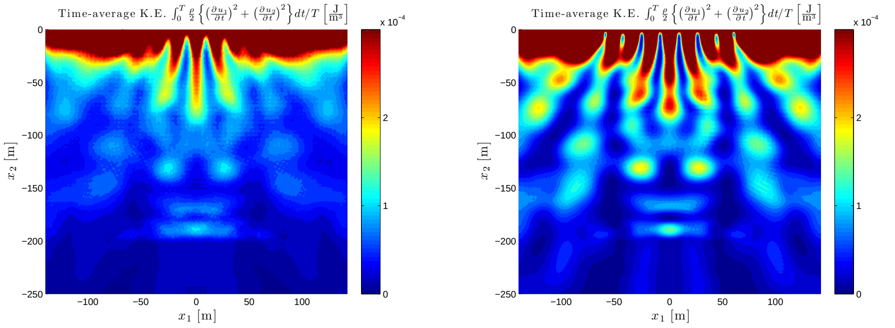

(a) K.E. for the optimized $f(t)$

(b) K.E. for the sinusoidal loading

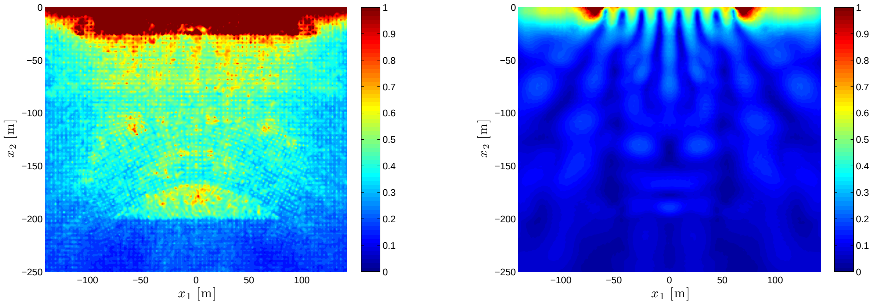

(c) Maximum amplitude of $\frac{\partial^2 u}{\partial t^2}$ for the optimized $f(t)$

(d) Maximum amplitude of $\frac{\partial^2 u}{\partial t^2}$ for the sinusoidal loading

Figure 4.29: The distributions of the time-averaged kinetic energy [J/m^3] and the maximum amplitude of $\frac{\partial^2 u}{\partial t^2}$ [m/s^2] in Ω_{reg} for the optimized loading signals or the sinusoidal loading signal $f_2(t) = 50\sin(2\pi \times 49t)\mathrm{kN/m}^2$ that employs the dominant frequencies of the optimized signals (the case 1C in Table 4.4).

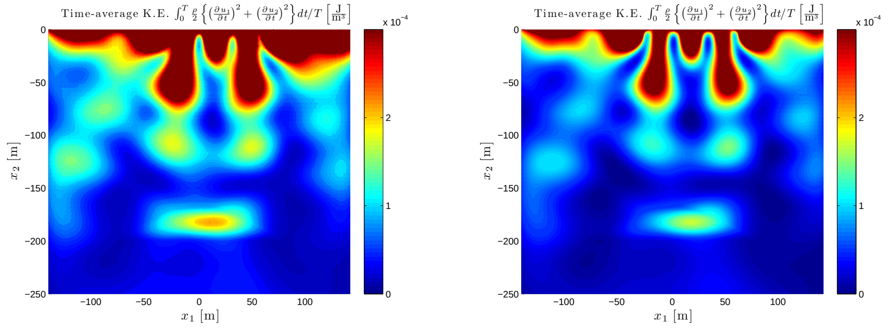

(a) K.E. for the optimized $f(t)$ (b) K.E. for the sinusoidal loading

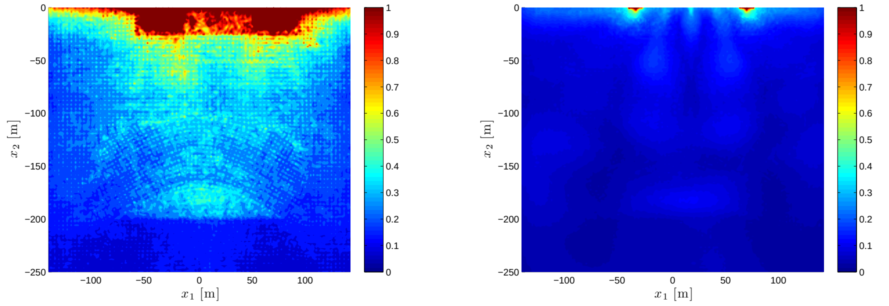

(c) Maximum amplitude of $\frac{\partial^2 u}{\partial t^2}$ for the optimized $f(t)$ (d) Maximum amplitude of $\frac{\partial^2 u}{\partial t^2}$ for the sinusoidal loading

Figure 4.30: The distributions of the time-averaged kinetic energy [J/m^3] and the maximum amplitude of $\frac{\partial^2 u}{\partial t^2}$ [m/s^2] in Ω_{reg} for the optimized loading signals or the sinusoidal loading signal $f_2(t) = 50\sin(2\pi \times 28.5t)\mathrm{kN/m}^2$ that employs the dominant frequencies of the optimized signals (the case 2A in Table 4.4).

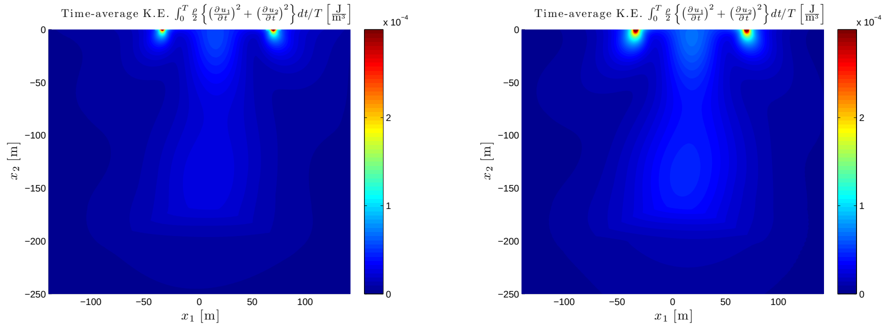

(a) K.E. for the optimized $f(t)$ (b) K.E. for the sinusoidal loading

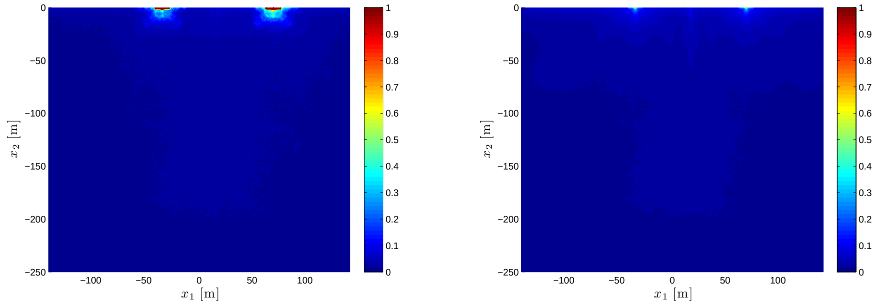

(c) Maximum amplitude of $\frac{\partial^2 u}{\partial t^2}$ for the optimized $f(t)$ (d) Maximum amplitude of $\frac{\partial^2 u}{\partial t^2}$ for the sinusoidal loading

Figure 4.31: The distributions of the time-averaged kinetic energy [J/m^3] and the maximum amplitude of $\frac{\partial^2 u}{\partial t^2}$ [m/s^2] in Ω_{reg} for the optimized loading signals or the sinusoidal loading signal $f_2(t) = 50\sin(2\pi \times 8.8t)\text{kN/m}^2$ that employs the dominant frequencies of the optimized signals (the case 2B in Table 4.4).

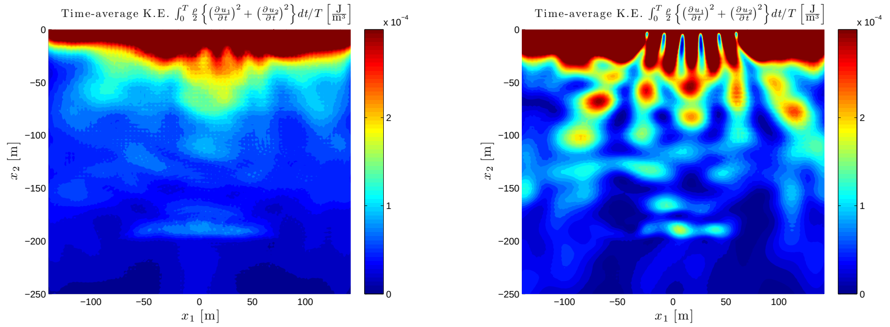

(a) K.E. for the optimized $f(t)$

(b) K.E. for the sinusoidal loading

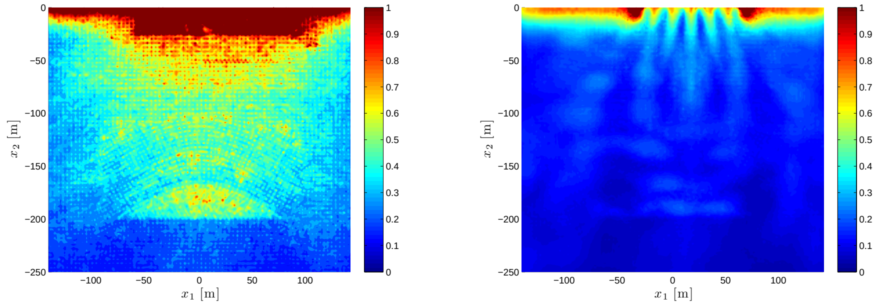

(c) Maximum amplitude of $\frac{\partial^2 u}{\partial t^2}$ for the optimized $f(t)$

(d) Maximum amplitude of $\frac{\partial^2 u}{\partial t^2}$ for the sinusoidal loading

Figure 4.32: The distributions of the time-averaged kinetic energy [J/m^3] and the maximum amplitude of $\frac{\partial^2 u}{\partial t^2}$ [m/s^2] in Ω_{reg} for the optimized loading signals or the sinusoidal loading signal $f_2(t) = 50\sin(2\pi \times 50t)$kN/m^2 that employs the dominant frequencies of the optimized signals (the case 2C in Table 4.4).

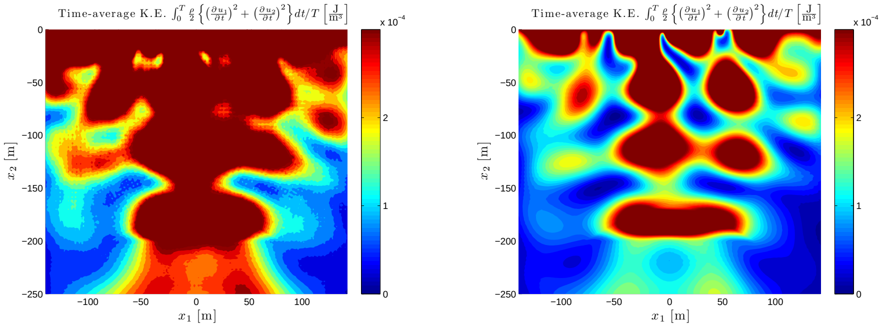

(a) K.E. for the optimized $f(t)$

(b) K.E. for the sinusoidal loading

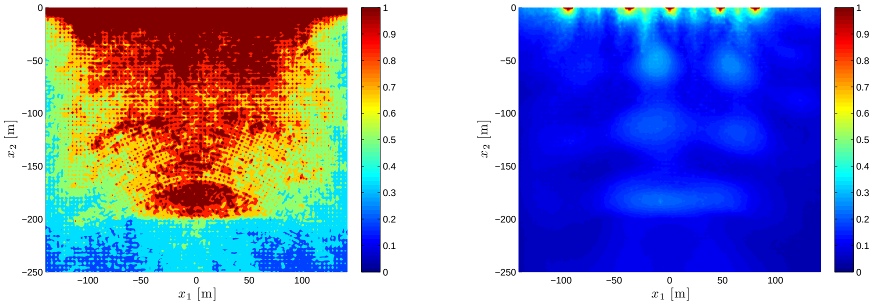

(c) Maximum amplitude of $\frac{\partial^2 u}{\partial t^2}$ for the optimized $f(t)$

(d) Maximum amplitude of $\frac{\partial^2 u}{\partial t^2}$ for the sinusoidal loading

Figure 4.33: The distributions of the time-averaged kinetic energy [J/m^3] and the maximum amplitude of $\frac{\partial^2 u}{\partial t^2}$ [m/s^2] in Ω_{reg} for the optimized loading signals or the sinusoidal loading signal $f_2(t) = 50\sin(2\pi \times 29t)\text{kN/m}^2$ that employs the dominant frequencies of the optimized signals (the case 3A in Table 4.4).

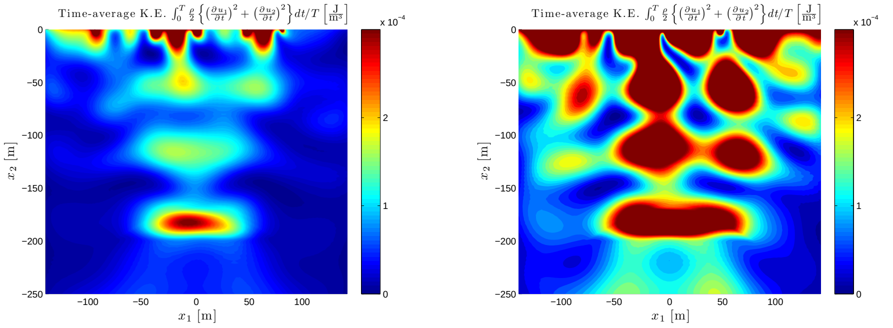

(a) K.E. for the optimized $f(t)$ (b) K.E. for the sinusoidal loading

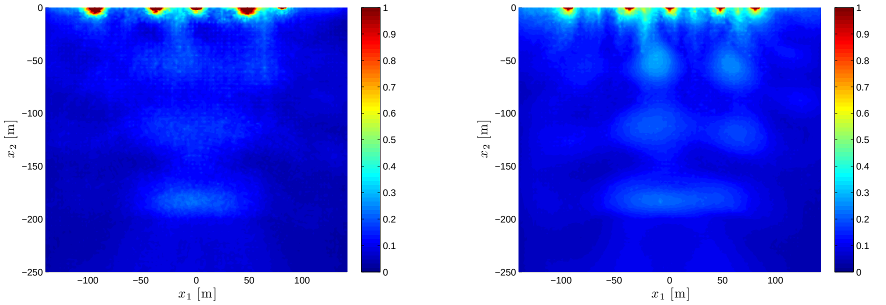

(c) Maximum amplitude of $\frac{\partial^2 u}{\partial t^2}$ for the optimized $f(t)$ (d) Maximum amplitude of $\frac{\partial^2 u}{\partial t^2}$ for the sinusoidal loading

Figure 4.34: The distributions of the time-averaged kinetic energy [J/m^3] and the maximum amplitude of $\frac{\partial^2 u}{\partial t^2}$ [m/s^2] in Ω_{reg} for the optimized loading signals or the sinusoidal loading signal $f_2(t) = 50\sin(2\pi \times 29t)\text{kN/m}^2$ that employs the dominant frequencies of the optimized signals (the case 3B in Table 4.4).

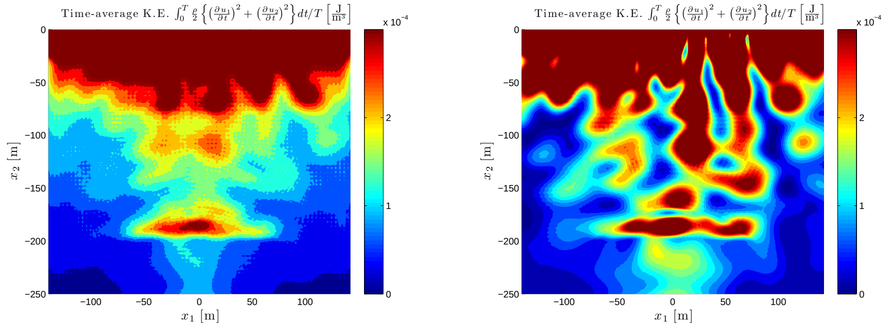

(a) K.E. for the optimized $f(t)$ (b) K.E. for the sinusoidal loading

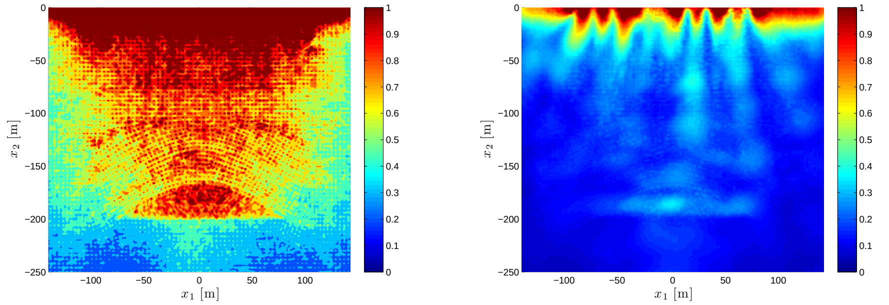

(c) Maximum amplitude of $\frac{\partial^2 u}{\partial t^2}$ for the optimized $f(t)$ (d) Maximum amplitude of $\frac{\partial^2 u}{\partial t^2}$ for the sinusoidal loading

Figure 4.35: The distributions of the time-averaged kinetic energy [J/m^3] and the maximum amplitude of $\frac{\partial^2 u}{\partial t^2}$ [m/s^2] in Ω_{reg} for the optimized loading signals or the sinusoidal loading signal $f_2(t) = 50\sin(2\pi \times 45t)\text{kN/m}^2$ that employs the dominant frequencies of the optimized signals (the case 3C in Table 4.4).

Chapter 5

Oil mobilization via ground sources – The poroelastic inverse-source problem in 1D

In this chapter, we discuss the mathematical and numerical modeling of inverting for the loading time signal of a wave source that can maximize the wave motion of the pore fluid within fluid-saturated porous permeable rock formations, surrounded by non-permeable semi-infinite elastic solid rock formations, in a one-dimensional setting. To this end, we use the finite element method to tackle the governing wave physics of a multi-layered system where Biot's poroelastic equations for the target layer and elastic wave equations for the surrounding layers are coupled. The numerical results show that our numerical optimizer recovers nicely the theoretical amplification frequencies corresponding to pore-fluid motion within hydrocarbon formations.

5.1 Problem definition

5.1.1 Governing wave physics

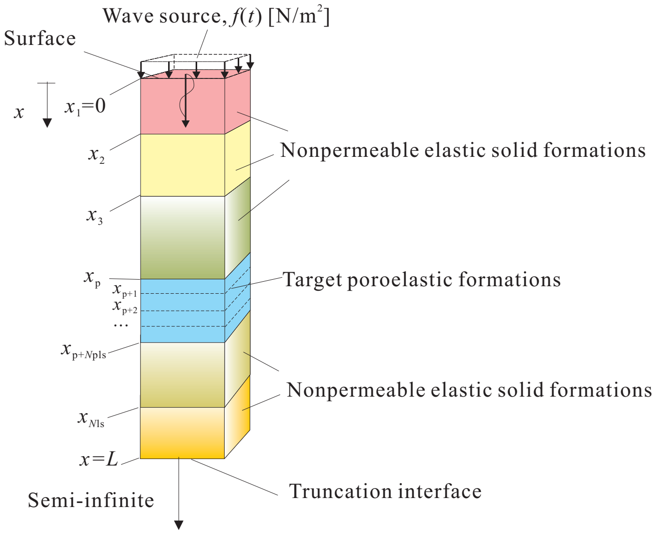

Figure 5.1: Targeted fluid-saturated porous permeable rock formations within a one-dimensional semi-infinite non-permeable elastic solid media system; truncated at depth $x = L$, subjected to a surface excitation.

We consider target fluid-saturated porous permeable (poroelastic) layers that are surrounded by non-permeable elastic solid layers. The semi-infinite extent of the original domain is truncated through the introduction of an absorbing boundary at some depth $x = L$. The propagation of waves within the coupled system ($\Omega = (0, L)$) is governed by the following PDEs (for brevity, the space and time dependency of the variables and coefficients are dropped):

$$\frac{\partial}{\partial x}\left((\lambda + 2\mu)\frac{\partial u_{\text{a}}}{\partial x}\right) - \rho\frac{\partial^2 u_{\text{a}}}{\partial t^2} = 0, \quad x \in (0, x_p) \text{ and } (x_{p+N_{\text{pls}}}, L), \;\; t \in (0, T], \tag{5.1}$$

and

$$\frac{\partial}{\partial x}\left((\lambda+2\mu+\alpha^2 Q)\frac{\partial u_{\mathrm{b}}}{\partial x}+\alpha Q\frac{\partial w}{\partial x}\right)-\rho\frac{\partial^2 u_{\mathrm{b}}}{\partial t^2}-\rho_f\frac{\partial^2 w}{\partial t^2}=0,$$
$$x\in(x_p,x_{p+N_{\mathrm{pls}}}),\quad t\in(0,T], \tag{5.2}$$

$$\frac{\partial}{\partial x}\left(\alpha Q\frac{\partial u_{\mathrm{b}}}{\partial x}+Q\frac{\partial w}{\partial x}\right)-\frac{1}{k}\frac{\partial w}{\partial t}-\rho_f\frac{\partial^2 u_{\mathrm{b}}}{\partial t^2}-\frac{\rho_f}{n}\frac{\partial^2 w}{\partial t^2}=0,$$
$$x\in(x_p,x_{p+N_{\mathrm{pls}}}),\quad t\in(0,T]. \tag{5.3}$$

Equation (5.1) is the equation of motion for a compressional wave in elastic solid layers ($x\in(0,x_p)$ and $(x_{p+N_{\mathrm{pls}}},L)$) in a one-dimensional setting. Equations (5.2) and (5.3) are the generalized Biot's coupled wave equations of fluid-saturated poroelastic layers ($x\in(x_p,x_{p+N_{\mathrm{pls}}})$) also in a one-dimensional setting[1]. (5.2) is the equation of motion for the solid-fluid mixture [73]; (5.3) is the generalized Darcy's law for the dynamic equilibrium of the fluid [73].

In (5.1)–(5.3), x denotes location, and t denotes time; x_i denotes a boundary or an interface atop the i-th layer where x_p and $x_{p+N_{\mathrm{pls}}}$ denote the locations of the two interfaces between the elastic solid layers and the poroelastic layers; the subscript p denotes the layer index of the top poroelastic formation; and the other subscript N_{pls} denotes the total number of poroelastic layers. T denotes the total observation time. $u_{\mathrm{a}}(x,t)$ denotes the displacement of the elastic solid formations; $u_{\mathrm{b}}(x,t)$ denotes the displacement of a

---

[1] The generalized equations of Biot's coupled wave equations [12, 13] in three-dimensional and one-dimensional settings are shown in, respectively, [72, 74] and [73]. The dimensional reduction from the three-dimensional equations to the one-dimensional equations is straightforward.

solid rock matrix of the poroelastic formations; and $w(x,t)$ denotes the relative displacement of pore-fluid motion with respect to the rock matrix. The material parameters, used in (5.1)–(5.3), are defined as follows:

Elastic wave equation (5.1)

- λ: Lamé's first parameter of elastic solid, $\lambda = \frac{\nu E}{(1+\nu)(1-2\nu)}$,
- μ: Shear modulus of elastic solid, $\mu = \frac{E}{2(1+\nu)}$,
- E: Elastic modulus of elastic solid,
- ν: Poisson's ratio of elastic solid,
- ρ: Mass density of elastic solid,

Biot's equations (5.2) and (5.3)

- λ: Lamé's first parameter of solid rock matrix, $\lambda = \frac{\nu E}{(1+\nu)(1-2\nu)}$,
- μ: Shear modulus of solid rock matrix, $\mu = \frac{E}{2(1+\nu)}$,
- E: Elastic modulus of solid rock matrix,
- ν: Poisson's ratio of solid rock matrix,
- ρ: Mass density of fluid-solid mixture, i.e., $\rho = (1-n)\rho_s + n\rho_f$,
- ρ_s: Mass density of solid rock matrix,
- ρ_f: Mass density of pore fluid,
- k: Fluid mobility, i.e., $k = \bar{k}/\eta$ [14],
- $\bar{k}$: Permeability,
- η: Viscosity of pore fluid,
- n: Porosity,
- α: Biot's material parameter, i.e., $\alpha = 1 - \frac{K_D}{K_S}$, where $n \leq \alpha \leq 1$,
- Q: Biot's material parameter, i.e., $\frac{1}{Q} = \frac{n}{K_f} + \frac{\alpha - n}{K_S}$, where $0 < Q \leq \infty$,
- K_S: Bulk modulus of undrained solid rock matrix,

- K_D: Bulk modulus of drained solid rock matrix, i.e., $K_D = \frac{E}{3(1-2\nu)}$,
- K_f: Bulk modulus of pore fluid.

In a fluid-saturated poroelastic medium, the following equation holds:

$$\sigma(x,t) = \sigma'(x,t) - P(x,t), \tag{5.4}$$

where $\sigma(x,t)$ denotes total stress; $\sigma'(x,t)$ denotes effective stress; and $P(x,t)$ denotes pore pressure, where $P(x,t)$ is positive for compression. $\sigma(x,t)$ and $P(x,t)$ are obtained from the displacement fields $u_{\mathrm{b}}(x,t)$ and $w(x,t)$ via the following constitutive equations:

$$\sigma = \left(\lambda + 2\mu + \alpha^2 Q\right)\frac{\partial u_{\mathrm{b}}}{\partial x} + \alpha Q \frac{\partial w}{\partial x}, \tag{5.5a}$$

$$P = -\left(\alpha Q \frac{\partial u_{\mathrm{b}}}{\partial x} + Q\frac{\partial w}{\partial x}\right). \tag{5.5b}$$

In addition, the governing PDEs are subjected to the following boundary and truncation interface conditions:

$$(\lambda(0) + 2\mu(0))\frac{\partial u_{\mathrm{a}}}{\partial x}(0,t) = -f(t), \quad t \in (0,T], \tag{5.6}$$

$$\frac{\partial u_{\mathrm{a}}}{\partial x}(L,t) + \frac{1}{c(L)}\frac{\partial u_{\mathrm{a}}}{\partial t}(L,t) = 0, \quad t \in (0,T]. \tag{5.7}$$

Equation (5.6) is the surface excitation boundary condition; (5.7) is the truncation interface condition with $c = \sqrt{\frac{\lambda+2\mu}{\rho}}$. The governing wave physics also include the following zero initial conditions:

$$\begin{aligned}
&u_{\mathrm{a}}(x,0) = 0, \quad u_{\mathrm{b}}(x,0) = 0, \quad w(x,0) = 0,\\
&\frac{\partial u_{\mathrm{a}}}{\partial t}(x,0) = 0, \quad \frac{\partial u_{\mathrm{b}}}{\partial t}(x,0) = 0, \quad \frac{\partial w}{\partial t}(x,0) = 0, \quad x \in (0,L).
\end{aligned} \tag{5.8}$$

We remark that the elastic wave equation (5.1), as well as Biot's wave equations (5.2) and (5.3) are coupled via the following conditions at the interfaces between the elastic solid layers and the poroelastic layers:

$$\begin{aligned} u_{\mathrm{a}}\big|_{x_i^-} &= u_{\mathrm{b}}\big|_{x_i^+}, \qquad i = p, \\ u_{\mathrm{a}}\big|_{x_i^+} &= u_{\mathrm{b}}\big|_{x_i^-}, \qquad i = (p + N_{\mathrm{pls}}), \end{aligned} \tag{5.9a}$$

$$\begin{aligned} (\lambda + 2\mu)\frac{\partial u_{\mathrm{a}}}{\partial x}\bigg|_{x_i^-} &= (\lambda + 2\mu + \alpha^2 Q)\frac{\partial u_{\mathrm{b}}}{\partial x} + \alpha Q \frac{\partial w}{\partial x}\bigg|_{x_i^+}, \quad i = p, \\ (\lambda + 2\mu)\frac{\partial u_{\mathrm{a}}}{\partial x}\bigg|_{x_i^+} &= (\lambda + 2\mu + \alpha^2 Q)\frac{\partial u_{\mathrm{b}}}{\partial x} + \alpha Q \frac{\partial w}{\partial x}\bigg|_{x_i^-}, \quad i = (p + N_{\mathrm{pls}}), \end{aligned} \tag{5.9b}$$

$$w\big|_{x_i} = 0, \quad i = p \text{ and } (p + N_{\mathrm{pls}}). \tag{5.9c}$$

Equations (5.9a) and (5.9b) are the rock matrix displacement and the total stress interface continuity conditions, respectively. Equation (5.9c) denotes the zero relative displacement of the pore fluid at the interfaces – (5.9c) is tantamount to the zero flux condition, i.e., $\frac{\partial P}{\partial x} = 0$.

Although the aforementioned governing PDEs can accommodate arbitrary heterogeneity of the material parameters, we explicitly consider a multi-layered system. For multi-layered elastic solid media, the following continuity conditions of displacements and tractions at the interfaces between the mutually-adjacent elastic solid layers (i.e., interface indices: $i = (2, \ldots, (p-1))$

and $((p + N_{\mathrm{pls}} + 1), \ldots, N_{\mathrm{ls}}))$ hold:

$$u_{\mathrm{a}}\Big|_{x_i^-} = u_{\mathrm{a}}\Big|_{x_i^+} \quad , \tag{5.10a}$$

$$(\lambda + 2\mu)\frac{\partial u_{\mathrm{a}}}{\partial x}\Big|_{x_i^-} = (\lambda + 2\mu)\frac{\partial u_{\mathrm{a}}}{\partial x}\Big|_{x_i^+} \quad , \tag{5.10b}$$

where N_{ls} denotes the total number of all layers in the system. In addition, the following continuity conditions hold at the interfaces within poroelastic layers (i.e., interface indices: $i = (p + 1), \ldots, (p + N_{\mathrm{pls}} - 1))$:

$$u_{\mathrm{b}}\Big|_{x_i^-} = u_{\mathrm{b}}\Big|_{x_i^+}, \tag{5.11a}$$

$$w\Big|_{x_i^-} = w\Big|_{x_i^+}, \tag{5.11b}$$

$$(\lambda + 2\mu + \alpha^2 Q)\frac{\partial u_{\mathrm{b}}}{\partial x} + \alpha Q \frac{\partial w}{\partial x}\Bigg|_{x_i^-} = (\lambda + 2\mu + \alpha^2 Q)\frac{\partial u_{\mathrm{b}}}{\partial x} + \alpha Q \frac{\partial w}{\partial x}\Bigg|_{x_i^+}, \tag{5.11c}$$

$$\alpha Q \frac{\partial u_{\mathrm{b}}}{\partial x} + Q \frac{\partial w}{\partial x}\Bigg|_{x_i^-} = \alpha Q \frac{\partial u_{\mathrm{b}}}{\partial x} + Q \frac{\partial w}{\partial x}\Bigg|_{x_i^+}, \tag{5.11d}$$

where (5.11a) and (5.11b) denote the continuity of rock matrix displacement and relative displacement of pore fluid, respectively; (5.11c) denotes the continuity of total stress; and (5.11d) denotes the continuity of pore pressure.

5.1.2 Objective functional

We attempt to identify the optimal loading time signal information that maximizes the kinetic energy only[2] in terms of $w(x,t)$ – the relative

---

[2] The kinetic energy of pore fluid at location x and time t is $\frac{\rho_f}{2}\left(\frac{\partial u}{\partial t}(x,t) + \frac{\partial w}{\partial t}(x,t)\right)^2$. Since we are, rather, interested in increasing the relative wave motion of pore fluid, we maximize $\rho_f\left(\frac{\partial w}{\partial t}(x,t)\right)^2$ which is the kinetic energy only in terms of $w(x,t)$, the relative fluid displacement.

displacement of pore fluid with respect to solid rock matrix within poroelastic layers. To this end, we minimize the following objective functional:

$$\mathcal{L} = \frac{1}{\int_{x_p}^{x_{p+N_{\text{pls}}}} \int_0^T \rho_f \left(\frac{\partial w}{\partial t}(x,t)\right)^2 dt dx}. \tag{5.12}$$

Equation (5.12) is the reciprocal form, of which the denominator is the temporal integral of the kinetic energy in terms of $w(x,t)$ that is spatially integrated over the poroelastic layers ($x \in (x_p, x_{p+N_{\text{pls}}})$).

5.2 Mathematical modeling

We discuss a mathematical approach for identifying the discretized force parameters f_i of a loading time signal that minimizes the objective functional (5.12) subjected to the governing wave physics described in (5.1)–(5.11). To tackle such a constrained minimization problem, we construct an augmented functional via the side-imposition of the governing wave physics into the objective functional. The first-order optimality conditions of the augmented functional lead to a triplet of state, adjoint, and control problems.

5.2.1 Augmented functional

We build an augmented functional by side-imposing the governing P-DEs (5.1), (5.2), and (5.3), as well as the associated conditions (5.6) and (5.7) into the objective functional (5.12), by means of Lagrange multipliers[3]

---

[3] In this chapter, λ without any subscript denotes Lamé's first parameter, whereas λ with a subscript denotes a Lagrange multiplier.

($\lambda_{u_{\rm a}}(x,t)$, $\lambda_{u_{\rm b}}(x,t)$, $\lambda_w(x,t)$, $\lambda_0(t)$, and $\lambda_L(t)$) as the following:

$$
\begin{aligned}
\mathcal{A} = \Bigg\{ & \frac{1}{\int_{x_p}^{x_{p+N_{\rm pls}}} \int_0^T \rho_f (\frac{\partial w}{\partial t})^2 dt dx} \\
&+ \int_0^{x_p} \int_0^T \lambda_{u_{\rm a}} \left[\frac{\partial}{\partial x} \left((\lambda + 2\mu) \frac{\partial u_{\rm a}}{\partial x} \right) - \rho \frac{\partial^2 u_{\rm a}}{\partial t^2} \right] dt dx \\
&+ \int_{x_{p+N_{\rm pls}}}^{L} \int_0^T \lambda_{u_{\rm a}} \left[\frac{\partial}{\partial x} \left((\lambda + 2\mu) \frac{\partial u_{\rm a}}{\partial x} \right) - \rho \frac{\partial^2 u_{\rm a}}{\partial t^2} \right] dt dx \\
&+ \int_{x_p}^{x_{p+N_{\rm pls}}} \int_0^T \lambda_{u_{\rm b}} \left[\frac{\partial}{\partial x} \left((\lambda + 2\mu + \alpha^2 Q) \frac{\partial u_{\rm b}}{\partial x} + \alpha Q \frac{\partial w}{\partial x} \right) \right. \\
&\qquad\qquad \left. - \rho \frac{\partial^2 u_{\rm b}}{\partial t^2} - \rho_f \frac{\partial^2 w}{\partial t^2} \right] dt dx \\
&+ \int_{x_p}^{x_{p+N_{\rm pls}}} \int_0^T \lambda_w \left[\frac{\partial}{\partial x} \left(\alpha Q \frac{\partial u_{\rm b}}{\partial x} + Q \frac{\partial w}{\partial x} \right) - \frac{1}{k} \frac{\partial w}{\partial t} - \rho_f \frac{\partial^2 u_{\rm b}}{\partial t^2} - \frac{\rho_f}{n} \frac{\partial^2 w}{\partial t^2} \right] dt dx \\
&+ \int_0^T \lambda_0(t) \left[(\lambda(0) + 2\mu(0)) \frac{\partial u_{\rm a}}{\partial x}(0,t) + f(t) \right] dt \\
&+ \int_0^T \lambda_L(t) (\lambda(L) + 2\mu(L)) \left[\frac{\partial u_{\rm a}}{\partial x}(L,t) + \frac{1}{c} \frac{\partial u_{\rm a}}{\partial t}(L,t) \right] dt \Bigg\}. \qquad (5.13)
\end{aligned}
$$

In (5.13), the initial value conditions (5.8) and the interface conditions (5.9)–(5.11) are implicitly imposed. The dimensions of $\lambda_{u_{\rm a}}, \lambda_{u_{\rm b}}, \lambda_w, \lambda_0$, and λ_L are all identical to each other.

5.2.2 The first-order optimality conditions

To arrive at the minimum of $\mathcal{A}$, the variations of $\mathcal{A}$ with respect to the state variables ($u_{\rm a}$, $u_{\rm b}$, and w), the adjoint variables (or, Lagrange multipliers) ($\lambda_{u_{\rm a}}$, $\lambda_{u_{\rm b}}$, λ_w, λ_0, and λ_L), and the control variable $\xi = f_i$ – the value of a force parameter used for the temporal approximation of a loading signal as in (3.33) – should vanish.

5.2.2.1 The first optimality condition

As the first optimality condition, the variation of $\mathcal{A}$ with respect to $\lambda_{u_{\mathrm{a}}}$, $\lambda_{u_{\mathrm{b}}}$, λ_w, λ_0, and λ_L should vanish for arbitrary variations $\delta\lambda_{u_{\mathrm{a}}}$, $\delta\lambda_{u_{\mathrm{b}}}$, $\delta\lambda_w$, $\delta\lambda_0$, and $\delta\lambda_L$ as the following:

$$\begin{aligned}\delta_{\lambda_{u_{\mathrm{a}}}}\mathcal{A} = &\int_0^{x_p}\int_0^T \delta\lambda_{u_{\mathrm{a}}}\left[\frac{\partial}{\partial x}\left((\lambda+2\mu)\frac{\partial u_{\mathrm{a}}}{\partial x}\right) - \rho\frac{\partial^2 u_{\mathrm{a}}}{\partial t^2}\right] dtdx \\ &+ \int_{x_{p+N_{\mathrm{pls}}}}^{L}\int_0^T \delta\lambda_{u_{\mathrm{a}}}\left[\frac{\partial}{\partial x}\left((\lambda+2\mu)\frac{\partial u_{\mathrm{a}}}{\partial x}\right) - \rho\frac{\partial^2 u_{\mathrm{a}}}{\partial t^2}\right] dtdx = 0, \end{aligned} \tag{5.14a}$$

$$\begin{aligned}\delta_{\lambda_{u_{\mathrm{b}}}}\mathcal{A} = \int_{x_p}^{x_{p+N_{\mathrm{pls}}}}\int_0^T \delta\lambda_{u_{\mathrm{b}}}\Bigg[&\frac{\partial}{\partial x}\left((\lambda+2\mu+\alpha^2 Q)\frac{\partial u_{\mathrm{b}}}{\partial x} + \alpha Q\frac{\partial w}{\partial x}\right) \\ &-\rho\frac{\partial^2 u_{\mathrm{b}}}{\partial t^2} - \rho_f\frac{\partial^2 w}{\partial t^2}\Bigg] dtdx = 0, \end{aligned} \tag{5.14b}$$

$$\begin{aligned}\delta_{\lambda_w}\mathcal{A} = \int_{x_p}^{x_{p+N_{\mathrm{pls}}}}\int_0^T \delta\lambda_w\Bigg[&\frac{\partial}{\partial x}\left(\alpha Q\frac{\partial u_{\mathrm{b}}}{\partial x} + Q\frac{\partial w}{\partial x}\right) \\ &-\frac{1}{k}\frac{\partial w}{\partial t} - \rho_f\frac{\partial^2 u_{\mathrm{b}}}{\partial t^2} - \frac{\rho_f}{n}\frac{\partial^2 w}{\partial t^2}\Bigg] dtdx = 0, \end{aligned} \tag{5.14c}$$

$$\delta_{\lambda_0}\mathcal{A} = \int_0^T \delta\lambda_0\left[(\lambda+2\mu)\frac{\partial u_{\mathrm{a}}}{\partial x}(0,t) + f(t)\right] dt = 0, \tag{5.14d}$$

$$\delta_{\lambda_L}\mathcal{A} = \int_0^T \delta\lambda_L(\lambda+2\mu)\left[\frac{\partial u_{\mathrm{a}}}{\partial x}(L,t) + \frac{1}{c}\frac{\partial u_{\mathrm{a}}}{\partial t}(L,t)\right] dt = 0. \tag{5.14e}$$

For (5.14a)–(5.14e) to vanish for arbitrary variations $\delta\lambda_{u_{\mathrm{a}}}$, $\delta\lambda_{u_{\mathrm{b}}}$, $\delta\lambda_w$, $\delta\lambda_0$, and $\delta\lambda_L$, we must satisfy *the state problem*, which is identical to the governing wave physics described in (5.1)–(5.11).

5.2.2.2 The second optimality condition

The second optimality condition requires the variation of $\mathcal{A}$ with respect to the state variables (u_a, u_b, and w) to vanish, i.e., $\delta_{u_\mathrm{a}}\mathcal{A} + \delta_{u_\mathrm{b}}\mathcal{A} + \delta_w\mathcal{A} = 0$, for arbitrary variations δu_a, δu_b, and δw. Such a vanishing variation recovers *the adjoint problem* (the explicit derivation of the adjoint problem is shown in Appendix D):

The adjoint problem:

$$\begin{aligned}
&\frac{\partial}{\partial x}\left((\lambda+2\mu)\frac{\partial \lambda_{u_\mathrm{a}}}{\partial x}\right) - \rho\frac{\partial^2 \lambda_{u_\mathrm{a}}}{\partial t^2} = 0,\\
&\quad x \in ((0, x_p) \text{ and } (x_{p+N_\mathrm{pls}}, L)), \quad t \in [0, T),
\end{aligned} \tag{5.15}$$

$$\begin{aligned}
&\frac{\partial}{\partial x}\left((\lambda+2\mu+\alpha^2 Q)\frac{\partial \lambda_{u_\mathrm{b}}}{\partial x} + (\alpha Q)\frac{\partial \lambda_w}{\partial x}\right) - \rho\frac{\partial^2 \lambda_{u_\mathrm{b}}}{\partial t^2} - \rho_f\frac{\partial^2 \lambda_w}{\partial t^2} = 0,\\
&\quad x \in (x_p, x_{p+N_\mathrm{pls}}), \quad t \in [0, T),
\end{aligned} \tag{5.16}$$

$$\begin{aligned}
&\frac{\partial}{\partial x}\left(\alpha Q\frac{\partial \lambda_{u_\mathrm{b}}}{\partial x} + Q\frac{\partial \lambda_w}{\partial x}\right) + \frac{1}{k}\frac{\partial \lambda_w}{\partial t} - \rho_f\frac{\partial^2 \lambda_{u_\mathrm{b}}}{\partial t^2} - \frac{\rho_f}{n}\frac{\partial^2 \lambda_w}{\partial t^2} - \mathcal{E}\rho_f\frac{\partial^4 w}{\partial t^4} = 0,\\
&\quad x \in (x_p, x_{p+N_\mathrm{pls}}), \quad t \in [0, T),
\end{aligned} \tag{5.17}$$

where $\mathcal{E}(x)$ is defined as the following:

$$\mathcal{E}(x) = \frac{-2}{\left(\int_{x_p}^{x_{p+N_\mathrm{pls}}}\int_0^T \rho_f[\frac{\partial w}{\partial t}]^2 dt dx\right)^2}. \tag{5.18}$$

The adjoint PDEs (5.15)–(5.17) are subjected to the following boundary and truncation interface conditions:

$$(\lambda(0)+2\mu(0))\frac{\partial \lambda_{u_\mathrm{a}}}{\partial x}(0,t)=0, \quad t\in[0,T), \tag{5.19}$$

$$\frac{\partial \lambda_{u_\mathrm{a}}}{\partial x}(L,t)-\frac{1}{c(L)}\frac{\partial \lambda_{u_\mathrm{a}}(t)}{\partial t}(L,t)=0, \quad t\in[0,T). \tag{5.20}$$

Here, we remark that $\lambda_0(t)$ and $\lambda_L(t)$ are absorbed into $\lambda_{u_\mathrm{a}}(x,t)$, i.e., $\lambda_0(t) = \lambda_{u_\mathrm{a}}(0,t)$ and $\lambda_L(t) = -\lambda_{u_\mathrm{a}}(L,t)$. Similarly to the state problem, the adjoint PDE (5.15) is coupled with the other adjoint PDEs (5.16) and (5.17) via the following conditions at the interfaces between the poroelastic layers and the elastic solid layers:

$$\begin{aligned} \lambda_{u_\mathrm{a}}\Big|_{x_i^-} &= \lambda_{u_\mathrm{b}}\Big|_{x_i^+}, \quad i=p, \\ \lambda_{u_\mathrm{a}}\Big|_{x_i^+} &= \lambda_{u_\mathrm{b}}\Big|_{x_i^-}, \quad i=p+N_\mathrm{pls}, \end{aligned} \tag{5.21a}$$

$$\begin{aligned} (\lambda+2\mu)\frac{\partial \lambda_{u_\mathrm{a}}}{\partial x}\Big|_{x_i^-} &= (\lambda+2\mu+\alpha^2 Q)\frac{\partial \lambda_{u_\mathrm{b}}}{\partial x}+(\alpha Q)\frac{\partial \lambda_w}{\partial x}\Big|_{x_i^+}, \quad i=p, \\ (\lambda+2\mu)\frac{\partial \lambda_{u_\mathrm{a}}}{\partial x}\Big|_{x_i^+} &= (\lambda+2\mu+\alpha^2 Q)\frac{\partial \lambda_{u_\mathrm{b}}}{\partial x}+(\alpha Q)\frac{\partial \lambda_w}{\partial x}\Big|_{x_i^-}, \quad i=p+N_\mathrm{pls}, \end{aligned} \tag{5.21b}$$

$$\lambda_w\Big|_{x_i}=0, \quad i=p \text{ and } p+N_\mathrm{pls}. \tag{5.21c}$$

Equations (5.21a), (5.21b), and (5.21c) replicate, respectively, the rock displacement-continuity ((5.9a)), the total stress-continuity ((5.9b)), and the zero relative-fluid-displacement ((5.9c)) conditions in the state problem; the adjoint problem is also subjected to the following final-value conditions:

$$\lambda_{u_\mathrm{a}}(x,T) = 0, \quad \frac{\partial \lambda_{u_\mathrm{a}}}{\partial t}(x,T) = 0, \quad x \in (0, x_p) \text{ and } (x_{p+N_\mathrm{pls}}, L), \tag{5.22a}$$

$$\frac{\partial \lambda_{u_\mathrm{b}}}{\partial t}(x,T) = \frac{-\mathcal{E}\rho_f}{\rho_f - \frac{\rho}{n}} \frac{\partial w}{\partial t}(x,T), \quad x \in (x_p, x_{p+N\mathrm{pls}}), \tag{5.22b}$$

$$\frac{\partial \lambda_w}{\partial t}(x,T) = \frac{\rho \mathcal{E} \rho_f}{\rho_f \left(\rho_f - \frac{\rho}{n}\right)} \frac{\partial w}{\partial t}(x,T), \quad x \in (x_p, x_{p+N\mathrm{pls}}). \tag{5.22c}$$

In addition, for a multi-layered system, the adjoint problem is subjected to the following continuity conditions at the interfaces between the mutually-neighboring elastic solid layers (i.e, the interface indices: $i = 2, \ldots, (p-1)$ and $(p + N_\mathrm{pls} + 1), \ldots, N_\mathrm{ls}$):

$$\lambda_{u_\mathrm{a}}\Big|_{x_i^-} = \lambda_{u_\mathrm{a}}\Big|_{x_i^+}, \tag{5.23a}$$

$$(\lambda + 2\mu)\frac{\partial \lambda_{u_\mathrm{a}}}{\partial x}\bigg|_{x_i^-} = (\lambda + 2\mu)\frac{\partial \lambda_{u_\mathrm{a}}}{\partial x}\bigg|_{x_i^+}, \tag{5.23b}$$

as well as the following continuity conditions at the interfaces between the mutually-adjacent poroelastic layers (i.e., the interface indices: $i = (p + 1), \ldots, (p + N_\mathrm{pls} - 1)$):

$$\lambda_{u_\mathrm{b}}\Big|_{x_i^-} = \lambda_{u_\mathrm{b}}\Big|_{x_i^+}, \tag{5.24a}$$

$$\lambda_w\Big|_{x_i^-} = \lambda_w\Big|_{x_i^+}, \tag{5.24b}$$

$$(\lambda + 2\mu + \alpha^2 Q)\frac{\partial \lambda_{u_\mathrm{b}}}{\partial x} + \alpha Q \frac{\partial \lambda_w}{\partial x}\bigg|_{x_i^-} = (\lambda + 2\mu + \alpha^2 Q)\frac{\partial \lambda_{u_\mathrm{b}}}{\partial x} + \alpha Q \frac{\partial \lambda_w}{\partial x}\bigg|_{x_i^+}, \tag{5.24c}$$

$$\alpha Q \frac{\partial \lambda_{u_\mathrm{b}}}{\partial x} + Q \frac{\partial \lambda_w}{\partial x}\bigg|_{x_i^-} = \alpha Q \frac{\partial \lambda_{u_\mathrm{b}}}{\partial x} + Q \frac{\partial \lambda_w}{\partial x}\bigg|_{x_i^+}, \tag{5.24d}$$

We remark that the adjoint PDEs include the governing differential operators that are identical to those of the state PDEs while the adjoint problem differs from the state problem with respect to the following points: first, the body force term $\mathcal{E}\rho_f \frac{\partial^4 w}{\partial t^4}$ in (5.17), as well as the final value conditions (5.22) drives the adjoint problem while the state problem is driven by the surface excitation; second, the adjoint problem is a final BVP such that the sign of the time derivative in the truncation condition (5.19) of the adjoint problem is reversed compared with that of the truncation condition (5.7) of the state problem (an initial BVP).

5.2.2.3 The third optimality condition

The variation of $\mathcal{A}$ with respect to the control variable ($\xi = f_i$) should vanish. This leads to the following control equation (the explicit derivation of the control equation is shown in Appendix D):

The control problem:

$$\delta_\xi \mathcal{A}(= \nabla_\xi \mathcal{A}) = \int_0^T \lambda_{u_\mathrm{a}}(0,t) \frac{\partial f(t)}{\partial \xi} dt = 0. \tag{5.25}$$

We remark that $\nabla_\xi \mathcal{A}$ is tantamount to the gradient of the objective functional $\nabla_\xi \mathcal{L}$ because the side-imposed constraints vanish owing to the satisfaction of the state problem.

5.3 Numerical implementation

To arrive at a stationary point of the augmented functional $\mathcal{A}$, we tackle solution of the triplet of the state, adjoint, and control problems by employing a reduced space approach. That is, (a) we first numerically resolve the state problem by using an initially guessed wave source loading time signal; (b) we then numerically solve the adjoint problem by using the state solution; (c) the reduced gradient is, in turn, computed by using the adjoint solution; and (d) we update the control parameters by employing conjugate-gradient(CG) scheme [19, 59] with an inexact line-search method. The numerical optimizer repeats the above procedure, (a)–(d), to iteratively solve for the control parameters that satisfy the vanishing control equation (the detailed procedure is described in Algorithm 1 in chapter 3). In this section, we describe the classic Galerkin finite element approach utilized for addressing the state and adjoint problems.

5.3.1 State problem semi-discrete form

We multiply the elastic wave equation (5.1) by a test function $s(x)$ and integrate over the elastic solid media ($x \in (x_1, x_p)$) that is situated atop the poroelastic layers. Then, integration by parts with respect to x gives rise to the weak form:

$$\int_{x_1}^{x_p} \frac{\partial s}{\partial x}\left((\lambda + 2\mu)\frac{\partial u_{\mathrm{a}}}{\partial x}\right) dx + \int_{x_1}^{x_p} s\rho \frac{\partial^2 u_{\mathrm{a}}}{\partial t^2} dx = s(\lambda + 2\mu)\frac{\partial u_{\mathrm{a}}}{\partial x}\bigg|_{x_p} - sf(t)\big|_{x_1}. \tag{5.26}$$

Similarly, for the elastic solid media ($x \in (x_{p+N_{\text{pls}}}, L)$) that is located below the poroelastic layers, there arises the following weak form:

$$\begin{aligned}
&\int_{x_{p+N_{\text{pls}}}}^{L} \frac{\partial s}{\partial x}\left((\lambda+2\mu)\frac{\partial u_{\text{a}}}{\partial x}\right)dx + \int_{x_{p+N_{\text{pls}}}}^{L} s\rho\frac{\partial^2 u_{\text{a}}}{\partial t^2}dx \\
&= - s\frac{(\lambda+2\mu)}{c}\frac{\partial u_{\text{a}}}{\partial t}\bigg|_{x=L} - s(\lambda+2\mu)\frac{\partial u_{\text{a}}}{\partial x}\bigg|_{x_{p+N_{\text{pls}}}}.
\end{aligned} \tag{5.27}$$

Similarly, by using the test function $s(x)$, we obtain the weak form of the Biot's first equation (5.2) for the poroelastic layers ($x \in (x_p, x_{p+N_{\text{pls}}})$):

$$\begin{aligned}
&\int_{x_p}^{x_{p+N_{\text{pls}}}} \frac{\partial s}{\partial x}\left((\lambda+2\mu+\alpha^2 Q)\frac{\partial u_{\text{b}}}{\partial x} + (\alpha Q)\frac{\partial w}{\partial x}\right)dx \\
&+ \int_{x_p}^{x_{p+N_{\text{pls}}}} s\left(\rho\frac{\partial^2 u_{\text{b}}}{\partial t^2} + \rho_f\frac{\partial^2 w}{\partial t^2}\right)dx \\
&= s\left((\lambda+2\mu+\alpha^2 Q)\frac{\partial u_{\text{b}}}{\partial x} + (\alpha Q)\frac{\partial w}{\partial x}\right)\bigg|_{x_{p+N_{\text{pls}}}} \\
&- s\left((\lambda+2\mu+\alpha^2 Q)\frac{\partial u_{\text{b}}}{\partial x} + (\alpha Q)\frac{\partial w}{\partial x}\right)\bigg|_{x_p}.
\end{aligned} \tag{5.28}$$

We, in turn, obtain the weak form of the Biot's second equation (5.3) by using a test function $v(x)$ as follows:

$$\begin{aligned}
&\int_{x_p}^{x_{p+N_{\text{pls}}}} \frac{\partial v}{\partial x}(\alpha Q)\frac{\partial u_{\text{b}}}{\partial x}dx + \int_{x_p}^{x_{p+N_{\text{pls}}}} \frac{\partial v}{\partial x}Q\frac{\partial w}{\partial x}dx \\
&+ \int_{x_p}^{x_{p+N_{\text{pls}}}} v\left[\frac{1}{k}\frac{\partial w}{\partial t} + \rho_f\frac{\partial^2 u_{\text{b}}}{\partial t^2} + \frac{\rho_f}{n}\frac{\partial^2 w}{\partial t^2}\right]dx = 0.
\end{aligned} \tag{5.29}$$

We then introduce the spatial approximation of the test functions $s(x)$ and $v(x)$, as well as the trial functions $u(x,t)$ and $w(x,t)$ as:

$$\begin{aligned}
&s(x) = \mathbf{s}^T\boldsymbol{\Phi}(x), \quad v(x) = \mathbf{v}^T\boldsymbol{\Psi}(x), \\
&u(x,t) = \boldsymbol{\Phi}^T(x)\mathbf{u}(t), \quad w(x,t) = \boldsymbol{\Psi}^T(x)\mathbf{w}(t),
\end{aligned} \tag{5.30}$$

where $\mathbf{s}$ and $\mathbf{v}$ denote the vectors of nodal solutions of, $s(x)$ and $v(x)$, respectively; $\mathbf{u}(t)$ and $\mathbf{w}(t)$ denote the vectors of nodal solutions of, $u(x,t)$ and $w(x,t)$ at time t, respectively. Here, we remark that, by virtue of the continuity conditions (5.9a), $u_{\mathrm{a}}(x,t)$ and $u_{\mathrm{b}}(x,t)$ are merged into $u(x,t)$. $\mathbf{\Phi}(x)$ and $\mathbf{\Psi}(x)$ are the vectors of shape functions for the spatial approximation of the trial and test functions. Owing to the finite element approximation, the summation of the weak forms (5.26), (5.27), and (5.28) yields the following time-dependent semi-discrete form:

$$\mathbf{K}_{uu}\mathbf{u} + \mathbf{K}_{uw}\mathbf{w} + \mathbf{C}_{uu}\frac{\partial \mathbf{u}}{\partial t} + \mathbf{M}_{uu}\frac{\partial^2 \mathbf{u}}{\partial t^2} + \mathbf{M}_{uw}\frac{\partial^2 \mathbf{w}}{\partial t^2} = \mathbf{F}_u, \tag{5.31}$$

where the specific forms of the matrices are:

$$\begin{aligned}
\mathbf{K}_{uu} &= \int_{x_1}^{x_p} (\lambda + 2\mu)\frac{\partial \mathbf{\Phi}}{\partial x}\frac{\partial \mathbf{\Phi}^T}{\partial x}dx + \int_{x_p}^{x_{p+N\mathrm{pls}}} (\lambda + 2\mu + \alpha^2 Q)\frac{\partial \mathbf{\Phi}}{\partial x}\frac{\partial \mathbf{\Phi}^T}{\partial x}dx \\
&\quad + \int_{x_{p+N\mathrm{pls}}}^{L} (\lambda + 2\mu)\frac{\partial \mathbf{\Phi}}{\partial x}\frac{\partial \mathbf{\Phi}^T}{\partial x}dx, \\
\mathbf{K}_{uw} &= \int_{x_p}^{x_{p+N\mathrm{pls}}} (\alpha Q)\frac{\partial \mathbf{\Phi}}{\partial x}\frac{\partial \mathbf{\Psi}^T}{\partial x}dx, \\
\mathbf{C}_{uu} &= \frac{(\lambda + 2\mu)}{c}\mathbf{\Phi}(L)\mathbf{\Phi}^T(L), \\
\mathbf{M}_{uu} &= \int_0^L \mathbf{\Phi}\rho\mathbf{\Phi}^T dx, \\
\mathbf{M}_{uw} &= \int_{x_p}^{x_{p+N\mathrm{pls}}} \mathbf{\Phi}\rho_f\mathbf{\Psi}^T dx, \\
\mathbf{F}_u &= \mathbf{\Phi}(0)f(t).
\end{aligned} \tag{5.32}$$

Similarly, the weak form (5.29) changes to the following time-dependent discrete form:

$$\mathbf{K}_{wu}\mathbf{u} + \mathbf{K}_{ww}\mathbf{w} + \mathbf{C}_{ww}\frac{\partial \mathbf{w}}{\partial t} + \mathbf{M}_{wu}\frac{\partial^2 \mathbf{u}}{\partial t^2} + \mathbf{M}_{ww}\frac{\partial^2 \mathbf{w}}{\partial t^2} = 0, \tag{5.33}$$

where the specific forms of the matrices are:

$$\begin{aligned}
\mathbf{K}_{wu} &= \int_{x_p}^{x_{p+N\text{pls}}} \frac{\partial \mathbf{\Psi}}{\partial x}(\alpha Q)\frac{\partial \mathbf{\Phi}^T}{\partial x}dx,\\
\mathbf{K}_{ww} &= \int_{x_p}^{x_{p+N\text{pls}}} \frac{\partial \mathbf{\Psi}}{\partial x}Q\frac{\partial \mathbf{\Psi}^T}{\partial x}dx,\\
\mathbf{C}_{ww} &= \int_{x_p}^{x_{p+N\text{pls}}} \mathbf{\Psi}\frac{1}{k}\mathbf{\Psi}^T dx,\\
\mathbf{M}_{wu} &= \int_{x_p}^{x_{p+N\text{pls}}} \mathbf{\Psi}\rho_f\mathbf{\Phi}^T dx,\\
\mathbf{M}_{ww} &= \int_{x_p}^{x_{p+N\text{pls}}} \mathbf{\Psi}\frac{\rho_f}{n}\mathbf{\Psi}^T dx.
\end{aligned} \tag{5.34}$$

Thus, (5.31) and (5.33) lead to the following time-dependent discrete form of the state problem:

$$\mathbf{M}\frac{\partial^2 \mathbf{ST}(t)}{\partial t^2} + \mathbf{C}\frac{\partial \mathbf{ST}(t)}{\partial t} + \mathbf{K}\ \mathbf{ST}(t) = \mathbf{F}_{\text{st}}, \tag{5.35}$$

where

$$\begin{aligned}
\mathbf{M} &= \begin{bmatrix} \mathbf{M}_{uu} & \mathbf{M}_{uw} \\ \mathbf{M}_{wu} & \mathbf{M}_{ww} \end{bmatrix}, \quad \mathbf{C} = \begin{bmatrix} \mathbf{C}_{uu} & \mathbf{0} \\ \mathbf{0} & \mathbf{C}_{ww} \end{bmatrix},\\
\mathbf{K} &= \begin{bmatrix} \mathbf{K}_{uu} & \mathbf{K}_{uw} \\ \mathbf{K}_{wu} & \mathbf{K}_{ww} \end{bmatrix}, \quad \mathbf{ST}(t) = \begin{bmatrix} \mathbf{u}(t) \\ \mathbf{w}(t) \end{bmatrix}, \quad \mathbf{F}_{\text{st}} = \begin{bmatrix} \mathbf{F}_u \\ \mathbf{0} \end{bmatrix}.
\end{aligned} \tag{5.36}$$

5.3.2 Adjoint problem semi-discrete form

Similarly to the state problem, by using the test functions $s(x)$ and $v(x)$, we build the weak forms of the adjoint PDEs as follows. First, the weak forms of the PDE (5.15) for the elastic solid formations ($x \in (x_1, x_p)$ and $(x_{p+N_{\text{pls}}}, L)$) are:

$$\int_{x_1}^{x_p} \frac{\partial s}{\partial x}\left((\lambda+2\mu)\frac{\partial \lambda_{u_{\text{a}}}}{\partial x}\right)dx + \int_{x_1}^{x_p} s\rho\frac{\partial^2 \lambda_{u_{\text{a}}}}{\partial t^2}dx = s(\lambda+2\mu)\frac{\partial \lambda_{u_{\text{a}}}}{\partial x}\bigg|_{x_p}, \tag{5.37a}$$

$$\begin{aligned}&\int_{x_{p+N_{\text{pls}}}}^{L} \frac{\partial s}{\partial x}\left((\lambda+2\mu)\frac{\partial \lambda_{u_{\text{a}}}}{\partial x}\right)dx + \int_{x_{p+N_{\text{pls}}}}^{L} s\rho\frac{\partial^2 \lambda_{u_{\text{a}}}}{\partial t^2}dx \\ &= s\frac{(\lambda+2\mu)}{c}\frac{\partial \lambda_{u_{\text{a}}}}{\partial t}\bigg|_{x=L} - s(\lambda+2\mu)\frac{\partial \lambda_{u_{\text{a}}}}{\partial x}\bigg|_{x_{p+N_{\text{pls}}}}.\end{aligned} \tag{5.37b}$$

Second, the weak form of the PDE (5.16) within the poroelastic formations ($x \in (x_p, x_{p+N_{\text{pls}}})$) is:

$$\begin{aligned}&\int_{x_p}^{x_{p+N_{\text{pls}}}} \frac{\partial s}{\partial x}(\lambda+2\mu+\alpha^2 Q)\frac{\partial \lambda_{u_{\text{b}}}}{\partial x}dx + \int_{x_p}^{x_{p+N_{\text{pls}}}} \frac{\partial s}{\partial x}(\alpha Q)\frac{\partial \lambda_w}{\partial x}dx \\ &\quad + \int_{x_p}^{x_{p+N_{\text{pls}}}} s\left[\rho\frac{\partial^2 \lambda_{u_{\text{b}}}}{\partial t^2} + \rho_f\frac{\partial^2 \lambda_w}{\partial t^2}\right]dx \\ &= s(\lambda+2\mu+\alpha^2 Q)\frac{\partial \lambda_{u_{\text{b}}}}{\partial x} + (\alpha Q)\frac{\partial \lambda_w}{\partial x}\bigg|_{x_{p+N_{\text{pls}}}} \\ &\quad - s(\lambda+2\mu+\alpha^2 Q)\frac{\partial \lambda_{u_{\text{b}}}}{\partial x} + (\alpha Q)\frac{\partial \lambda_w}{\partial x}\bigg|_{x_p},\end{aligned} \tag{5.38}$$

and the weak form of the PDE (5.17) within the poroelastic formations ($x \in (x_p, x_{p+N_{\text{pls}}})$) is:

$$\begin{aligned}&\int_{x_p}^{x_{p+N_{\text{pls}}}} \frac{\partial v}{\partial x}(\alpha Q)\frac{\partial \lambda_{u_{\text{b}}}}{\partial x}dx + \int_{x_p}^{x_{p+N_{\text{pls}}}} \frac{\partial v}{\partial x}Q\frac{\partial \lambda_w}{\partial x}dx \\ &+ \int_{x_p}^{x_{p+N_{\text{pls}}}} v\left[-\frac{\partial \lambda_w}{\partial t}\frac{1}{k} + \rho_f\frac{\partial^2 \lambda_{u_{\text{b}}}}{\partial t^2} + \frac{\rho_f}{n}\frac{\partial^2 \lambda_w}{\partial t^2} + \mathcal{E}\rho_f\frac{\partial^2 w}{\partial t^2}\right]dx = 0.\end{aligned} \tag{5.39}$$

We then introduce the approximation of the test functions $s(x)$ and $v(x)$, as well as trial functions $\lambda_u(x,t)$ and $\lambda_w(x,t)$ as:

$$\begin{aligned} & s(x) = \mathbf{s}^T \boldsymbol{\Phi}(x), \quad v(x) = \mathbf{v}^T \boldsymbol{\Psi}(x), \\ & \lambda_u(x,t) = \boldsymbol{\Phi}^T(x) \boldsymbol{\lambda}_u(t), \quad \lambda_w(x,t) = \boldsymbol{\Psi}^T(x) \boldsymbol{\lambda}_w(t), \end{aligned} \tag{5.40}$$

where, owing to the continuity condition (5.21a), $\lambda_{u_\mathrm{a}}(x,t)$ and $\lambda_{u_\mathrm{b}}(x,t)$ are merged into $\lambda_u(x,t)$. $\boldsymbol{\lambda}_u(t)$ and $\boldsymbol{\lambda}_w(t)$ denotes the vector of the nodal solutions of $\lambda_u(x,t)$ and $\lambda_w(x,t)$, respectively. Then, similarly to the state problem, the weak forms of the adjoint problem change to the following time-dependent discrete form of the adjoint problem:

$$\mathbf{M} \frac{\partial^2 \boldsymbol{\lambda}(t)}{\partial t^2} - \mathbf{C} \frac{\partial \boldsymbol{\lambda}(t)}{\partial t} + \mathbf{K} \; \boldsymbol{\lambda}(t) = \mathbf{F}_{\mathrm{adj}}, \tag{5.41}$$

where the adjoint solution vector $\boldsymbol{\lambda}(t)$ is defined as the following:

$$\boldsymbol{\lambda}(t) = \left[\begin{array}{c} \boldsymbol{\lambda}_u(t) \\ \boldsymbol{\lambda}_w(t) \end{array} \right]. \tag{5.42}$$

The specific forms of the matrices $\mathbf{M}$, $\mathbf{C}$, and $\mathbf{K}$ are already shown in (5.36); the force vector $\mathbf{F}_{\mathrm{adj}}$ is defined as:

$$\mathbf{F}_{\mathrm{adj}} = - \left[\begin{array}{c} \mathbf{0} \\ \mathcal{E} \int_{x_p}^{x_{p+N_{\mathrm{pls}}}} \rho_f \boldsymbol{\Psi} \boldsymbol{\Psi}^T dx \frac{\partial^2 \mathbf{w}}{\partial t^2} \end{array} \right]. \tag{5.43}$$

Time integration

We resolve the semi-discrete forms (5.35) and (5.41) by using the Newmark time integration scheme. Accordingly, the discrete solutions of state and adjoint problems are obtained by solving the following systems of equations.

$$\begin{aligned}
&\left[\mathbf{M}+\mathbf{C}\frac{\Delta t}{2}+\mathbf{K}\frac{(\Delta t)^2}{4}\right]\frac{\partial^2 \mathbf{ST}_{(s+1)}}{\partial t^2}\\
&=\mathbf{F}_{\mathrm{st}(s+1)}-\mathbf{C}\left[\frac{\partial \mathbf{ST}_{(s)}}{\partial t}+\frac{\partial^2 \mathbf{ST}_{(s)}}{\partial t^2}\frac{\Delta t}{2}\right]\\
&\quad-\mathbf{K}\left[\mathbf{ST}_{(s)}+\frac{\partial \mathbf{ST}_{(s)}}{\partial t}(\Delta t)+\frac{\partial^2 \mathbf{ST}_{(s)}}{\partial t^2}\frac{(\Delta t)^2}{4}\right],
\end{aligned} \tag{5.44}$$

$$\begin{aligned}
&\left[\mathbf{M}+\mathbf{C}\frac{\Delta t}{2}+\mathbf{K}\frac{(\Delta t)^2}{4}\right]\frac{\partial^2 \boldsymbol{\lambda}_{(s)}}{\partial t^2}\\
&=\mathbf{F}_{\mathrm{adj}(s)}+\mathbf{C}\left[\frac{\partial \boldsymbol{\lambda}_{(s+1)}}{\partial t}-\frac{\partial^2 \boldsymbol{\lambda}_{(s+1)}}{\partial t^2}\frac{\Delta t}{2}\right]\\
&-\mathbf{K}\left[\boldsymbol{\lambda}_{(s+1)}-\frac{\partial \boldsymbol{\lambda}_{(s+1)}}{\partial t}\Delta t+\frac{\partial^2 \boldsymbol{\lambda}_{(s+1)}}{\partial t^2}\frac{(\Delta t)^2}{4}\right],
\end{aligned} \tag{5.45}$$

where Δt is the time step; (s) and $(s+1)$ denote evaluation of the nodal vectors at the s-th and $(s+1)$-th time steps; and the time-line of the evaluation of solution in (5.45) is reversed with respect to that of (5.44). We remark that the system matrix in (5.44) is identical to that in (5.45) such that only one system matrix inversion is required for addressing both state and adjoint problems per each iteration of updating control parameters. By using the discrete adjoint solution, we evaluate the reduced gradient as follows:

$$\begin{aligned}
\nabla_{(\xi=f_i)}\mathcal{L} &= \int_0^T \lambda_{u_\mathrm{a}}(0,t)\frac{\partial f(t)}{\partial f_i}dt\\
&= \int_0^T \boldsymbol{\Phi}^T(0)\boldsymbol{\lambda}_u(t)\varphi_i(t).
\end{aligned} \tag{5.46}$$

Equation (5.46) provides the search-direction information to the numerical optimizer for updating control parameters.

We have thus far discussed the numerical implementation for solving the state and adjoint problems, as well as evaluating the gradient of the objective functional. We validated the derivation and implementation of the state, adjoint, and control problems by comparing the values of the components of the gradient computed by (5.46) with those of the numerical gradient obtained by the finite difference scheme (per (3.37)); the comparison shows excellent agreement. By using the numerical optimizer, implemented per the above discussion, we conduct the following numerical experiments.

5.4 Numerical results

In this section, we discuss the numerical solution of the forward problem for a multi-layered system in which Biot's wave equations and the elastic wave equation are coupled to each other. We will then show that our numerical optimizer leads to the optimal loading time signal of a wave source that can maximize the kinetic energy in terms of the relative displacement of pore fluid, i.e., $w(x,t)$. Such optimized time signals recover the amplification frequencies in regard to the wave motion of pore fluid.

5.4.1 Forward solution

In this section, we attempt to verify our forward numerical solution of the wave response within a multi-layered system in which Biot's wave equations are coupled with the elastic wave equation (henceforth, a coupled-poroelastic-elastic-layers system).

5.4.1.1 Poroelastic validation study

As the theoretical basis of the validation, we note that, Biot's equations (5.2) and (5.3) reduce to the equation of motion for an elastic solid (5.1), provided that the Biot's material parameter α and porosity n are equal to each other and approach zero together, i.e., $(\alpha = n) \to 0$.

Thus, in order to verify the numerical solution of the coupled-poroelastic-elastic-layers system, we compare (a) the solution of the coupled-poroelastic-elastic-layers system that employs the case of $((\alpha = n) \to 0)$ with (b) the solution of a multi-layered system in which all layers are occupied by elastic solids (henceforth, the all-elastic-solid-layers system). The two systems use the same elastic moduli E, Poisson's ratios ν, and the mass densities ρ_s of all layers for this comparison.

First, we obtain the numerical solution of the truncated four-layered coupled-poroelastic-elastic-layers system, of which the third layer is a poroelastic layer (Fig. 5.2). We use very small values of n and α, i.e., $n = \alpha = 1 \times 10^{-10}$, for the poroelastic layer. We use realistic values – corresponding to a typical hydrocarbon reservoir rock formation – of the other parameters of the poroelastic layer, such as the permeability $\bar{k}$, pore-fluid viscosity η, pore-fluid density ρ_f, and the bulk modulus of pore fluid K_f (see Table 5.1). We use a linear-linear element pair for the approximation of $u(x,t)$ and $w(x,t)$, with an element size of 4m; the total observation time is $T = 10$s, and the time step is $\Delta t = 0.001$s. The modified Ricker pulse loading described in (4.54) is used with a central frequency of $f = 15$Hz.

Next, we obtain the finite element solution of elastic wave response of the all-elastic-solid-layers system of semi-infinite extent, again shown in Fig. 5.2 except that the third layer is replaced by an elastic solid layer. To this end, we use the forward numerical solver implemented per the description in chapter 3. For this elastic wave solution, we use again the same values of E, ν, and ρ_s for each layer shown in Table 5.1. We use isoparametric linear elements with element size 4m; T is 10s, and Δt is 0.001s.

As seen in Figures 5.3 and 5.4, the comparison of the numerical solution of the coupled-poroelastic-elastic-layers system with that of the all-elastic-solid-layers system shows excellent agreement. The truncation interface condition, as well as the displacement-continuity conditions at the interfaces are clearly shown.

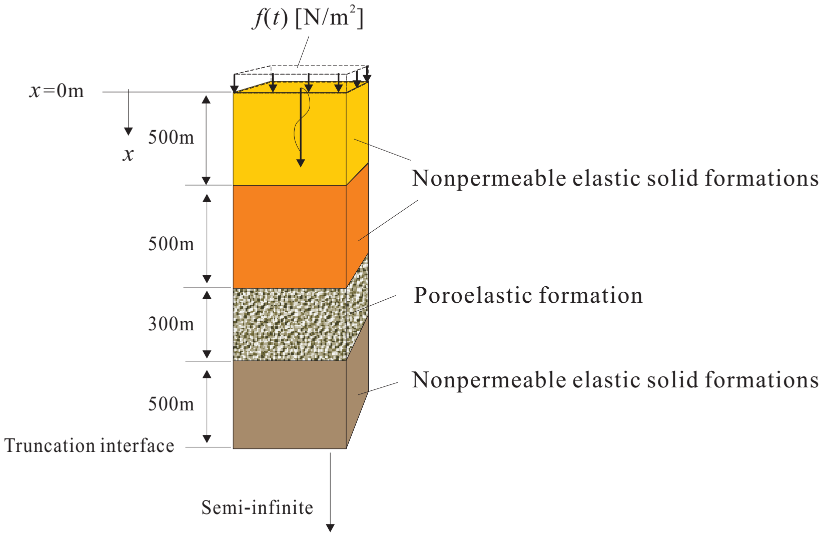

Figure 5.2: Four layered semi-infinite coupled-poroelastic-elastic-layers system truncated at depth $x = 1800$m.

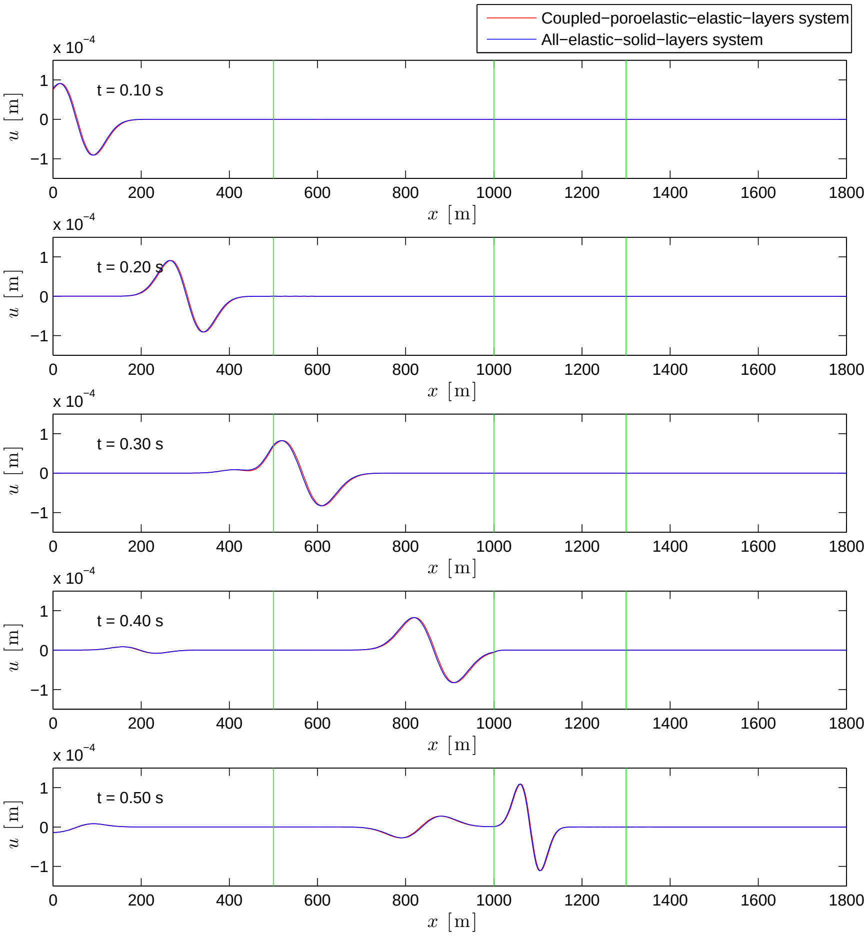

Figure 5.3: Comparison of the numerical solution of $u(x,t)$ of the coupled-poroelastic-elastic-layers system employing $((\alpha = n) \to 0)$ with that of all-elastic-solid-layers system, $0.1\text{s} \le t \le 0.5\text{s}$.

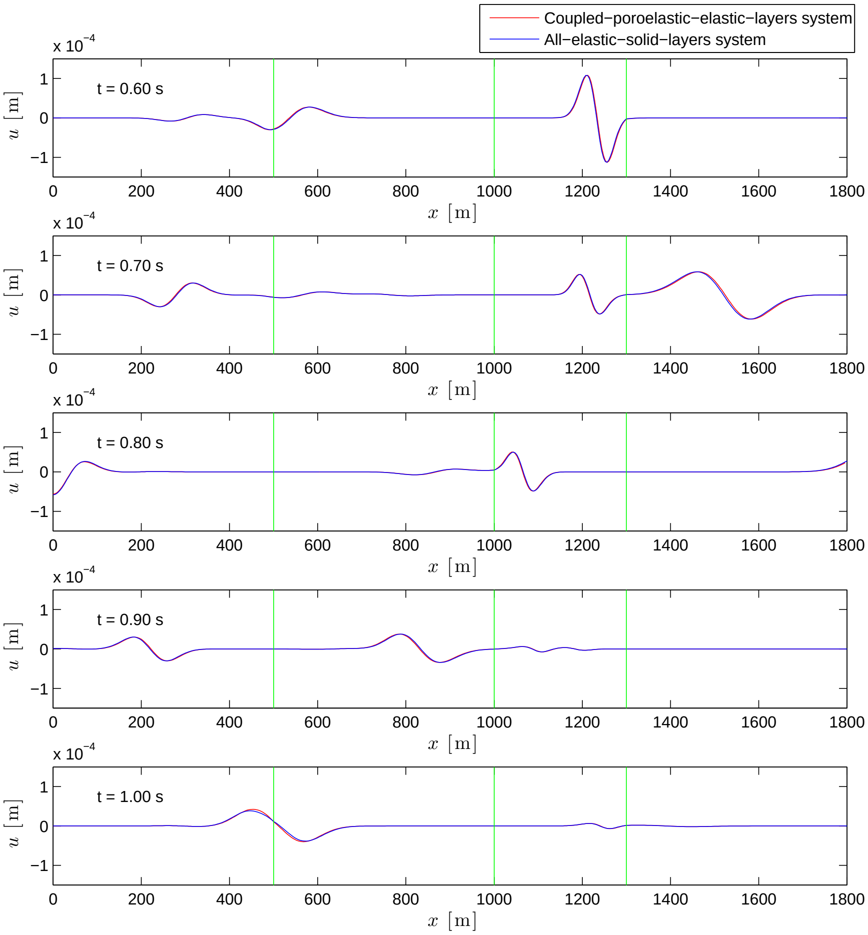

Figure 5.4: Comparison of the numerical solution of $u(x,t)$ of the coupled-poroelastic-elastic-layers system employing $((\alpha = n) \to 0)$ with that of all-elastic-solid-layers system, $0.6\text{s} \leq t \leq 1.0\text{s}$.

	Layer 1	Layer 2	Layer 3 (poroelastic)	Layer 4
Length [m]	500	500	300	500
E [N/m^2]	1.25×10^{10}	1.8×10^{10}	4.5×10^9	3.2×10^{10}
ν	0.0	0.0	0.0	0.0
ρ_s [kg/m^3]	2000	2000	2000	2000
ρ_f [kg/m^3]			860	
n			1.0×10^{-10}	
α			1.0×10^{-10}	
K_D [N/m^2]			1.5×10^9	
K_s [N/m^2]			$K_D/(1-\alpha)$	
K_f [N/m^2]			7.0×10^8	
η [cp]			5	
$\bar{k}$ [md]			100	

Table 5.1: Rock properties of the 4-layered coupled-poroelastic-elastic-layers system: we employ quite small values of $\alpha = n$ in order to replicate the numerical solution of the all-elastic-solid-layers system.

5.4.1.2 Wave response within a fluid-saturated poroelastic layer

Next, we study the wave motion of the rock matrix and the pore fluid within a fluid-saturated poroelastic layer when the values of n and α are realistic. To this end, we solve for the numerical solution of the wave response of the coupled-poroelastic-elastic-layers system, shown in Fig. 5.2, for which the material parameters are described in Table 5.1, except for α =0.667 and $n = 0.3$. We then again compare it with the solution of the all-elastic-solid-layers system to see any distinction between the wave responses of the two different systems.

As seen in Fig. 5.5, the wave speed, corresponding to $u(x,t)$, within the poroelastic third layer of the coupled-poroelastic-elastic-layers system appears to be greater than that of the elastic third layer of the all-elastic-solid-layers system. We argue that this wave behavior is physically correct, as follows.

The theoretical wave speed[4] of the wave motion $u(x,t)$ in the third layer of this coupled-poroelastic-elastic-layers system is $v_{p(\text{poroelastic})}^{(\text{theoretical})} = 1683.7\text{m/s}$, while that[5] in the third layer of the all-elastic-solid-layers system is $v_{p(\text{elastic})}^{(\text{theoretical})}$ $=1500\text{m/s}$. Such theoretical evaluation of the wave speed is nearly consistent with our observation from the numerical solution: the finite element solution, as illustrated in Fig. 5.5, yields $v_{p(\text{poroelastic})}^{(\text{numerical})} = 1666.6\text{m/s}$, which is only 0.97% smaller than the theoretical value (1683.7m/s), as well as $v_{p(\text{elastic})}^{(\text{numerical})} = 1500\text{m/s}$, which is identical to the theoretical value.

Figure 5.6 shows the relative displacement field of the pore-fluid motion $w(x,t)$. We note that the amplitude of $w(x,t)$ is nearly seven orders of magnitude smaller than that of $u(x,t)$. Given such a low fluid mobility ($\bar{k} = 100\text{md}$ and η=5cp), the absolute fluid displacement, i.e., $u(x,t) + w(x,t)$, is almost identical to the rock matrix displacement $u(x,t)$, such that $w(x,t)$ is quite small compared with $u(x,t)$. In addition, Fig. 5.7 shows that the order of magnitude of the amplitude of the pore pressure $P(x,t)$ is as large as that of

---

[4] We use $v_{p(\text{poroelastic})}^{(\text{theoretical})} = \sqrt{\frac{\lambda+2\mu+\alpha^2 Q}{\rho}}$: if there is a high viscosity-coupling (the fluid mobility $k \to 0$) between the solid rock matrix and the pore fluid within a fully-saturated poroelastic layer, there is only one longitudinal wave of the speed, i.e., $v_{p(\text{poroelastic})}^{(\text{theoretical})} = \sqrt{\frac{\lambda+2\mu+\alpha^2 Q}{\rho}}$, within the poroelastic layer [20].

[5] We use $v_{p(\text{elastic})}^{(\text{theoretical})} = \sqrt{\frac{\lambda+2\mu}{\rho}}$.

the total stress field $\sigma(x,t)$ within the poroelastic layer in this example.

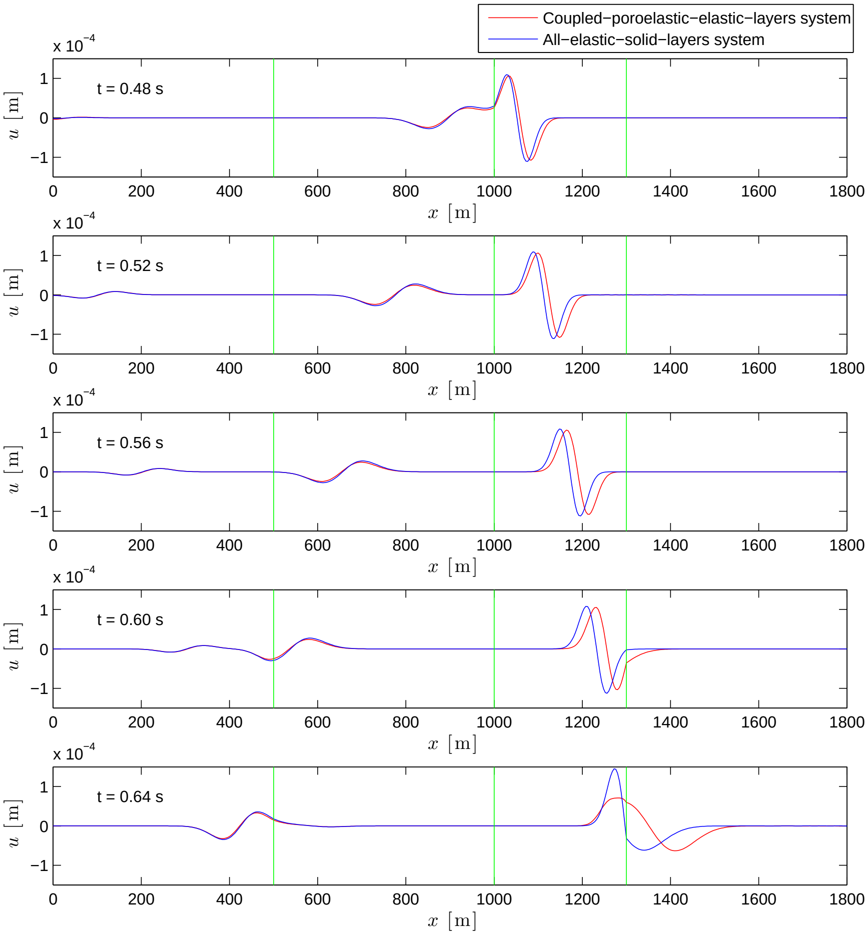

Figure 5.5: Comparison of the numerical solution of $u(x,t)$ of the coupled-poroelastic-elastic-layers system (using $\alpha = 0.667$ and $n = 0.3$) with that of all-elastic-solid-layers system, $0.48\text{s} \leq t \leq 0.64\text{s}$.

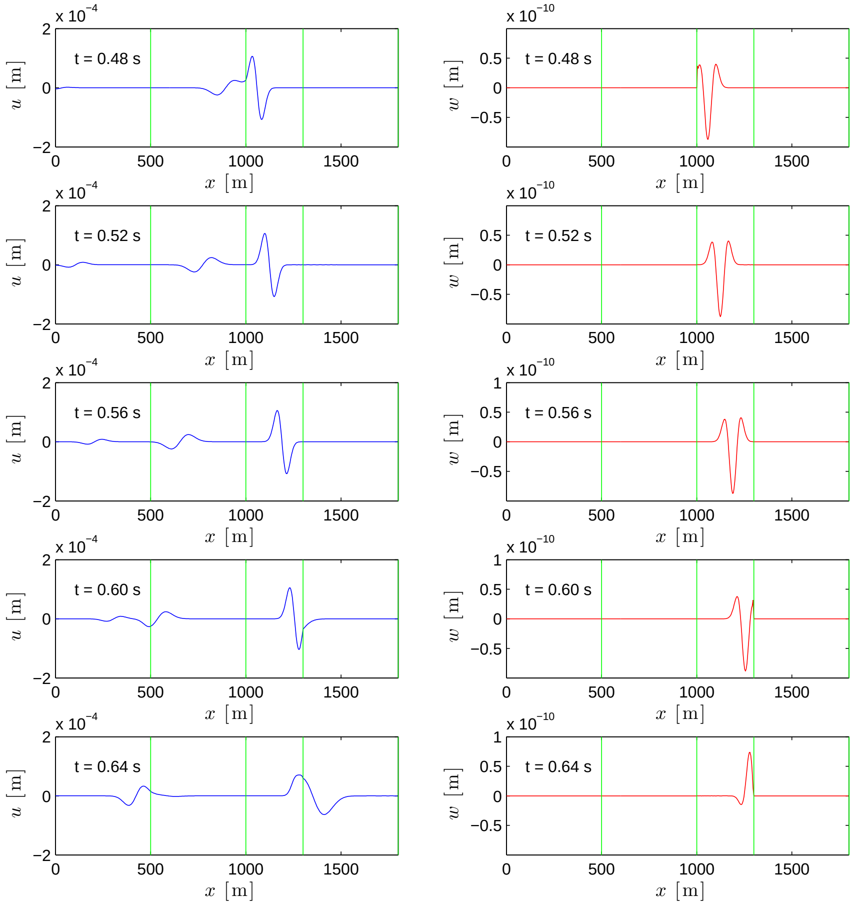

Figure 5.6: The numerical solution of $u(x,t)$ and $w(x,t)$ of the coupled-poroelastic-elastic-layers system employing $\alpha = 0.667$ and $n = 0.3$, $0.48\text{s} \leq t \leq 0.64\text{s}$.

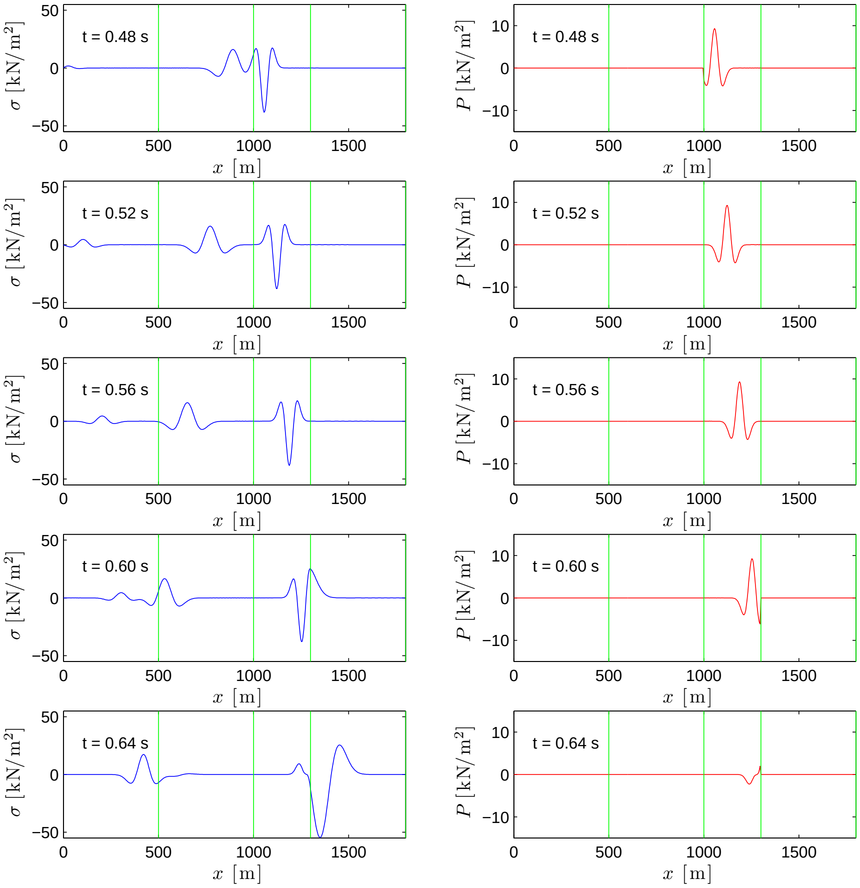

Figure 5.7: The numerical solution of $\sigma(x,t)$ and $P(x,t)$ of the coupled-poroelastic-elastic-layers system employing $\alpha = 0.667$ and $n = 0.3$; $P(x,t)$ is positive for compression.

5.4.2 Wave source optimal signals

In this section, we discuss a numerical example of the identification of the optimal loading time signals of wave sources that maximize the kinetic energy in terms of the relative displacement $w(x, t)$ of pore fluid within target poroelastic formations that are embedded within elastic solid layered system.

To this end, we employ a five-layered subsurface formation model shown in Fig. 5.8: the third layer is the targeted oil-saturated poroelastic formation while the surrounding layers are non-permeable elastic solid formations. The material parameters of the formations are described in Table 5.2.

We minimize (5.12) by using four initially guessed perturbation-like time signals of duration 5s, temporally discretized by using, respectively, 100, 125, 200, and 250 quadratic elements for each numerical experiment. We require that the amplitude of the force parameters does not exceed 50kN/m^2. The total observation time is $T = 5\text{s}$, and the time step for resolving the state and adjoint problems is $\Delta t = 0.001\text{s}$.

Figure 5.9 demonstrates that the optimization procedures using 100, 125, 200, and 250 elements converge in time signals with dominant frequencies, 11.8, 19.0, 27.2, and 42.6Hz, respectively. The recovered frequencies correspond to the strong local minima of the objective functional (5.12) with respect to a frequency f of a harmonic excitation $f(t) = 50 \sin(2\pi f t)\text{kN/m}^2$ (Fig. 5.10). Hence, these optimization experiments display that our numerical optimizer successfully recovers the amplification frequencies of the pore fluid wave motion within targeted poroelastic formations.

Figure 5.11 shows the wave response $\frac{\partial w}{\partial t}$, within the targeted poroelastic formation, induced by the optimized loading shown in Fig. 5.9(d) and a non-optimal sinusoidal loading $f(t) = 50\sin(2\pi ft)\text{kN/m}^2$ with the frequency of $f = 15\text{Hz}$. The amplitude of $\frac{\partial w}{\partial t}$ induced by the optimized loading seems to be 2–3 times greater than that induced by the non-optimal loading.

However, an increased oil recovery rate due to such an oscillatory fluid motion solely induced by the reservoir shaking is difficult to evaluate and yet unknown.

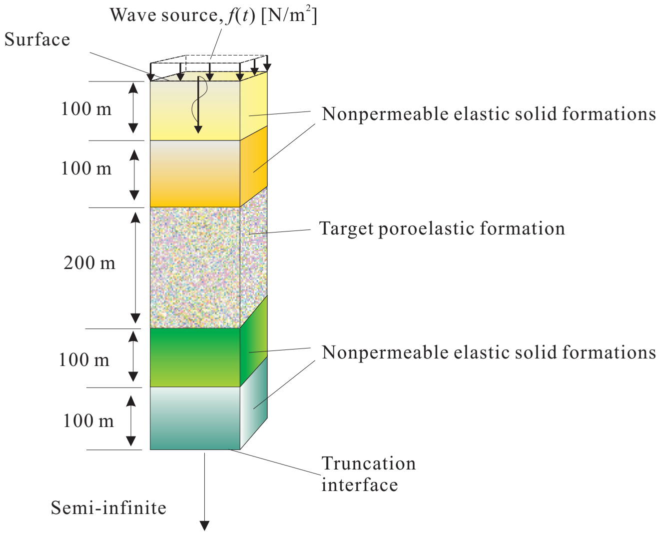

Figure 5.8: A five-layered system of a semi-infinite extent truncated at depth $x = 600$m, with a poroelastic layer surrounded by non-permeable elastic solid layers.

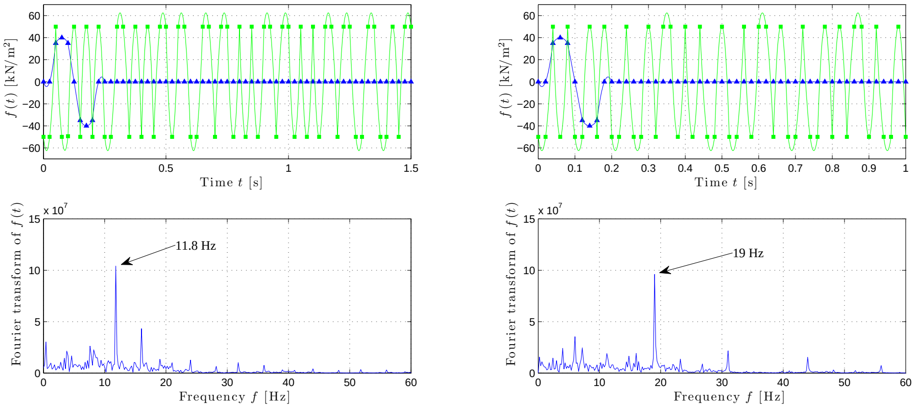

(a) The optimized $f(t)$ discretized by using 100 elements

(b) The optimized $f(t)$ discretized by using 125 elements

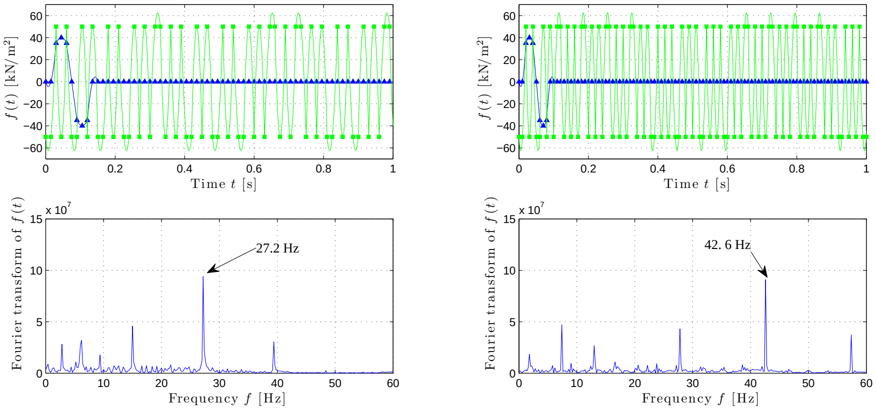

(c) The optimized $f(t)$ discretized by using 200 elements

(d) The optimized $f(t)$ discretized by using 250 elements

Figure 5.9: Close-up views of optimal loading signals that are finally converged via the minimization of (5.12) and the frequency spectra of the optimized loadings.

	Layer 1	Layer 2	Layer 3 (poroelastic)	Layer 4	Layer 5
Length [m]	100	100	200	100	100
E [N/m^2]	4.0×10^9	4.8×10^9	1.0×10^9	5.5×10^9	6.0×10^9
ν	0.2	0.2	0.2	0.2	0.2
ρ_s [kg/m^3]	2000	2000	2000	2000	2000
ρ_f [kg/m^3]			860		
n			0.3		
K_D [N/m^2]			5.6×10^8		
K_s [N/m^2]			8.3×10^8		
K_f [N/m^2]			7.0×10^8		
η [cp]			5		
$\bar{k}$ [md]			100		

Table 5.2: Rock properties of the 5-layered subsurface formation system shown in Fig. 5.8.

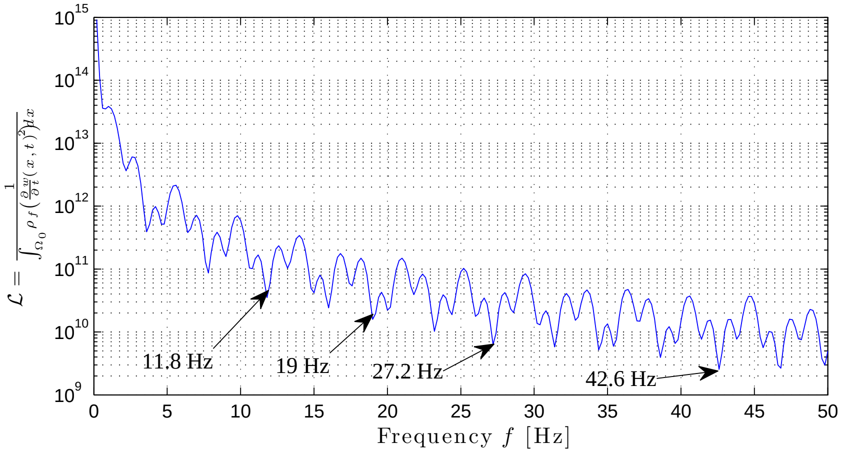

Figure 5.10: The distribution of the objective functional (5.12) with respect to frequencies $f = 0.1$–50Hz for a sinusoidal excitation $f(t) = 50\sin(2\pi f t)$kN/m^2 for the 5-layered subsurface formation model in Fig. 5.8; the optimization experiments recover 11.8, 19.0, 27.2, and 42.6Hz.

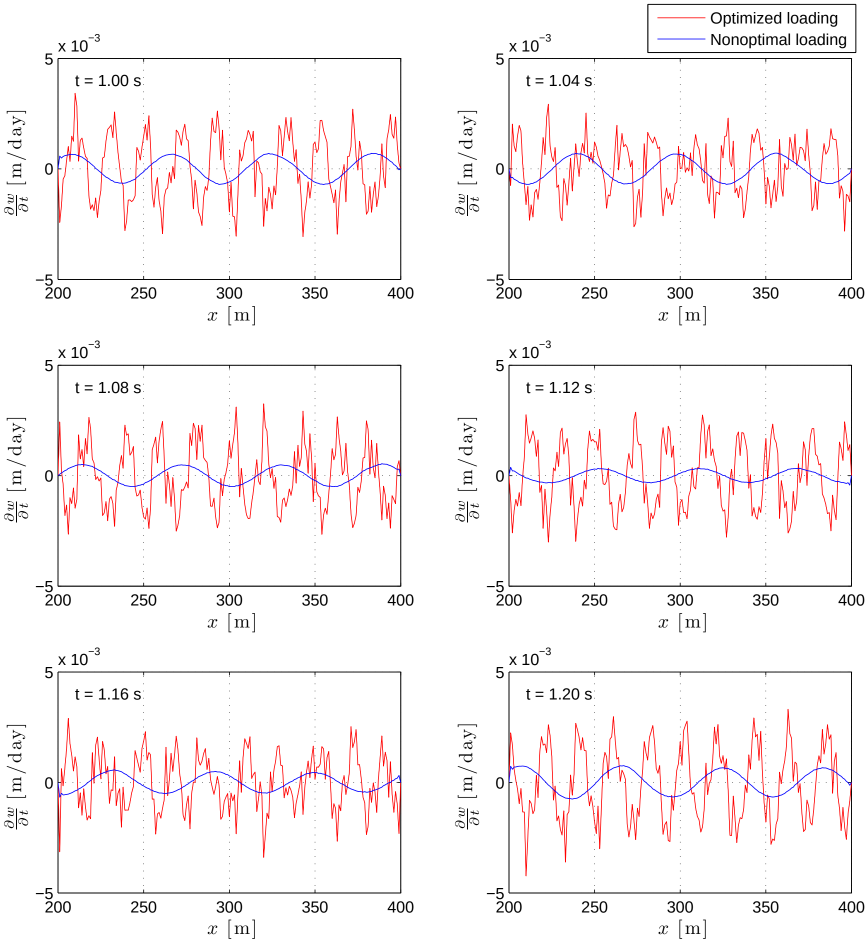

Figure 5.11: The wave responses within the poroelastic formation of the formation model in Fig. 5.8, induced by the optimized load shown in Fig. 5.9(d) and a non-optimal harmonic load $f(t) = 50\sin(2\pi \times 15t)\text{kN/m}^2$.

5.5 Summary

- In this chapter we describe the mathematical and numerical modeling for maximizing pore-fluid wave motion within target poroelastic formations surrounded by non-permeable elastic solid formations of semi-infinite extent. In this setting, Biot's equations coupled with the elastic wave equations govern the wave physics. The Lagrangian functional was built via the side-imposition of the governing wave PDEs system into the reciprocal of the spatial and temporal integral functional of kinetic energy in terms of relative fluid wave motion.

- We solved Biot's equations coupled with the elastic wave equations by means of the classic Galerkin finite element method in order to address the state and adjoint problems as the satisfaction of the first-order optimality conditions. Numerical results showed that our numerical forward solver leads to physically-consistent wave response, and our numerical optimizer results in wave source optimal loading signals with the amplification frequencies corresponding to the relative pore-fluid wave motion.

- We remark that reservoir shaking induces oscillatory pore-fluid motion, such that there is no wave-induced net flow of total pore-fluid in or out of the poroelastic formations. Therefore, the correlation between a wave-induced increased oil recovery rate and the motion of oscillatory fluid is difficult to quantify at this point.

  To connect this missing link, we suggest to consider hysteresis behavior (path dependency of the flow of oil within an oil reservoir, for which permeability varies spatially) to evaluate the amount of remaining oil mobilized from low- to high-permeability areas. That is, in general, the oil/water ratio of the pore fluid moving from low- to high-permeability areas is greater than that of the fluid moving in the opposite direction. Thus, we may approximate the volume of mobilized oil through the cross-flow at the interface between two different areas by temporally and spatially integrating, over the observation time and the area of interface, a fraction of fluid's velocity field only in the direction from low- to high-permeability areas.

Chapter 6

Conclusions

6.1 Summary

The purpose of this dissertation was to explore, via computational modeling, the feasibility of focusing elastic wave energy to target reservoirs to increase oil mobility, and therefore, allow for recovery, where none could previously be possible, and/or increased production rates. To this end, we presented a systematic framework, based on casting the associated mathematical problem as an inverse-source optimization problem. In particular, we were able to demonstrate via numerical experiments that the developed algorithm will robustly find optimal wave source signals that would maximize the kinetic energy, or another desired mobility metric, at the targeted formation.

We have already discussed the conclusions at the end of each of the preceding chapters. In short:

- Wellbore wave sources, by themselves, will not be capable of generating sufficient oil mobility in homogeneous or heterogeneous reservoirs, but stand a better chance in fractured reservoirs, especially if the fluid pumping action is directed at the fractured space.

- Surface wave sources are better suited for increasing oil mobility, under certain conditions and despite the loss of energy due to attenuation (radiation or other) and/or energy concentration at the surface.

- If the wave sources are deployed without regard to optimally placing them, i.e., by a dense grid-based deployment, then it is suggested that the equipment operate at one of the formation's amplification frequencies. As discussed, there is no resonance frequency, in the classic sense. The amplification frequencies of the formation can be found either by a frequency sweep of the forward solution of the associated wave propagation problem, or through the described inverse-source problem. The former is likely to be less expensive computationally, but is limited in other ways (explained earlier and below).

- Though the numerical optimizer arrived in most cases at monochromatic source signals whose frequency was one of the formation's amplification frequencies, the location of the sources is also of importance. We have seen that it is possible to deploy the sources such that transient signals, whose frequency content is not monochromatic, or whose dominant frequency is not one of the formation's amplification frequencies, would result in maximization of the mobility metric. This suggests that optimizing over both location and frequency content is necessary. It is conceivable that constructive wave interference may have a motion amplification effect stronger than that the blind deployment of sources operating at the amplification frequencies.

- We have used the results of previously published research on oil mobility to evaluate whether the motion resulting from the solution of the inverse-source problem could indeed result in oil mobilization. Specifically, we used previously published acceleration threshold values. For most of our simulations we used the kinetic energy as the metric to be maximized, but also produced results where we sought to maximize the acceleration field at the target formation. Under certain conditions (shallow reservoirs), the induced motion meets the acceleration threshold.

6.2 Future research directions

To bridge the gap between the optimal wave source conditions recovered in our numerical problem settings and those for a realistic EOR application, we suggest extending our presented work as follows:

- The procedure, nearly unaltered, could be extended to the all-important three-dimensional case of a deeper reservoir, where a poroelastic targeted inclusion is surrounded by non-permeable rock formations. Various maximization metrics could be equally well accommodated.
- In the presented work, we used the kinetic energy and the acceleration field as maximization metrics, i.e., as indirect mobility metrics. Other metrics should be explored. For example, pressure gradients across the interfaces between low and high permeability areas are also possible, in order to explore the possibility of inducing cross-flow.

- We conjectured that, in addition to the amplitude and frequency content of the loading signals, the location of the wave sources plays a critical role in maximizing the desired metrics within a target reservoir. Thus, studying a new optimization problem that includes the spatial distribution of the wave sources as additional control parameters is of importance.

- Along the same line of thinking, regarding the optimal placement of the wave sources, it would be of interest to explore whether the combination of wellbore, in-reservoir, and surface sources, judiciously triggered, could further illuminate the target formation, and enhance oil mobility.

- The research discussed herein was exclusively focused at the reservoir scale. In fact, the mobility threshold values were obtained from previous research that focused at the ganglion scale. We believe that more studies are necessary at the pore, single ganglion, and ganglion-colony scales to better quantify the mobility thresholds. Once this is accomplished, the process described herein can be used with either the same or improved metrics, and the new mobility thresholds.

Lastly, we remark that the inverse-source problem discussed herein can be used to model other problems where wave focusing is of interest, most notably in medical applications. These include focusing for tumor treatment, and lithotripsy applications.

Appendices

Appendix A

On the first-order optimality conditions in the 1D elastic case

We show the details of the derivation of the first-order optimality conditions shown in chapter 3. The vanishing variation conditions of the augmented functional (3.6) with respect to the state variables ($u(x,t)$), and the control variable ($\xi = f_i$), respectively, lead to the adjoint and control problems as follows.

A.1 The second condition

By applying the variation, taking into account that δu and $\frac{\partial \delta u}{\partial t}$ vanish at $t = 0$, and operating on the first term, (3.9) reduces to:

$$\begin{aligned}\delta_u \mathcal{A} = &-\frac{2\left\{\int_{\Omega_0}\rho\left[\frac{\partial u}{\partial t}\delta u\right]dx\Big|_{t=T} - \int_{\Omega_0}\int_0^T\rho\left[\frac{\partial^2 u}{\partial t^2}\delta u\right]dtdx\right\}}{\left(\int_{\Omega_0}\int_0^T\rho[\frac{\partial u}{\partial t}]^2dtdx\right)^2}\\ &+\int_0^L\int_0^T\lambda\left[\frac{\partial}{\partial x}\left(E\frac{\partial \delta u}{\partial x}\right)-\rho\frac{\partial^2\delta u}{\partial t^2}\right]dtdx\\ &+\int_0^T\lambda_0\left[E\frac{\partial \delta u}{\partial x}\right]dt\Big|_{x=0}+\int_0^T\lambda_L\left[E\frac{\partial\delta u}{\partial x}+\frac{E}{c}\frac{\partial \delta u}{\partial t}\right]dt\Big|_{x=L}=0. \quad \text{(A.1)}\end{aligned}$$

Next, we isolate the second term, whose first component becomes (for a layered medium case):

$$\begin{aligned}
&\int_0^L \int_0^T \lambda \frac{\partial}{\partial x}\left(E\frac{\partial \delta u}{\partial x}\right) dtdx \\
&= \int_0^L \int_0^T \lambda \frac{\partial E}{\partial x}\frac{\partial \delta u}{\partial x} + \lambda E \frac{\partial^2 \delta u}{\partial x^2}\; dtdx \\
&= \sum_{i=1}^{N_{\mathrm{ls}}} \left\{ \int_{x_i^+}^{x_{i+1}^-} \int_0^T \lambda \frac{\partial E}{\partial x}\frac{\partial \delta u}{\partial x} + \lambda E \frac{\partial^2 \delta u}{\partial x^2}\; dtdx \right\} \\
&= \sum_{i=1}^{N_{\mathrm{ls}}} \left\{ \left[\int_0^T \lambda \frac{\partial E}{\partial x}\delta u dt\right]_{x_i^+}^{x_{i+1}^-} - \int_{x_i^+}^{x_{i+1}^-}\int_0^T \frac{\partial}{\partial x}\left(\lambda \frac{\partial E}{\partial x}\right)\delta u\; dtdx \right. \\
&\qquad \left. + \left[\int_0^T \lambda E \frac{\partial \delta u}{\partial x} dt\right]_{x_i^+}^{x_{i+1}^-} - \int_{x_i^+}^{x_{i+1}^-}\int_0^T \frac{\partial}{\partial x}\left(\lambda E\right)\frac{\partial \delta u}{\partial x}\; dtdx \right\}. \qquad \text{(A.2)}
\end{aligned}$$

Equation (A.2) can be rearranged to yield:

$$\begin{aligned}
&\int_0^L \int_0^T \lambda \frac{\partial}{\partial x}\left(E\frac{\partial \delta u}{\partial x}\right) dtdx \\
&= \sum_{i=1}^{N_{\mathrm{ls}}-1} \left\{ \int_0^T \lambda E \frac{\partial \delta u}{\partial x} dt\bigg|_{x=x_{i+1}^-} - \int_0^T \lambda E \frac{\partial \delta u}{\partial x} dt\bigg|_{x=x_{i+1}^+} \right. \\
&\qquad \left. - \int_0^T \left(E\frac{\partial \lambda}{\partial x}\right)\delta u dt\bigg|_{x=x_{i+1}^-} + \int_0^T \left(E\frac{\partial \lambda}{\partial x}\right)\delta u dt\bigg|_{x=x_{i+1}^+} \right\} \\
&\quad - \int_0^T \lambda E \frac{\partial \delta u}{\partial x} dt\bigg|_{x=0} + \int_0^T \lambda E \frac{\partial \delta u}{\partial x} dt\bigg|_{x=L} \\
&\quad + \int_0^T \left(E\frac{\partial \lambda}{\partial x}\right)\delta u dt\bigg|_{x=0} - \int_0^T \left(E\frac{\partial \lambda}{\partial x}\right)\delta u dt\bigg|_{x=L} \\
&\quad + \int_0^L \int_0^T \frac{\partial}{\partial x}\left(\frac{\partial \lambda}{\partial x}E\right)\delta u\; dtdx. \qquad \text{(A.3)}
\end{aligned}$$

Next, the second component of the second term in (A.1), after integration by parts with respect to time, leads to the following:

$$\begin{aligned}
&\int_0^L \int_0^T \lambda\rho \frac{\partial^2 \delta u}{\partial t^2}\, dtdx \\
&= \int_0^L \rho\lambda \frac{\partial \delta u}{\partial t}\, dx\Big|_{t=T} - \int_0^L \rho \frac{\partial \lambda}{\partial t} \delta u \, dx\Big|_{t=T} + \int_0^L \int_0^T \rho \frac{\partial^2 \lambda}{\partial t^2} \delta u \, dtdx. \qquad \text{(A.4)}
\end{aligned}$$

In addition,

$$\int_0^T \lambda_L \frac{E}{c} \frac{\partial \delta u}{\partial t}\, dt\Big|_{x=L} = \lambda_L \frac{E}{c} \delta u\Big|_{x=L,t=T} - \int_0^T \frac{\partial \lambda_L}{\partial t} \frac{E}{c}\, \delta u dt\Big|_{x=L}. \qquad \text{(A.5)}$$

Then, by combining (A.3), (A.4), and (A.5), (A.1) can be rearranged as:

$$\begin{aligned}
\delta_u \mathcal{A} = &\int_0^L \int_0^T \delta u \left[\frac{\partial}{\partial x} \left(\frac{\partial \lambda}{\partial x} E \right) - \rho \frac{\partial^2 \lambda}{\partial t^2} + \mathcal{E}(x) \rho \frac{\partial^2 u}{\partial t^2} \right] dtdx \\
&+ \int_0^L \delta u \left[\rho \frac{\partial \lambda}{\partial t} - \mathcal{E}(x) \rho \frac{\partial u}{\partial t} \right] dx\Big|_{t=T} \\
&- \int_0^L \rho\lambda \frac{\partial \delta u}{\partial t}\, dx\Big|_{t=T} + \lambda_L \frac{E}{c} \delta u\Big|_{x=L,t=T} \\
&- \int_0^T \lambda E \frac{\partial \delta u}{\partial x}\, dt\Big|_{x=0} + \int_0^T \lambda_0 E \frac{\partial \delta u}{\partial x}\, dt\Big|_{x=0} \\
&+ \int_0^T \lambda E \frac{\partial \delta u}{\partial x} dt\Big|_{x=L} + \int_0^T \lambda_L E \frac{\partial \delta u}{\partial x} dt\Big|_{x=L} \\
&+ \int_0^T E \frac{\partial \lambda}{\partial x} \delta u dt\Big|_{x=0} - \int_0^T \left[\frac{\partial \lambda_L}{\partial t} \frac{E}{c} + E \frac{\partial \lambda}{\partial x} \right] \delta u dt\Big|_{x=L} \\
&+ \sum_{i=1}^{N_{\mathrm{ls}}-1} \left\{ \int_0^T \lambda E \frac{\partial \delta u}{\partial x} dt\Big|_{x=x_{i+1}^-} - \int_0^T \lambda E \frac{\partial \delta u}{\partial x} dt\Big|_{x=x_{i+1}^+} \right. \\
&\qquad \left. - \int_0^T E \frac{\partial \lambda}{\partial x} \delta u dt\Big|_{x=x_{i+1}^-} + \int_0^T E \frac{\partial \lambda}{\partial x} \delta u dt\Big|_{x=x_{i+1}^+} \right\} = 0, \qquad \text{(A.6)}
\end{aligned}$$

The variation condition (A.6) vanishes for arbitrary variations δu if the adjoint problem (3.12) is satisfied.

A.2 The third condition

Equation (3.18) reduces to the following:

$$\begin{aligned}\delta_\xi \mathcal{A} = &- \int_0^L \int_0^T E\frac{\partial \lambda}{\partial x}\frac{\partial \dot{u}}{\partial x} + \rho\lambda\frac{\partial^2 \dot{u}}{\partial t^2} + \mathcal{E}(x)\rho\frac{\partial u}{\partial t}\frac{\partial \dot{u}}{\partial t}\, dtdx \\ &- \int_0^L \int_0^T E\frac{\partial \dot{\lambda}}{\partial x}\frac{\partial u}{\partial x} + \rho\dot{\lambda}\frac{\partial^2 u}{\partial t^2}\, dtdx \\ &+ \int_0^T \dot{\lambda}f(t) + \lambda\frac{\partial f(t)}{\partial \xi}\, dt\bigg|_{x=0} \\ &- \int_0^T \dot{\lambda}\frac{E}{c}\frac{\partial u}{\partial t} + \lambda\frac{E}{c}\frac{\partial \dot{u}}{\partial t}\, dt\bigg|_{x=L} = 0, \end{aligned} \tag{A.7}$$

where $(\dot{})$ denotes the derivative of the subtended function with respect to ξ. To further simplify (A.7), we introduce a weak form of the state problem using $\dot{\lambda}$ as the weight function, to obtain:

$$\int_0^L \int_0^T \dot{\lambda}\left\{\frac{\partial}{\partial x}\left(E\frac{\partial u}{\partial x}\right) - \rho\frac{\partial^2 u}{\partial t^2}\right\} dtdx = 0. \tag{A.8}$$

After integration by parts, (A.8) becomes:

$$\int_0^L \int_0^T E\frac{\partial \dot{\lambda}}{\partial x}\frac{\partial u}{\partial x} + \dot{\lambda}\rho\frac{\partial^2 u}{\partial t^2}\, dtdx = \left[\int_0^T \dot{\lambda}E\frac{\partial u}{\partial x}dt\right]_{x=0}^{x=L}. \tag{A.9}$$

Similarly, we introduce a weak form of the adjoint problem with $\dot{u}$ as the weight function to obtain:

$$\int_0^L \int_0^T \dot{u}\left\{\frac{\partial}{\partial x}\left(\frac{\partial \lambda}{\partial x}E\right) - \rho\frac{\partial^2 \lambda}{\partial t^2} + \mathcal{E}(x)\rho\frac{\partial^2 u}{\partial t^2}\right\} dtdx = 0, \tag{A.10}$$

which, after integration by parts, leads to the following:

$$\int_0^L \int_0^T \frac{\partial \dot{u}}{\partial x}\frac{\partial \lambda}{\partial x}E + \rho\frac{\partial^2 \dot{u}}{\partial t^2}\lambda + \frac{\partial \dot{u}}{\partial t}\mathcal{E}(x)\rho\frac{\partial u}{\partial t}\, dtdx = \int_0^T \dot{u}\frac{\partial \lambda}{\partial x}Edt\bigg|_{x=L}. \tag{A.11}$$

Because of (A.9) and (A.11), (A.7) simplifies to the following:

$$\begin{aligned}\delta_\xi \mathcal{A} = & -\left[\int_0^T E\dot{\lambda}\frac{\partial u}{\partial x}dt\right]_{x=0}^{x=L} - \int_0^T E\dot{u}\frac{\partial \lambda}{\partial x}dt\bigg|_{x=L} \\ & + \int_0^T \left[\dot{\lambda}f(t) + \lambda\frac{\partial f(t)}{\partial \xi}\right] dt\bigg|_{x=0} - \int_0^T \left[\dot{\lambda}\frac{E}{c}\frac{\partial u}{\partial t} + \lambda\frac{E}{c}\frac{\partial \dot{u}}{\partial t}\right] dt\bigg|_{x=L}.\end{aligned} \tag{A.12}$$

There also holds:

$$-\left[\int_0^T E\dot{\lambda}\frac{\partial u}{\partial x}dt\right]_{x=0}^{x=L} = \int_0^T \dot{\lambda}\frac{E}{c}\frac{\partial u}{\partial t}dt\bigg|_{x=L} - \int_0^T \dot{\lambda}f(t)dt\bigg|_{x=0}, \tag{A.13}$$

$$-\int_0^T \lambda\frac{E}{c}\frac{\partial \dot{u}}{\partial t}\, dt\bigg|_{x=L} = \int_0^T E\frac{\partial \lambda}{\partial x}\dot{u}\, dt\bigg|_{x=L}, \tag{A.14}$$

and thus, (A.12) reduces finally to the control equation (3.19).

Appendix B

On the first-order optimality conditions in the 2D elastic case

In chapter 4, the vanishing variation conditions of the augmented functional (4.13) with respect to the state variables ($\mathbf{u}_{\mathrm{a}}$, $\mathbf{u}_{\mathrm{b}}$, $\mathbf{S}_{\mathrm{a}}$, and $\mathbf{S}_{\mathrm{b}}$), and the control variable ($\xi = f_{2_i}$), respectively, lead to the adjoint and control problems in the following manner.

B.1 The second condition

The variation of the augmented functional $\mathcal{A}$ with respect to state variables ($\mathbf{u}_{\mathrm{a}}$, $\mathbf{u}_{\mathrm{b}}$, $\mathbf{S}_{\mathrm{a}}$, and $\mathbf{S}_{\mathrm{b}}$) should vanish. Such a variation with respect to the multiple state variables, can be derived as:

$$\delta_{\mathbf{u},\mathbf{S}}\mathcal{A} = \delta_{\mathbf{u}_{\mathrm{a}}}\mathcal{A} + \delta_{\mathbf{u}_{\mathrm{b}}}\mathcal{A} + \delta_{\mathbf{S}_{\mathrm{a}}}\mathcal{A} + \delta_{\mathbf{S}_{\mathrm{b}}}\mathcal{A}. \tag{B.1}$$

We derive $\delta_{\mathbf{u}_\mathrm{a}}\mathcal{A}$, $\delta_{\mathbf{u}_\mathrm{b}}\mathcal{A}$, $\delta_{\mathbf{S}_\mathrm{a}}\mathcal{A}$, and $\delta_{\mathbf{S}_\mathrm{b}}\mathcal{A}$ separately. We first derive $\delta_{\mathbf{u}_\mathrm{a}}\mathcal{A}$. Here, $\delta_{\mathbf{u}_\mathrm{a}}\mathcal{A}$ can be split as: $\delta_{\mathbf{u}_\mathrm{a}}\mathcal{A} = \delta_{u_{\mathrm{a}_1}}\mathcal{A} + \delta_{u_{\mathrm{a}_2}}\mathcal{A}$, and $\delta_{u_{\mathrm{a}_1}}\mathcal{A}$ can be derived as:

$$\begin{aligned}
\delta_{u_{\mathrm{a}_1}}\mathcal{A} =& \frac{-\int_{\Omega_0}\int_0^T 2\rho\left[\frac{\partial u_{\mathrm{a}_1}}{\partial t}\frac{\partial \delta u_{\mathrm{a}_1}}{\partial t}\right] dtd\Omega}{\left(\int_{\Omega_0}\int_0^T \rho\left[\left(\frac{\partial u_{\mathrm{a}_1}}{\partial t}\right)^2 + \left(\frac{\partial u_{\mathrm{a}_2}}{\partial t}\right)^2\right] dtd\Omega\right)^2} \\
& - \int_{\Omega_0}\int_0^T \lambda_{u_{\mathrm{a}_1}}\rho\frac{\partial^2 \delta u_{\mathrm{a}_1}}{\partial t^2} dtd\Omega \\
& - \frac{1}{2}\int_{\Omega_0}\int_0^T \lambda_{S_{\mathrm{a}_{1j}}}\frac{\partial^2 \delta u_{\mathrm{a}_1}}{\partial x_j \partial t} + \lambda_{S_{\mathrm{a}_{i1}}}\frac{\partial^2 \delta u_{\mathrm{a}_1}}{\partial x_i \partial t}\ dtd\Omega,
\end{aligned} \tag{B.2}$$

where the Einstein summation convention is used. From (B.2), integration by parts recovers the following:

$$\begin{aligned}
\delta_{u_{\mathrm{a}_1}}\mathcal{A} =& \frac{-\int_{\Omega_0} 2\rho\frac{\partial u_{\mathrm{a}_1}}{\partial t}\delta u_{\mathrm{a}_1} d\Omega\Big|_{t=T} + \int_{\Omega_0}\int_0^T\left[2\rho\frac{\partial^2 u_{\mathrm{a}_1}}{\partial t^2}\delta u_{\mathrm{a}_1}\right] dtd\Omega}{\left(\int_{\Omega_0}\int_0^T \rho\left[\left(\frac{\partial u_{\mathrm{a}_1}}{\partial t}\right)^2 + \left(\frac{\partial u_{\mathrm{a}_2}}{\partial t}\right)^2\right] dtd\Omega\right)^2} \\
& - \int_{\Omega_0} \lambda_{u_{\mathrm{a}_1}}\rho\frac{\partial \delta u_{\mathrm{a}_1}}{\partial t} d\Omega\Big|_{t=T} + \int_{\Omega_0}\frac{\partial \lambda_{u_{\mathrm{a}_1}}}{\partial t}\rho\delta u_{\mathrm{a}_1} d\Omega\Big|_{t=T} \\
& - \int_{\Omega_0}\int_0^T \frac{\partial^2 \lambda_{u_{\mathrm{a}_1}}}{\partial t^2}\rho\delta u_{\mathrm{a}_1} dtd\Omega \\
& - \frac{1}{2}\left\{\int_{\Omega_0} \lambda_{S_{\mathrm{a}_{1j}}}\frac{\partial \delta u_{\mathrm{a}_1}}{\partial x_j} d\Omega\Big|_{t=T} - \int_{\Omega_0}\int_0^T \frac{\partial \lambda_{S_{\mathrm{a}_{1j}}}}{\partial t}\frac{\partial \delta u_{\mathrm{a}_1}}{\partial x_j} dtd\Omega\right\} \\
& - \frac{1}{2}\left\{\int_{\Omega_0} \lambda_{S_{\mathrm{a}_{i1}}}\frac{\partial \delta u_{\mathrm{a}_1}}{\partial x_i} d\Omega\Big|_{t=T} - \int_{\Omega_0}\int_0^T \frac{\partial \lambda_{S_{\mathrm{a}_{i1}}}}{\partial t}\frac{\partial \delta u_{\mathrm{a}_1}}{\partial x_i} dtd\Omega\right\}.
\end{aligned} \tag{B.3}$$

Similarly, we derive $\delta_{u_{\mathrm{a}_2}}\mathcal{A}$. Then, the summation of $\delta_{u_{\mathrm{a}_1}}\mathcal{A}$ and $\delta_{u_{\mathrm{a}_2}}\mathcal{A}$ yields:

$$\begin{aligned}
&\delta_{\mathbf{u}_{\mathrm{a}}}\mathcal{A} = \delta_{u_{\mathrm{a}_1}}\mathcal{A} + \delta_{u_{\mathrm{a}_2}}\mathcal{A}\\
=&\frac{-\int_{\Omega_0} 2\rho\frac{\partial\mathbf{u}_{\mathrm{a}}}{\partial t}\cdot\delta\mathbf{u}_{\mathrm{a}}d\Omega\Big|_{t=T} + \int_{\Omega_0}\int_0^T\left[2\rho\frac{\partial^2\mathbf{u}_{\mathrm{a}}}{\partial t^2}\cdot\delta\mathbf{u}_{\mathrm{a}}\right]dtd\Omega}{\left(\int_{\Omega_0}\int_0^T\rho\left[\frac{\partial\delta\mathbf{u}_{\mathrm{a}}}{\partial t}\cdot\frac{\partial\delta\mathbf{u}_{\mathrm{a}}}{\partial t}\right]dtd\Omega\right)^2}\\
&-\int_{\Omega_0}\boldsymbol{\lambda}_{u_{\mathrm{a}}}\cdot\rho\frac{\partial\delta\mathbf{u}_{\mathrm{a}}}{\partial t}d\Omega\Big|_{t=T} + \int_{\Omega_0}\frac{\partial\boldsymbol{\lambda}_{u_{\mathrm{a}}}}{\partial t}\cdot\rho\delta\mathbf{u}_{\mathrm{a}}d\Omega\Big|_{t=T}\\
&-\int_{\Omega_0}\int_0^T\frac{\partial^2\boldsymbol{\lambda}_{u_{\mathrm{a}}}}{\partial t^2}\cdot\rho\delta\mathbf{u}_{\mathrm{a}}dtd\Omega\\
&-\frac{1}{2}\left\{\int_{\Omega_0}\boldsymbol{\lambda}_{S_{\mathrm{a}}}:\nabla\delta\mathbf{u}_{\mathrm{a}}d\Omega\Big|_{t=T} - \int_{\Omega_0}\int_0^T\frac{\partial\boldsymbol{\lambda}_{S_{\mathrm{a}}}}{\partial t}:\nabla\delta\mathbf{u}_{\mathrm{a}}dtd\Omega\right\}\\
&-\frac{1}{2}\left\{\int_{\Omega_0}\boldsymbol{\lambda}_{S_{\mathrm{a}}}:\nabla\delta\mathbf{u}_{\mathrm{a}}^T d\Omega\Big|_{t=T} - \int_{\Omega_0}\int_0^T\frac{\partial\boldsymbol{\lambda}_{S_{\mathrm{a}}}}{\partial t}:\nabla\delta\mathbf{u}_{\mathrm{a}}^T dtd\Omega\right\}.
\end{aligned}\tag{B.4}$$

Likewise, $\delta_{\mathbf{u}_{\mathrm{b}}}\mathcal{A}$ is derived as follows:

$$\begin{aligned}
\delta_{\mathbf{u}_{\mathrm{b}}}\mathcal{A} =&\delta_{u_{\mathrm{b}_1}}\mathcal{A} + \delta_{u_{\mathrm{b}_2}}\mathcal{A}\\
=&-\int_{\Omega\backslash\Omega_0}\boldsymbol{\lambda}_{u_{\mathrm{b}}}\cdot\rho a\frac{\partial\delta\mathbf{u}_{\mathrm{b}}}{\partial t}d\Omega\Big|_{t=T} + \int_{\Omega\backslash\Omega_0}\frac{\partial\boldsymbol{\lambda}_{u_{\mathrm{b}}}}{\partial t}\cdot\rho a\delta\mathbf{u}_{\mathrm{b}}d\Omega\Big|_{t=T}\\
&-\int_{\Omega\backslash\Omega_0}\int_0^T\frac{\partial^2\boldsymbol{\lambda}_{u_{\mathrm{b}}}}{\partial t^2}\cdot\rho a\delta\mathbf{u}_{\mathrm{b}}dtd\Omega\\
&-\int_{\Omega\backslash\Omega_0}\boldsymbol{\lambda}_{u_{\mathrm{b}}}\cdot\rho b\delta\mathbf{u}_{\mathrm{b}}d\Omega\Big|_{t=T} + \int_{\Omega\backslash\Omega_0}\int_0^T\frac{\partial\boldsymbol{\lambda}_{u_{\mathrm{b}}}}{\partial t}\cdot\rho b\delta\mathbf{u}_{\mathrm{b}}dtd\Omega\\
&-\int_{\Omega\backslash\Omega_0}\int_0^T\boldsymbol{\lambda}_{u_{\mathrm{b}}}\cdot\rho c\delta\mathbf{u}_{\mathrm{b}}dtd\Omega\\
&-\int_{\Omega\backslash\Omega_0}\int_0^T\boldsymbol{\lambda}_{S_{\mathrm{b}}}:\frac{1}{2}\left[\Lambda_p^T\nabla\delta\mathbf{u}_{\mathrm{b}} + \nabla\delta\mathbf{u}_{\mathrm{b}}^T\Lambda_p\right]dtd\Omega\\
&-\int_{\Omega\backslash\Omega_0}\boldsymbol{\lambda}_{S_{\mathrm{b}}}:\frac{1}{2}\left[\Lambda_e^T\nabla\delta\mathbf{u}_{\mathrm{b}} + \nabla\delta\mathbf{u}_{\mathrm{b}}^T\Lambda_e\right]d\Omega\Big|_{t=T}\\
&+\int_{\Omega\backslash\Omega_0}\int_0^T\frac{\partial\boldsymbol{\lambda}_{S_{\mathrm{b}}}}{\partial t}:\frac{1}{2}\left[\Lambda_e^T\nabla\delta\mathbf{u}_{\mathrm{b}} + \nabla\delta\mathbf{u}_{\mathrm{b}}^T\Lambda_e\right]dtd\Omega,
\end{aligned}\tag{B.5}$$

and we derive $\delta_{\mathbf{S}_\mathrm{a}}\mathcal{A}$:

$$\begin{aligned}\delta_{\mathbf{S}_\mathrm{a}}\mathcal{A} =& \delta_{S_{\mathrm{a}_{11}}}\mathcal{A} + \delta_{S_{\mathrm{a}_{12}}}\mathcal{A} + \delta_{S_{\mathrm{a}_{21}}}\mathcal{A} + \delta_{S_{\mathrm{a}_{22}}}\mathcal{A} = \\ =& \int_{\Omega_0} \boldsymbol{\lambda}_{u_\mathrm{a}} \cdot \mathbf{div}(\delta \mathbf{S}_\mathrm{a}^T) d\Omega \bigg|_{t=T} - \int_{\Omega_0}\int_0^T \frac{\partial \boldsymbol{\lambda}_{u_\mathrm{a}}}{\partial t} \cdot \mathbf{div}(\delta \mathbf{S}_\mathrm{a}^T) dt d\Omega \\ &+ \int_{\Omega_0} \boldsymbol{\lambda}_{S_\mathrm{a}} : \left(\mathcal{D}\left[\frac{\partial \delta \mathbf{S}_\mathrm{a}}{\partial t}\right]\right) dt d\Omega \bigg|_{t=T} - \int_{\Omega_0} \frac{\partial \boldsymbol{\lambda}_{S_\mathrm{a}}}{\partial t} : (\mathcal{D}\left[\delta \mathbf{S}_\mathrm{a}\right]) dt d\Omega \bigg|_{t=T} \\ &+ \int_{\Omega_0}\int_0^T \frac{\partial^2 \boldsymbol{\lambda}_{S_\mathrm{a}}}{\partial t^2} : (\mathcal{D}\left[\delta \mathbf{S}_\mathrm{a}\right]) dt d\Omega, \qquad \text{(B.6)}\end{aligned}$$

as well as $\delta_{\mathbf{S}_\mathrm{b}}\mathcal{A}$:

$$\begin{aligned}
\delta_{\mathbf{S}_\mathrm{b}}\mathcal{A} =& \delta_{S_{\mathrm{b}_{11}}}\mathcal{A} + \delta_{S_{\mathrm{b}_{12}}}\mathcal{A} + \delta_{S_{\mathrm{b}_{21}}}\mathcal{A} + \delta_{S_{\mathrm{b}_{22}}}\mathcal{A} \\
=& \int_{\Omega\setminus\Omega_0} \boldsymbol{\lambda}_{u_\mathrm{b}} \cdot \mathbf{div}\left(\delta\mathbf{S}_\mathrm{b}^T\tilde{\Lambda}_e\right) d\Omega\bigg|_{t=T} \\
&- \int_{\Omega\setminus\Omega_0}\int_0^T \frac{\partial\boldsymbol{\lambda}_{u_\mathrm{b}}}{\partial t} \cdot \mathbf{div}\left(\delta\mathbf{S}_\mathrm{b}^T\tilde{\Lambda}_e\right) dtd\Omega \\
&+ \int_{\Omega\setminus\Omega_0}\int_0^T \boldsymbol{\lambda}_{u_\mathrm{b}} \cdot \mathbf{div}\left(\delta\mathbf{S}_\mathrm{b}^T\tilde{\Lambda}_p\right) dtd\Omega \\
&+ \int_{\Omega\setminus\Omega_0} \boldsymbol{\lambda}_{S_\mathrm{b}} : \left\{\Lambda_e^T\left(\mathcal{D}\left[\frac{\partial\delta\mathbf{S}_\mathrm{b}}{\partial t}\right]\right)\Lambda_e\right\} d\Omega\bigg|_{t=T} \\
&- \int_{\Omega\setminus\Omega_0} \frac{\partial\boldsymbol{\lambda}_{S_\mathrm{b}}}{\partial t} : \left\{\Lambda_e^T\left(\mathcal{D}\left[\delta\mathbf{S}_\mathrm{b}\right]\right)\Lambda_e\right\} d\Omega\bigg|_{t=T} \\
&+ \int_{\Omega\setminus\Omega_0}\int_0^T \frac{\partial^2\boldsymbol{\lambda}_{S_\mathrm{b}}}{\partial t^2} : \left\{\Lambda_e^T\left(\mathcal{D}\left[\delta\mathbf{S}_\mathrm{b}\right]\right)\Lambda_e\right\} dtd\Omega \\
&+ \int_{\Omega\setminus\Omega_0} \boldsymbol{\lambda}_{S_\mathrm{b}} : \left\{\Lambda_e^T\left(\mathcal{D}\left[\delta\mathbf{S}_\mathrm{b}\right]\right)\Lambda_p\right\} d\Omega\bigg|_{t=T} \\
&- \int_{\Omega\setminus\Omega_0}\int_0^T \frac{\partial\boldsymbol{\lambda}_{S_\mathrm{b}}}{\partial t} : \left\{\Lambda_e^T\left(\mathcal{D}\left[\delta\mathbf{S}_\mathrm{b}\right]\right)\Lambda_p\right\} dtd\Omega \\
&+ \int_{\Omega\setminus\Omega_0} \boldsymbol{\lambda}_{S_\mathrm{b}} : \left\{\Lambda_p^T\left(\mathcal{D}\left[\delta\mathbf{S}_\mathrm{b}\right]\right)\Lambda_e\right\} d\Omega\bigg|_{t=T} \\
&- \int_{\Omega\setminus\Omega_0}\int_0^T \frac{\partial\boldsymbol{\lambda}_{S_\mathrm{b}}}{\partial t} : \left\{\Lambda_p^T\left(\mathcal{D}\left[\delta\mathbf{S}_\mathrm{b}\right]\right)\Lambda_e\right\} dtd\Omega \\
&+ \int_{\Omega\setminus\Omega_0}\int_0^T \boldsymbol{\lambda}_{S_\mathrm{b}} : \left\{\Lambda_p^T\left(\mathcal{D}\left[\delta\mathbf{S}_\mathrm{b}\right]\right)\Lambda_p\right\} dtd\Omega \\
&+ \int_{\Gamma_\mathrm{load}} \boldsymbol{\lambda}_\mathrm{F}\delta\mathbf{S}_\mathrm{b}^T\boldsymbol{n}d\Gamma\bigg|_{t=T} - \int_0^T\int_{\Gamma_\mathrm{load}} \frac{\partial\boldsymbol{\lambda}_\mathrm{F}}{\partial t}\delta\mathbf{S}_\mathrm{b}^T\boldsymbol{n}dtd\Gamma. \qquad \text{(B.7)}
\end{aligned}$$

Then, the summation of (B.4), (B.5), (B.6), and (B.7) leads to the following:

$$
\begin{aligned}
\delta_{\mathbf{u},\mathbf{S}}\mathcal{A} =& \delta_{\mathbf{u}_\mathrm{a}}\mathcal{A} + \delta_{\mathbf{u}_\mathrm{b}}\mathcal{A} + \delta_{\mathbf{S}_\mathrm{a}}\mathcal{A} + \delta_{\mathbf{S}_\mathrm{b}}\mathcal{A} \\
=& - \int_{\Omega_0} \mathcal{E}(\boldsymbol{x})\rho\frac{\partial \mathbf{u}_\mathrm{a}}{\partial t} \cdot \delta\mathbf{u}_\mathrm{a} d\Omega\bigg|_{t=T} + \int_{\Omega_0}\int_0^T \mathcal{E}(\boldsymbol{x})\rho\frac{\partial^2 \mathbf{u}_\mathrm{a}}{\partial t^2} \cdot \delta\mathbf{u}_\mathrm{a} dtd\Omega \\
& - \int_{\Omega\backslash\Omega_0} \mathcal{E}(\boldsymbol{x})\rho\frac{\partial \mathbf{u}_\mathrm{b}}{\partial t} \cdot \delta\mathbf{u}_\mathrm{b} d\Omega\bigg|_{t=T} + \int_{\Omega\backslash\Omega_0}\int_0^T \mathcal{E}(\boldsymbol{x})\rho\frac{\partial^2 \mathbf{u}_\mathrm{b}}{\partial t^2} \cdot \delta\mathbf{u}_\mathrm{b} dtd\Omega \\
& - \int_{\Omega_0} \boldsymbol{\lambda}_{u_\mathrm{a}} \cdot \rho\frac{\partial \delta\mathbf{u}_\mathrm{a}}{\partial t} d\Omega\bigg|_{t=T} + \int_{\Omega_0} \frac{\partial \boldsymbol{\lambda}_{u_\mathrm{a}}}{\partial t} \cdot \rho\delta\mathbf{u}_\mathrm{a} d\Omega\bigg|_{t=T} \\
& - \int_{\Omega_0}\int_0^T \frac{\partial^2 \boldsymbol{\lambda}_{u_\mathrm{a}}}{\partial t^2} \cdot \rho\delta\mathbf{u}_\mathrm{a} dtd\Omega \\
& - \frac{1}{2}\left\{\int_{\Omega_0} \boldsymbol{\lambda}_{S_\mathrm{a}} : \nabla\delta\mathbf{u}_\mathrm{a} d\Omega\bigg|_{t=T} - \int_{\Omega_0}\int_0^T \frac{\partial \boldsymbol{\lambda}_{S_\mathrm{a}}}{\partial t} : \nabla\delta\mathbf{u}_\mathrm{a} dtd\Omega\right\} \\
& - \frac{1}{2}\left\{\int_{\Omega_0} \boldsymbol{\lambda}_{S_\mathrm{a}} : \nabla\delta\mathbf{u}_\mathrm{a}^T d\Omega\bigg|_{t=T} - \int_{\Omega_0}\int_0^T \frac{\partial \boldsymbol{\lambda}_{S_\mathrm{a}}}{\partial t} : \nabla\delta\mathbf{u}_\mathrm{a}^T dtd\Omega\right\} \\
& - \int_{\Omega\backslash\Omega_0} \boldsymbol{\lambda}_{u_\mathrm{b}} \cdot \rho a\frac{\partial \delta\mathbf{u}_\mathrm{b}}{\partial t} d\Omega\bigg|_{t=T} + \int_{\Omega\backslash\Omega_0} \frac{\partial \boldsymbol{\lambda}_{u_\mathrm{b}}}{\partial t} \cdot \rho a\delta\mathbf{u}_\mathrm{b} d\Omega\bigg|_{t=T} \\
& - \int_{\Omega\backslash\Omega_0}\int_0^T \frac{\partial^2 \boldsymbol{\lambda}_{u_\mathrm{b}}}{\partial t^2} \cdot \rho a\delta\mathbf{u}_\mathrm{b} dtd\Omega \\
& - \int_{\Omega\backslash\Omega_0} \boldsymbol{\lambda}_{u_\mathrm{b}} \cdot \rho b\delta\mathbf{u}_\mathrm{b} d\Omega\bigg|_{t=T} + \int_{\Omega\backslash\Omega_0}\int_0^T \frac{\partial \boldsymbol{\lambda}_{u_\mathrm{b}}}{\partial t} \cdot \rho b\delta\mathbf{u}_\mathrm{b} dtd\Omega \\
& - \int_{\Omega\backslash\Omega_0}\int_0^T \boldsymbol{\lambda}_{u_\mathrm{b}} \cdot \rho c\delta\mathbf{u}_\mathrm{b} dtd\Omega \\
& - \int_{\Omega\backslash\Omega_0}\int_0^T \boldsymbol{\lambda}_{S_\mathrm{b}} : \frac{1}{2}\left[\Lambda_p^T\nabla\delta\mathbf{u}_\mathrm{b} + \nabla\delta\mathbf{u}_\mathrm{b}^T\Lambda_p\right] dtd\Omega \\
& - \int_{\Omega\backslash\Omega_0} \boldsymbol{\lambda}_{S_\mathrm{b}} : \frac{1}{2}\left[\Lambda_e^T\nabla\delta\mathbf{u}_\mathrm{b} + \nabla\delta\mathbf{u}_\mathrm{b}^T\Lambda_e\right] d\Omega\bigg|_{t=T} \\
& + \int_{\Omega\backslash\Omega_0}\int_0^T \frac{\partial \boldsymbol{\lambda}_{S_\mathrm{b}}}{\partial t} : \frac{1}{2}\left[\Lambda_e^T\nabla\delta\mathbf{u}_\mathrm{b} + \nabla\delta\mathbf{u}_\mathrm{b}^T\Lambda_e\right] dtd\Omega
\end{aligned}
$$

$$
\begin{aligned}
&+\int_{\Omega_0} \boldsymbol{\lambda}_{u_\mathrm{a}} \cdot \mathbf{div}(\delta\mathbf{S}_\mathrm{a}^T)d\Omega\bigg|_{t=T} - \int_{\Omega_0}\int_0^T \frac{\partial\boldsymbol{\lambda}_{u_\mathrm{a}}}{\partial t}\cdot \mathbf{div}(\delta\mathbf{S}_\mathrm{a}^T)dtd\Omega \\
&+\int_{\Omega_0} \boldsymbol{\lambda}_{S_\mathrm{a}} : \left(\mathcal{D}\left[\frac{\partial\delta\mathbf{S}_\mathrm{a}}{\partial t}\right]\right)d\Omega\bigg|_{t=T} - \int_{\Omega_0}\frac{\partial\boldsymbol{\lambda}_{S_\mathrm{a}}}{\partial t} : \left(\mathcal{D}\left[\delta\mathbf{S}_\mathrm{a}\right]\right)d\Omega\bigg|_{t=T} \\
&+\int_{\Omega_0}\int_0^T \frac{\partial^2\boldsymbol{\lambda}_{S_\mathrm{a}}}{\partial t^2} : \left(\mathcal{D}\left[\delta\mathbf{S}_\mathrm{a}\right]\right)dtd\Omega \\
&+\int_{\Omega\backslash\Omega_0} \boldsymbol{\lambda}_{u_\mathrm{b}} \cdot \mathbf{div}\left(\delta\mathbf{S}_\mathrm{b}^T\tilde{\Lambda}_e\right)d\Omega\bigg|_{t=T} \\
&-\int_{\Omega\backslash\Omega_0}\int_0^T \frac{\partial\boldsymbol{\lambda}_{u_\mathrm{b}}}{\partial t}\cdot \mathbf{div}\left(\delta\mathbf{S}_\mathrm{b}^T\tilde{\Lambda}_e\right)dtd\Omega \\
&+\int_{\Omega\backslash\Omega_0}\int_0^T \boldsymbol{\lambda}_{u_\mathrm{b}}\cdot \mathbf{div}\left(\delta\mathbf{S}_\mathrm{b}^T\tilde{\Lambda}_p\right)dtd\Omega \\
&+\int_{\Omega\backslash\Omega_0} \boldsymbol{\lambda}_{S_\mathrm{b}} : \left\{\Lambda_e^T\left(\mathcal{D}\left[\frac{\partial\delta\mathbf{S}_\mathrm{b}}{\partial t}\right]\right)\Lambda_e\right\}d\Omega\bigg|_{t=T} \\
&-\int_{\Omega\backslash\Omega_0} \frac{\partial\boldsymbol{\lambda}_{S_\mathrm{b}}}{\partial t} : \left\{\Lambda_e^T\left(\mathcal{D}\left[\delta\mathbf{S}_\mathrm{b}\right]\right)\Lambda_e\right\}d\Omega\bigg|_{t=T} \\
&+\int_{\Omega\backslash\Omega_0}\int_0^T \frac{\partial^2\boldsymbol{\lambda}_{S_\mathrm{b}}}{\partial t^2} : \left\{\Lambda_e^T\left(\mathcal{D}\left[\delta\mathbf{S}_\mathrm{b}\right]\right)\Lambda_e\right\}dtd\Omega \\
&+\int_{\Omega\backslash\Omega_0} \boldsymbol{\lambda}_{S_\mathrm{b}} : \left\{\Lambda_e^T\left(\mathcal{D}\left[\delta\mathbf{S}_\mathrm{b}\right]\right)\Lambda_p\right\}d\Omega\bigg|_{t=T} \\
&-\int_{\Omega\backslash\Omega_0}\int_0^T \frac{\partial\boldsymbol{\lambda}_{S_\mathrm{b}}}{\partial t} : \left\{\Lambda_e^T\left(\mathcal{D}\left[\delta\mathbf{S}_\mathrm{b}\right]\right)\Lambda_p\right\}dtd\Omega \\
&+\int_{\Omega\backslash\Omega_0} \boldsymbol{\lambda}_{S_\mathrm{b}} : \left\{\Lambda_p^T\left(\mathcal{D}\left[\delta\mathbf{S}_\mathrm{b}\right]\right)\Lambda_e\right\}d\Omega\bigg|_{t=T} \\
&-\int_{\Omega\backslash\Omega_0}\int_0^T \frac{\partial\boldsymbol{\lambda}_{S_\mathrm{b}}}{\partial t} : \left\{\Lambda_p^T\left(\mathcal{D}\left[\delta\mathbf{S}_\mathrm{b}\right]\right)\Lambda_e\right\}dtd\Omega \\
&+\int_{\Omega\backslash\Omega_0}\int_0^T \boldsymbol{\lambda}_{S_\mathrm{b}} : \left\{\Lambda_p^T\left(\mathcal{D}\left[\delta\mathbf{S}_\mathrm{b}\right]\right)\Lambda_p\right\}dtd\Omega \\
&+\int_{\Gamma_\mathrm{load}} \boldsymbol{\lambda}_\mathrm{F}\delta\mathbf{S}_\mathrm{b}^T\boldsymbol{n}dtd\Gamma\bigg|_{t=T} - \int_0^T\int_{\Gamma_\mathrm{load}} \frac{\partial\boldsymbol{\lambda}_\mathrm{F}}{\partial t}\delta\mathbf{S}_\mathrm{b}^T\boldsymbol{n}dtd\Gamma. \qquad \text{(B.8)}
\end{aligned}
$$

Here, (B.8) can be split into two parts as: $\delta_{\mathbf{u},\mathbf{S}}\mathcal{A} = \delta_{\mathbf{u},\mathbf{S}}\mathcal{A}^{(T)} + \delta_{\mathbf{u},\mathbf{S}}\mathcal{A}^{(\int_0^T)}$. $\delta_{\mathbf{u},\mathbf{S}}\mathcal{A}^{(T)}$ denotes the terms that are temporally associated only with time $t = T$; $\delta_{\mathbf{u},\mathbf{S}}\mathcal{A}^{(\int_0^T)}$ denotes the terms that include the temporal integration for (0, T]. Due to the tensor identities (B.35a), (B.35c), and (B.35d), $\delta_{\mathbf{u},\mathbf{S}}\mathcal{A}^{(T)}$ then changes to the following:

$$
\begin{aligned}
&\delta_{\mathbf{u},\mathbf{S}}\mathcal{A}^{(T)} \\
&= \int_{\Omega_0} -\rho\mathcal{E}\frac{\partial \mathbf{u}_{\mathrm{a}}}{\partial t}\cdot\delta\mathbf{u}_{\mathrm{a}} + \frac{\partial \boldsymbol{\lambda}_{u_{\mathrm{a}}}}{\partial t}\cdot\rho\delta\mathbf{u}_{\mathrm{a}}d\Omega\bigg|_{t=T} - \int_{\Omega_0}\boldsymbol{\lambda}_{u_{\mathrm{a}}}\cdot\rho\frac{\partial\delta\mathbf{u}_{\mathrm{a}}}{\partial t}d\Omega\bigg|_{t=T} \\
&- \int_{\Omega_0}\frac{1}{2}\left(\boldsymbol{\lambda}_{S_{\mathrm{a}}} + \boldsymbol{\lambda}_{S_{\mathrm{a}}}^T\right) : \nabla\delta\mathbf{u}_{\mathrm{a}}d\Omega\bigg|_{t=T} \\
&+ \int_{\Omega\setminus\Omega_0}\left(-\rho\mathcal{E}\frac{\partial\mathbf{u}_{\mathrm{b}}}{\partial t} + \frac{\partial\boldsymbol{\lambda}_{u_{\mathrm{b}}}}{\partial t}\rho a - \boldsymbol{\lambda}_{u_{\mathrm{b}}}\rho b\right)\cdot\delta\mathbf{u}_{\mathrm{b}}d\Omega\bigg|_{t=T} \\
&- \int_{\Omega\setminus\Omega_0}\boldsymbol{\lambda}_{u_{\mathrm{b}}}\cdot\rho a\frac{\partial\delta\mathbf{u}_{\mathrm{b}}}{\partial t}d\Omega\bigg|_{t=T} \\
&- \int_{\Omega\setminus\Omega_0}\frac{1}{2}\left(\Lambda_e\boldsymbol{\lambda}_{S_{\mathrm{b}}} + \Lambda_e\boldsymbol{\lambda}_{S_{\mathrm{b}}}^T\right) : \nabla\delta\mathbf{u}_{\mathrm{b}}d\Omega\bigg|_{t=T} + \int_{\Omega_0}\boldsymbol{\lambda}_{u_{\mathrm{a}}}\cdot div(\delta\mathbf{S}_{\mathrm{a}}^T)d\Omega\bigg|_{t=T} \\
&+ \int_{\Omega_0}\boldsymbol{\lambda}_{S_{\mathrm{a}}} : \left(\mathcal{D}\left[\frac{\partial\delta\mathbf{S}_{\mathrm{a}}}{\partial t}\right]\right)d\Omega\bigg|_{t=T} - \int_{\Omega_0}\frac{\partial\boldsymbol{\lambda}_{S_{\mathrm{a}}}}{\partial t} : \left(\mathcal{D}\left[\delta\mathbf{S}_{\mathrm{a}}\right]\right)d\Omega\bigg|_{t=T} \\
&+ \int_{\Omega\setminus\Omega_0}\boldsymbol{\lambda}_{u_{\mathrm{b}}}\cdot\mathbf{div}\left(\delta\mathbf{S}_{\mathrm{b}}^T\tilde{\Lambda}_e\right)d\Omega\bigg|_{t=T} \\
&- \int_{\Omega\setminus\Omega_0}\frac{\partial\boldsymbol{\lambda}_{S_{\mathrm{b}}}}{\partial t} : \left\{\Lambda_e^T\left(\mathcal{D}\left[\delta\mathbf{S}_{\mathrm{b}}\right]\right)\Lambda_e\right\}d\Omega\bigg|_{t=T} \\
&+ \int_{\Omega\setminus\Omega_0}\boldsymbol{\lambda}_{S_{\mathrm{b}}} : \left\{\Lambda_e^T\left(\mathcal{D}\left[\frac{\partial\delta\mathbf{S}_{\mathrm{b}}}{\partial t}\right]\right)\Lambda_e + \Lambda_e^T\left(\mathcal{D}\left[\delta\mathbf{S}_{\mathrm{b}}\right]\right)\Lambda_p\right. \\
&\qquad\qquad \left. + \Lambda_p^T\left(\mathcal{D}\left[\delta\mathbf{S}_{\mathrm{b}}\right]\right)\Lambda_e\right\}d\Omega\bigg|_{t=T} \\
&+ \int_{\Gamma_{\mathrm{load}}}\boldsymbol{\lambda}_{\mathrm{F}}\delta\mathbf{S}_{\mathrm{b}}^T\boldsymbol{n}d\Gamma\bigg|_{t=T} \qquad \text{(B.9)}
\end{aligned}
$$

By virtue of the tensor identities shown in (B.35a), (B.35b), (B.35c), and (B.35d), $\delta_{\mathbf{u},\mathbf{S}}\mathcal{A}^{(\int_0^T)}$ changes to the following:

$$
\begin{aligned}
&\delta_{\mathbf{u},\mathbf{S}}\mathcal{A}^{(\int_0^T)} \\
&\quad= \int_{\Omega_0}\int_0^T \left(\rho\mathcal{E}\frac{\partial^2\mathbf{u}_{\mathrm{a}}}{\partial t^2} - \frac{\partial^2\boldsymbol{\lambda}_{u_{\mathrm{a}}}}{\partial t^2}\rho\right)\cdot\delta\mathbf{u}_{\mathrm{a}} dtd\Omega \\
&\qquad+ \frac{1}{2}\int_{\Omega_0}\int_0^T \frac{\partial\boldsymbol{\lambda}_{S_{\mathrm{a}}}}{\partial t} : \nabla\delta\mathbf{u}_{\mathrm{a}} + \frac{\partial\boldsymbol{\lambda}_{S_{\mathrm{a}}}^T}{\partial t} : \nabla\delta\mathbf{u}_{\mathrm{a}}\; dtd\Omega \\
&\qquad- \int_{\Omega\backslash\Omega_0}\int_0^T \left(\frac{\partial^2\boldsymbol{\lambda}_{u_{\mathrm{b}}}}{\partial t^2}\rho a - \frac{\partial\boldsymbol{\lambda}_{u_{\mathrm{b}}}}{\partial t}\rho b + \boldsymbol{\lambda}_{u_{\mathrm{b}}}\rho c - \rho\mathcal{E}\frac{\partial^2\mathbf{u}_{\mathrm{b}}}{\partial t^2}\right)\cdot\delta\mathbf{u}_{\mathrm{b}} dtd\Omega \\
&\qquad- \int_{\Omega\backslash\Omega_0}\int_0^T \frac{1}{2}\left[\Lambda_p\boldsymbol{\lambda}_{S_{\mathrm{b}}} : \nabla\delta\mathbf{u}_{\mathrm{b}} + \Lambda_p\boldsymbol{\lambda}_{S_{\mathrm{b}}}^T : \nabla\delta\mathbf{u}_{\mathrm{b}}\right] dtd\Omega \\
&\qquad+ \int_{\Omega\backslash\Omega_0}\int_0^T \frac{1}{2}\left[\Lambda_e\frac{\partial\boldsymbol{\lambda}_{S_{\mathrm{b}}}}{\partial t} : \nabla\delta\mathbf{u}_{\mathrm{b}} + \Lambda_e\frac{\partial\boldsymbol{\lambda}_{S_{\mathrm{b}}}^T}{\partial t} : \nabla\delta\mathbf{u}_{\mathrm{b}}\right] dtd\Omega \\
&\qquad- \int_{\Omega_0}\int_0^T \operatorname{div}\left(\delta\mathbf{S}_{\mathrm{a}}\frac{\partial\boldsymbol{\lambda}_{u_{\mathrm{a}}}}{\partial t}\right) - \nabla\frac{\partial\boldsymbol{\lambda}_{u_{\mathrm{a}}}}{\partial t} : \delta\mathbf{S}_{\mathrm{a}}^T\; dtd\Omega \\
&\qquad+ \int_{\Omega_0}\int_0^T \frac{\partial^2\boldsymbol{\lambda}_{S_{\mathrm{a}}}}{\partial t^2} : \left(\mathcal{D}\left[\delta\mathbf{S}_{\mathrm{a}}\right]\right) dtd\Omega - \int_0^T\int_{\Gamma_{\mathrm{load}}} \frac{\partial\boldsymbol{\lambda}_{\mathrm{F}}}{\partial t}\delta\mathbf{S}_{\mathrm{b}}^T\boldsymbol{n} dtd\Gamma \\
&\qquad- \int_{\Omega\backslash\Omega_0}\int_0^T \operatorname{div}\left(\left\{\delta\mathbf{S}_{\mathrm{b}}^T\tilde{\Lambda}_e\right\}^T\frac{\partial\boldsymbol{\lambda}_{u_{\mathrm{b}}}}{\partial t}\right) - \nabla\frac{\partial\boldsymbol{\lambda}_{u_{\mathrm{b}}}}{\partial t} : \delta\mathbf{S}_{\mathrm{b}}^T\tilde{\Lambda}_e\; dtd\Omega \\
&\qquad+ \int_{\Omega\backslash\Omega_0}\int_0^T \operatorname{div}\left(\left\{\delta\mathbf{S}_{\mathrm{b}}^T\tilde{\Lambda}_p\right\}^T\boldsymbol{\lambda}_{u_{\mathrm{b}}}\right) - \nabla\boldsymbol{\lambda}_{u_{\mathrm{b}}} : \delta\mathbf{S}_{\mathrm{b}}^T\tilde{\Lambda}_p\; dtd\Omega \\
&\qquad+ \int_{\Omega\backslash\Omega_0}\int_0^T \frac{\partial^2\boldsymbol{\lambda}_{S_{\mathrm{b}}}}{\partial t^2} : \left\{\Lambda_e^T\left(\mathcal{D}\left[\delta\mathbf{S}_{\mathrm{b}}\right]\right)\Lambda_e\right\} dtd\Omega \\
&\qquad- \int_{\Omega\backslash\Omega_0}\int_0^T \frac{\partial\boldsymbol{\lambda}_{S_{\mathrm{b}}}}{\partial t} : \left\{\Lambda_e^T\left(\mathcal{D}\left[\delta\mathbf{S}_{\mathrm{b}}\right]\right)\Lambda_p\right\} dtd\Omega \\
&\qquad- \int_{\Omega\backslash\Omega_0}\int_0^T \frac{\partial\boldsymbol{\lambda}_{S_{\mathrm{b}}}}{\partial t} : \left\{\Lambda_p^T\left(\mathcal{D}\left[\delta\mathbf{S}_{\mathrm{b}}\right]\right)\Lambda_e\right\} dtd\Omega \\
&\qquad+ \int_{\Omega\backslash\Omega_0}\int_0^T \boldsymbol{\lambda}_{S_{\mathrm{b}}} : \left\{\Lambda_p^T\left(\mathcal{D}\left[\delta\mathbf{S}_{\mathrm{b}}\right]\right)\Lambda_p\right\} dtd\Omega, \qquad \text{(B.10)}
\end{aligned}
$$

where div(·) denotes the divergence operator of a vector. Due to the divergence theorem and the tensor identities (B.35a) and (B.35c), (B.10) changes to the following:

$$
\begin{aligned}
&\delta_{\mathbf{u},\mathbf{S}}\mathcal{A}^{(\int_0^T)} \\
&= \int_{\Omega_0}\int_0^T \left(\rho\mathcal{E}\frac{\partial^2\mathbf{u}_{\mathrm{a}}}{\partial t^2} - \frac{\partial^2\boldsymbol{\lambda}_{u_{\mathrm{a}}}}{\partial t^2}\rho\right)\cdot\delta\mathbf{u}_{\mathrm{a}}dtd\Omega \\
&\quad + \frac{1}{2}\int_{\Omega_0}\int_0^T \left(\frac{\partial\boldsymbol{\lambda}_{S_{\mathrm{a}}}}{\partial t} + \frac{\partial\boldsymbol{\lambda}_{S_{\mathrm{a}}}^T}{\partial t}\right) : \nabla\delta\mathbf{u}_{\mathrm{a}}dtd\Omega \\
&\quad - \int_{\Omega\setminus\Omega_0}\int_0^T \left(\frac{\partial^2\boldsymbol{\lambda}_{u_{\mathrm{b}}}}{\partial t^2}\rho a - \frac{\partial\boldsymbol{\lambda}_{u_{\mathrm{b}}}}{\partial t}\rho b + \boldsymbol{\lambda}_{u_{\mathrm{b}}}\rho c - \rho\mathcal{E}\frac{\partial^2\mathbf{u}_{\mathrm{b}}}{\partial t^2}\right)\cdot\delta\mathbf{u}_{\mathrm{b}}dtd\Omega \\
&\quad + \int_{\Omega\setminus\Omega_0}\int_0^T \frac{1}{2}\left[-\Lambda_p\boldsymbol{\lambda}_{S_{\mathrm{b}}} - \Lambda_p\boldsymbol{\lambda}_{S_{\mathrm{b}}}^T + \Lambda_e\frac{\partial\boldsymbol{\lambda}_{S_{\mathrm{b}}}}{\partial t} + \Lambda_e\frac{\partial\boldsymbol{\lambda}_{S_{\mathrm{b}}}^T}{\partial t}\right] : \nabla\delta\mathbf{u}_{\mathrm{b}}dtd\Omega \\
&\quad - \int_{\Gamma_{\mathrm{int}}}\int_0^T \left(\delta\mathbf{S}_{\mathrm{a}}\frac{\partial\boldsymbol{\lambda}_{u_{\mathrm{a}}}}{\partial t}\right)\cdot -\boldsymbol{n}dtd\Gamma + \int_{\Omega_0}\int_0^T \left(\nabla\frac{\partial\boldsymbol{\lambda}_{u_{\mathrm{a}}}}{\partial t}\right)^T : \delta\mathbf{S}_{\mathrm{a}}dtd\Omega \\
&\quad + \int_{\Omega_0}\int_0^T \frac{\partial^2\boldsymbol{\lambda}_{S_{\mathrm{a}}}}{\partial t^2} : (\mathcal{D}\left[\delta\mathbf{S}_{\mathrm{a}}\right])dtd\Omega \\
&\quad - \int_{\Gamma_{\mathrm{free}}+\Gamma_{\mathrm{fixed}}+\Gamma_{\mathrm{int}}}\int_0^T \left(\left\{\delta\mathbf{S}_{\mathrm{b}}^T\tilde{\Lambda}_e\right\}^T\frac{\partial\boldsymbol{\lambda}_{u_{\mathrm{b}}}}{\partial t}\right)\cdot\boldsymbol{n}dtd\Gamma \\
&\quad + \int_{\Gamma_{\mathrm{free}}+\Gamma_{\mathrm{fixed}}+\Gamma_{\mathrm{int}}}\int_0^T \left(\left\{\delta\mathbf{S}_{\mathrm{b}}^T\tilde{\Lambda}_p\right\}^T\boldsymbol{\lambda}_{u_{\mathrm{b}}}\right)\cdot\boldsymbol{n}dtd\Gamma \\
&\quad + \int_{\Omega\setminus\Omega_0}\int_0^T \tilde{\Lambda}_e\left(\nabla\frac{\partial\boldsymbol{\lambda}_{u_{\mathrm{b}}}}{\partial t}\right)^T : \delta\mathbf{S}_{\mathrm{b}}dtd\Omega \\
&\quad - \int_{\Omega\setminus\Omega_0}\int_0^T \tilde{\Lambda}_p\left(\nabla\boldsymbol{\lambda}_{u_{\mathrm{b}}}\right)^T : \delta\mathbf{S}_{\mathrm{b}}dtd\Omega \\
&\quad + \int_{\Omega\setminus\Omega_0}\int_0^T \frac{\partial^2\boldsymbol{\lambda}_{S_{\mathrm{b}}}}{\partial t^2} : \left\{\Lambda_e^T\left(\mathcal{D}\left[\delta\mathbf{S}_{\mathrm{b}}\right]\right)\Lambda_e\right\}dtd\Omega \\
&\quad - \int_{\Omega\setminus\Omega_0}\int_0^T \frac{\partial\boldsymbol{\lambda}_{S_{\mathrm{b}}}}{\partial t} : \left\{\Lambda_e^T\left(\mathcal{D}\left[\delta\mathbf{S}_{\mathrm{b}}\right]\right)\Lambda_p\right\}dtd\Omega
\end{aligned}
$$

$$
\begin{aligned}
&-\int_{\Omega\backslash\Omega_0}\int_0^T \frac{\partial \boldsymbol{\lambda}_{S_\mathrm{b}}}{\partial t} : \left\{\Lambda_p^T\left(\mathcal{D}\left[\delta\mathbf{S}_\mathrm{b}\right]\right)\Lambda_e\right\} dtd\Omega \\
&+\int_{\Omega\backslash\Omega_0}\int_0^T \boldsymbol{\lambda}_{S_\mathrm{b}} : \left\{\Lambda_p^T\left(\mathcal{D}\left[\delta\mathbf{S}_\mathrm{b}\right]\right)\Lambda_p\right\} dtd\Omega - \int_{\Gamma_\mathrm{load}}\int_0^T \frac{\partial \boldsymbol{\lambda}_\mathrm{F}}{\partial t}\delta\mathbf{S}_\mathrm{b}^T\boldsymbol{n}\,dtd\Gamma.
\end{aligned}
\tag{B.11}
$$

Because of (B.36a) and (B.36b), (B.11) becomes:

$$
\begin{aligned}
&\delta_{\mathbf{u},\mathbf{S}}\mathcal{A}^{(\int_0^T)} \\
&\quad= \int_{\Omega_0}\int_0^T \left(\rho\mathcal{E}\frac{\partial^2\mathbf{u}_\mathrm{a}}{\partial t^2} - \frac{\partial^2\boldsymbol{\lambda}_{u_\mathrm{a}}}{\partial t^2}\rho\right)\cdot\delta\mathbf{u}_\mathrm{a}dtd\Omega \\
&\qquad+ \frac{1}{2}\int_{\Omega_0}\int_0^T \left(\frac{\partial\boldsymbol{\lambda}_{S_\mathrm{a}}}{\partial t} + \frac{\partial\boldsymbol{\lambda}_{S_\mathrm{a}}^T}{\partial t}\right) : \nabla\delta\mathbf{u}_\mathrm{a}dtd\Omega \\
&\qquad- \int_{\Omega\backslash\Omega_0}\int_0^T \left(\frac{\partial^2\boldsymbol{\lambda}_{u_\mathrm{b}}}{\partial t^2}\rho a - \frac{\partial\boldsymbol{\lambda}_{u_\mathrm{b}}}{\partial t}\rho b + \boldsymbol{\lambda}_{u_\mathrm{b}}\rho c - \rho\mathcal{E}\frac{\partial^2\mathbf{u}_\mathrm{b}}{\partial t^2}\right)\cdot\delta\mathbf{u}_\mathrm{b}dtd\Omega \\
&\qquad+ \int_{\Omega\backslash\Omega_0}\int_0^T \frac{1}{2}\left[-\Lambda_p\boldsymbol{\lambda}_{S_\mathrm{b}} - \Lambda_p\boldsymbol{\lambda}_{S_\mathrm{b}}^T + \Lambda_e\frac{\partial\boldsymbol{\lambda}_{S_\mathrm{b}}}{\partial t} + \Lambda_e\frac{\partial\boldsymbol{\lambda}_{S_\mathrm{b}}^T}{\partial t}\right] : \nabla\delta\mathbf{u}_\mathrm{b}dtd\Omega \\
&\qquad+ \int_{\Gamma_\mathrm{int}}\int_0^T \left(\delta\mathbf{S}_\mathrm{a}\frac{\partial\boldsymbol{\lambda}_{u_\mathrm{a}}}{\partial t}\right)\cdot\boldsymbol{n}\,dtd\Gamma + \int_{\Omega_0}\int_0^T \left(\nabla\frac{\partial\boldsymbol{\lambda}_{u_\mathrm{a}}}{\partial t}\right)^T : \delta\mathbf{S}_\mathrm{a}dtd\Omega \\
&\qquad+ \int_{\Omega_0}\int_0^T \left(\mathcal{D}\left[\frac{\partial^2\boldsymbol{\lambda}_{S_\mathrm{a}}}{\partial t^2}\right]\right) : \delta\mathbf{S}_\mathrm{a}dtd\Omega \\
&\qquad- \int_{\Gamma_\mathrm{free}+\Gamma_\mathrm{fixed}}\int_0^T \left(\left\{\delta\mathbf{S}_\mathrm{b}^T\tilde{\Lambda}_e\right\}^T\frac{\partial\boldsymbol{\lambda}_{u_\mathrm{b}}}{\partial t}\right)\cdot\boldsymbol{n}\,dtd\Gamma \\
&\qquad- \int_{\Gamma_\mathrm{int}}\int_0^T \left(\delta\mathbf{S}_\mathrm{b}\frac{\partial\boldsymbol{\lambda}_{u_\mathrm{b}}}{\partial t}\right)\cdot\boldsymbol{n}\,dtd\Gamma \\
&\qquad+ \int_{\Omega\backslash\Omega_0}\int_0^T \left\{\tilde{\Lambda}_e\left(\nabla\frac{\partial\boldsymbol{\lambda}_{u_\mathrm{b}}}{\partial t}\right)^T - \tilde{\Lambda}_p\left(\nabla\boldsymbol{\lambda}_{u_\mathrm{b}}\right)^T\right\} : \delta\mathbf{S}_\mathrm{b}dtd\Omega \\
&\qquad+ \int_{\Gamma_\mathrm{free}+\Gamma_\mathrm{fixed}}\int_0^T \left(\left\{\delta\mathbf{S}_\mathrm{b}^T\tilde{\Lambda}_p\right\}^T\boldsymbol{\lambda}_{u_\mathrm{b}}\right)\cdot\boldsymbol{n}\,dtd\Gamma \\
&\qquad+ \int_{\Omega\backslash\Omega_0}\int_0^T \left\{\mathcal{D}\left[\Lambda_e^T\frac{\partial^2\boldsymbol{\lambda}_{S_\mathrm{b}}}{\partial t^2}\Lambda_e\right]\right\} : \delta\mathbf{S}_\mathrm{b}dtd\Omega
\end{aligned}
$$

$$
\begin{aligned}
&-\int_{\Omega\backslash\Omega_0}\int_0^T \left\{\mathcal{D}\left[\Lambda_e^T\frac{\partial \boldsymbol{\lambda}_{S_\mathrm{b}}}{\partial t}\Lambda_p\right]\right\}:\delta\mathbf{S}_\mathrm{b}dtd\Omega\\
&-\int_{\Omega\backslash\Omega_0}\int_0^T \left\{\mathcal{D}\left[\Lambda_p^T\frac{\partial \boldsymbol{\lambda}_{S_\mathrm{b}}}{\partial t}\Lambda_e\right]\right\}:\delta\mathbf{S}_\mathrm{b}dtd\Omega\\
&+\int_{\Omega\backslash\Omega_0}\int_0^T \left\{\mathcal{D}\left[\Lambda_p^T\boldsymbol{\lambda}_{S_\mathrm{b}}\Lambda_p\right]\right\}:\delta\mathbf{S}_\mathrm{b}dtd\Omega-\int_{\Gamma_\mathrm{load}}\int_0^T\frac{\partial\boldsymbol{\lambda}_\mathrm{F}}{\partial t}\delta\mathbf{S}_\mathrm{b}^T\boldsymbol{n}dtd\Gamma.
\end{aligned}
\tag{B.12}
$$

By virtue of (B.35b), (B.12) changes to:

$$
\begin{aligned}
&\delta_{\mathbf{u},\mathbf{S}}\mathcal{A}^{(\int_0^T)} \\
&\quad = \int_{\Omega_0}\int_0^T \left(\rho\mathcal{E}\frac{\partial^2\mathbf{u}_\mathrm{a}}{\partial t^2} - \frac{\partial^2\boldsymbol{\lambda}_{u_\mathrm{a}}}{\partial t^2}\rho - \frac{1}{2}\mathbf{div}\left(\frac{\partial\boldsymbol{\lambda}_{S_\mathrm{a}}}{\partial t} + \frac{\partial\boldsymbol{\lambda}_{S_\mathrm{a}}^T}{\partial t}\right)\right)\cdot\delta\mathbf{u}_\mathrm{a}\,dtd\Omega \\
&\qquad + \frac{1}{2}\int_{\Gamma_\mathrm{int}}\int_0^T \left\{\left(\frac{\partial\boldsymbol{\lambda}_{S_\mathrm{a}}}{\partial t} + \frac{\partial\boldsymbol{\lambda}_{S_\mathrm{a}}^T}{\partial t}\right)(-\boldsymbol{n}) + \left[\frac{\partial\boldsymbol{\lambda}_{S_\mathrm{b}}}{\partial t} + \frac{\partial\boldsymbol{\lambda}_{S_\mathrm{b}}^T}{\partial t}\right]\boldsymbol{n}\right\}\cdot\delta\mathbf{u}_\mathrm{a}\,dtd\Gamma \\
&\qquad - \int_{\Omega\setminus\Omega_0}\left(\frac{\partial^2\boldsymbol{\lambda}_{u_\mathrm{b}}}{\partial t^2}\rho a - \frac{\partial\boldsymbol{\lambda}_{u_\mathrm{b}}}{\partial t}\rho b + \boldsymbol{\lambda}_{u_\mathrm{b}}\rho c - \rho\mathcal{E}\frac{\partial^2\mathbf{u}_\mathrm{b}}{\partial t^2}\right. \\
&\qquad\qquad\qquad \left. + \frac{1}{2}\mathbf{div}\left[-\Lambda_p\boldsymbol{\lambda}_{S_\mathrm{b}} - \Lambda_p\boldsymbol{\lambda}_{S_\mathrm{b}}^T + \Lambda_e\frac{\partial\boldsymbol{\lambda}_{S_\mathrm{b}}}{\partial t} + \Lambda_e\frac{\partial\boldsymbol{\lambda}_{S_\mathrm{b}}^T}{\partial t}\right]\right)\cdot\delta\mathbf{u}_\mathrm{b}\,dtd\Omega \\
&\qquad + \frac{1}{2}\int_{\Gamma_\mathrm{free}}\int_0^T \left(\left[-\Lambda_p\boldsymbol{\lambda}_{S_\mathrm{b}} - \Lambda_p\boldsymbol{\lambda}_{S_\mathrm{b}}^T + \Lambda_e\frac{\partial\boldsymbol{\lambda}_{S_\mathrm{b}}}{\partial t} + \Lambda_e\frac{\partial\boldsymbol{\lambda}_{S_\mathrm{b}}^T}{\partial t}\right]\boldsymbol{n}\right)\cdot\delta\mathbf{u}_\mathrm{b}\,dtd\Gamma \\
&\qquad + \int_{\Gamma_\mathrm{int}}\int_0^T \left(\frac{\partial\boldsymbol{\lambda}_{u_\mathrm{a}}}{\partial t} - \frac{\partial\boldsymbol{\lambda}_{u_\mathrm{b}}}{\partial t}\right)\cdot\left(\delta\mathbf{S}_\mathrm{a}^T\boldsymbol{n} = \delta\mathbf{S}_\mathrm{b}^T\boldsymbol{n}\right)dtd\Gamma \\
&\qquad + \int_{\Omega_0}\int_0^T \left(\left(\nabla\frac{\partial\boldsymbol{\lambda}_{u_\mathrm{a}}}{\partial t}\right)^T + \mathcal{D}\left[\frac{\partial^2\boldsymbol{\lambda}_{S_\mathrm{a}}}{\partial t^2}\right]\right) : \delta\mathbf{S}_\mathrm{a}\,dtd\Omega \\
&\qquad - \int_{\Gamma_\mathrm{fixed}}\int_0^T \frac{\partial\boldsymbol{\lambda}_{u_\mathrm{b}}}{\partial t}\cdot\left(\left\{\delta\mathbf{S}_\mathrm{b}^T\tilde{\Lambda}_e\right\}\boldsymbol{n}\right)dtd\Gamma - \int_{\Gamma_\mathrm{load}}\int_0^T \frac{\partial\boldsymbol{\lambda}_{u_\mathrm{b}}}{\partial t}\cdot\left(\delta\mathbf{S}_\mathrm{b}^T\boldsymbol{n}\right)dtd\Gamma \\
&\qquad + \int_{\Gamma_\mathrm{fixed}}\int_0^T \boldsymbol{\lambda}_{u_\mathrm{b}}\cdot\left(\left\{\delta\mathbf{S}_\mathrm{b}^T\tilde{\Lambda}_p\right\}\boldsymbol{n}\right)dtd\Gamma \\
&\qquad + \int_{\Omega\setminus\Omega_0}\int_0^T \left\{\tilde{\Lambda}_e\left(\nabla\frac{\partial\boldsymbol{\lambda}_{u_\mathrm{b}}}{\partial t}\right)^T - \tilde{\Lambda}_p\left(\nabla\boldsymbol{\lambda}_{u_\mathrm{b}}\right)^T\right. \\
&\qquad\qquad\qquad \left. + \mathcal{D}\left[\Lambda_e^T\frac{\partial^2\boldsymbol{\lambda}_{S_\mathrm{b}}}{\partial t^2}\Lambda_e - \Lambda_e^T\frac{\partial\boldsymbol{\lambda}_{S_\mathrm{b}}}{\partial t}\Lambda_p - \Lambda_p^T\frac{\partial\boldsymbol{\lambda}_{S_\mathrm{b}}}{\partial t}\Lambda_e + \Lambda_p^T\boldsymbol{\lambda}_{S_\mathrm{b}}\Lambda_p\right]\right\} \\
&\qquad\qquad\qquad : \delta\mathbf{S}_\mathrm{b}\,dtd\Omega \\
&\qquad - \int_{\Gamma_\mathrm{load}}\int_0^T \frac{\partial\boldsymbol{\lambda}_\mathrm{F}}{\partial t}\cdot\delta\mathbf{S}_\mathrm{b}^T\boldsymbol{n}\,dtd\Gamma.
\end{aligned}
\tag{B.13}
$$

Here, it can be shown that:

$$\begin{aligned}
&\int_{\Omega_0}\int_0^T \left\{ \left(\nabla \frac{\partial \boldsymbol{\lambda}_{u_\mathrm{a}}}{\partial t}\right)^T + \mathcal{D}\left[\frac{\partial^2 \boldsymbol{\lambda}_{S_\mathrm{a}}}{\partial t^2}\right]\right\} : \delta \mathbf{S}_\mathrm{a} dt d\Omega \\
&= \int_{\Omega_0}\int_0^T \delta\mathbf{S}_\mathrm{a} : \left\{ \left(\mathcal{D}\left[\frac{\partial^2 \boldsymbol{\lambda}^{sym}_{S_\mathrm{a}}}{\partial t^2}\right]\right) + \frac{1}{2}\left[\nabla \frac{\partial \boldsymbol{\lambda}_{u_\mathrm{a}}}{\partial t} + \left(\nabla\frac{\partial \boldsymbol{\lambda}_{u_\mathrm{a}}}{\partial t}\right)^T\right]\right\} dt d\Omega,
\end{aligned} \tag{B.14}$$

as well as

$$\begin{aligned}
&\int_{\Omega\backslash\Omega_0}\int_0^T \left\{ \tilde{\Lambda}_e \left(\nabla \frac{\partial \boldsymbol{\lambda}_{u_\mathrm{b}}}{\partial t}\right)^T - \tilde{\Lambda}_p \left(\nabla \boldsymbol{\lambda}_{u_\mathrm{b}}\right)^T \right. \\
&\qquad \left. + \mathcal{D}\left[\Lambda_e^T \frac{\partial^2 \boldsymbol{\lambda}_{S_\mathrm{b}}}{\partial t^2}\Lambda_e - \Lambda_e^T \frac{\partial \boldsymbol{\lambda}_{S_\mathrm{b}}}{\partial t}\Lambda_p - \Lambda_p^T \frac{\partial \boldsymbol{\lambda}_{S_\mathrm{b}}}{\partial t}\Lambda_e + \Lambda_p^T \boldsymbol{\lambda}_{S_\mathrm{b}} \Lambda_p\right]\right\} \\
&\qquad : \delta \mathbf{S}_\mathrm{b} dt d\Omega \\
&= \int_{\Omega\backslash\Omega_0}\int_0^T \left\{ \frac{1}{2}\left\{ \tilde{\Lambda}_e \left(\nabla \frac{\partial \boldsymbol{\lambda}_{u_\mathrm{b}}}{\partial t}\right)^T + \left(\nabla \frac{\partial \boldsymbol{\lambda}_{u_\mathrm{b}}}{\partial t}\right)\tilde{\Lambda}_e \right\} \right. \\
&\qquad - \frac{1}{2}\left\{ \tilde{\Lambda}_p (\nabla \boldsymbol{\lambda}_{u_\mathrm{b}})^T + (\nabla \boldsymbol{\lambda}_{u_\mathrm{b}})\tilde{\Lambda}_p \right\} \\
&\qquad \left. + \mathcal{D}\left[\Lambda_e^T \frac{\partial^2 \boldsymbol{\lambda}^{sym}_{S_\mathrm{b}}}{\partial t^2}\Lambda_e - \Lambda_e^T \frac{\partial \boldsymbol{\lambda}^{sym}_{S_\mathrm{b}}}{\partial t}\Lambda_p - \Lambda_p^T \frac{\partial \boldsymbol{\lambda}^{sym}_{S_\mathrm{b}}}{\partial t}\Lambda_e + \Lambda_p^T \boldsymbol{\lambda}^{sym}_{S_\mathrm{b}} \Lambda_p\right]\right\} \\
&\qquad : \delta \mathbf{S}_\mathrm{b} dt d\Omega.
\end{aligned} \tag{B.15}$$

Then, via (B.14) and (B.15), the summation of (B.9) and (B.13) becomes

$$
\begin{aligned}
&\delta_{\mathbf{u},\mathbf{S}}\mathcal{A} \\
&= \int_{\Omega_0} \left(-\rho\mathcal{E}\frac{\partial \mathbf{u}_{\mathrm{a}}}{\partial t} \cdot \delta\mathbf{u}_{\mathrm{a}} + \frac{\partial \boldsymbol{\lambda}_{u_{\mathrm{a}}}}{\partial t} \cdot \rho\delta\mathbf{u}_{\mathrm{a}} \right) d\Omega \bigg|_{t=T} \\
&\quad - \int_{\Omega_0} \boldsymbol{\lambda}_{u_{\mathrm{a}}} \cdot \rho \frac{\partial \delta\mathbf{u}_{\mathrm{a}}}{\partial t} d\Omega \bigg|_{t=T} - \int_{\Omega_0} \boldsymbol{\lambda}^{sym}_{S_{\mathrm{a}}} : \nabla\delta\mathbf{u}_{\mathrm{a}} d\Omega \bigg|_{t=T} \\
&\quad + \int_{\Omega\backslash\Omega_0} \left(-\rho\mathcal{E}\frac{\partial \mathbf{u}_{\mathrm{b}}}{\partial t} + \frac{\partial \boldsymbol{\lambda}_{u_{\mathrm{b}}}}{\partial t}\rho a - \boldsymbol{\lambda}_{u_{\mathrm{b}}}\rho b \right) \cdot \delta\mathbf{u}_{\mathrm{b}} d\Omega \bigg|_{t=T} \\
&\quad - \int_{\Omega\backslash\Omega_0} \boldsymbol{\lambda}_{u_{\mathrm{b}}} \cdot \rho a \frac{\partial \delta\mathbf{u}_{\mathrm{b}}}{\partial t} d\Omega \bigg|_{t=T} \\
&\quad - \int_{\Omega\backslash\Omega_0} \left(\Lambda_e \boldsymbol{\lambda}^{sym}_{S_{\mathrm{b}}} \right) : \nabla\delta\mathbf{u}_{\mathrm{b}} d\Omega \bigg|_{t=T} + \int_{\Omega_0} \boldsymbol{\lambda}_{u_{\mathrm{a}}} \cdot \mathbf{div}(\delta\mathbf{S}_{\mathrm{a}}^T) d\Omega \bigg|_{t=T} \\
&\quad + \int_{\Omega_0} \boldsymbol{\lambda}_{S_{\mathrm{a}}} : \left(\mathcal{D}\left[\frac{\partial \delta\mathbf{S}_{\mathrm{a}}}{\partial t} \right] \right) d\Omega \bigg|_{t=T} - \int_{\Omega_0} \frac{\partial \boldsymbol{\lambda}_{S_{\mathrm{a}}}}{\partial t} : \left(\mathcal{D}\left[\delta\mathbf{S}_{\mathrm{a}} \right] \right) d\Omega \bigg|_{t=T} \\
&\quad + \int_{\Omega\backslash\Omega_0} \boldsymbol{\lambda}_{u_{\mathrm{b}}} \cdot \mathbf{div}\left(\delta\mathbf{S}_{\mathrm{b}}^T \tilde{\Lambda}_e \right) d\Omega \bigg|_{t=T} - \int_{\Omega\backslash\Omega_0} \frac{\partial \boldsymbol{\lambda}_{S_{\mathrm{b}}}}{\partial t} : \left\{ \Lambda_e^T \left(\mathcal{D}\left[\delta\mathbf{S}_{\mathrm{b}} \right] \right) \Lambda_e \right\} d\Omega \bigg|_{t=T} \\
&\quad + \int_{\Omega\backslash\Omega_0} \boldsymbol{\lambda}_{S_{\mathrm{b}}} : \left\{ \Lambda_e^T \left(\mathcal{D}\left[\frac{\partial \delta\mathbf{S}_{\mathrm{b}}}{\partial t} \right] \right) \Lambda_e + \Lambda_e^T \left(\mathcal{D}\left[\frac{\partial \delta\mathbf{S}_{\mathrm{b}}}{\partial t} \right] \right) \Lambda_p \right. \\
&\qquad\qquad\qquad \left. \Lambda_p^T \left(\mathcal{D}\left[\frac{\partial \delta\mathbf{S}_{\mathrm{b}}}{\partial t} \right] \right) \Lambda_e \right\} d\Omega \bigg|_{t=T} \\
&\quad + \int_{\Gamma_{\mathrm{load}}} \boldsymbol{\lambda}_{\mathrm{F}} \delta\mathbf{S}_{\mathrm{b}}^T \boldsymbol{n} dt d\Gamma \bigg|_{t=T} \\
&\quad + \int_{\Omega_0} \int_0^T \left(\rho\mathcal{E}\frac{\partial^2 \mathbf{u}_{\mathrm{a}}}{\partial t^2} - \frac{\partial^2 \boldsymbol{\lambda}_{u_{\mathrm{a}}}}{\partial t^2}\rho - \mathbf{div}\left(\frac{\partial \boldsymbol{\lambda}^{sym}_{S_{\mathrm{a}}}}{\partial t} \right) \right) \cdot \delta\mathbf{u}_{\mathrm{a}} dt d\Omega \\
&\quad - \int_{\Gamma_{\mathrm{int}}} \int_0^T \left(\frac{\partial \boldsymbol{\lambda}^{sym}_{S_{\mathrm{a}}}}{\partial t} \boldsymbol{n} \right) \cdot \delta\mathbf{u}_{\mathrm{a}} dt d\Gamma \\
&\quad + \int_{\Gamma_{\mathrm{int}}} \int_0^T \left(\frac{\partial \boldsymbol{\lambda}^{sym}_{S_{\mathrm{b}}}}{\partial t} \boldsymbol{n} \right) \cdot \delta\mathbf{u}_{\mathrm{b}} dt d\Gamma
\end{aligned}
$$

$$
\begin{aligned}
&- \int_{\Omega\setminus\Omega_0}\int_0^T \left(\frac{\partial^2 \boldsymbol{\lambda}_{u_\mathrm{b}}}{\partial t^2}\rho a - \frac{\partial \boldsymbol{\lambda}_{u_\mathrm{b}}}{\partial t}\rho b + \boldsymbol{\lambda}_{u_\mathrm{b}}\rho c - \rho\mathcal{E}\frac{\partial^2 \mathbf{u}_\mathrm{b}}{\partial t^2} \right. \\
&\qquad\qquad \left. + \mathbf{div}\left[-\Lambda_p \boldsymbol{\lambda}^{sym}_{S_\mathrm{b}} + \Lambda_e \frac{\partial \boldsymbol{\lambda}^{sym}_{S_\mathrm{b}}}{\partial t} \right] \right) \cdot \delta\mathbf{u}_\mathrm{b}\, dt d\Omega \\
&+ \int_{\Gamma_\mathrm{free}}\int_0^T \left(\left[-\Lambda_p \boldsymbol{\lambda}^{sym}_{S_\mathrm{b}} + \Lambda_e \frac{\partial \boldsymbol{\lambda}^{sym}_{S_\mathrm{b}}}{\partial t} \right] \boldsymbol{n} \right) \cdot \delta\mathbf{u}_\mathrm{b}\, dt d\Gamma \\
&+ \int_{\Gamma_\mathrm{int}}\int_0^T \left(\frac{\partial \boldsymbol{\lambda}_{u_\mathrm{a}}}{\partial t} \cdot \delta\mathbf{S}_\mathrm{a}^T \boldsymbol{n} \right) dt d\Gamma \\
&- \int_{\Gamma_\mathrm{int}}\int_0^T \left(\frac{\partial \boldsymbol{\lambda}_{u_\mathrm{b}}}{\partial t} \cdot \delta\mathbf{S}_\mathrm{b}^T \boldsymbol{n} \right) dt d\Gamma \\
&+ \int_{\Omega_0}\int_0^T \delta\mathbf{S}_\mathrm{a} : \left\{ \left(\mathcal{D}\left[\frac{\partial^2 \boldsymbol{\lambda}^{sym}_{S_\mathrm{a}}}{\partial t^2} \right] \right) + \frac{1}{2}\left[\nabla \frac{\partial \boldsymbol{\lambda}_{u_\mathrm{a}}}{\partial t} + \left(\nabla \frac{\partial \boldsymbol{\lambda}_{u_\mathrm{a}}}{\partial t} \right)^T \right] \right\} dt d\Omega \\
&- \int_{\Gamma_\mathrm{fixed}}\int_0^T \frac{\partial \boldsymbol{\lambda}_{u_\mathrm{b}}}{\partial t} \cdot \left(\left\{ \delta\mathbf{S}_\mathrm{b}^T \tilde{\Lambda}_e \right\} \boldsymbol{n} \right) dt d\Gamma - \int_{\Gamma_\mathrm{load}}\int_0^T \frac{\partial \boldsymbol{\lambda}_{u_\mathrm{b}}}{\partial t} \cdot \left(\delta\mathbf{S}_\mathrm{b}^T \boldsymbol{n} \right) dt d\Gamma \\
&+ \int_{\Gamma_\mathrm{fixed}}\int_0^T \boldsymbol{\lambda}_{u_\mathrm{b}} \cdot \left(\left\{ \delta\mathbf{S}_\mathrm{b}^T \tilde{\Lambda}_p \right\} \boldsymbol{n} \right) dt d\Gamma \\
&+ \int_{\Omega\setminus\Omega_0}\int_0^T \left\{ \frac{1}{2}\left(\tilde{\Lambda}_e \left(\nabla \frac{\partial \boldsymbol{\lambda}_{u_\mathrm{b}}}{\partial t} \right)^T + \left(\nabla \frac{\partial \boldsymbol{\lambda}_{u_\mathrm{b}}}{\partial t} \right) \tilde{\Lambda}_e \right) \right. \\
&\qquad\qquad - \frac{1}{2}\left(\tilde{\Lambda}_p (\nabla \boldsymbol{\lambda}_{u_\mathrm{b}})^T + (\nabla \boldsymbol{\lambda}_{u_\mathrm{b}}) \tilde{\Lambda}_p \right) \\
&\qquad\qquad \left. + \mathcal{D}\left[\Lambda_e^T \frac{\partial^2 \boldsymbol{\lambda}^{sym}_{S_\mathrm{b}}}{\partial t^2} \Lambda_e - \Lambda_e^T \frac{\partial \boldsymbol{\lambda}^{sym}_{S_\mathrm{b}}}{\partial t} \Lambda_p - \Lambda_p^T \frac{\partial \boldsymbol{\lambda}^{sym}_{S_\mathrm{b}}}{\partial t} \Lambda_e + \Lambda_p^T \boldsymbol{\lambda}^{sym}_{S_\mathrm{b}} \Lambda_p \right] \right\} \\
&\qquad\qquad : \delta\mathbf{S}_\mathrm{b}\, dt d\Omega \\
&- \int_{\Gamma_\mathrm{load}}\int_0^T \frac{\partial \boldsymbol{\lambda}_\mathrm{F}}{\partial t} \cdot \delta\mathbf{S}_\mathrm{b}^T \boldsymbol{n}\, dt d\Gamma.
\end{aligned}
\tag{B.16}
$$

(B.16) vanishes for arbitrary variations $\delta\mathbf{u}_\mathrm{a}$, $\delta\mathbf{u}_\mathrm{b}$, $\delta\mathbf{S}_\mathrm{a}$, and $\delta\mathbf{S}_\mathrm{b}$, provided that we satisfy the adjoint problem (4.14)–(4.19).

B.2 The third condition

We take the variation of the augmented functional with respect to a control variable ξ, which is tantamount to the discretized force parameters f_{2_i}, as the following :

$$
\begin{aligned}
\delta_\xi \mathcal{A} &= \frac{\partial \mathcal{A}}{\partial \xi} \\
&= \frac{\partial}{\partial \xi} \left\{ \frac{1}{\int_{\Omega_0} \int_0^T \rho \left[\left(\frac{\partial u_{\mathrm{a}_1}}{\partial t} \right)^2 + \left(\frac{\partial u_{\mathrm{a}_2}}{\partial t} \right)^2 \right] dt d\Omega} \right. \\
&\quad + \int_{\Omega_0} \int_0^T \boldsymbol{\lambda}_{u_\mathrm{a}} \cdot \left[\mathbf{div} \left(\frac{\partial \mathbf{S}_\mathrm{a}^T}{\partial t} \right) - \rho \frac{\partial^2 \mathbf{u}_\mathrm{a}}{\partial t^2} \right] dt d\Omega \\
&\quad + \int_{\Omega_0} \int_0^T \boldsymbol{\lambda}_{S_\mathrm{a}} : \left[\mathcal{D} \left[\frac{\partial^2 \mathbf{S}_\mathrm{a}}{\partial t^2} \right] - \frac{1}{2} \left\{ \nabla \frac{\partial \mathbf{u}_\mathrm{a}}{\partial t} + \left(\nabla \frac{\partial \mathbf{u}_\mathrm{a}}{\partial t} \right)^T \right\} \right] dt d\Omega \\
&\quad + \int_{\Omega \backslash \Omega_0} \int_0^T \boldsymbol{\lambda}_{u_\mathrm{b}} \cdot \left[\mathbf{div} \left(\frac{\partial \mathbf{S}_\mathrm{b}^T}{\partial t} \tilde{\Lambda}_e + \mathbf{S}_\mathrm{b}^T \tilde{\Lambda}_p \right) \right. \\
&\qquad\qquad \left. - \rho \left(a \frac{\partial^2 \mathbf{u}_\mathrm{b}}{\partial t^2} + b \frac{\partial \mathbf{u}_\mathrm{a}}{\partial t} + c \mathbf{u}_\mathrm{b} \right) \right] dt d\Omega \\
&\quad + \int_{\Omega \backslash \Omega_0} \int_0^T \boldsymbol{\lambda}_{S_\mathrm{b}} : \left[\Lambda_e^T \left(\mathcal{D} \left[\frac{\partial^2 \mathbf{S}_\mathrm{b}}{\partial t^2} \right] \right) \Lambda_e + \Lambda_e^T \left(\mathcal{D} \left[\frac{\partial \mathbf{S}_\mathrm{b}}{\partial t} \right] \right) \Lambda_p \right. \\
&\qquad\qquad + \Lambda_p^T \left(\mathcal{D} \left[\frac{\partial \mathbf{S}_\mathrm{b}}{\partial t} \right] \right) \Lambda_e + \Lambda_p^T (\mathcal{D} \left[\mathbf{S}_\mathrm{b} \right]) \Lambda_p \\
&\qquad\qquad - \frac{1}{2} \left\{ \Lambda_p^T \nabla \mathbf{u}_\mathrm{b} + (\nabla \mathbf{u}_\mathrm{b})^T \Lambda_p \right\} \\
&\qquad\qquad \left. - \frac{1}{2} \left\{ \Lambda_e^T \nabla \frac{\partial \mathbf{u}_\mathrm{b}}{\partial t} + \left(\nabla \frac{\partial \mathbf{u}_\mathrm{b}}{\partial t} \right)^T \Lambda_e \right\} \right] dt d\Omega \\
&\quad \left. + \int_{\Gamma_\mathrm{load}} \int_0^T \boldsymbol{\lambda}_\mathrm{F} \cdot \left[\frac{\partial \mathbf{S}_\mathrm{b}^T}{\partial t} \boldsymbol{n} - \mathbf{f}(\boldsymbol{x}, t) \right] dt d\Gamma \right\}. \qquad \text{(B.17)}
\end{aligned}
$$

The first term in (B.17), via integration by parts with respect to time, changes to:

$$\begin{aligned}
&\frac{\partial}{\partial \xi}\left(\frac{1}{\int_{\Omega_0}\int_0^T \rho\left(\frac{\partial u_{\mathrm{a}_1}}{\partial t}\right)^2+\left(\frac{\partial u_{\mathrm{a}_2}}{\partial t}\right)^2 dt d\Omega}\right)\\
&\qquad = -\int_{\Omega_0} \rho\mathcal{E}\frac{\partial \mathbf{u}_{\mathrm{a}}}{\partial t}\cdot \dot{\mathbf{u}}_{\mathrm{a}} d\Omega\bigg|_{t=T} + \int_{\Omega_0}\int_0^T \rho\mathcal{E}\frac{\partial^2 \mathbf{u}_{\mathrm{a}}}{\partial t^2}\cdot \dot{\mathbf{u}}_{\mathrm{a}} dt d\Omega\\
&\qquad\quad -\int_{\Omega\setminus\Omega_0} \rho\mathcal{E}\frac{\partial \mathbf{u}_{\mathrm{b}}}{\partial t}\cdot \dot{\mathbf{u}}_{\mathrm{b}} d\Omega\bigg|_{t=T} + \int_{\Omega\setminus\Omega_0}\int_0^T \rho\mathcal{E}\frac{\partial^2 \mathbf{u}_{\mathrm{b}}}{\partial t^2}\cdot \dot{\mathbf{u}}_{\mathrm{b}} dt d\Omega, \qquad \text{(B.18)}
\end{aligned}$$

where $(\dot{\ })$ denotes the derivative of the subtended function with respect to ξ. The second term of (B.17) changes as the following:

$$\begin{aligned}
&\frac{\partial}{\partial \xi}\left\{\int_{\Omega_0}\int_0^T \boldsymbol{\lambda}_{u_{\mathrm{a}}}\cdot\left[\mathbf{div}\left(\frac{\partial \mathbf{S}_{\mathrm{a}}^T}{\partial t}\right)-\rho\frac{\partial^2 \mathbf{u}_{\mathrm{a}}}{\partial t^2}\right] dt d\Omega\right\}\\
&\quad = \int_{\Omega_0}\int_0^T \dot{\boldsymbol{\lambda}}_{u_{\mathrm{a}}}\cdot\left[\mathbf{div}\left(\frac{\partial \mathbf{S}_{\mathrm{a}}^T}{\partial t}\right)-\rho\frac{\partial^2 \mathbf{u}_{\mathrm{a}}}{\partial t^2}\right] dt d\Omega\\
&\qquad + \int_{\Omega_0}\int_0^T \boldsymbol{\lambda}_{u_{\mathrm{a}}}\cdot\left[\mathbf{div}\left(\frac{\partial \dot{\mathbf{S}}_{\mathrm{a}}^T}{\partial t}\right)-\rho\frac{\partial^2 \dot{\mathbf{u}}_{\mathrm{a}}}{\partial t^2}\right] dt d\Omega, \qquad \text{(B.19)}
\end{aligned}$$

whereby $\mathbf{div}\left(\frac{\partial \mathbf{S}_{\mathrm{a}}^T}{\partial t}\right)-\rho\frac{\partial^2 \mathbf{u}_{\mathrm{a}}}{\partial t^2}=0$, as shown in the state problem (4.1a). Thus, (B.19) reduces to:

$$\int_{\Omega_0}\int_0^T \boldsymbol{\lambda}_{u_{\mathrm{a}}}\cdot\left[\mathbf{div}\left(\frac{\partial \dot{\mathbf{S}}_{\mathrm{a}}^T}{\partial t}\right)-\rho\frac{\partial^2 \dot{\mathbf{u}}_{\mathrm{a}}}{\partial t^2}\right] dt d\Omega. \qquad \text{(B.20)}$$

Via integration by parts, (B.20) becomes:

$$\int_{\Omega_0} \mathcal{E}\frac{\partial \mathbf{u}_{\mathrm{a}}}{\partial t}\cdot \rho\dot{\mathbf{u}}_{\mathrm{a}} d\Omega\bigg|_{t=T} - \int_{\Omega_0}\int_0^T \frac{\partial \boldsymbol{\lambda}_{u_{\mathrm{a}}}}{\partial t}\cdot \mathbf{div}\left(\dot{\mathbf{S}}_{\mathrm{a}}^T\right) + \frac{\partial^2 \boldsymbol{\lambda}_{u_{\mathrm{a}}}}{\partial t^2}\cdot \rho\dot{\mathbf{u}}_{\mathrm{a}} dt d\Omega. \quad \text{(B.21)}$$

Similarly, the third term of (B.17) changes as the following:

$$\begin{aligned}
&\frac{\partial}{\partial \xi}\left\{\int_{\Omega_0}\int_0^T \boldsymbol{\lambda}_{S_\mathrm{a}} : \left\{\left(\mathcal{D}\left[\frac{\partial^2 \mathbf{S}_\mathrm{a}}{\partial t^2}\right]\right) - \frac{1}{2}\left[\nabla \frac{\partial \mathbf{u}_\mathrm{a}}{\partial t} + \left(\nabla \frac{\partial \mathbf{u}_\mathrm{a}}{\partial t}\right)^T\right]\right\} dt d\Omega\right\} \\
&= \int_{\Omega_0}\int_0^T \frac{\partial^2 \boldsymbol{\lambda}_{S_\mathrm{a}}}{\partial t^2} : \left(\mathcal{D}\left[\dot{\mathbf{S}}_\mathrm{a}\right]\right) dt d\Omega \\
&\quad + \int_{\Omega_0}\int_0^T \frac{\partial \boldsymbol{\lambda}_{S_\mathrm{a}}}{\partial t} : \frac{1}{2}\left[\nabla \dot{\mathbf{u}}_\mathrm{a} + (\nabla \dot{\mathbf{u}}_\mathrm{a})^T\right] dt d\Omega.
\end{aligned} \tag{B.22}$$

The fourth term of (B.17) changes as the following:

$$\begin{aligned}
&\frac{\partial}{\partial \xi}\left\{\int_{\Omega \backslash \Omega_0}\int_0^T \boldsymbol{\lambda}_{u_\mathrm{b}} \cdot \left[\mathbf{div}\left(\frac{\partial \mathbf{S}_\mathrm{b}^T}{\partial t}\tilde{\Lambda}_e + \mathbf{S}_\mathrm{b}^T \tilde{\Lambda}_p\right)\right.\right. \\
&\qquad\qquad \left.\left. - \ \rho\left(a\frac{\partial^2 \mathbf{u}_\mathrm{b}}{\partial t^2} + b\frac{\partial \mathbf{u}_\mathrm{b}}{\partial t} + c\mathbf{u}_\mathrm{b}\right)\right] dt d\Omega\right\} \\
&= \int_{\Omega \backslash \Omega_0} \mathcal{E}\frac{\partial \mathbf{u}_\mathrm{b}}{\partial t} \cdot \rho a \dot{\mathbf{u}}_\mathrm{b} d\Omega\bigg|_{t=T} - \int_{\Omega \backslash \Omega_0}\int_0^T \frac{\partial^2 \boldsymbol{\lambda}_{u_\mathrm{b}}}{\partial t^2} \cdot \rho a \dot{\mathbf{u}}_\mathrm{b} dt d\Omega \\
&\quad - \int_{\Omega \backslash \Omega_0}\int_0^T \frac{\partial \boldsymbol{\lambda}_{u_\mathrm{b}}}{\partial t} \cdot \left[\mathbf{div}\left(\dot{\mathbf{S}}_\mathrm{b}^T \tilde{\Lambda}_e\right) - \rho b \dot{\mathbf{u}}_\mathrm{b}\right] dt d\Omega \\
&\quad + \int_{\Omega \backslash \Omega_0}\int_0^T \boldsymbol{\lambda}_{u_\mathrm{b}} \cdot \left[\mathbf{div}\left(\dot{\mathbf{S}}_\mathrm{b}^T \tilde{\Lambda}_p\right) - \rho c \dot{\mathbf{u}}_\mathrm{b}\right] dt d\Omega.
\end{aligned} \tag{B.23}$$

The fifth term of (B.17) changes as the following:

$$
\begin{aligned}
&\frac{\partial}{\partial \xi}\int_{\Omega\setminus\Omega_0}\int_0^T \boldsymbol{\lambda}_{S_{\mathrm{b}}} : \Bigg\{ \Lambda_e^T \left(\mathcal{D}\left[\frac{\partial^2 \mathbf{S}_{\mathrm{b}}}{\partial t^2}\right]\right)\Lambda_e + \Lambda_e^T \left(\mathcal{D}\left[\frac{\partial \mathbf{S}_{\mathrm{b}}}{\partial t}\right]\right)\Lambda_p \\
&\qquad\qquad + \Lambda_p^T \left(\mathcal{D}\left[\frac{\partial \mathbf{S}_{\mathrm{b}}}{\partial t}\right]\right)\Lambda_e + \Lambda_p^T \left(\mathcal{D}\left[\mathbf{S}_{\mathrm{b}}\right]\right)\Lambda_p \\
&\qquad\qquad - \frac{1}{2}\left[\Lambda_p^T \nabla \mathbf{u}_{\mathrm{b}} + (\nabla \mathbf{u}_{\mathrm{b}})^T \Lambda_p\right] \\
&\qquad\qquad - \frac{1}{2}\left[\Lambda_e^T \nabla \frac{\partial \mathbf{u}_{\mathrm{b}}}{\partial t} + \left(\frac{\partial \mathbf{u}_{\mathrm{b}}}{\partial t}\right)^T \Lambda_e\right]\Bigg\} dt d\Omega \\
&= \int_{\Omega\setminus\Omega_0}\int_0^T \frac{\partial^2 \boldsymbol{\lambda}_{S_{\mathrm{b}}}}{\partial t^2} : \left\{\Lambda_e^T \left(\mathcal{D}\left[\dot{\mathbf{S}}_{\mathrm{b}}\right]\right)\Lambda_e\right\} dt d\Omega \\
&\quad - \int_{\Omega\setminus\Omega_0}\int_0^T \frac{\partial \boldsymbol{\lambda}_{S_{\mathrm{b}}}}{\partial t} : \Bigg\{\Lambda_e^T \left(\mathcal{D}\left[\dot{\mathbf{S}}_{\mathrm{b}}\right]\right)\Lambda_p + \Lambda_p^T \left(\mathcal{D}\left[\dot{\mathbf{S}}_{\mathrm{b}}\right]\right)\Lambda_e \\
&\qquad\qquad\qquad - \frac{1}{2}\left[\Lambda_e^T \nabla \dot{\mathbf{u}}_{\mathrm{b}} + \left(\nabla \dot{\mathbf{u}}_{\mathrm{b}}\right)^T \Lambda_e\right]\Bigg\} dt d\Omega \\
&\quad + \int_{\Omega\setminus\Omega_0}\int_0^T \boldsymbol{\lambda}_{S_{\mathrm{b}}} : \left\{\Lambda_p^T \left(\mathcal{D}\left[\dot{\mathbf{S}}_{\mathrm{b}}\right]\right)\Lambda_p - \frac{1}{2}\left[\Lambda_p^T \nabla \dot{\mathbf{u}}_{\mathrm{b}} + \left(\nabla \dot{\mathbf{u}}_{\mathrm{b}}\right)^T \Lambda_p\right]\right\} dt d\Omega.
\end{aligned}
\tag{B.24}
$$

Lastly, the sixth term of (B.17) changes as the following:

$$
\begin{aligned}
&\frac{\partial}{\partial \xi}\left\{\int_{\Gamma_{\mathrm{load}}}\int_0^T \boldsymbol{\lambda}_{\mathrm{F}} \cdot \left[\frac{\partial \mathbf{S}_{\mathrm{b}}^T}{\partial t}\boldsymbol{n} - \mathbf{f}\right] dt d\Gamma\right\} \\
&= \int_{\Gamma_{\mathrm{load}}}\int_0^T \boldsymbol{\lambda}_{\mathrm{F}} \cdot \left[\frac{\partial \dot{\mathbf{S}}_{\mathrm{b}}^T}{\partial t}\boldsymbol{n} - \dot{\mathbf{f}}\right] dt d\Gamma.
\end{aligned}
\tag{B.25}
$$

Due to (B.18), (B.21), (B.22), (B.23), (B.24), and (B.25), (B.17) changes to:

$$
\begin{aligned}
&\delta_\xi \mathcal{A} \\
&= \int_{\Omega_0} \int_0^T \left\{ \mathcal{E}\rho \frac{\partial^2 \mathbf{u}_{\mathrm{a}}}{\partial t^2} \cdot \dot{\mathbf{u}}_{\mathrm{a}} - \frac{\partial^2 \boldsymbol{\lambda}_{u_{\mathrm{a}}}}{\partial t^2} \cdot \rho \dot{\mathbf{u}}_{\mathrm{a}} + \frac{\partial \boldsymbol{\lambda}_{S_{\mathrm{a}}}}{\partial t} : \frac{1}{2} \left[\nabla \dot{\mathbf{u}}_{\mathrm{a}} + \left(\nabla \dot{\mathbf{u}}_{\mathrm{a}}\right)^T \right] \right\} dt d\Omega \\
&\quad + \int_{\Omega_0} \int_0^T \left\{ -\frac{\partial \boldsymbol{\lambda}_{u_{\mathrm{a}}}}{\partial t} \cdot \mathbf{div} \left(\dot{\mathbf{S}}_{\mathrm{a}}^T \right) + \frac{\partial^2 \boldsymbol{\lambda}_{S_{\mathrm{a}}}}{\partial t^2} : \left(\mathcal{D} \left[\dot{\mathbf{S}}_{\mathrm{a}} \right] \right) \right\} dt d\Omega \\
&\quad + \int_{\Omega \backslash \Omega_0} \int_0^T \left\{ -\frac{\partial^2 \boldsymbol{\lambda}_{u_{\mathrm{b}}}}{\partial t^2} \cdot \rho a \dot{\mathbf{u}}_{\mathrm{b}} + \frac{\partial \boldsymbol{\lambda}_{u_{\mathrm{b}}}}{\partial t} \cdot \rho b \dot{\mathbf{u}}_{\mathrm{b}} - \boldsymbol{\lambda}_{u_{\mathrm{b}}} \cdot \rho c \dot{\mathbf{u}}_{\mathrm{b}} + \mathcal{E}\rho \frac{\partial^2 \mathbf{u}_{\mathrm{b}}}{\partial t^2} \cdot \mathbf{u}_{\mathrm{b}} \right. \\
&\qquad\qquad + \frac{\partial \boldsymbol{\lambda}_{S_{\mathrm{b}}}}{\partial t} : \frac{1}{2} \left[\Lambda_e^T \nabla \dot{\mathbf{u}}_{\mathrm{b}} + \left(\nabla \dot{\mathbf{u}}_{\mathrm{b}}\right)^T \Lambda_e \right] \\
&\qquad\qquad \left. - \boldsymbol{\lambda}_{S_{\mathrm{b}}} : \frac{1}{2} \left[\Lambda_p^T \nabla \dot{\mathbf{u}}_{\mathrm{b}} + \left(\nabla \dot{\mathbf{u}}_{\mathrm{b}}\right)^T \Lambda_p \right] \right\} dt d\Omega \\
&\quad + \int_{\Omega \backslash \Omega_0} \int_0^T \left[-\frac{\partial \boldsymbol{\lambda}_{u_{\mathrm{b}}}}{\partial t} \cdot \mathbf{div} \left(\dot{\mathbf{S}}_{\mathrm{b}}^T \tilde{\Lambda}_e \right) + \boldsymbol{\lambda}_{u_{\mathrm{b}}} \cdot \mathbf{div} \left(\dot{\mathbf{S}}_{\mathrm{b}}^T \tilde{\Lambda}_p \right) \right. \\
&\qquad\qquad + \frac{\partial^2 \boldsymbol{\lambda}_{S_{\mathrm{b}}}}{\partial t^2} : \left\{ \Lambda_e^T \left(\mathcal{D} \left[\dot{\mathbf{S}}_{\mathrm{b}} \right] \right) \Lambda_e \right\} \\
&\qquad\qquad - \frac{\partial \boldsymbol{\lambda}_{S_{\mathrm{b}}}}{\partial t} : \left\{ \Lambda_e^T \left(\mathcal{D} \left[\dot{\mathbf{S}}_{\mathrm{b}} \right] \right) \Lambda_p + \Lambda_p^T \left(\mathcal{D} \left[\dot{\mathbf{S}}_{\mathrm{b}} \right] \right) \Lambda_e \right\} \\
&\qquad\qquad \left. + \boldsymbol{\lambda}_{S_{\mathrm{b}}} : \left\{ \Lambda_p^T \left(\mathcal{D} \left[\dot{\mathbf{S}}_{\mathrm{b}} \right] \right) \Lambda_p \right\} \right] dt d\Omega \\
&\quad + \int_{\Gamma_{\mathrm{load}}} \int_0^T \boldsymbol{\lambda}_{\mathrm{F}} \cdot \left[\frac{\partial \dot{\mathbf{S}}_{\mathrm{b}}^T}{\partial t} \boldsymbol{n} - \dot{\mathbf{f}} \right] dt d\Gamma. \qquad \text{(B.26)}
\end{aligned}
$$

By using the tensor identities (B.35a) and (B.35b), as well as the divergence theorem, the first term of (B.26) changes to:

$$
\begin{aligned}
&\int_{\Omega_0}\int_0^T \left\{ \mathcal{E}\rho \frac{\partial^2 \mathbf{u}_{\mathrm{a}}}{\partial t^2} \cdot \dot{\mathbf{u}}_{\mathrm{a}} - \frac{\partial^2 \boldsymbol{\lambda}_{u_{\mathrm{a}}}}{\partial t^2} \cdot \rho \dot{\mathbf{u}}_{\mathrm{a}} + \frac{\partial \boldsymbol{\lambda}_{S_{\mathrm{a}}}}{\partial t} : \frac{1}{2}\left[\nabla \dot{\mathbf{u}}_{\mathrm{a}} + \left(\nabla \dot{\mathbf{u}}_{\mathrm{a}}\right)^T \right] \right\} dt d\Omega \\
&= \int_{\Omega_0}\int_0^T \left\{ \mathcal{E}\rho \frac{\partial^2 \mathbf{u}_{\mathrm{a}}}{\partial t^2} - \frac{\partial^2 \boldsymbol{\lambda}_{u_{\mathrm{a}}}}{\partial t^2}\rho - \mathbf{div}\left(\frac{\partial \boldsymbol{\lambda}^{sym}_{S_{\mathrm{a}}}}{\partial t} \right) \right\} \cdot \dot{\mathbf{u}}_{\mathrm{a}} dt d\Omega \\
&\quad + \int_{\Gamma_{\mathrm{int}}}\int_0^T \left(\frac{\partial \boldsymbol{\lambda}^{sym}_{S_{\mathrm{a}}}}{\partial t} \dot{\mathbf{u}}_{\mathrm{a}} \right) \cdot -\boldsymbol{n} dt d\Gamma \\
&= \int_{\Gamma_{\mathrm{int}}}\int_0^T \left(\frac{\partial \boldsymbol{\lambda}^{sym}_{S_{\mathrm{a}}}}{\partial t} \dot{\mathbf{u}}_{\mathrm{a}} \right) \cdot -\boldsymbol{n} dt d\Gamma. \qquad \text{(B.27)}
\end{aligned}
$$

Similarly, owing to the tensor identities (B.35b) and (B.36a), as well as the divergence theorem, the second term of (B.26) changes to:

$$
\begin{aligned}
&\int_{\Omega_0}\int_0^T \left\{ -\frac{\partial \boldsymbol{\lambda}_{u_{\mathrm{a}}}}{\partial t} \cdot \mathbf{div}\left(\dot{\mathbf{S}}^T_{\mathrm{a}} \right) + \frac{\partial^2 \boldsymbol{\lambda}_{S_{\mathrm{a}}}}{\partial t^2} : \left(\mathcal{D}\left[\dot{\mathbf{S}}_{\mathrm{a}} \right] \right) \right\} dt d\Omega \\
&= \int_{\Gamma_{\mathrm{int}}}\int_0^T -\left(\dot{\mathbf{S}}_{\mathrm{a}} \frac{\partial \boldsymbol{\lambda}_{u_{\mathrm{a}}}}{\partial t} \right) \cdot -\boldsymbol{n} dt d\Gamma. \qquad \text{(B.28)}
\end{aligned}
$$

Likewise, due to the tensor identities (B.35b), (B.35c), and (B.35d), as well as the divergence theorem, the third term of (B.26) changes to:

$$
\begin{aligned}
&\int_{\Omega\setminus\Omega_0}\int_0^T \left\{ -\frac{\partial^2 \boldsymbol{\lambda}_{u_{\mathrm{b}}}}{\partial t^2} \cdot \rho a \dot{\mathbf{u}}_{\mathrm{b}} + \frac{\partial \boldsymbol{\lambda}_{u_{\mathrm{b}}}}{\partial t} \cdot \rho b \dot{\mathbf{u}}_{\mathrm{b}} - \boldsymbol{\lambda}_{u_{\mathrm{b}}} \cdot \rho c \dot{\mathbf{u}}_{\mathrm{b}} + \mathcal{E}\rho \frac{\partial^2 \mathbf{u}_{\mathrm{b}}}{\partial t^2} \cdot \mathbf{u}_{\mathrm{b}} \right. \\
&\qquad + \frac{\partial \boldsymbol{\lambda}_{S_{\mathrm{b}}}}{\partial t} : \frac{1}{2}\left[\Lambda_e^T \nabla \dot{\mathbf{u}}_{\mathrm{b}} + \left(\nabla \dot{\mathbf{u}}_{\mathrm{b}}\right)^T \Lambda_e \right] \\
&\qquad \left. - \boldsymbol{\lambda}_{S_{\mathrm{b}}} : \frac{1}{2}\left[\Lambda_p^T \nabla \dot{\mathbf{u}}_{\mathrm{b}} + \left(\nabla \dot{\mathbf{u}}_{\mathrm{b}}\right)^T \Lambda_p \right] \right\} dt d\Omega \\
&= \int_{\Gamma_{\mathrm{int}}}\int_0^T \left[\left(\frac{\partial \boldsymbol{\lambda}^{sym}_{S_{\mathrm{b}}}}{\partial t} \right) \boldsymbol{n} \right] \cdot \dot{\mathbf{u}}_{\mathrm{b}} dt d\Gamma. \qquad \text{(B.29)}
\end{aligned}
$$

Again, because of (B.15), (B.35b), (B.35c), (B.36b), and the divergence theorem, the fourth term of (B.26) changes to:

$$\begin{aligned}
&\int_{\Omega\setminus\Omega_0}\int_0^T \Bigg\{ -\frac{\partial \boldsymbol{\lambda}_{u_\mathrm{b}}}{\partial t}\cdot \mathbf{div}\left(\dot{\mathbf{S}}_\mathrm{b}^T\tilde{\Lambda}_e\right) + \boldsymbol{\lambda}_{u_\mathrm{b}}\cdot\mathbf{div}\left(\dot{\mathbf{S}}_\mathrm{b}^T\tilde{\Lambda}_p\right) \\
&\qquad + \frac{\partial^2\boldsymbol{\lambda}_{S_\mathrm{b}}}{\partial t^2} : \left\{\Lambda_e^T\left(\mathcal{D}\left[\dot{\mathbf{S}}_\mathrm{b}\right]\right)\Lambda_e\right\} \\
&\qquad - \frac{\partial\boldsymbol{\lambda}_{S_\mathrm{b}}}{\partial t} : \left\{\Lambda_e^T\left(\mathcal{D}\left[\dot{\mathbf{S}}_\mathrm{b}\right]\right)\Lambda_p + \Lambda_p^T\left(\mathcal{D}\left[\dot{\mathbf{S}}_\mathrm{b}\right]\right)\Lambda_e\right\} \\
&\qquad + \boldsymbol{\lambda}_{S_\mathrm{b}} : \left\{\Lambda_p^T\left(\mathcal{D}\left[\dot{\mathbf{S}}_\mathrm{b}\right]\right)\Lambda_p\right\}\Bigg\}\, dtd\Omega \\
={}&\int_{\Gamma_\mathrm{free}}\int_0^T \left[-\left(\tilde{\Lambda}_e\dot{\mathbf{S}}_\mathrm{b}\frac{\partial\boldsymbol{\lambda}_{u_\mathrm{b}}}{\partial t}\right) + \left(\tilde{\Lambda}_p\dot{\mathbf{S}}_\mathrm{b}\boldsymbol{\lambda}_{u_\mathrm{b}}\right)\right]\cdot\boldsymbol{n}dtd\Gamma \\
&- \int_{\Gamma_\mathrm{int}}\int_0^T \left(\dot{\mathbf{S}}_\mathrm{b}\frac{\partial\boldsymbol{\lambda}_{u_\mathrm{b}}}{\partial t}\right)\cdot\boldsymbol{n}dtd\Gamma.
\end{aligned} \tag{B.30}$$

Thus, due to (B.27), (B.28), (B.29), and (B.30), (B.26) changes to:

$$\begin{aligned}
\delta_\xi\mathcal{A} ={}&\int_{\Gamma_\mathrm{free}\setminus\Gamma_\mathrm{load}}\int_0^T \left[-\left(\tilde{\Lambda}_e\dot{\mathbf{S}}_\mathrm{b}\frac{\partial\boldsymbol{\lambda}_{u_\mathrm{b}}}{\partial t}\right) + \left(\tilde{\Lambda}_p\dot{\mathbf{S}}_\mathrm{b}\boldsymbol{\lambda}_{u_\mathrm{b}}\right)\right]\cdot\boldsymbol{n}dtd\Gamma \\
&- \int_{\Gamma_\mathrm{load}}\int_0^T \left(\dot{\mathbf{S}}_\mathrm{b}^T\boldsymbol{n}\right)\cdot\frac{\partial\boldsymbol{\lambda}_{u_\mathrm{b}}}{\partial t}dtd\Gamma \\
&+ \int_{\Gamma_\mathrm{load}}\int_0^T \boldsymbol{\lambda}_\mathrm{F}\cdot\left(\frac{\partial\dot{\mathbf{S}}_\mathrm{b}^T}{\partial t}\boldsymbol{n} - \dot{\mathbf{f}}\right)dtd\Gamma.
\end{aligned} \tag{B.31}$$

By taking integration by parts with respect to time, (B.31) changes to:

$$\begin{aligned}
\delta_\xi\mathcal{A} ={}&\int_{\Gamma_\mathrm{free}\setminus\Gamma_\mathrm{load}}\int_0^T \left[-\left(\tilde{\Lambda}_e\dot{\mathbf{S}}_\mathrm{b}\frac{\partial\boldsymbol{\lambda}_{u_\mathrm{b}}}{\partial t}\right) + \left(\tilde{\Lambda}_p\dot{\mathbf{S}}_\mathrm{b}\boldsymbol{\lambda}_{u_\mathrm{b}}\right)\right]\cdot\boldsymbol{n}dtd\Gamma \\
&- \left[\int_{\Gamma_\mathrm{load}}\left(\dot{\mathbf{S}}_\mathrm{b}^T\boldsymbol{n}\right)\cdot\boldsymbol{\lambda}_{u_\mathrm{b}}d\Gamma\right]_{t=0}^{t=T} + \int_{\Gamma_\mathrm{load}}\int_0^T\left(\frac{\partial\dot{\mathbf{S}}_\mathrm{b}^T}{\partial t}\boldsymbol{n}\right)\cdot\boldsymbol{\lambda}_{u_\mathrm{b}}dtd\Gamma \\
&+ \int_{\Gamma_\mathrm{load}}\int_0^T \boldsymbol{\lambda}_\mathrm{F}\cdot\left(\frac{\partial\dot{\mathbf{S}}_\mathrm{b}^T}{\partial t}\boldsymbol{n} - \dot{\mathbf{f}}\right)dtd\Gamma.
\end{aligned} \tag{B.32}$$

Then, (B.32) changes to:

$$\begin{aligned}\delta_{\xi}\mathcal{A} = &\int_{\Gamma_{\text{free}}\setminus\Gamma_{\text{load}}}\int_0^T \left[-\left(\tilde{\Lambda}_e\dot{\mathbf{S}}_{\text{b}}\frac{\partial\boldsymbol{\lambda}_{u_{\text{b}}}}{\partial t}\right)+\left(\tilde{\Lambda}_p\dot{\mathbf{S}}_{\text{b}}\boldsymbol{\lambda}_{u_{\text{b}}}\right)\right]\cdot\boldsymbol{n}dtd\Gamma \\ &+\int_{\Gamma_{\text{load}}}\int_0^T \boldsymbol{\lambda}_{u_{\text{b}}}\cdot\dot{\mathbf{f}}dtd\Gamma. \end{aligned} \tag{B.33}$$

Then, by integration by parts again, (B.33) reduces to:

$$\delta_{\xi}\mathcal{A} = \int_{\Gamma_{\text{load}}}\int_0^T \boldsymbol{\lambda}_{u_{\text{b}}}\cdot\dot{\mathbf{f}}dtd\Gamma. \tag{B.34}$$

The vanishing condition of (B.34) leads to the control equation (4.26).

B.3 Auxiliary tensor identities

In the course of the derivation of the adjoint problem (4.14)–(4.19), we use the following tensor identities:

$$\mathbf{A}:\mathbf{B}^T = \mathbf{A}^T:\mathbf{B}, \tag{B.35a}$$

$$\mathbf{div}(\mathbf{A})\cdot\boldsymbol{v} = \text{div}(\mathbf{A}^T\boldsymbol{v}) - \nabla\boldsymbol{v}:\mathbf{A}, \tag{B.35b}$$

$$\mathbf{A}:\mathbf{BC} = \mathbf{CA}^T:\mathbf{B}^T, \tag{B.35c}$$

$$\mathbf{A}:\mathbf{BC} = \mathbf{B}^T\mathbf{A}:\mathbf{C}, \tag{B.35d}$$

where **A**, **B**, and **C** denote second-order tensors; $\boldsymbol{v}$ denotes a vector. In addition, we employ the following tensor relations:

$$\mathbf{A}:(\mathcal{D}[\mathbf{S}]) = (\mathcal{D}[\mathbf{A}]):\mathbf{S}, \tag{B.36a}$$

$$\begin{aligned}&\mathbf{A}:\left\{\begin{bmatrix} B_1 & 0 \\ 0 & B_2\end{bmatrix}(\mathcal{D}\,[\mathbf{S}])\begin{bmatrix} C_1 & 0 \\ 0 & C_2\end{bmatrix}\right\} \\ &=\left\{\mathcal{D}\left[\begin{bmatrix} B_1 & 0 \\ 0 & B_2\end{bmatrix}\mathbf{A}\begin{bmatrix} C_1 & 0 \\ 0 & C_2\end{bmatrix}\right]\right\}:\mathbf{S},\end{aligned} \tag{B.36b}$$

where $\mathcal{D}$ denotes the 4-th order compliance tensor as shown in (4.6). (B.36a) can be proven by:

$$\begin{aligned}
&\mathbf{A} : (\mathcal{D}[\mathbf{S}]) \\
=&\begin{bmatrix} A_{11} & A_{12} \\ A_{21} & A_{22} \end{bmatrix} : \begin{bmatrix} \left\{\frac{(1-\nu^2)S_{11}}{E} - \frac{\nu(1+\nu)S_{22}}{E}\right\} & \frac{S_{12}}{2\mu} \\ \frac{S_{21}}{2\mu} & \left\{\frac{(1-\nu^2)S_{22}}{E} - \frac{\nu(1+\nu)S_{11}}{E}\right\} \end{bmatrix} \\
=&A_{11}\left\{\frac{(1-\nu^2)S_{11}}{E} - \frac{\nu(1+\nu)S_{22}}{E}\right\} + A_{12}\frac{S_{12}}{2\mu} \\
&+ A_{21}\frac{S_{21}}{2\mu} + A_{22}\left\{\frac{(1-\nu^2)S_{22}}{E} - \frac{\nu(1+\nu)S_{11}}{E}\right\} \\
=&\left\{\frac{(1-\nu^2)A_{11}}{E} - \frac{\nu(1+\nu)A_{22}}{E}\right\} S_{11} + \frac{A_{12}}{2\mu}S_{12} \\
&+ \frac{A_{21}}{2\mu}S_{21} + \left\{\frac{(1-\nu^2)A_{22}}{E} - \frac{\nu(1+\nu)A_{11}}{E}\right\} S_{22} \\
=&\begin{bmatrix} \left\{\frac{(1-\nu^2)A_{11}}{E} - \frac{\nu(1+\nu)A_{22}}{E}\right\} & \frac{A_{12}}{2\mu} \\ \frac{A_{21}}{2\mu} & \left\{\frac{(1-\nu^2)A_{22}}{E} - \frac{\nu(1+\nu)A_{11}}{E}\right\} \end{bmatrix} : \begin{bmatrix} S_{11} & S_{12} \\ S_{21} & S_{22} \end{bmatrix} \\
=&(\mathcal{D}[\mathbf{A}]) : \mathbf{S},
\end{aligned} \tag{B.37}$$

and (B.36b) can be shown by:

$$\begin{aligned}
&\mathbf{A}:\left\{\begin{bmatrix} B_1 & 0 \\ 0 & B_2 \end{bmatrix}\left(\mathcal{D}\left[\mathbf{S}\right]\right)\begin{bmatrix} C_1 & 0 \\ 0 & C_2 \end{bmatrix}\right\} \\
=&\mathbf{A}:\left\{\begin{bmatrix} B_1 & 0 \\ 0 & B_2 \end{bmatrix}\begin{bmatrix} \left(\mathcal{D}\left[\mathbf{S}\right]\right)_{11} & \left(\mathcal{D}\left[\mathbf{S}\right]\right)_{12} \\ \left(\mathcal{D}\left[\mathbf{S}\right]\right)_{21} & \left(\mathcal{D}\left[\mathbf{S}\right]\right)_{22} \end{bmatrix}\begin{bmatrix} C_1 & 0 \\ 0 & C_2 \end{bmatrix}\right\} \\
=&\mathbf{A}:\left\{\begin{bmatrix} B_1 & 0 \\ 0 & B_2 \end{bmatrix}\begin{bmatrix} C_1\left(\mathcal{D}\left[\mathbf{S}\right]\right)_{11} & C_2\left(\mathcal{D}\left[\mathbf{S}\right]\right)_{12} \\ C_1\left(\mathcal{D}\left[\mathbf{S}\right]\right)_{21} & C_2\left(\mathcal{D}\left[\mathbf{S}\right]\right)_{22} \end{bmatrix}\right\} \\
=&\begin{bmatrix} A_{11} & A_{12} \\ A_{21} & A_{22} \end{bmatrix}:\begin{bmatrix} B_1C_1\left(\mathcal{D}\left[\mathbf{S}\right]\right)_{11} & B_1C_2\left(\mathcal{D}\left[\mathbf{S}\right]\right)_{12} \\ B_2C_1\left(\mathcal{D}\left[\mathbf{S}\right]\right)_{21} & B_2C_2\left(\mathcal{D}\left[\mathbf{S}\right]\right)_{22} \end{bmatrix} \\
=&A_{11}B_1C_1\left(\mathcal{D}\left[\mathbf{S}\right]\right)_{11}+A_{12}B_1C_2\left(\mathcal{D}\left[\mathbf{S}\right]\right)_{12} \\
&+A_{21}B_2C_1\left(\mathcal{D}\left[\mathbf{S}\right]\right)_{21}+A_{22}B_2C_2\left(\mathcal{D}\left[\mathbf{S}\right]\right)_{22} \\
=&A_{11}B_1C_1\left(\frac{(1-\nu^2)S_{11}}{E}-\frac{\nu(1+\nu)S_{22}}{E}\right)+A_{12}B_1C_2\frac{S_{12}}{2\mu} \\
&+A_{21}B_2C_1\frac{S_{21}}{2\mu}+A_{22}B_2C_2\left(\frac{(1-\nu^2)S_{22}}{E}-\frac{\nu(1+\nu)S_{11}}{E}\right) \\
=&\begin{bmatrix} A_{11}B_1C_1\left(\frac{(1-\nu^2)}{E}\right)-A_{22}B_2C_2\left(\frac{\nu(1+\nu)}{E}\right), & \frac{A_{12}B_1C_2}{2\mu} \\ \frac{A_{21}B_2C_1}{2\mu}, & A_{22}B_2C_2\left(\frac{(1-\nu^2)}{E}\right)-A_{11}B_1C_1\left(\frac{\nu(1+\nu)}{E}\right) \end{bmatrix}:\begin{bmatrix} S_{11} & S_{12} \\ S_{21} & S_{22} \end{bmatrix} \\
=&\left(\mathcal{D}\begin{bmatrix} A_{11}B_1C_1 & A_{12}B_1C_2 \\ A_{21}B_2C_1 & A_{22}B_2C_2 \end{bmatrix}\right):\mathbf{S} \\
=&\left(\mathcal{D}\left[\begin{bmatrix} A_{11}B_1 & A_{12}B_1 \\ A_{21}B_2 & A_{22}B_2 \end{bmatrix}\begin{bmatrix} C_1 & 0 \\ 0 & C_2 \end{bmatrix}\right]\right):\mathbf{S} \\
=&\left(\mathcal{D}\left[\begin{bmatrix} B_1 & 0 \\ 0 & B_2 \end{bmatrix}\begin{bmatrix} A_{11} & A_{12} \\ A_{21} & A_{22} \end{bmatrix}\begin{bmatrix} C_1 & 0 \\ 0 & C_2 \end{bmatrix}\right]\right):\mathbf{S} \\
=&\left(\mathcal{D}\left[\begin{bmatrix} B_1 & 0 \\ 0 & B_2 \end{bmatrix}\mathbf{A}\begin{bmatrix} C_1 & 0 \\ 0 & C_2 \end{bmatrix}\right]\right):\mathbf{S}.
\end{aligned} \tag{B.38}$$

Appendix C

On the 2D semi-discrete forms (4.33) and (4.43)

We show the specific forms of the matrices of the time-dependent discrete forms (4.33) and (4.43) used for solving the state and adjoint problems in chapter 4, respectively. First, the components of the matrices in (4.33) – the semi-discrete form of the state problem in the two-dimensional setting – are defined as:

$$\begin{aligned}
M_{11}^{\text{st}} &= \int_{\Omega} \rho a \boldsymbol{\Phi}\boldsymbol{\Phi}^T d\Omega, \\
M_{22}^{\text{st}} &= \int_{\Omega} \rho a \boldsymbol{\Phi}\boldsymbol{\Phi}^T d\Omega, \\
M_{33}^{\text{st}} &= \int_{\Omega} \frac{(1-\nu^2)}{E} \alpha_1\alpha_1 \boldsymbol{\Psi}\boldsymbol{\Psi}^T d\Omega, \\
M_{34}^{\text{st}} &= -\int_{\Omega} \frac{\nu(1+\nu)}{E} \alpha_1\alpha_1 \boldsymbol{\Psi}\boldsymbol{\Psi}^T d\Omega, \\
M_{43}^{\text{st}} &= -\int_{\Omega} \frac{\nu(1+\nu)}{E} \alpha_2\alpha_2 \boldsymbol{\Psi}\boldsymbol{\Psi}^T d\Omega, \\
M_{44}^{\text{st}} &= \int_{\Omega} \frac{(1-\nu^2)}{E} \alpha_2\alpha_2 \boldsymbol{\Psi}\boldsymbol{\Psi}^T d\Omega, \\
M_{55}^{\text{st}} &= \int_{\Omega} \frac{1}{2\mu} 2\alpha_1\alpha_2 \boldsymbol{\Psi}\boldsymbol{\Psi}^T d\Omega,
\end{aligned} \tag{C.1}$$

and

$$
\begin{aligned}
C_{11}^{\text{st}} &= \int_\Omega \rho b \boldsymbol{\Phi}\boldsymbol{\Phi}^T d\Omega,\\
C_{13}^{\text{st}} &= \int_\Omega \alpha_2 \frac{\partial \boldsymbol{\Phi}}{\partial x_1}\boldsymbol{\Psi}^T d\Omega,\\
C_{15}^{\text{st}} &= \int_\Omega \alpha_1 \frac{\partial \boldsymbol{\Phi}}{\partial x_2}\boldsymbol{\Psi}^T d\Omega,\\
C_{22}^{\text{st}} &= \int_\Omega \rho b \boldsymbol{\Phi}\boldsymbol{\Phi}^T d\Omega,\\
C_{24}^{\text{st}} &= \int_\Omega \alpha_1 \frac{\partial \boldsymbol{\Phi}}{\partial x_2}\boldsymbol{\Psi}^T d\Omega,\\
C_{25}^{\text{st}} &= \int_\Omega \alpha_2 \frac{\partial \boldsymbol{\Phi}}{\partial x_1}\boldsymbol{\Psi}^T d\Omega,\\
C_{31}^{\text{st}} &= -\int_\Omega \alpha_1 \boldsymbol{\Phi}\frac{\partial \boldsymbol{\Phi}^T}{\partial x_1} d\Omega,\\
C_{33}^{\text{st}} &= \int_\Omega \frac{(1-\nu^2)(2\alpha_1\beta_1)}{E}\boldsymbol{\Psi}\boldsymbol{\Psi}^T d\Omega,\\
C_{34}^{\text{st}} &= -\int_\Omega \frac{\nu(1+\nu)(2\alpha_1\beta_1)}{E}\boldsymbol{\Psi}\boldsymbol{\Psi}^T d\Omega,\\
C_{41}^{\text{st}} &= -\int_\Omega \alpha_2 \boldsymbol{\Phi}\frac{\partial \boldsymbol{\Phi}^T}{\partial x_2} d\Omega,\\
C_{43}^{\text{st}} &= \int_\Omega \frac{(1-\nu^2)(2\alpha_2\beta_2)}{E}\boldsymbol{\Psi}\boldsymbol{\Psi}^T d\Omega,\\
C_{44}^{\text{st}} &= -\int_\Omega \frac{\nu(1+\nu)(2\alpha_2\beta_2)}{E}\boldsymbol{\Psi}\boldsymbol{\Psi}^T d\Omega,\\
C_{51}^{\text{st}} &= -\int_\Omega \alpha_1 \boldsymbol{\Psi}\frac{\partial \boldsymbol{\Phi}^T}{\partial x_2} d\Omega,\\
C_{52}^{\text{st}} &= -\int_\Omega \alpha_2 \boldsymbol{\Psi}\frac{\partial \boldsymbol{\Phi}^T}{\partial x_1} d\Omega,\\
C_{55}^{\text{st}} &= \int_\Omega \frac{(\alpha_1\beta_2+\beta_1\alpha_2)}{\mu}\boldsymbol{\Psi}\boldsymbol{\Psi}^T d\Omega,
\end{aligned}
\tag{C.2}
$$

and

$$
\begin{aligned}
K_{11}^{\mathrm{st}} &= \int_\Omega \rho c \boldsymbol{\Phi}\boldsymbol{\Phi}^T d\Omega, \\
K_{13}^{\mathrm{st}} &= \int_\Omega \beta_2 \frac{\partial \boldsymbol{\Phi}}{\partial x_1} \boldsymbol{\Psi}^T d\Omega, \\
K_{15}^{\mathrm{st}} &= \int_\Omega \beta_1 \frac{\partial \boldsymbol{\Phi}}{\partial x_2} \boldsymbol{\Psi}^T d\Omega, \\
K_{22}^{\mathrm{st}} &= \int_\Omega \rho c \boldsymbol{\Phi}\boldsymbol{\Phi}^T d\Omega, \\
K_{24}^{\mathrm{st}} &= \int_\Omega \beta_1 \frac{\partial \boldsymbol{\Phi}}{\partial x_2} \boldsymbol{\Psi}^T d\Omega, \\
K_{25}^{\mathrm{st}} &= \int_\Omega \beta_2 \frac{\partial \boldsymbol{\Phi}}{\partial x_1} \boldsymbol{\Psi}^T d\Omega, \\
K_{31}^{\mathrm{st}} &= -\int_\Omega \beta_1 \boldsymbol{\Psi} \frac{\partial \boldsymbol{\Phi}^T}{\partial x_1} d\Omega, \\
K_{33}^{\mathrm{st}} &= \int_\Omega \frac{(1-\nu^2)(2\beta_1\beta_1)}{E} \boldsymbol{\Psi}\boldsymbol{\Psi}^T d\Omega, \\
K_{34}^{\mathrm{st}} &= -\int_\Omega \frac{\nu(1+\nu)(2\beta_1\beta_1)}{E} \boldsymbol{\Psi}\boldsymbol{\Psi}^T d\Omega, \\
K_{41}^{\mathrm{st}} &= -\int_\Omega \beta_2 \boldsymbol{\Psi} \frac{\partial \boldsymbol{\Phi}^T}{\partial x_2} d\Omega, \\
K_{43}^{\mathrm{st}} &= -\int_\Omega \frac{\nu(1+\nu)(2\beta_2\beta_2)}{E} \boldsymbol{\Psi}\boldsymbol{\Psi}^T d\Omega, \\
K_{44}^{\mathrm{st}} &= \int_\Omega \frac{(1-\nu^2)(2\beta_2\beta_2)}{E} \boldsymbol{\Psi}\boldsymbol{\Psi}^T d\Omega, \\
K_{51}^{\mathrm{st}} &= -\int_\Omega \beta_1 \boldsymbol{\Psi} \frac{\partial \boldsymbol{\Phi}^T}{\partial x_2} d\Omega, \\
K_{52}^{\mathrm{st}} &= -\int_\Omega \beta_2 \boldsymbol{\Psi} \frac{\partial \boldsymbol{\Phi}^T}{\partial x_1} d\Omega, \\
K_{55}^{\mathrm{st}} &= \int_\Omega \frac{(\beta_1\beta_2)}{\mu} \boldsymbol{\Psi}\boldsymbol{\Psi}^T d\Omega. \qquad \text{(C.3)}
\end{aligned}
$$

Second, the components of the matrices in (4.43) – the semi-discrete form of the adjoint problem in the two-dimensional setting – are defined as:

$$
\begin{aligned}
M_{11}^{\text{adj}} &= \int_{\Omega} \rho a \mathbf{\Phi}\mathbf{\Phi}^T d\Omega, \\
M_{22}^{\text{adj}} &= \int_{\Omega} \rho a \mathbf{\Phi}\mathbf{\Phi}^T d\Omega, \\
M_{33}^{\text{adj}} &= \int_{\Omega} \frac{(1-\nu^2)}{E}\alpha_1\alpha_1 \mathbf{\Psi}\mathbf{\Psi}^T d\Omega, \\
M_{34}^{\text{adj}} &= -\int_{\Omega} \frac{\nu(1+\nu)}{E}\alpha_2\alpha_2 \mathbf{\Psi}\mathbf{\Psi}^T d\Omega, \\
M_{43}^{\text{adj}} &= -\int_{\Omega} \frac{\nu(1+\nu)}{E}\alpha_1\alpha_1 \mathbf{\Psi}\mathbf{\Psi}^T d\Omega, \\
M_{44}^{\text{adj}} &= \int_{\Omega} \frac{(1-\nu^2)}{E}\alpha_2\alpha_2 \mathbf{\Psi}\mathbf{\Psi}^T d\Omega, \\
M_{55}^{\text{adj}} &= \int_{\Omega} \frac{1}{2\mu} 2\alpha_1\alpha_2 \mathbf{\Psi}\mathbf{\Psi}^T d\Omega, \qquad \text{(C.4)}
\end{aligned}
$$

and

$$
\begin{aligned}
C_{11}^{\text{adj}} &= -\int_{\Omega} \rho b \boldsymbol{\Phi}\boldsymbol{\Phi}^{T} d\Omega, \\
C_{13}^{\text{adj}} &= -\int_{\Omega} \alpha_1 \frac{\partial \boldsymbol{\Phi}}{\partial x_1} \boldsymbol{\Psi}^{T} d\Omega, \\
C_{15}^{\text{adj}} &= -\int_{\Omega} \alpha_1 \frac{\partial \boldsymbol{\Phi}}{\partial x_2} \boldsymbol{\Psi}^{T} d\Omega, \\
C_{21}^{\text{adj}} &= -\int_{\Omega} \rho b \boldsymbol{\Phi}\boldsymbol{\Phi}^{T} d\Omega \\
C_{24}^{\text{adj}} &= -\int_{\Omega} \alpha_2 \frac{\partial \boldsymbol{\Phi}}{\partial x_2} \boldsymbol{\Psi}^{T} d\Omega, \\
C_{25}^{\text{adj}} &= -\int_{\Omega} \alpha_2 \frac{\partial \boldsymbol{\Phi}}{\partial x_1} \boldsymbol{\Psi}^{T} d\Omega, \\
C_{31}^{\text{adj}} &= \int_{\Omega} \alpha_2 \boldsymbol{\Psi} \frac{\partial \boldsymbol{\Phi}^{T}}{\partial x_1} d\Omega, \\
C_{33}^{\text{adj}} &= -\int_{\Omega} \frac{(1-\nu^2)(2\alpha_1\beta_1)}{E} \boldsymbol{\Psi}\boldsymbol{\Psi}^{T} d\Omega, \\
C_{34}^{\text{adj}} &= \int_{\Omega} \frac{\nu(1+\nu)(2\alpha_2\beta_2)}{E} \boldsymbol{\Psi}\boldsymbol{\Psi}^{T} d\Omega, \\
C_{42}^{\text{adj}} &= \int_{\Omega} \alpha_1 \boldsymbol{\Psi} \frac{\partial \boldsymbol{\Phi}^{T}}{\partial x_2} d\Omega, \\
C_{43}^{\text{adj}} &= \int_{\Omega} \frac{\nu(1+\nu)(2\alpha_1\beta_1)}{E} \boldsymbol{\Psi}\boldsymbol{\Psi}^{T} d\Omega, \\
C_{44}^{\text{adj}} &= -\int_{\Omega} \frac{(1-\nu^2)(2\alpha_2\beta_2)}{E} \boldsymbol{\Psi}\boldsymbol{\Psi}^{T} d\Omega, \\
C_{51}^{\text{adj}} &= \int_{\Omega} \alpha_1 \boldsymbol{\Psi} \frac{\partial \boldsymbol{\Phi}^{T}}{\partial x_2} d\Omega, \\
C_{52}^{\text{adj}} &= \int_{\Omega} \alpha_2 \boldsymbol{\Psi} \frac{\partial \boldsymbol{\Phi}^{T}}{\partial x_1} d\Omega, \\
C_{55}^{\text{adj}} &= -\int_{\Omega} \frac{(\alpha_1\beta_2 + \beta_1\alpha_2)}{\mu} \boldsymbol{\Psi}\boldsymbol{\Psi}^{T} d\Omega,
\end{aligned}
\tag{C.5}
$$

and

$$
\begin{aligned}
K_{11}^{\text{adj}} &= \int_\Omega \rho c \boldsymbol{\Phi}\boldsymbol{\Phi}^T d\Omega, \\
K_{13}^{\text{adj}} &= \int_\Omega \beta_1 \frac{\partial \boldsymbol{\Phi}}{\partial x_1} \boldsymbol{\Psi}^T d\Omega, \\
K_{15}^{\text{adj}} &= \int_\Omega \beta_1 \frac{\partial \boldsymbol{\Phi}}{\partial x_2} \boldsymbol{\Psi}^T d\Omega, \\
K_{22}^{\text{adj}} &= \int_\Omega \rho c \boldsymbol{\Phi}\boldsymbol{\Phi}^T d\Omega, \\
K_{24}^{\text{adj}} &= \int_\Omega \beta_2 \frac{\partial \boldsymbol{\Phi}}{\partial x_2} \boldsymbol{\Psi}^T d\Omega, \\
K_{25}^{\text{adj}} &= \int_\Omega \beta_2 \frac{\partial \boldsymbol{\Phi}}{\partial x_1} \boldsymbol{\Psi}^T d\Omega, \\
K_{31}^{\text{adj}} &= -\int_\Omega \beta_2 \boldsymbol{\Psi} \frac{\partial \boldsymbol{\Phi}^T}{\partial x_1} d\Omega, \\
K_{33}^{\text{adj}} &= \int_\Omega \frac{(1-\nu^2)(\beta_1\beta_1)}{E} \boldsymbol{\Psi}\boldsymbol{\Psi}^T d\Omega, \\
K_{34}^{\text{adj}} &= -\int_\Omega \frac{\nu(1+\nu)(\beta_2\beta_2)}{E} \boldsymbol{\Psi}\boldsymbol{\Psi}^T d\Omega, \\
K_{42}^{\text{adj}} &= -\int_\Omega \beta_1 \boldsymbol{\Psi} \frac{\partial \boldsymbol{\Phi}^T}{\partial x_2} d\Omega, \\
K_{43}^{\text{adj}} &= -\int_\Omega \frac{\nu(1+\nu)(\beta_1\beta_1)}{E} \boldsymbol{\Psi}\boldsymbol{\Psi}^T d\Omega, \\
K_{44}^{\text{adj}} &= \int_\Omega \frac{(1-\nu^2)(\beta_2\beta_2)}{E} \boldsymbol{\Psi}\boldsymbol{\Psi}^T d\Omega, \\
K_{51}^{\text{adj}} &= -\int_\Omega \beta_1 \boldsymbol{\Psi} \frac{\partial \boldsymbol{\Phi}^T}{\partial x_2} d\Omega, \\
K_{52}^{\text{adj}} &= -\int_\Omega \beta_2 \boldsymbol{\Psi} \frac{\partial \boldsymbol{\Phi}^T}{\partial x_1} d\Omega, \\
K_{55}^{\text{adj}} &= \int_\Omega \frac{(\beta_1\beta_2)}{\mu} \boldsymbol{\Psi}\boldsymbol{\Psi}^T d\Omega. \qquad \text{(C.6)}
\end{aligned}
$$

Appendix D

On the first-order optimality conditions in the 1D poroelastic case

The vanishing variational conditions of the augmented functional $\mathcal{A}$ shown in (5.13) with respect to the state variables ($u(x,t)$ and $w(x,t)$) and the control variable ($\xi = f_i$), respectively, lead to the adjoint and control problems in chapter 5 as follows.

D.1 The second condition

The variation of the augmented functional (5.13) with respect to the state variables ($u(x,t)$ and $w(x,t)$) should vanish, i.e., $\delta_{u,w}\mathcal{A} = 0$. The variation $\delta_{u,w}\mathcal{A}$ can be obtained as:

$$\delta_{u,w}\mathcal{A} = \delta_u\mathcal{A} + \delta_w\mathcal{A}. \tag{D.1}$$

First, we evaluate the variation $\delta_u \mathcal{A}$ as follows:

$$\begin{aligned}
\delta_u \mathcal{A} =& \delta_{u_{\mathrm{a}}} \mathcal{A} + \delta_{u_{\mathrm{b}}} \mathcal{A} \\
=& \int_0^{x_p} \int_0^T \lambda_{u_{\mathrm{a}}} \left[\frac{\partial}{\partial x} \left((\lambda + 2\mu) \frac{\partial \delta u_{\mathrm{a}}}{\partial x} \right) - \rho \frac{\partial^2 \delta u_{\mathrm{a}}}{\partial t^2} \right] dt dx \\
&+ \int_{x_{p+N_{\mathrm{pls}}}}^{L} \int_0^T \lambda_{u_{\mathrm{a}}} \left[\frac{\partial}{\partial x} \left((\lambda + 2\mu) \frac{\partial \delta u_{\mathrm{a}}}{\partial x} \right) - \rho \frac{\partial^2 \delta u_{\mathrm{a}}}{\partial t^2} \right] dt dx \\
&+ \int_{x_p}^{x_{p+N_{\mathrm{pls}}}} \int_0^T \lambda_{u_{\mathrm{b}}} \left[\frac{\partial}{\partial x} \left((\lambda + 2\mu + \alpha^2 Q) \frac{\partial \delta u_{\mathrm{b}}}{\partial x} \right) - \rho \frac{\partial^2 \delta u_{\mathrm{b}}}{\partial t^2} \right] dt dx \\
&+ \int_{x_p}^{x_{p+N_{\mathrm{pls}}}} \int_0^T \lambda_w \left[\frac{\partial}{\partial x} \left(\alpha Q \frac{\partial \delta u_{\mathrm{b}}}{\partial x} \right) - \rho_f \frac{\partial^2 \delta u_{\mathrm{b}}}{\partial t^2} \right] dt dx \\
&+ \int_0^T \lambda_0(t) \left[(\lambda(0) + 2\mu(0)) \frac{\partial \delta u_{\mathrm{a}}}{\partial x}(0, t) + f(t) \right] dt \\
&+ \int_0^T \lambda_L(t) (\lambda(L) + 2\mu(L)) \left[\frac{\partial \delta u_{\mathrm{a}}}{\partial x}(L, t) + \frac{1}{c} \frac{\partial \delta u_{\mathrm{a}}}{\partial t}(L, t) \right] dt. \qquad \text{(D.2)}
\end{aligned}$$

By considering a multi-layered system, we show that (D.2) changes to:

$$\begin{aligned}
&\delta_u\mathcal{A} = \\
&\sum_{i=1}^{p-1}\left\{\int_{x_i^+}^{x_{i+1}^-}\int_0^T \lambda_{u_\mathrm{a}}\left[\frac{\partial}{\partial x}\left((\lambda+2\mu)\frac{\partial\delta u_\mathrm{a}}{\partial x}\right)-\rho\frac{\partial^2\delta u_\mathrm{a}}{\partial t^2}\right]dtdx\right\} \\
&+\sum_{i=p+N_\mathrm{pls}}^{N_\mathrm{ls}-1}\left\{\int_{x_i^+}^{x_{i+1}^-}\int_0^T \lambda_{u_\mathrm{a}}\left[\frac{\partial}{\partial x}\left((\lambda+2\mu)\frac{\partial\delta u_\mathrm{a}}{\partial x}\right)-\rho\frac{\partial^2\delta u_\mathrm{a}}{\partial t^2}\right]dtdx\right\} \\
&+\sum_{i=p}^{p+N_\mathrm{pls}-1}\left\{\int_{x_i^+}^{x_{i+1}^-}\int_0^T \lambda_{u_\mathrm{b}}\left[\frac{\partial}{\partial x}\left((\lambda+2\mu+\alpha^2 Q)\frac{\partial\delta u_\mathrm{b}}{\partial x}\right)-\rho\frac{\partial^2\delta u_\mathrm{b}}{\partial t^2}\right]dtdx\right\} \\
&+\sum_{i=p}^{p+N_\mathrm{pls}-1}\left\{\int_{x_i^+}^{x_{i+1}^-}\int_0^T \lambda_{w}\left[\frac{\partial}{\partial x}\left(\alpha Q\frac{\partial\delta u_\mathrm{b}}{\partial x}\right)-\rho_f\frac{\partial^2\delta u_\mathrm{b}}{\partial t^2}\right]dtdx\right\} \\
&+\int_0^T \lambda_0(t)\left[(\lambda(0)+2\mu(0))\frac{\partial\delta u_\mathrm{a}}{\partial x}(0,t)+f(t)\right]dt \\
&+\int_0^T \lambda_L(t)(\lambda(L)+2\mu(L))\left[\frac{\partial\delta u_\mathrm{a}}{\partial x}(L,t)+\frac{1}{c}\frac{\partial\delta u_\mathrm{a}}{\partial t}(L,t)\right]dt. \qquad \text{(D.3)}
\end{aligned}$$

By virtue of integration by parts with respect to time and space, (D.3) changes to:

$$
\begin{aligned}
&\delta_u\mathcal{A} = \\
&+\int_0^{x_p}\int_0^T \left(\frac{\partial}{\partial x}\left((\lambda+2\mu)\frac{\partial\lambda_{u_\mathrm{a}}}{\partial x}\right)-\rho\frac{\partial^2\lambda_{u_\mathrm{a}}}{\partial t^2}\right)\delta u_\mathrm{a}dtdx \\
&+\int_{x_{p+N_\mathrm{pls}}}^{L}\int_0^T \left(\frac{\partial}{\partial x}\left((\lambda+2\mu)\frac{\partial\lambda_{u_\mathrm{a}}}{\partial x}\right)-\rho\frac{\partial^2\lambda_{u_\mathrm{a}}}{\partial t^2}\right)\delta u_\mathrm{a}dtdx \\
&+\int_{x_p}^{x_{p+N_\mathrm{pls}}}\int_0^T \left(\frac{\partial}{\partial x}\left((\lambda+2\mu+\alpha^2Q)\frac{\partial\lambda_{u_\mathrm{b}}}{\partial x}\right)-\rho\frac{\partial^2\lambda_{u_\mathrm{b}}}{\partial t^2}\right)\delta u_\mathrm{b}dtdx \\
&+\int_{x_p}^{x_{p+N_\mathrm{pls}}}\int_0^T \left(\frac{\partial}{\partial x}\left(\alpha Q\frac{\partial\lambda_w}{\partial x}\right)-\rho_f\frac{\partial^2\lambda_w}{\partial t^2}\right)\delta u_\mathrm{b}dtdx \\
&-\int_0^{x_p}\lambda_{u_\mathrm{a}}\rho\frac{\partial\delta u_\mathrm{a}}{\partial t}dx\bigg|_{t=T}+\int_0^{x_p}\frac{\partial\lambda_{u_\mathrm{a}}}{\partial t}\rho\delta u_\mathrm{a}dx\bigg|_{t=T} \\
&-\int_{x_{p+N_\mathrm{pls}}}^{L}\lambda_{u_\mathrm{a}}\rho\frac{\partial\delta u_\mathrm{a}}{\partial t}dx\bigg|_{t=T}+\int_{x_{p+N_\mathrm{pls}}}^{L}\frac{\partial\lambda_{u_\mathrm{a}}}{\partial t}\rho\delta u_\mathrm{a}dx\bigg|_{t=T} \\
&-\int_{x_p}^{x_{p+N_\mathrm{pls}}}\lambda_{u_\mathrm{b}}\rho\frac{\partial\delta u_\mathrm{b}}{\partial t}dx\bigg|_{t=T}+\int_{x_p}^{x_{p+N_\mathrm{pls}}}\frac{\partial\lambda_{u_\mathrm{b}}}{\partial t}\rho\delta u_\mathrm{b}dx\bigg|_{t=T} \\
&-\int_{x_p}^{x_{p+N_\mathrm{pls}}}\lambda_w\rho_f\frac{\partial\delta u_\mathrm{b}}{\partial t}dx\bigg|_{t=T}+\int_{x_p}^{x_{p+N_\mathrm{pls}}}\frac{\partial\lambda_w}{\partial t}\rho_f\delta u_\mathrm{b}dx\bigg|_{t=T} \\
&+\int_0^T\lambda_0(t)(\lambda(0)+2\mu(0))\frac{\partial\delta u_\mathrm{a}}{\partial x}(0,t)dt \\
&+\int_0^T\lambda_L(t)(\lambda(L)+2\mu(L))\ \frac{\partial\delta u_\mathrm{a}}{\partial x}(L,t)\ dt+\lambda_L(T)\frac{(\lambda(L)+2\mu(L))}{c}\delta u_\mathrm{a}(L,T) \\
&-\int_0^T\frac{\partial\lambda_L(t)}{\partial t}\frac{(\lambda(L)+2\mu(L))}{c}\delta u_\mathrm{a}(L,t)dt \\
&+\sum_{i=1}^{p-1}\left\{\left[\int_0^T\lambda_{u_\mathrm{a}}\ (\lambda+2\mu)\frac{\partial\delta u_\mathrm{a}}{\partial x}\ dt\right]_{x_i^+}^{x_{i+1}^-}-\left[\int_0^T(\lambda+2\mu)\frac{\partial\lambda_{u_\mathrm{a}}}{\partial x}\delta u_\mathrm{a}dt\right]_{x_i^+}^{x_{i+1}^-}\right\}
\end{aligned}
$$

$$
\begin{aligned}
&+\sum_{i=p+N_{\mathrm{pls}}}^{N_{\mathrm{ls}}-1}\left\{\left[\int_0^T \lambda_{u_{\mathrm{a}}}\,(\lambda+2\mu)\frac{\partial \delta u_{\mathrm{a}}}{\partial x}\,dt\right]_{x_i^+}^{x_{i+1}^-}\right.\\
&\qquad\qquad\left.-\left[\int_0^T (\lambda+2\mu)\frac{\partial \lambda_{u_{\mathrm{a}}}}{\partial x}\delta u_{\mathrm{a}}dt\right]_{x_i^+}^{x_{i+1}^-}\right\}\\
&+\sum_{i=p}^{p+N_{\mathrm{pls}}-1}\left\{\left[\int_0^T \lambda_{u_{\mathrm{b}}}\,(\lambda+2\mu+\alpha^2 Q)\frac{\partial \delta u_{\mathrm{b}}}{\partial x}\,dt\right]_{x_i^+}^{x_{i+1}^-}\right.\\
&\qquad\qquad\left.-\left[\int_0^T (\lambda+2\mu+\alpha^2 Q)\frac{\partial \lambda_{u_{\mathrm{b}}}}{\partial x}\delta u_{\mathrm{b}}dt\right]_{x_i^+}^{x_{i+1}^-}\right\}\\
&+\sum_{i=p}^{p+N_{\mathrm{pls}}-1}\left\{\left[\int_0^T \lambda_w\left(\alpha Q\frac{\partial \delta u_{\mathrm{b}}}{\partial x}\right)dt\right]_{x_i^+}^{x_{i+1}^-}-\left[\int_0^T \alpha Q\frac{\partial \lambda_w}{\partial x}\delta u_{\mathrm{b}}dt\right]_{x_i^+}^{x_{i+1}^-}\right\}.
\end{aligned}
\tag{D.4}
$$

Second, we obtain $\delta_w\mathcal{A}$ in the following manner.

$$
\begin{aligned}
&\delta_w\mathcal{A}\\
&=\frac{-2\left(\int_{x_p}^{x_{p+N_{\mathrm{pls}}}}\rho_f\frac{\partial w}{\partial t}\delta w dx\Big|_{t=T}-\int_{x_p}^{x_{p+N_{\mathrm{pls}}}}\int_0^T\rho_f\frac{\partial^2 w}{\partial t^2}\delta w dt dx\right)}{\left(\int_{x_p}^{x_{p+N_{\mathrm{pls}}}}\int_0^T\rho_f[\frac{\partial w}{\partial t}(x,t)]^2 dt dx\right)^2}\\
&+\sum_{i=p}^{p+N_{\mathrm{pls}}-1}\left\{\int_{x_i^+}^{x_{i+1}^-}\int_0^T\lambda_{u_{\mathrm{b}}}(x,t)\left[\frac{\partial}{\partial x}\left(\alpha Q\frac{\partial \delta w}{\partial x}\right)-\rho_f\frac{\partial^2\delta w}{\partial t^2}\right]dt dx\right\}\\
&+\sum_{i=p}^{p+N_{\mathrm{pls}}-1}\left\{\int_{x_i^+}^{x_{i+1}^-}\int_0^T\lambda_w(x,t)\left[\frac{\partial}{\partial x}\left(Q\frac{\partial \delta w}{\partial x}\right)-\frac{1}{k}\frac{\partial\delta w}{\partial t}-\frac{\rho_f}{n}\frac{\partial^2\delta w}{\partial t^2}\right]dt dx\right\}.
\end{aligned}
\tag{D.5}
$$

Via integration by parts with respect to space and time, (D.5) changes to:

$$
\begin{aligned}
&\delta_w\mathcal{A}\\
=&\mathcal{E}\int_{x_p}^{x_{p+N_{\text{pls}}}} \rho_f\frac{\partial w}{\partial t}\delta w dx\bigg|_{t=T} - \int_{x_p}^{x_{p+N_{\text{pls}}}} \frac{\lambda_w}{k}\delta w dx\bigg|_{t=T}\\
&-\int_{x_p}^{x_{p+N_{\text{pls}}}} \lambda_{u_{\text{b}}}\rho_f\frac{\partial \delta w}{\partial t}dx\bigg|_{t=T} + \int_{x_p}^{x_{p+N_{\text{pls}}}} \frac{\partial \lambda_{u_{\text{b}}}}{\partial t}\rho_f\delta w dx\bigg|_{t=T}\\
&-\int_{x_p}^{x_{p+N_{\text{pls}}}} \lambda_w\frac{\rho_f}{n}\frac{\partial \delta w}{\partial t}dx\bigg|_{t=T} + \int_{x_p}^{x_{p+N_{\text{pls}}}} \frac{\partial \lambda_w}{\partial t}\frac{\rho_f}{n}\delta w dx\bigg|_{t=T}\\
&+\sum_{i=p}^{p+N_{\text{pls}}-1}\left\{\left[\int_0^T \lambda_{u_{\text{b}}}\ \alpha Q\frac{\partial \delta w}{\partial x}\ dt\right]_{x_i^+}^{x_{i+1}^-} - \left[\int_0^T \frac{\partial \lambda_{u_{\text{b}}}}{\partial x}\alpha Q\delta w dt\right]_{x_i^+}^{x_{i+1}^-}\right\}\\
&+\sum_{i=p}^{p+N_{\text{pls}}-1}\left\{\left[\int_0^T \lambda_w\ Q\frac{\partial \delta w}{\partial x}\ dt\right]_{x_i^+}^{x_{i+1}^-} - \left[\int_0^T \frac{\partial \lambda_w}{\partial x}Q\delta w dt\right]_{x_i^+}^{x_{i+1}^-}\right\}\\
&+\int_{x_p}^{x_{p+N_{\text{pls}}}}\int_0^T \Bigg(\frac{\partial}{\partial x}\left(\alpha Q\frac{\partial \lambda_{u_{\text{b}}}}{\partial x}\right) + \frac{\partial}{\partial x}\left(Q\frac{\partial \lambda_w}{\partial x}\right) + \frac{1}{k}\frac{\partial \lambda_w}{\partial t}\\
&\qquad\qquad -\rho_f\frac{\partial^2 \lambda_{u_{\text{b}}}}{\partial t^2} - \frac{\rho_f}{n}\frac{\partial^2 \lambda_w}{\partial t^2} - \mathcal{E}\rho_f\frac{\partial^2 w}{\partial t^2}\Bigg)\delta w dt dx. \qquad \text{(D.6)}
\end{aligned}
$$

Next, $\delta_{u,w}\mathcal{A}(=\delta_u\mathcal{A}+\delta_w\mathcal{A})$ is split into three parts as follows: $\delta_{u,w}\mathcal{A} = \delta_{u,w}\mathcal{A}^{\int\int} + \delta_{u,w}\mathcal{A}^{\text{etc}} + \delta_{u,w}\mathcal{A}^{T}$, where $\delta_{u,w}\mathcal{A}^{\int\int}$ denotes the terms associated with the spatial and temporal integrals of the adjoint PDEs; $\delta_{u,w}\mathcal{A}^{\text{etc}}$ denotes the temporal integral terms at specific locations; $\delta_{u,w}\mathcal{A}^{T}$ denotes the spatial integrals temporally associated only with time $t=T$. We show $\delta_{u,w}\mathcal{A}^{\int\int}$, $\delta_{u,w}\mathcal{A}^{\text{etc}}$, and $\delta_{u,w}\mathcal{A}^{T}$ in the following. First, $\delta_{u,w}\mathcal{A}^{\int\int}$ is:

$$
\begin{aligned}
&\delta_{u,w}\mathcal{A}^{\int\int}\\
&\quad=\int_0^{x_p}\int_0^T\left\{\frac{\partial}{\partial x}\left((\lambda+2\mu)\frac{\partial\lambda_{u_\mathrm{a}}}{\partial x}\right)-\rho\frac{\partial^2\lambda_{u_\mathrm{a}}}{\partial t^2}\right\}\delta u_\mathrm{a}dtdx\\
&\qquad+\int_{x_{p+N_\mathrm{pls}}}^{L}\int_0^T\left\{\frac{\partial}{\partial x}\left((\lambda+2\mu)\frac{\partial\lambda_{u_\mathrm{a}}}{\partial x}\right)-\rho\frac{\partial^2\lambda_{u_\mathrm{a}}}{\partial t^2}\right\}\delta u_\mathrm{a}dtdx\\
&\qquad+\int_{x_p}^{x_{p+N_\mathrm{pls}}}\int_0^T\left\{\frac{\partial}{\partial x}\left((\lambda+2\mu+\alpha^2Q)\frac{\partial\lambda_{u_\mathrm{b}}}{\partial x}\right)+\frac{\partial}{\partial x}\left(\alpha Q\frac{\partial\lambda_w}{\partial x}\right)\right.\\
&\qquad\qquad\qquad\qquad\left.-\rho\frac{\partial^2\lambda_{u_\mathrm{b}}}{\partial t^2}-\rho_f\frac{\partial^2\lambda_w}{\partial t^2}\right\}\delta u_\mathrm{b}dtdx\\
&\qquad+\int_{x_p}^{x_{p+N_\mathrm{pls}}}\int_0^T\left\{\frac{\partial}{\partial x}\left(\alpha Q\frac{\partial\lambda_{u_\mathrm{b}}}{\partial x}\right)+\frac{\partial}{\partial x}\left(Q\frac{\partial\lambda_w}{\partial x}\right)+\frac{1}{k}\frac{\partial\lambda_w}{\partial t}\right.\\
&\qquad\qquad\qquad\qquad\left.-\rho_f\frac{\partial^2\lambda_{u_\mathrm{b}}}{\partial t^2}-\frac{\rho_f}{n}\frac{\partial^2\lambda_w}{\partial t^2}-\mathcal{E}\rho_f\frac{\partial^2 w}{\partial t^2}\right\}\delta wdtdx. \qquad \text{(D.7)}
\end{aligned}
$$

The vanishing of (D.7) recovers the adjoint PDEs shown in (5.15)–(5.17). Second, $\delta_{u,w}\mathcal{A}^{\text{etc}}$ is the following:

$$
\begin{aligned}
&\delta_{u,w}\mathcal{A}^{\text{etc}} \\
&= \int_0^T (\lambda_0 - \lambda_{u_\text{a}})\,(\lambda + 2\mu)\frac{\partial \delta u_\text{a}}{\partial x}\;dt\bigg|_{x=0} \\
&\quad + \int_0^T (\lambda + 2\mu)\frac{\partial \lambda_{u_\text{a}}}{\partial x}\delta u_\text{a} dt\bigg|_{x=0} \\
&\quad + \int_0^T \lambda_{u_\text{a}}(\lambda + 2\mu)\frac{\partial \delta u_\text{a}}{\partial x} dt\bigg|_{x_p^-} \\
&\quad - \int_0^T \lambda_{u_\text{b}}\left((\lambda + 2\mu + \alpha^2 Q)\frac{\partial \delta u_\text{b}}{\partial x} + \alpha Q\frac{\partial \delta w}{\partial x}\right) dt\bigg|_{x_p^+} \\
&\quad - \int_0^T (\lambda + 2\mu)\frac{\partial \lambda_{u_\text{a}}}{\partial x}\delta u_\text{a} dt\bigg|_{x_p^-} \\
&\quad + \int_0^T \left((\lambda + 2\mu + \alpha^2 Q)\frac{\partial \lambda_{u_\text{b}}}{\partial x} + \frac{\partial \lambda_w}{\partial x}\alpha Q\right)\delta u_\text{b} dt\bigg|_{x_p^+} \\
&\quad + \int_0^T \lambda_{u_\text{b}}\left((\lambda + 2\mu + \alpha^2 Q)\frac{\partial \delta u_\text{b}}{\partial x} + \alpha Q\frac{\partial \delta w}{\partial x}\right) dt\bigg|_{x_{p+N_\text{pls}}^-} \\
&\quad - \int_0^T \lambda_{u_\text{a}}\left((\lambda + 2\mu)\frac{\partial \delta u_\text{a}}{\partial x}\right) dt\bigg|_{x_{p+N_\text{pls}}^+} \\
&\quad - \int_0^T \lambda_w\left(\alpha Q\frac{\partial \delta u_\text{b}}{\partial x} + Q\frac{\partial \delta w}{\partial x}\right) dt\bigg|_{x_p^+} \\
&\quad + \int_0^T \lambda_w\left(\alpha Q\frac{\partial \delta u_\text{b}}{\partial x} + Q\frac{\partial \delta w}{\partial x}\right) dt\bigg|_{x_{p+N_\text{pls}}^-}
\end{aligned}
$$

$$
\begin{aligned}
&+ \int_0^T (\lambda + 2\mu) \frac{\partial \lambda_{u_\mathrm{a}}}{\partial x} \delta u_\mathrm{a} dt \bigg|_{x^+_{p+N_\mathrm{pls}}} \\
&- \int_0^T \left((\lambda + 2\mu + \alpha^2 Q) \frac{\partial \lambda_{u_\mathrm{b}}}{\partial x} + \alpha Q \frac{\partial \lambda_w}{\partial x} \right) \delta u_\mathrm{b} dt \Bigg|_{x^-_{p+N_\mathrm{pls}}} \\
&+ \int_0^T \left(\lambda_{u_\mathrm{a}} + \lambda_L \right) (\lambda + 2\mu) \frac{\partial \delta u_\mathrm{a}}{\partial x} \, dt \bigg|_{x=L} \\
&- \int_0^T \left(\frac{\partial \lambda_{u_\mathrm{a}}}{\partial x} + \frac{\partial \lambda_L}{\partial t} \frac{1}{c} \right) (\lambda + 2\mu) \delta u_\mathrm{a} dt \bigg|_{x=L} \\
&+ \sum_{i=2}^{p-1} \Bigg\{ \int_0^T \lambda_{u_\mathrm{a}} \left((\lambda + 2\mu) \frac{\partial \delta u_\mathrm{a}}{\partial x} \right) dt \bigg|_{x_i^-} \\
&\qquad\qquad - \int_0^T \lambda_{u_\mathrm{a}} \left((\lambda + 2\mu) \frac{\partial \delta u_\mathrm{a}}{\partial x} \right) dt \bigg|_{x_i^+} \Bigg\} \\
&- \sum_{i=2}^{p-1} \Bigg\{ \int_0^T (\lambda + 2\mu) \frac{\partial \lambda_{u_\mathrm{a}}}{\partial x} \delta u_\mathrm{a} dt \bigg|_{x_i^-} \\
&\qquad\qquad - \int_0^T (\lambda + 2\mu) \frac{\partial \lambda_{u_\mathrm{a}}}{\partial x} \delta u_\mathrm{a} dt \bigg|_{x_i^+} \Bigg\} \\
&+ \sum_{i=p+N_\mathrm{pls}+1}^{N_\mathrm{ls}-1} \Bigg\{ \int_0^T \lambda_{u_\mathrm{a}} \left((\lambda + 2\mu) \frac{\partial \delta u_\mathrm{a}}{\partial x} \right) dt \bigg|_{x_i^-} \\
&\qquad\qquad - \int_0^T \lambda_{u_\mathrm{a}} \left((\lambda + 2\mu) \frac{\partial \delta u_\mathrm{a}}{\partial x} \right) dt \bigg|_{x_i^+} \Bigg\}
\end{aligned}
$$

$$
\begin{aligned}
&- \sum_{i=p+N_{\mathrm{pls}}+1}^{N_{\mathrm{ls}}-1} \left\{ \int_0^T (\lambda + 2\mu) \frac{\partial \lambda_{u_{\mathrm{a}}}}{\partial x} \delta u_{\mathrm{a}} dt \bigg|_{x_i^-} \right. \\
&\qquad\qquad \left. - \int_0^T (\lambda + 2\mu) \frac{\partial \lambda_{u_{\mathrm{a}}}}{\partial x} \delta u_{\mathrm{a}} dt \bigg|_{x_i^+} \right\} \\
&+ \sum_{i=p+1}^{p+N_{\mathrm{pls}}-1} \left\{ \int_0^T \lambda_{u_{\mathrm{b}}} \left((\lambda + 2\mu + \alpha^2 Q) \frac{\partial \delta u_{\mathrm{b}}}{\partial x} + \alpha Q \frac{\partial \delta w}{\partial x} \right) dt \bigg|_{x_i^-} \right. \\
&\qquad\qquad \left. - \int_0^T \lambda_{u_{\mathrm{b}}} \left((\lambda + 2\mu + \alpha^2 Q) \frac{\partial \delta u_{\mathrm{b}}}{\partial x} + \alpha Q \frac{\partial \delta w}{\partial x} \right) dt \bigg|_{x_i^+} \right\} \\
&- \sum_{i=p+1}^{p+N_{\mathrm{pls}}-1} \left\{ \int_0^T \left((\lambda + 2\mu + \alpha^2 Q) \frac{\partial \lambda_{u_{\mathrm{b}}}}{\partial x} + \alpha Q \frac{\partial \lambda_w}{\partial x} \right) \delta u_{\mathrm{b}} dt \bigg|_{x_i^-} \right. \\
&\qquad\qquad \left. - \int_0^T \left((\lambda + 2\mu + \alpha^2 Q) \frac{\partial \lambda_{u_{\mathrm{b}}}}{\partial x} + \alpha Q \frac{\partial \lambda_w}{\partial x} \right) \delta u_{\mathrm{b}} dt \bigg|_{x_i^+} \right\} \\
&+ \sum_{i=p+1}^{p+N_{\mathrm{pls}}-1} \left\{ \int_0^T \lambda_w \left(\alpha Q \frac{\partial \delta u_{\mathrm{b}}}{\partial x} + Q \frac{\partial \delta w}{\partial x} \right) dt \bigg|_{x_i^-} \right. \\
&\qquad\qquad \left. - \int_0^T \lambda_w \left(\alpha Q \frac{\partial \delta u_{\mathrm{b}}}{\partial x} + Q \frac{\partial \delta w}{\partial x} \right) \bigg|_{x_i^+} dt \right\} \\
&- \sum_{i=p+1}^{p+N_{\mathrm{pls}}-1} \left\{ \int_0^T \left(\alpha Q \frac{\partial \lambda_{u_{\mathrm{b}}}}{\partial x} + Q \frac{\partial \lambda_w}{\partial x} \right) \delta w dt \bigg|_{x_i^-} \right. \\
&\qquad\qquad \left. - \int_0^T \left(\alpha Q \frac{\partial \lambda_{u_{\mathrm{b}}}}{\partial x} + Q \frac{\partial \lambda_w}{\partial x} \right) \delta w dt \bigg|_{x_i^+} \right\}. \qquad \text{(D.8)}
\end{aligned}
$$

The vanishing of (D.8) recovers the boundary and interface conditions of the adjoint problem shown in (5.19)–(5.21c). Lastly, we show $\delta_{u,w}\mathcal{A}^T$:

$$\begin{aligned}
\delta_{u,w}\mathcal{A}^T = & -\int_0^{x_p} \lambda_{u_\mathrm{a}}\rho\frac{\partial \delta u_\mathrm{a}}{\partial t}dx\bigg|_{t=T} + \int_0^{x_p} \frac{\partial \lambda_{u_\mathrm{a}}}{\partial t}\rho\delta u_\mathrm{a}dx\bigg|_{t=T} \\
& - \int_{x_{p+N_\mathrm{pls}}}^{L} \lambda_{u_\mathrm{a}}\rho\frac{\partial \delta u_\mathrm{a}}{\partial t}dx\bigg|_{t=T} + \int_{x_{p+N_\mathrm{pls}}}^{L} \frac{\partial \lambda_{u_\mathrm{a}}}{\partial t}\rho\delta u_\mathrm{a}dx\bigg|_{t=T} \\
& - \int_{x_p}^{x_{p+N_\mathrm{pls}}} \lambda_{u_\mathrm{b}}\rho\frac{\partial \delta u_\mathrm{b}}{\partial t}dx\bigg|_{t=T} + \int_{x_p}^{x_{p+N_\mathrm{pls}}} \frac{\partial \lambda_{u_\mathrm{b}}}{\partial t}\rho\delta u_\mathrm{b}dx\bigg|_{t=T} \\
& - \int_{x_p}^{x_{p+N_\mathrm{pls}}} \lambda_{w}\rho_f\frac{\partial \delta u_\mathrm{b}}{\partial t}dx\bigg|_{t=T} + \int_{x_p}^{x_{p+N_\mathrm{pls}}} \frac{\partial \lambda_{w}}{\partial t}\rho_f\delta u_\mathrm{b}dx\bigg|_{t=T} \\
& + \int_{x_p}^{x_{p+N_\mathrm{pls}}} \mathcal{E}\rho_f\frac{\partial w}{\partial t}\delta w dx\bigg|_{t=T} - \int_{x_p}^{x_{p+N_\mathrm{pls}}} \frac{\lambda_w}{k}\delta w dx\bigg|_{t=T} \\
& - \int_{x_p}^{x_{p+N_\mathrm{pls}}} \lambda_{u_\mathrm{b}}\rho_f\frac{\partial \delta w}{\partial t}dx\bigg|_{t=T} + \int_{x_p}^{x_{p+N_\mathrm{pls}}} \frac{\partial \lambda_{u_\mathrm{b}}}{\partial t}\rho_f\delta w dx\bigg|_{t=T} \\
& - \int_{x_p}^{x_{p+N_\mathrm{pls}}} \lambda_{w}\frac{\rho_f}{n}\frac{\partial \delta w}{\partial t}dx\bigg|_{t=T} + \int_{x_p}^{x_{p+N_\mathrm{pls}}} \frac{\partial \lambda_{w}}{\partial t}\frac{\rho_f}{n}\delta w dx\bigg|_{t=T} \\
& + \lambda_L(t)\frac{(\lambda(L)+2\mu(L))}{c}\delta u_\mathrm{a}(L,t)\bigg|_{t=T}. \qquad \text{(D.9)}
\end{aligned}$$

The vanishing of (D.9) recovers the final value conditions of the adjoint problem shown in (5.22a)–(5.22c).

D.2 The third condition

As the third optimality condition, we obtain the variation of $\mathcal{A}$ with respect to the control variable ξ in the following manner:

$$
\begin{aligned}
\delta_\xi \mathcal{A} =& \frac{\partial \mathcal{A}}{\partial \xi} \\
=& \mathcal{E} \int_{x_p}^{x_{p+N\mathrm{pls}}} \rho_f \frac{\partial w}{\partial t} \dot{w} dx \bigg|_{t=T} - \mathcal{E} \int_{x_p}^{x_{p+N\mathrm{pls}}} \int_0^T \rho_f \frac{\partial^2 w}{\partial t^2} \dot{w} dtdx \\
&+ \int_0^{x_p} \int_0^T \dot{\lambda}_{u_a} \left\{ \frac{\partial}{\partial x} \left((\lambda + 2\mu) \frac{\partial u_{\mathrm{a}}}{\partial x} \right) - \rho \frac{\partial^2 u_{\mathrm{a}}}{\partial t^2} \right\} dtdx \\
&+ \int_0^{x_p} \int_0^T \lambda_{u_a} \left\{ \frac{\partial}{\partial x} \left((\lambda + 2\mu) \frac{\partial \dot{u}_{\mathrm{a}}}{\partial x} \right) - \rho \frac{\partial^2 \dot{u}_{\mathrm{a}}(x,t)}{\partial t^2} \right\} dtdx \\
&+ \int_{x_{p+N\mathrm{pls}}}^{L} \int_0^T \dot{\lambda}_{u_a} \left\{ \frac{\partial}{\partial x} \left((\lambda + 2\mu) \frac{\partial u_{\mathrm{a}}}{\partial x} \right) - \rho \frac{\partial^2 u_{\mathrm{a}}}{\partial t^2} \right\} dtdx \\
&+ \int_{x_{p+N\mathrm{pls}}}^{L} \int_0^T \lambda_{u_a} \left\{ \frac{\partial}{\partial x} \left((\lambda + 2\mu) \frac{\partial \dot{u}_{\mathrm{a}}}{\partial x} \right) - \rho \frac{\partial^2 \dot{u}_{\mathrm{a}}}{\partial t^2} \right\} dtdx \\
&+ \int_{x_p}^{x_{p+N\mathrm{pls}}} \int_0^T \dot{\lambda}_{u_b} \left\{ \frac{\partial}{\partial x} \left((\lambda + 2\mu + \alpha^2 Q) \frac{\partial u_{\mathrm{b}}}{\partial x} + \alpha Q \frac{\partial w}{\partial x} \right) \right. \\
&\qquad\qquad\qquad \left. - \rho \frac{\partial^2 u_{\mathrm{b}}}{\partial t^2} - \rho_f \frac{\partial^2 w}{\partial t^2} \right\} dtdx \\
&+ \int_{x_p}^{x_{p+N\mathrm{pls}}} \int_0^T \lambda_{u_b} \left\{ \frac{\partial}{\partial x} \left((\lambda + 2\mu + \alpha^2 Q) \frac{\partial \dot{u}_{\mathrm{b}}}{\partial x} + \alpha Q \frac{\partial \dot{w}}{\partial x} \right) \right. \\
&\qquad\qquad\qquad \left. - \rho \frac{\partial^2 \dot{u}_{\mathrm{b}}}{\partial t^2} - \rho_f \frac{\partial^2 \dot{w}}{\partial t^2} \right\} dtdx \\
&+ \int_{x_p}^{x_{p+N\mathrm{pls}}} \int_0^T \dot{\lambda}_{w} \left\{ \frac{\partial}{\partial x} \left(\alpha Q \frac{\partial u_{\mathrm{b}}}{\partial x} + Q \frac{\partial w}{\partial x} \right) - \frac{1}{k} \frac{\partial w}{\partial t} \right. \\
&\qquad\qquad\qquad \left. - \rho_f \frac{\partial^2 u_{\mathrm{b}}}{\partial t^2} - \frac{\rho_f}{n} \frac{\partial^2 w}{\partial t^2} \right\} dtdx
\end{aligned}
$$

$$
\begin{aligned}
&+\int_{x_p}^{x_{p+N\mathrm{pls}}}\int_0^T \lambda_w \left\{ \frac{\partial}{\partial x}\left(\alpha Q \frac{\partial \dot{u}_{\mathrm{b}}}{\partial x} + Q\frac{\partial \dot{w}}{\partial x}\right) - \frac{1}{k}\frac{\partial \dot{w}}{\partial t} \right.\\
&\qquad\qquad\qquad\qquad \left. -\rho_f \frac{\partial^2 \dot{u}_{\mathrm{b}}}{\partial t^2} - \frac{\rho_f}{n}\frac{\partial^2 \dot{w}}{\partial t^2} \right\} dt dx\\
&+\int_0^T \dot{\lambda}_0(t)\left\{ (\lambda(0)+2\mu(0))\frac{\partial u_{\mathrm{a}}}{\partial x}(0,t) + f(t) \right\} dt\\
&+\int_0^T \lambda_0(t)\left\{ (\lambda(0)+2\mu(0))\frac{\partial \dot{u}_{\mathrm{a}}}{\partial x}(0,t) + \dot{f}(t) \right\} dt\\
&+\int_0^T \dot{\lambda}_L(t)(\lambda(L)+2\mu(L))\left\{ \frac{\partial u_{\mathrm{a}}}{\partial x}(L,t) + \frac{1}{c}\frac{\partial u_{\mathrm{a}}}{\partial t}(L,t) \right\} dt\\
&+\int_0^T \lambda_L(t)(\lambda(L)+2\mu(L))\left\{ \frac{\partial \dot{u}_{\mathrm{a}}}{\partial x}(L,t) + \frac{1}{c}\frac{\partial \dot{u}_{\mathrm{a}}}{\partial t}(L,t) \right\} dt, \qquad \text{(D.10)}
\end{aligned}
$$

where $(\dot{\ })$ denotes the derivative of the subtended variable with respect to ξ. Because of the satisfaction of the state PDEs, (D.10) reduces to the following:

$$
\begin{aligned}
\delta_\xi \mathcal{A} =& \frac{\partial \mathcal{A}}{\partial \xi}\\
=& \mathcal{E}\int_{x_p}^{x_{p+N\text{pls}}} \rho_f \frac{\partial w}{\partial t}\dot{w}dx\Big|_{t=T} - \mathcal{E}\int_{x_p}^{x_{p+N\text{pls}}}\int_0^T \rho_f \frac{\partial^2 w}{\partial t^2}\dot{w}dtdx\\
&+ \int_0^{x_p}\int_0^T \lambda_{u_a}\left\{\frac{\partial}{\partial x}\left((\lambda+2\mu)\frac{\partial \dot{u}_\text{a}}{\partial x}\right) - \rho\frac{\partial^2 \dot{u}_\text{a}}{\partial t^2}\right\}dtdx\\
&+ \int_{x_{p+N\text{pls}}}^{L}\int_0^T \lambda_{u_a}\left\{\frac{\partial}{\partial x}\left((\lambda+2\mu)\frac{\partial \dot{u}_\text{a}}{\partial x}\right) - \rho\frac{\partial^2 \dot{u}_\text{a}}{\partial t^2}\right\}dtdx\\
&+ \int_{x_p}^{x_{p+N\text{pls}}}\int_0^T \lambda_{u_b}\left\{\frac{\partial}{\partial x}\left((\lambda+2\mu+\alpha^2 Q)\frac{\partial \dot{u}_\text{b}}{\partial x} + \alpha Q\frac{\partial \dot{w}}{\partial x}\right)\right.\\
&\qquad\qquad\qquad\left. -\rho\frac{\partial^2 \dot{u}_\text{b}}{\partial t^2} - \rho_f\frac{\partial^2 \dot{w}}{\partial t^2}\right\}dtdx\\
&+ \int_{x_p}^{x_{p+N\text{pls}}}\int_0^T \lambda_w(x,t)\left\{\frac{\partial}{\partial x}\left(\alpha Q\frac{\partial \dot{u}_\text{b}}{\partial x} + Q\frac{\partial \dot{w}}{\partial x}\right) - \frac{1}{k}\frac{\partial \dot{w}}{\partial t}\right.\\
&\qquad\qquad\qquad\left. -\rho_f\frac{\partial^2 \dot{u}_\text{b}}{\partial t^2} - \frac{\rho_f}{n}\frac{\partial^2 \dot{w}}{\partial t^2}\right\}dtdx\\
&+ \int_0^T \lambda_0(t)\left\{(\lambda(0)+2\mu(0))\frac{\partial \dot{u}_\text{a}}{\partial x}(0,t) + \dot{f}(t)\right\}dt\\
&+ \int_0^T \lambda_L(t)(\lambda(L)+2\mu(L))\left\{\frac{\partial \dot{u}_\text{a}}{\partial x}(L,t) + \frac{1}{c}\frac{\partial \dot{u}_\text{a}}{\partial t}(L,t)\right\}dt.
\end{aligned}
\tag{D.11}
$$

Next, we take integration by parts of (D.11) with respect to space and time. $\delta_\xi\mathcal{A}$ is then split into three parts as $\delta_\xi\mathcal{A} = \delta_\xi\mathcal{A}^{\int\int} + \delta_\xi\mathcal{A}^{T} + \delta_\xi\mathcal{A}^{\text{etc}}$, where $\delta_\xi\mathcal{A}^{\int\int}$ denotes the terms that include the spatial and temporal integrals of the adjoint PDEs; $\delta_\xi\mathcal{A}^{T}$ denotes the spatial integral terms temporally associated with time $t = T$ only; $\delta_\xi\mathcal{A}^{\text{etc}}$ denotes the temporal integrals associated with specific locations. First, we show $\delta_\xi \mathcal{A}^{\int\int}$ in the following:

$$
\begin{aligned}
\delta_\xi \mathcal{A} = & \int_0^{x_p} \int_0^T \left\{ \frac{\partial}{\partial x} \left((\lambda + 2\mu) \frac{\partial \lambda_{u_\mathrm{a}}}{\partial x} \right) - \rho \frac{\partial^2 \lambda_{u_\mathrm{a}}}{\partial t^2} \right\} \dot{u}_\mathrm{a} dt dx \\
& + \int_{x_{p+N\mathrm{pls}}}^{L} \int_0^T \left\{ \frac{\partial}{\partial x} \left((\lambda + 2\mu) \frac{\partial \lambda_{u_\mathrm{a}}}{\partial x} \right) - \rho \frac{\partial^2 \lambda_{u_\mathrm{a}}}{\partial t^2} \right\} \dot{u}_\mathrm{a} dt dx \\
& + \int_{x_p}^{x_{p+N\mathrm{pls}}} \int_0^T \left\{ \frac{\partial}{\partial x} \left((\lambda + 2\mu + \alpha^2 Q) \frac{\partial \lambda_{u_\mathrm{b}}}{\partial x} \right) + \frac{\partial}{\partial x} \left(\alpha Q \frac{\partial \lambda_w}{\partial x} \right) \right. \\
& \qquad\qquad \left. - \rho \frac{\partial^2 \lambda_{u_\mathrm{b}}}{\partial t^2} - \rho_f \frac{\partial^2 \lambda_w}{\partial t^2} \right\} \dot{u}_\mathrm{b} dt dx \\
& + \int_{x_p}^{x_{p+N\mathrm{pls}}} \int_0^T \left\{ \frac{\partial}{\partial x} \left(\alpha Q \frac{\partial \lambda_{u_\mathrm{b}}}{\partial x} \right) + \frac{\partial}{\partial x} \left(Q \frac{\partial \lambda_w}{\partial x} \right) + \frac{1}{k} \frac{\partial \lambda_w}{\partial t} \right. \\
& \qquad\qquad \left. - \rho_f \frac{\partial^2 \lambda_{u_\mathrm{b}}}{\partial t^2} - \frac{\rho_f}{n} \frac{\partial^2 \lambda_w}{\partial t^2} - \mathcal{E} \rho_f \frac{\partial^2 w}{\partial t^2} \right\} \dot{w} dt dx. \qquad \text{(D.12)}
\end{aligned}
$$

(D.12) vanishes because of the satisfaction of the adjoint PDEs. Second, $\delta_\xi \mathcal{A}^T$ is the following:

$$
\begin{aligned}
&\delta_\xi \mathcal{A}^T \\
=& - \int_0^{x_p} \lambda_{u_\mathrm{a}} \rho \frac{\partial \dot{u}_\mathrm{a}}{\partial t} dx \bigg|_{t=T} + \int_0^{x_p} \frac{\partial \lambda_{u_\mathrm{a}}}{\partial t} \rho \dot{u}_\mathrm{a} dx \bigg|_{t=T} \\
&- \int_{x_{p+N\mathrm{pls}}}^{L} \lambda_{u_\mathrm{a}} \rho \frac{\partial \dot{u}_\mathrm{a}}{\partial t} dx \bigg|_{t=T} + \int_{x_{p+N\mathrm{pls}}}^{L} \frac{\partial \lambda_{u_\mathrm{a}}}{\partial t} \rho \dot{u}_\mathrm{a} dx \bigg|_{t=T} \\
&- \int_{x_p}^{x_{p+N\mathrm{pls}}} \lambda_{u_\mathrm{b}} \rho \frac{\partial \dot{u}_\mathrm{b}}{\partial t} dx \bigg|_{t=T} + \int_{x_p}^{x_{p+N\mathrm{pls}}} \frac{\partial \lambda_{u_\mathrm{b}}}{\partial t} \rho \dot{u}_\mathrm{b} dx \bigg|_{t=T} \\
&- \int_{x_p}^{x_{p+N\mathrm{pls}}} \lambda_w \rho_f \frac{\partial \dot{u}_\mathrm{b}}{\partial t} dx \bigg|_{t=T} + \int_{x_p}^{x_{p+N\mathrm{pls}}} \frac{\partial \lambda_w}{\partial t} \rho_f \dot{u}_\mathrm{b} dx \bigg|_{t=T} \\
&- \int_{x_p}^{x_{p+N\mathrm{pls}}} \lambda_{u_\mathrm{b}} \rho_f \frac{\partial \dot{w}}{\partial t} dx \bigg|_{t=T} + \int_{x_p}^{x_{p+N\mathrm{pls}}} \frac{\partial \lambda_{u_\mathrm{b}}}{\partial t} \rho_f \dot{w} dx \bigg|_{t=T} \\
&- \int_{x_p}^{x_{p+N\mathrm{pls}}} \lambda_w \frac{\rho_f}{n} \frac{\partial \dot{w}}{\partial t} dx \bigg|_{t=T} + \int_{x_p}^{x_{p+N\mathrm{pls}}} \frac{\partial \lambda_w}{\partial t} \frac{\rho_f}{n} \dot{w} dx \bigg|_{t=T} \\
&- \int_{x_p}^{x_{p+N\mathrm{pls}}} \frac{\lambda_w}{k} \dot{w} dx \bigg|_{t=T} + \mathcal{E} \int_{x_p}^{x_{p+N\mathrm{pls}}} \rho_f \frac{\partial w}{\partial t} \dot{w} dx \bigg|_{t=T} \\
&+ \lambda_L(t) \frac{(\lambda(L) + 2\mu(L))}{c} \dot{u}_\mathrm{a}(L,t) \bigg|_{t=T} .
\end{aligned}
\tag{D.13}
$$

Because of the final-value condition, in the adjoint problem, shown in (5.22a), (D.13) is simplified to the following:

$$
\begin{aligned}
\delta_\xi \mathcal{A}^T =& \int_{x_p}^{x_{p+N\mathrm{pls}}} \left(\frac{\partial \lambda_{u_\mathrm{b}}}{\partial t} \rho + \frac{\partial \lambda_w}{\partial t} \rho_f \right) \dot{u}_\mathrm{b} dx \bigg|_{t=T} \\
&+ \int_{x_p}^{x_{p+N\mathrm{pls}}} \left(\frac{\partial \lambda_{u_\mathrm{b}}}{\partial t} \rho_f + \frac{\partial \lambda_w}{\partial t} \frac{\rho_f}{n} - \frac{\lambda_w}{k} + \mathcal{E} \rho_f \frac{\partial w}{\partial t} \right) \dot{w} dx \bigg|_{t=T} .
\end{aligned}
\tag{D.14}
$$

Then, due to the satisfaction of the other adjoint final value conditions, shown in (5.22b) and (5.22c), (D.14) vanishes, i.e., $\delta_\xi \mathcal{A}^\mathrm{T} = 0$. Lastly, $\delta_\xi \mathcal{A}^\mathrm{etc}$ is the following:

$$
\begin{aligned}
&\delta_\xi \mathcal{A}^{\mathrm{etc}} \\
&= \left[\int_0^T \lambda_{u_\mathrm{a}}(\lambda+2\mu)\frac{\partial \dot{u}_\mathrm{a}}{\partial x}dt\right]_{x=0}^{x_p^-} - \left[\int_0^T (\lambda+2\mu)\frac{\partial \lambda_{u_\mathrm{a}}}{\partial x}\dot{u}_\mathrm{a}dt\right]_{x=0}^{x_p^-} \\
&+ \left[\int_0^T \lambda_{u_\mathrm{a}}(\lambda+2\mu)\frac{\partial \dot{u}_\mathrm{a}}{\partial x}dt\right]_{x^+_{p+N\mathrm{pls}}}^{x=L} - \left[\int_0^T (\lambda+2\mu)\frac{\partial \lambda_{u_\mathrm{a}}}{\partial x}\dot{u}_\mathrm{a}dt\right]_{x^+_{p+N\mathrm{pls}}}^{x=L} \\
&+ \left[\int_0^T \lambda_{u_\mathrm{b}}(\lambda+2\mu+\alpha^2 Q)\frac{\partial \dot{u}_\mathrm{b}}{\partial x}dt\right]_{x_p^+}^{x^-_{p+N\mathrm{pls}}} \\
&- \left[\int_0^T (\lambda+2\mu+\alpha^2 Q)\frac{\partial \lambda_{u_\mathrm{b}}}{\partial x}\dot{u}_\mathrm{b}dt\right]_{x_p^+}^{x^-_{p+N\mathrm{pls}}} \\
&+ \left[\int_0^T \lambda_w \alpha Q\frac{\partial \dot{u}_\mathrm{b}}{\partial x}dt\right]_{x_p^+}^{x^-_{p+N\mathrm{pls}}} - \left[\int_0^T \alpha Q\frac{\partial \lambda_w}{\partial x}\dot{u}_\mathrm{b}dt\right]_{x_p^+}^{x^-_{p+N\mathrm{pls}}} \\
&+ \left[\int_0^T \lambda_{u_\mathrm{b}} \alpha Q\frac{\partial \dot{w}}{\partial x}dt\right]_{x_p^+}^{x^-_{p+N\mathrm{pls}}} - \left[\int_0^T \alpha Q\frac{\partial \lambda_{u_\mathrm{b}}}{\partial x}\dot{w}dt\right]_{x_p^+}^{x^-_{p+N\mathrm{pls}}} \\
&+ \left[\int_0^T \lambda_w Q\frac{\partial \dot{w}}{\partial x}dt\right]_{x_p^+}^{x^-_{p+N\mathrm{pls}}} - \left[\int_0^T Q\frac{\partial \lambda_w}{\partial x}\dot{w}dt\right]_{x_p^+}^{x^-_{p+N\mathrm{pls}}} \\
&+ \int_0^T \lambda_0(t)\left[(\lambda(0)+2\mu(0))\frac{\partial \dot{u}_\mathrm{a}}{\partial x}(0,t)+\dot{f}(t)\right]dt \\
&+ \int_0^T \lambda_L(t)(\lambda(L)+2\mu(L))\left[\frac{\partial \dot{u}_\mathrm{a}}{\partial x}(L,t)\right]dt \\
&- \int_0^T \frac{\partial \lambda_L(t)}{\partial t}\frac{(\lambda(L)+2\mu(L))}{c}\dot{u}_\mathrm{a}(L,t)dt. \qquad \text{(D.15)}
\end{aligned}
$$

Due to the boundary and interface conditions in the adjoint problem, as well as the zero relative displacement of pore fluid at $x = x_p$ and $x = x^-_{p+N\mathrm{pls}}$ in the state problem, (D.15) reduces to:

$$
\delta_\xi \mathcal{A}^{\mathrm{etc}} = \int_0^T \lambda_0(t)\dot{f}(t)dt = \int_0^T \lambda_{u_\mathrm{a}}(t)\frac{\partial f(t)}{\partial f_i}dt, \qquad \text{(D.16)}
$$

which is the final form of the variation $\delta_\xi \mathcal{A}$. Hence, the vanishing of $\delta_\xi \mathcal{A}$ recovers the control equation (5.25).

Bibliography

[1] M. Abramowitz and I. Stegun. *Handbook of Mathematical Functions*. Dover Publication, 1964.

[2] M. M. Amro, M. A. Al-Mobarky, and E. S. Al-Homadhi. Improved oil recovery by application of ultrasound waves to waterflooding. In *SPE Middle East Oil and Gas Show and Conference, SPE 105370-MS*, Kingdom of Bahrain, 2007. Society of Petroleum Engineers.

[3] V. S. Averbakh, S. N. Vlasov, and Y. M. Zaslavsky. Motion of a liquid droplet in a capillary under the action of static force and an acoustic field. *Radiophysics and Quantum Electronics*, 43:142–147, 2000.

[4] R. Bachrach, A. Nur, and A. Agnon. Liquefaction and dynamic poroelasticity in soft sediments. *Journal of Geophysical Research*, 106:13,515–13,526, 2001.

[5] V. I. Barabanov and M. V. Pavlov. Increasing oil production from depleted fields through seismic stimulation. *First break*, 27:97–102, 2009.

[6] F. V. D. Bas, E. D. Rouffignac, P. Zuiderwijk, and D. V. Batenburg. Near wellbore stimulation by acoustic waves. In *Abu Dhabi International Conference and Exhibition, SPE 88767-MS*, Abu Dhabi, United Arab Emirates, 2004. Society of Petroleum Engineers.

[7] E. B. Becker, G. F. Carey, and J. T. Oden. *Finite Elements*. Prentice Hall, 1981.

[8] R. E. Beckham, A. Abdel-Fattah, P. M. Roberts, R. Ibrahim, and S. Tarimala. Mobilization of colloidal particles by low-frequency dynamic stress stimulation. *Langmuir*, 26:19–27, 2010.

[9] I. A. Beresnev. Theory of vibratory mobilization on nonwetting fluids entrapped in pore constrictions. *Geophysics*, 71:47–56, 2006.

[10] I. A. Beresnev and W. Deng. Viscosity effects in vibratory mobilization of residual oil. *Geophysics*, 75:79–85, 2010.

[11] I. A. Beresnev and P. Johnson. Elastic-wave stimulation of oil production: A review of methods and results. *Geophysics*, 59:1000–1017, 1994.

[12] M. A. Biot. Theory of propagation of elastic waves in a fluid-saturated porous solid. I. Low-frequency range. *Journal of the Acoustical Society of America*, 28:168–178, 1956.

[13] M. A. Biot. Mechanics of deformation and acoustic propagation in porous media. *Journal of Applied Physics*, 33:1482–1498, 1962.

[14] T. Bourbie, O. Coussy, and B. Zinszner. *Acoustics of Porous Media*. Gulf Publishing Company, 1987.

[15] C. Bremmer, G. Harris, A. Kosmala, B. Nicholson, A. Ollre, M. Pearcy, C. J. Salmas, and S. C. Solanki. Evolving technologies: electrical submersible pumps. *Schlumberger Oilfield Review*, pages 30–43, 2006.

[16] S. C. Chapra and R. P. Canale. *Numerical Methods for Engineers*. McGraw-Hill, 2006.

[17] H. Cinco-L., Samaniego-V., F., and N. Dominguez-A. Transient pressure behavior for a well with a finite-conductivity vertical fracture. *SPE Journal*, pages 253–264, 1978.

[18] J. E. Elkhoury, E. E. Brodsky, and D. C. Agnew. Seismic waves increase permeability. *Nature*, 441:1135–1138, 2006.

[19] R. Fletcher and C. M. Reeves. Function minimization by conjugate gradients. *Computer Journal*, 7:149–154, 1951.

[20] A. Gajo. Influence of viscous coupling in propagation of elastic waves in saturated soil. *Journal of Geotechnical Engineering*, 121:636–644, 1995.

[21] A. Gajo and L. Mongiovi. An analytical solution for the transient response of saturated linear elastic porous media. *International Journal For Numerical and Analytical Methods in Geomechanics*, 19:399–413, 1995.

[22] A. Gajo, A. Saetta, and R. Vitaliani. Evaluation of three- and two-field finite element methods for the dynamical response of saturated soil. *International Journal For Numerical Methods in Engineering*, 37:1231–1247, 1994.

[23] F. Gassmann. Uber die elastizitat poroser medien. *Veirteljahrsschrift der Naturforschenden Gesellschaft in Zurich*, 96:1–23, 1951.

[24] P. Göransson. A 3-D, symmetric, finite element formulation of the Biot equations with application to acoustic wave propagation through an elastic porous medium. *International Journal for Numerical Methods in Engineering*, 41:167–192, 1998.

[25] K. F. Graff. *Wave Motion in Elastic Solids*. Dover Publications, 1991.

[26] J. Groenenboom, S. Wong, T. Meling, R. Zschuppe, and B. Davidson. Pulsed water injection during waterflooding. In *International Improved Oil Recovery Conference in Asia Pacific SPE 84856*, Kuala Lumpur, Malaysia, 2003. Society of Petroleum Engineers.

[27] X. Guo, Z. Du, G. Li, and Z. Shu. High frequency vibration recovery enhancement technology in the heavy oil fields of China. In *SPE International Thermal Operations and Heavy Oil Symposium and Western Regional Meeting SPE 86956*, Bakersfield, California, 2004. Society of Petroleum Engineers.

[28] T. Hamida and T. Babadagli. Capillary interaction of different oleic and aqueous phases between matrix and fracture under ultrasonic waves. In *SPE Europec/EAGE Annual Conference, SPE 94105*, Madrid, Spain, 2005. Society of Petroleum Engineers.

[29] T. Hamida and T. Babadagli. Effect of ultrasonic waves on the capillary imbibition recovery of oil. In *SPE Asia Pacific Oil and Gas Conference and Exhibition, SPE 92124*, Jakarta, Indonesia, 2005. Society of Petroleum Engineers.

[30] T. Hamida and T. Babadagli. Effects of ultrasonic waves on immiscible and miscible displacement in porous media. In *SPE Annual Technical Conference and Exhibition, SPE 95327*, Dallas, Texas, 2005. Society of Petroleum Engineers.

[31] M. Hilpert, G. H. Jirka, and E. J. Plate. Capillarity-induced resonance of oil blobs in capillary tubes and porous media. *Geophysics*, 65:874–883, 2000.

[32] M. Huang and O. C. Zienkiewicz. New unconditionally stable staggered solution procedures for coupled soil-pore fluid dynamic problems. *International Journal For Numerical Methods in Engineering*, 43:1029–1052, 1998.

[33] C. Huh. Improved oil recovery by seismic vibration: a preliminary assessment of possible mechanisms. In *International Petroleum Conference SPE 103870*, Cancun, Mexico, 2006. Society of Petroleum Engineers.

[34] P. P. Iassonov and I. A. Beresnev. A model for enhanced fluid percolation in porous media by application of low-frequency elastic waves. *Journal of Geophysical Research*, 108:2138–2146, 2003.

[35] The International Energy Agency (IEA). *World Energy Outlook 2010*. The International Energy Agency, 2010.

[36] C. Jeong, C. Huh, and L. F. Kallivokas. On the feasibility of inducing oil mobilization in existing reservoirs via wellbore harmonic fluid action.

Journal of Petroleum Science and Engineering, 76:116–123, 2011.

[37] C. Jeong, L. F. Kallivokas, C. Huh, and L. W. Lake. Optimization of sources for focusing wave energy in targeted formations. *Journal of Geophysics and Engineering*, 7:242–256, 2010.

[38] C. Jeong, L. F. Kallivokas, C. Huh, and L. W. Lake. Maximization of oil mobility within a hydrocarbon reservoir for elastic wave-based enhanced oil recovery. In *SPE Annual Technical Conference and Exhibition*, Denver, Colorado, October 30–November 2 2011. Society of Petroleum Engineers.

[39] P. A. Johnson, P. Bodin, J. Gomberg, F. Pearce, F. Lawrence, and F.-Y. Menq. Inducing in situ, nonlinear soil response applying an active source. *Journal of Geophysical Research*, 114:B05304, 2009.

[40] M. E. Kalinski. Effect of vibroseis arrays on ground vibrations: A numerical study. *Journal of Environmental and Engineering Geophysics*, 12:281–287, 2007.

[41] W. Karush. *Minima of functions of several variables with inequalities as side constraints*. Master thesis, The University of Chicago, 1939.

[42] S. Kostrov and W. Wooden. In situ seismic stimulation shows promise for revitalizing mature fields. *Oil and Gas Journal*, pages 2–25, 2005.

[43] S. Kostrov and W. Wooden. Possible mechanisms and case studies for enhancement of oil recovery and production using in-situ seismic stimu-

lation. In *SPE/DOE Symposium on Improved Oil Recovery SPE 114025*, Tulsa, Oklahoma, USA, 2008. Society of Petroleum Engineers.

[44] O. L. Kouznetsov, E. M. Simkin, G. V. Chilingar, and S. A. Katz. Improved oil recovery by application of vibro-energy to waterflooded sandstones. *Journal of Petroleum Science and Engineering*, 19:191–200, 1998.

[45] S. Kucukcoban. *The inverse medium problem in PML-truncated elastic media*. Doctoral dissertation, The University of Texas at Austin, 2010.

[46] S. Kucukcoban and L. F. Kallivokas. Mixed perfectly-matched-layers for direct transient analysis. In *The 2009 Joint ASCE-ASME-SES Conference on Mechanics and Materials*, Blacksburg, VA, June 24-27 2009.

[47] S. Kucukcoban and L. F. Kallivokas. Mixed perfectly-matched-layers for direct transient analysis in 2D elastic heterogeneous media. *Computer Methods in Applied Mechanics and Engineering*, 200:57–76, 2011.

[48] H. W. Kuhn and A. W. Tucker. Nonlinear programming. In J. Neyman, editor, *The Second Berkeley Symposium on Mathematical Statistics and Probability(University of California Press)*, 1951.

[49] O. L. Kuznetsov, E. M. Simkin, G. V. Chilingar, M. V. Gorfunkel, and J. O. Robertson. Seismic techniques of enhanced oil recovery: experimental and field results. *Energy Source*, 24:877–889, 2002.

[50] V. V. Kuznetsov and A. V. Nikolaev. *Elaboration of physical principles of vibro-seismic action on oil reservoir (Razrabotka fizicheskikh os-*

nov vibroseismicheskogo vozdeystviya na neftianouyou zalezh). Report (in Russian), Institute of Physics of the Earth, 1990.

[51] István Lakatos. Global oil demand and role of chemical EOR methods in the 21st century. *International Journal of Oil, Gas and Coal Technology*, 1:46–64, 2008.

[52] L. W. Lake. *Enhanced Oil Recovery.* Englewood Cliffs, NJ: Prentice Hall, 1989.

[53] L. W. Lake, R. L. Schmidt, and P. B. Venuto. A niche for enhanced oil recovery in the 1990s. *Schlumberger Oilfield Review*, 4:55–61, 1992.

[54] R. W. Lewis and B. A. Schrefler. *The Finite Element Method in the Static and Dynamic Deformation and Consolidation of Porous Media.* Wiley, 1999.

[55] W. Li, R. D. Vigil, I. A. Beresnev, P. P. Iassonov, and R. Ewing. Vibration-induced mobilization of trapped oil ganglia in porous media: Experimental validation of a capillary-physics mechanism. *Journal of Colloid and Interface Science*, 289:193–199, 2005.

[56] Y. Li, R. C. K. Wong, and K. C. Yeung. Analysis of transient pressure response near a horizontal well – a coupled diffusion-deformation approach. *Journal of Canadian Petroleum Technology*, 39:56–61, 2000.

[57] C. S. Matthews and D. G. Russell. *Pressure buildup and flow tests in wells.* Soc. Petrol. Eng., 1967.

[58] V. N. Nikolaevskiy, G. P. Lopukhov, Y. Liao, and M. J. Economides. Residual oil reservoir recovery with seismic vibrations. *SPE Production and Facilities*, pages 89–94, 1996.

[59] J. Nocedal and S. Wright. *Numerical Optimization.* New York, NY: Springer, 2006.

[60] D. G. Osika. *Fluid Regime of Seismically Active Regions (Fluidniy Rejim Seismicheski-aktivnikh Oblastey)(in Russian).* Nauka Press, 1981.

[61] W. W. Owens and D. L. Archer. Waterflood pressure pulsing for fractured reservoirs. *Journal of Petroleum Technology*, pages 745–752, 1966.

[62] Y. Pan and R. N. Horne. Resonant behavior of saturated porous media. *Journal of Geophysical Research*, 105:11021–11208, 2000.

[63] B. N. Paulsson. *Nondestructive Downhole Seismic Vibrator Source and Processes of Utilizing the Vibrator to Obtain Information about Geologic Formations (Patent number: 4805725).* United States Patent, 1989.

[64] G. A. Pope and M. Baviere. *Reduction of capillary forces by surfactant. In: Baviere, M. (Editors), Basic Concepts in Enhanced Oil Recovery Processes.* Elsevier, Amsterdam, 1991.

[65] S. R. Pride, E. G. Flekkø, and O. Aursjø. Seismic stimulation for enhanced oil recovery. *Geophysics*, 73:23–35, 2008.

[66] P. M. Roberts and A. I. Abdel-Fattah. Seismic stress stimulation mobilizes colloids trapped in a porous rock. *Earth and Planetary Science Letters*, 284:538–543, 2009.

[67] P. M. Roberts, I. B. Esipov, and E. L. Majer. Elastic wave stimulation of oil reservoirs: Promising EOR technology? *The Leading Edge*, 22:448–453, 2003.

[68] P. M. Roberts, A. Sharma, V. Uddameri, M. Monagle, D. E. Dale, and L. K. Steck. Enhanced DNAPL transport in a sand core during dynamic stress stimulation. *Environmental Engineering Science*, 18:67–79, 2001.

[69] M. Schanz. Application of 3D time domain boundary element formulation to wave propagation in poroelastic solids. *Engineering Analysis with Boundary Elements*, 25:363–376, 2001.

[70] M. Schanz. Poroelastodynamics: linear models, analytical solutions, and numerical methods. *Applied Mechanics Reviews*, 62:030803, 2009.

[71] S. V. Serdyukov and M. V. Kurlenya. Seismic stimulation of oil reservoirs. *Russian Geology and Geophysics*, 48:960–967, 2007.

[72] B. R. Simon, J. S.-S. Wu, and O. C. Zienkiewicz. Evaluation of higher order, mixed and Hermitean finite element procedures for dynamic analysis of saturated porous media using one-dimensional models. *International Journal For Numerical and Analytical Methods in Geomechanics*, 10:483–499, 1986.

[73] B. R. Simon, O. C. Zienkiewicz, and D. K. Paul. An analytical solution for the transient response of saturated porous elastic solids. *International Journal For Numerical and Analytical Methods in Geomechanics*, 8:381–398, 1984.

[74] B. R. Simon, O. C. Zienkiewicz, and D. K. Paul. Evaluation of $u - w$ and $u - \pi$ finite element methods for the dynamic response of saturated porous media using one-dimensional models. *International Journal For Numerical and Analytical Methods in Geomechanics*, 10:461–462, 1986.

[75] M. N. Smimova. Effect of earthquakes on the oil yield of the Gudermes field (Northeastern Caucasus). *Izvestiya Academy of Sciences, USSR, Fizika Zemli (Physics of the Solid Earth)*, 12:71–76, 1968.

[76] T. Spanos, D. Shand, B. Davidson, M. Samaroo, and M. Dusseault. Pressure pulsing at the reservoir scale: a new IOR approach. *Journal of Canadian Petroleum Technology*, 42:16–28, 2003.

[77] K. V. Steinbrugge and D. F. Moran. An engineering study of the Southern California earthquake of July 21, 1952, and its aftershocks. *Bulletin of the Seismological Society of America*, 44:279–283, 1954.

[78] M. T. Stirpe, M. T. Guzman, E. Manrique, and V. Alvarado. Cyclic water injection simulations for evaluations of its potential in Lagocinco field. In *SPE/DOE Symposium on Improved Oil Recovery*, Tulsa, Oklahoma, USA, 2004. Society of Petroleum Engineers.

[79] L. Surguchev, A. Koundin, O. Melberg, T. Rolfsvåg, and W. P. Menard. Cyclic water injection: improved oil recovery at zero cost. *Petroleum Geoscience*, 8:89–95, 2002.

[80] E. T. Vogler and C. V. Chrysikopoulos. An experimental study of acoustically enhanced NAPL dissolution in porous media. *Environmental and Energy Engineering*, 12:3271–3280, 2004.

[81] G. I. Voytov, D. G. Osika, T. G. Grechukhina, and I. A. Plotnikov. Some geological and geochemical consequences of the Daghestan earthquake of may 14, 1970. *Transactions of the USSR Academy of Sciences, Earth Science Sections*, 202:576–579, 1972.

[82] R. V. Westermark, J. F. Brett, and D. R. Maloney. Enhanced oil recovery with downhole vibration stimulation. In *SPE Production and Operations Symposium, SPE 67303-MS*, Oklahoma City, Oklahoma, 2001. Society of Petroleum Engineers.

[83] R. V. Westermark, J. F. Brett, and D. R. Maloney. Using downhole vibration stimulation for enhanced oil recovery. *World Oil*, pages 57–66, 2001.

[84] J. E. White. *Underground sound application of seismic waves*. Elsevier, Amsterdam, 1983.

[85] T. Zhu and H. Xutao. Downhole harmonic vibration oil-displacement

system: a new IOR tool. In *SPE Western Regional Meeting SPE 94001-MS*, Irvine, California, 2005. Society of Petroleum Engineers.

[86] X. Zhu and G. A. Mcmechan. Numerical simulation of seismic response of poroelastic reservoirs using Biot theory. *Geophysics*, 56:328–339, 1991.

[87] O. C. Zienkiewicz and T. Shiomi. Dynamic behavior of saturated porous media; the generalized Biot formulation and its numerical solution. *International Journal For Numerical and Analytical Methods in Geomechanics*, 8:71–96, 1984.

Vita

Chanseok Jeong graduated from Hansung Science High School, Seoul, South Korea in February 1999, and received his Bachelor of Science in Civil Engineering from Yonsei University, Seoul in February 2003. As a recipient of a graduate research fellowship from the Korean Science and Engineering Foundation, he joined the graduate program in the Department of Civil, Architectural and Environmental Engineering at the University of Texas at Austin in August 2004. He earned his Master of Science in Engineering in Civil Engineering in December 2006 having completed his Master's Thesis on the "Shape detection and localization of a scatterer embedded in a halfplane." Following his MS studies he was admitted to the doctoral program at the University of Texas at Austin. In 2010, he was awarded the William S. Livingston Fellowship that is annually given to the most outstanding nominees among those nominated for the graduate school continuation fellowship at the University of Texas at Austin based on significant research accomplishments. Also in 2010, he was awarded the Society of Petroleum Engineers STAR Fellowship, and was a finalist for the Computational Mechanics Student Paper Competition organized by the Engineering Mechanics Institute (EMI) of ASCE. His finalist status was recognized at the EMI 2010 Conference in Los Angeles, CA in August 2010.

Permanent address: c.jeong@utexas.edu

This dissertation was typeset with LaTeX[†] by the author.

[†] LaTeX is a document preparation system developed by Leslie Lamport as a special version of Donald Knuth's TeX Program.